Manufacturing Gradients into Battery Electrode Architecture using Ultrasonic Spray Deposition

Matthew Tudball

A Thesis submitted to the Department of Chemical Engineering, University College London, in partial fulfilment of the requirements for the degree of Doctor of Philosophy.

Electrochemical Innovation Lab
Department of Chemical Engineering
University College London
2025

Declaration

I, Matthew Tudball, confirm that the work presented in my thesis is my own. Where information has been derived from other sources, I confirm that this has been indicated in the thesis

Name of candidate Signature of candidate

Matthew Tudball

Date

11/03/2025

Dedication

To my mum, Julie. Thanks for the guidance, love and support, I couldn’t have done any of this without you!

And for my Grandad, Allan, and my Uncle David.

Presentations arising from this Study

Materials Research Society Spring Meeting, San Francisco, USA, April 2023, Title: *Ultrasonic Spray Deposition and its Uses in Manufacturing New Bespoke Graded Electrodes for Energy Storage Devices.*

Electrochemical Society Prime, Honolulu, Hawaii, USA, October 2024, Title: *Solid State Gradients: One Step Aqueous Spray Deposition of Novel Graduated Cathode/Solid Electrolyte Interfaces for Improved Solid State Batteries.*

Poster Presentations arising from this Study

Faraday Institution Early Career Researcher Conference, Warwick, UK, November 2022, Title: *Manufacturing Through-Thickness Gradient Electrodes for Li-S Batteries.*

STFC Early Career Researchers Conference, Abingdon, UK, May 2023, Title: *Using Ultrasonic Spray Deposition to Manufacture Graded Cathodes.*

Faraday Institution Conference, Birmingham, UK, September 2023, Title: *Using Ultrasonic Spray Deposition to Manufacture Battery Electrodes.*

Publications arising from this Study

M. Tudball, W. Dawson, J. Cruddos, F. Iacoviello, A. Morrison, A. J. E. Rettie and T. Miller, *Sustain. Energy Fuels*, DOI:10.1039/D4SE01736F.

Abstract

The breadth and impact of lithium batteries has grown rapidly and will continue to increase as energy storage becomes a crucial method of reducing carbon emissions, through electrification of transport and the balancing of renewable electricity generators. Current state-of-the-art transition metal oxide/graphite-based batteries are nearing their theoretical limits, therefore new materials and technologies will be relied on for the necessary increases in performance and safety of future energy storage.

Spray deposition encompasses a range of aerosol-based coating techniques which build thin films of material in a layer-by-layer fashion, allowing precise control over the through-thickness structure of the electrode.

In this work, a spray deposition-based technique for electrode manufacture is developed with the aim of creating through-thickness gradients within battery materials to solve critical issues which plague these chemistries. This gradient spray technique was applied to three different battery chemistries: lithium sulfur, solid-state and silicon anodes, with the intent to demonstrate the importance of non-homogenous electrode design in optimising the electrochemical performance of a wide-range of materials. Graded electrodes were manufactured, characterised and tested to further understand the influence of the gradient on the intrinsic properties of the battery. Gold catalyst gradients in lithium sulfur cathodes improved capacity retention at high discharge rates when gold content was increased towards the electrode surface. Graded cathode to polymer electrolyte electrodes reduced resistance and improved battery lifetime and performance in solid-state batteries. Finally, grading silicon towards the current collector was shown to extend the lifetime of silicon/graphite anodes. Considerations were made into the commercial viability of spray deposition as a battery manufacture technique, with a focus on reduced manufacture time and cost, through combination with traditional slurry-based methods. The goal of this work was to explore proof-of-concept designs for a commercially viable electrode manufacture method that promoted complex and intricate designs to progress new battery technologies.

Impact Statement

The manufacture of battery electrodes is crucial in determining the cost, performance and safety of batteries, which hold a key role in the global reduction of carbon emissions necessary to prevent further climate change. While current manufacturing methods are optimised for state-of-the-art battery materials, new developments in battery chemistry and electrode structure require more complex designs that can only be achieved with new manufacturing techniques. Novel battery technologies can benefit from specific electrode design and the introduction of electrode non-homogeneity in influencing key battery performance metrics, thus accelerating the technologies and prompting commercial and industrial adoption. Many of these novel battery technologies offer reductions in cost, alongside increased capacity and lifetime when compared to traditional transition metal oxide/graphite lithium-ion batteries which is crucial for the growing EV and energy storage market.

Spray deposition is an industrially relevant technique for manufacturing thin films on a wide variety of substrates. Adapting the spray process for battery materials opens up a wide variety of potential structures and adaptations of typical and new battery materials. The layer-by-layer nature of the spray method allows for material or structural gradients to be introduced into the electrode, therefore optimising both sides of the film for their specific environments and functions. This thesis aims to develop a gradient spray technique and apply it to a range of new battery materials with the aim of improving performance and remediating key issues. This work benefits the battery electrode manufacturing community by demonstrating and proving the benefits of a more specific deposition approach and exhibits spray deposition as a viable industrial manufacture method for large scale battery manufacture. This proof-of-concept work aims to develop an under-researched technique and demonstrate the benefits in a wide range of battery materials. It is shown that gradient manufacturing can be used to tackle key battery characteristics such as rate performance, resistance build-up, and battery lifetime in lithium sulfur, solid-state and silicon/graphite batteries respectively. In addition, a combination slurry-coating/spray deposition method is demonstrated to further reduce manufacturing cost and time while maintaining electrode design specificity,

a technique which would not incur much additional cost to current manufacturers and could greatly enhance battery performance. While this work covers three main battery materials, this is not exhaustive and it is hoped that others find further battery chemistries in which greater electrode design specificity is required.

This thesis contains novel manufacturing techniques, alongside significant battery performance improvement through the use of graded materials. This work was done in conjunction and collaboration with the UK's Faraday Institution. The results of these collaboration were disseminated through talks and posters at conferences, notably at the Materials Research Society and Electrochemical Society annual meetings. The methodology created in this work has been utilised to manufacture materials that have now been patented, and has been included in published journal articles. Much of this work has been conducted in collaboration with other institutions, across the UK and abroad, notably with Oxford University and Arizona State University.

Acknowledgements

Thanks to Tom Miller, my supervisor, who led this topsy turvy journey through all the various random projects which I found myself working on. Without his supervision I would have not have been able to piece it all together. His expertise, skill and reassuring presence were vital to this work and my peace of mind and I can't thank him enough.

Níamh, my partner, who valiantly dealt with my complaining about spray coaters, dysfunctional batteries and a million other things, showing unwavering support in the face of obscure rambling. Her endless joy, excitement and love of planning holidays kept me sane. Thank you Níamh for all your kind words, patience and love, I could not have done any of this without you.

I am unsure of how to thank the friends I have made in the EIL over the last almost five years, so here is a list of names in the order the I remember them while writing this: chess-master and connoisseur of geographical locations - Tommy, the best holiday companion - Josh, queens master - Alice, Huw, my fellow flagophile and all-round silly boy - Charlie, an Awesomely Fun Man - Brandon, German - Isabel, South African - Sams, food recommendations and never music reccs - Will, Taylor Swift - Katrina, a very calming presence - Hamish, for the limitless compliments - Shangwei, networking king - Arthur, secret raver - Iain, walking dictionary - Thomas, the best boss I've had so far - Keenan, a very clever man – Andrew, 'what have I done wrong this time' - Toby, the most helpful and lovely people - Claire and Lizzie, master of gossip - Franny, ping pong champ - Ami, fellow yellowbelly - Liam, Eggman and Gigman - William and Sion and many more.

And to those friends outside of the windowless box in which we work, the wibbly and the wobblies - Eren and Fran, for always being at the pub - Jork, the entire west hampstead gang for the endless opportunities to drink, the three J's of £20 ryanair flights, my sister for bring Tosca and Spencer into my life, for running swimming and cycling – Ruben, for being such a chatterbox - Pete, out of spite - my old chemistry teacher, Andy, Lance and Steven Toast.

….. and no one else comes to mind.

On top of these lovely people, I want to thank reverse-chess, crosswords, geoguessr, flags and various other geography games, audiobooks, album club, Birkbeck, IOE and the Marly arms (never TCR bar), the Hoxton cabin, the garden cinema and of course UCell (mainly greenman).

I've had the most fun, the most laughs, the most stress, work and silliness with all these people, and I wish I could stay here forever. Unfortunately the real world awaits me, but a part of me will always stay in this basement, at my messy desk on my gaffa-taped chair chatting science and a lot of nonsense with my mates.

…. Oh yeah and I guess Kofi maybe, I suppose I chatted to him a few times.

UCL Research Paper Declaration Form

referencing the doctoral candidate's own published work(s)

Please use this form to declare if parts of your thesis are already available in another format, e.g. if data, text, or figures:

- *have been uploaded to a preprint server*
- *are in submission to a peer-reviewed publication*
- *have been published in a peer-reviewed publication, e.g. journal, textbook.*

This form should be completed as many times as necessary. For instance, if you have seven thesis chapters, two of which containing material that has already been published, you would complete this form twice.

1. **For a research manuscript that has already been published** (if not yet published, please skip to section 2)

   a) **What is the title of the manuscript?**

   Enhancing solid-state battery performance with spray-deposited gradient composite cathodes.

   b) **Please include a link to or doi for the work**

   https://doi.org/10.1039/D4SE01736F

   c) **Where was the work published?**

   Sustainable Energy & Fuels

   d) **Who published the work?** (e.g. OUP)

   Royal Society of Chemistry

   e) **When was the work published?**

   28 Jan 2025

   f) **List the manuscript's authors in the order they appear on the publication**

   Matt P. Tudball, Will J. Dawson, Joshua H. Cruddos, Francesco Iacoviello, Andrew R. T. Morrison, Alexander J. E. Rettie, Thomas S. Miller

   g) **Was the work peer reviewed?**

   Yes

   h) **Have you retained the copyright?**

   Yes

   i) **Was an earlier form of the manuscript uploaded to a preprint server?** (e.g. medRxiv). If 'Yes', please give a link or doi)

   No

   If 'No', please seek permission from the relevant publisher and check the box next to the below statement:

   ☒

*I acknowledge permission of the publisher named under **1d** to include in this thesis portions of the publication named as included in **1c**.*

2. **For a research manuscript prepared for publication but that has not yet been published** (if already published, please skip to section 3)

   a) **What is the current title of the manuscript?**

   N/A

   b) **Has the manuscript been uploaded to a preprint server?** (e.g. medRxiv; if 'Yes', please give a link or doi)

   N/A

   c) **Where is the work intended to be published?** (e.g. journal names)

   N/A

   d) **List the manuscript's authors in the intended authorship order**

   N/A

   e) **Stage of publication** (e.g. in submission)

   N/A

3. **For multi-authored work, please give a statement of contribution covering all authors** (if single-author, please skip to section 4)

   Matt P. Tudball: Experimental work, analysis, writing. Will J. Dawson: X-ray experimental work, methodology, data analysis, review. Joshua H. Cruddos: EIS data analysis, methodology. Francesco Iacoviello: X-ray experimental work. Andrew R. T. Morrison: General paper review, analysis. Alexander J. E. Rettie: Funding Acquisition, resources. Thomas S. Miller: Funding acquisition, resources, and conceptualisation.

4. **In which chapter(s) of your thesis can this material be found?**

   5

5. **e-Signatures confirming that the information above is accurate** (this form should be co-signed by the supervisor/ senior author unless this is not appropriate, e.g. if the paper was a single-author work)

   Candidate
   Matthew Tudball
   Date:
   10/03/2025
   Supervisor/ Senior Author (where appropriate)

   Date
   11/03/2025

Table of Contents

List of Tables

List of Figures

List of Appendices

List of Abbreviations

Abbreviations	Definition
%	Percentage
°	Degrees
°C	Degrees Celsius
µA	Microamps
µl	Microlitres
µm	Micrometre
2D	Two-dimensional
3D	Three-dimensional
A g^{-1}	Amps per gram
ACN	Acetonitrile
ALD	Atomic layer deposition
ASSB	All solid-state batteries
C	C-rate
CAM	Cathode active material
cm	Centimetres
cm^2	Centimetres squared
CMC	Sodium carboxymethylcellulose
CPE	Composite polymer electrolytes
CVD	Chemical vapour deposition
DC	Direct current
Deriv	Derivative
DI Water	De-ionised water
DME	2-dimethoxyethane
DOL	1,3-dioxolane
DRT	Distribution of relaxation times
EDX	Energy dispersive X-ray spectroscopy
EIS	Electrochemical impedance spectroscopy
ESD	Electrostatic spray deposition
FEC	Fluorinated ethylene carbonate
g	Grams

GPa	Gigapascals
GPE	Gelled polymer electrolytes
GWh	Gigawatt hour
h	Hours
HCL	Hydrochloric acid
Hz	Hertz
-Im(Z)	Imaginary impedance
IPA	Isopropyl alcohol
IPCC	The Intergovernmental Panel on Climate Change
ITO	Indium tin oxide
keV	Kiloelectron volts
kHz	kilohertz
kV	Kilovolt
kV	Kilovolts
kWh	Kilowatt hour
L(N)MO	Lithium (nickel) manganese oxide
LATP	Lithium Aluminium Titanium Phosphate
LBL	Layer-by-layer
LFP	Lithium iron phosphate
LIPON	Lithium phosphorous oxynitride
Li-S	Lithium sulfur
LiSTAr	Lithium Sulfur Technology Accelerator
LiTFSI	Bis(trifluoromethane)sulfonimide lithium
LLZO	Al-Doped Lithium Lanthanum Zirconate Garnet
LSV	Linear scan voltammetry
LTO	Lithium titanate
M	Molarity
m min^{-1}	Metres per minute
m s^{-1}	Metres per second
mA cm^{-2}	Milliamps per centimetre
mAh	Milliamp hours
mAh g^{-1}	Milliamp hour per gram
mAh g$^{-1}_{AM}$	Milliamp hours per gram of active material

mAh g_S^{-1}	Milliamp hours per gram of sulfur
mg	Milligrams
mg mL^{-1}	Milligrams per millilitre
mHZ	Millihertz
MHz	Megahertz
mL	Millilitre
mL min^{-1}	Millilitres per minute
MLD	Molecular layer deposition
Mm	Millimetres
M_n	Number average molecular weight
MPa	Megapascals
MTI	Materials Technology Institute
mV	Millivolts
M_v	Viscosity average molecular weight
M_w	Weight average molecular weight
NEI	Nanopowder Enterprises Incorporated Nanomyte BE-70
Nextrode	Next Generation Electrode
nm	Nanometres
NMC	Nickel manganese cobalt oxide
NMP	*N*-Methyl-2-pyrrolidone
O	Warburg resistance
OCV	Open circuit voltage
P(PEGMA)	Poly(poly(ethylene glycol) methyl ether methacrylate)
PAA	Polyacrylic acid
PC	Propylene carbonate
PEDOT:PSS	Poly(3,4-ethylenedioxythiophene) polystyrene sulfonate
PEO	Polyethylene oxide
pH	Potential of hydrogen
PMA	Poly(N-methyl-malonic amide)
Psi	Pounds per square inch
PVDF	Polyvinylidene fluoride
PVP	Polyvinylpyrrolidone
Q_{theo}	Theoretical capacity

Re(Z)	Real impedance
s	Seconds
S cm^{-2}	Siemens per centimetre squared
SBR	Styrene-butadiene rubber
SEI	Solid electrolyte interface
SEM	Scanning electron microscope
SOFC	Solid oxide fuel cells
SPE	Solid polymer electrolytes
SSE	Solid-state electrolytes
STFC	Science and Technology Facilities Council
T_g	Glass transition temperature
THF	Tetrahydrofuran
USD	Ultrasonic spray deposition
V	Volts
VC	Vinyl carbonate
W	Watts
w	With
wt%	Weight percentage
X-ray CT	X-ray computed tomography
Z'	Real impedance
Z''	Imaginary impedance
Ω	Ohms
Ω/□	Ohms per square
Ωcm^{-2}	Ohms per centimetre squared

Chapter 1 Introduction

1.1 Overview

The twenty-first century faces an unprecedented climate crisis, marked by rising global temperatures, extreme weather events, and the depletion of natural resources. This urgency calls for transformative approaches across energy generation, storage, and consumption to mitigate greenhouse gas emissions. Battery technology has emerged as pivotal for achieving a sustainable, low-carbon energy future. Renewable energy sources such as wind and solar are inconsistent, thus energy storage technologies that balance power generation with demand can further reduce reliance on fossil fuels. Batteries, as a dominant energy storage technology, play a critical role in enabling renewable energy systems and supporting resilient energy grids alongside powering the shift in transportation towards electric vehicles.

Batteries convert chemical potential energy into electrical energy through electrochemical reactions that occur within the device; rechargeable batteries can be utilised many times repeatedly to store and transmit energy. Lithium-ion batteries have emerged as the key chemistry in this field and are abundant in day-to-day life, powering personal electronics and electric vehicles worldwide due to lithium's high energy density.[1] The ever-growing need for higher capacity, longer lifetime and greater durability of batteries inspires research into new technologies and chemistries, often focussing on safety, energy density and affordability.[2]

Current battery technologies, especially lithium-ion, depend on finite and often environmentally detrimental resources like lithium, cobalt, and nickel, which are associated with mining practices that can cause substantial environmental and social harm. The reliance on these expensive and scarce materials keeps prices relatively high, and fluctuations in these resource markets can drive up costs further. Replacing some of these elements gives more economic stability alongside resource longevity and in some cases further improves battery capacity.[3] Safety is another significant concern as current lithium-ion batteries are susceptible to overheating and fires, due to the flammable nature of the liquid electrolyte. Early warning systems and monitoring systems provide some

reassurance but replacing this liquid electrolyte with a solid one reduces the risks and paves the way towards the use of higher capacity materials.[4]

As demands in lithium-based batteries increases, work into optimisation of current and new materials is crucial to compete with and ultimately replace existing technologies. Industrial manufacturing methods are built for speed and consistency but lack the ability for specific material and thin-film design.[5] All battery materials require intricate fabrication of thin electrode materials, the properties of which affect the performance and lifetime of the cell. Spray deposition is a potential industrial manufacture method for battery electrodes which unlocks the ability for the manufacture of non-homogenous electrodes, therefore specific location-based challenges within the electrode can be tackled. Precise control over the through-thickness properties of an electrode can be used to optimise electrical and ionic conductivity and has the potential to minimise issues which are seen as crucial obstructions in the commercialisation of new battery technologies.

This work is focussed on the spray deposition of three battery materials, particularly the manufacture of gradients within these materials to further optimise both the performance and the lifetime of the cell. The three battery materials researched here are: gold catalysed sulfur cathodes for lithium sulfur batteries, polymer electrolytes for solid-state batteries and high-capacity silicon/graphite anodes.

1.2 Lithium-ion batteries

The lithium-ion battery began in the 1970's with Whittingham's lithium titanium di-sulfide rechargeable battery.[6] This was furthered by Goodenough's[7] work on lithium cobalt oxide cathodes and Yoshino's work[8] on carbon anodes; the metal oxide/graphite battery was commercialised by Sony in 1991. The lithium-ion battery used today generally consists of a metal oxide cathode (positive) and a graphite anode (negative) which act as intercalation hosts for lithium ions which move back and forth between them in a 'rocking chair'-like fashion. The mass adoption of lithium-ion batteries is a result of their high capacity and long lifespan and thus they have replaced more traditional battery types like nickel metal hydride and lead acid in most functions.[3]

Many metal oxide cathode compositions have been utilised with different materials offering alternative benefits such as: $LiCoO_2$; a high capacity cathode which is used for lightweight portable electronics and $LiFePO_4$ (LFP); a lower capacity but longer lifetime cathode which is used for electric vehicles and grid storage,[9] see Figure 1-1.

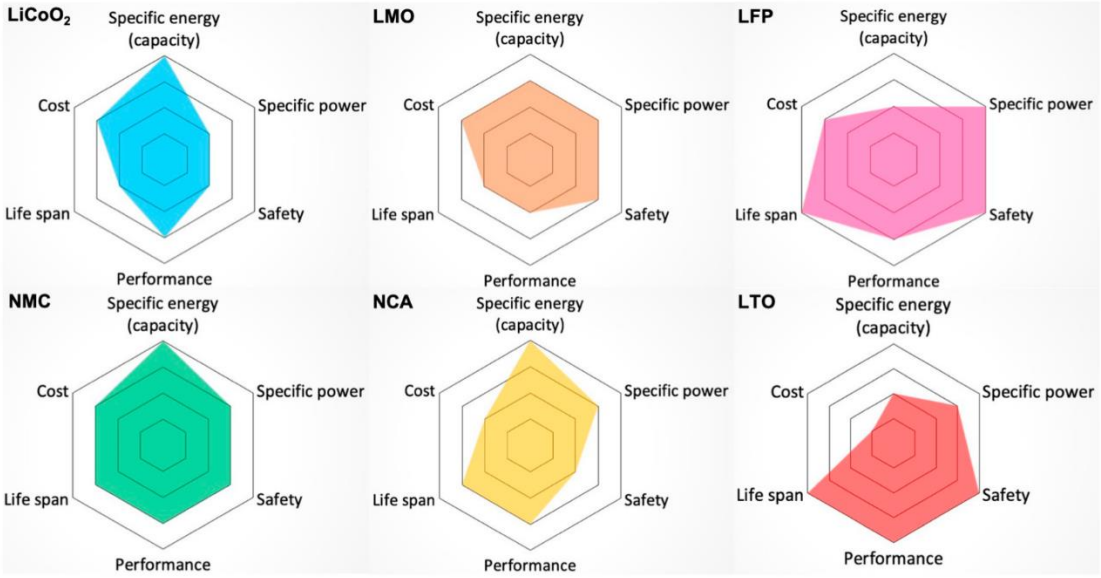

Figure 1-1: *Comparison of different battery cathode materials in terms of key characteristics. Reproduced from Miao et al.*[9]

Lithium-ion batteries function through the movement of lithium ions from one electrode to the other via an organic liquid medium termed the electrolyte, see Figure 1-2. Upon charging, lithium ions move to the anode where they intercalate between the graphite layers and combine with an electron. On discharge they lose this electron and move towards the cathode where they intercalate and subsequently recombine with the electron. Between the two electrodes is an electrically non-conductive separator which prevents internal electron flow thereby allowing for energy storage in a chemical form.

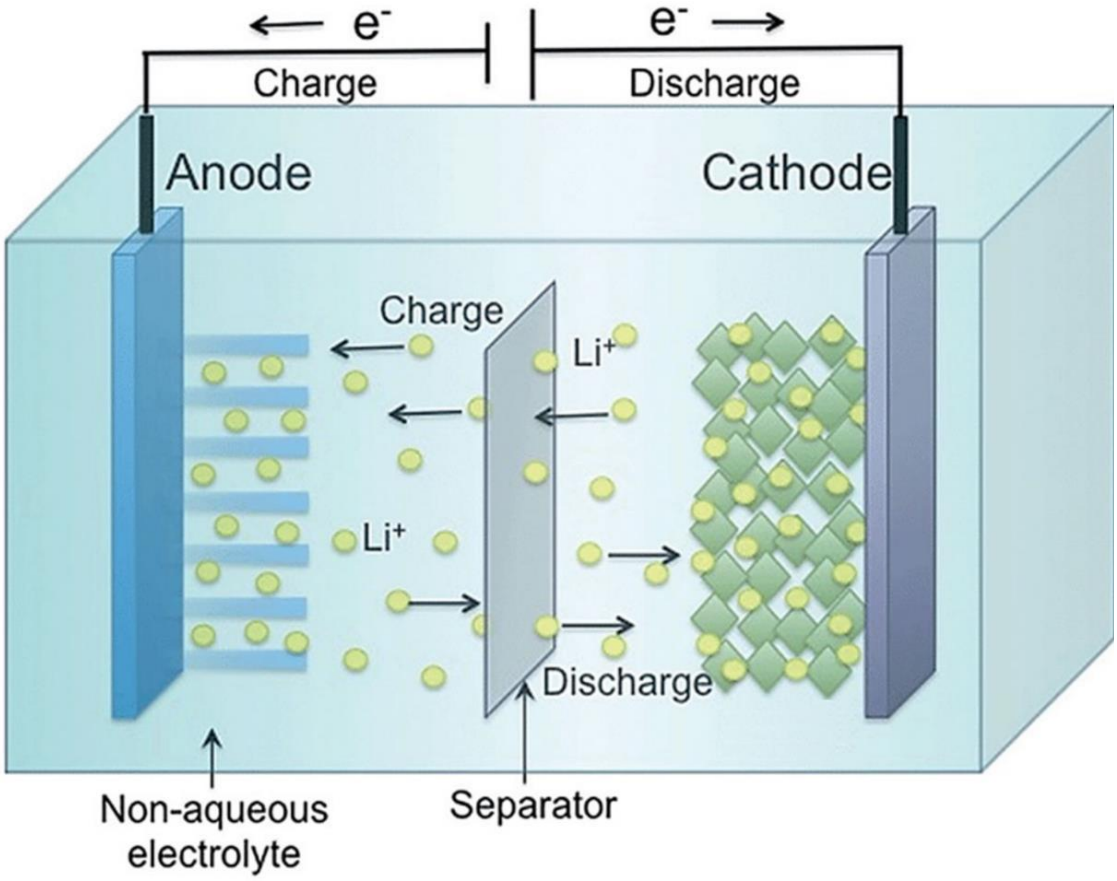

Figure 1-2: *Illustration of a traditional lithium-ion battery. Reproduced from Roy et al.*[10]

The electrochemical reactions of a lithium-ion battery involve the movement of both lithium ions and electrons from one electrode to the other. Table 1-1 indicates the reversible electrochemical reactions upon discharge of an LFP/graphite battery, demonstrating the movement of Li^+ and e^- from the anode to the cathode.

Table 1-1: *The electrochemical reactions of a lithium-ion (LFP) battery*

Electrode	Reaction
Anode	$Li_nC_6 \rightleftharpoons Li_0C_6 + nLi^+ + ne^-$
Cathode	$Li_{m-n}FePO_4 + nLi^+ + ne^- \rightleftharpoons Li_mFePO_4$
Total	$Li_nC_6 + Li_{m-n}FePO_4 \rightleftharpoons Li_0C_6 + Li_mFePO_4$

Due to an ever-growing need for improvements in all characteristics of lithium-ion batteries, new electrode materials and chemistries may advance battery safety, capacity, cost, and lifetime. For example, silicon-containing anodes increase

battery capacity but are hampered by poor cycle life often degrading quickly thus slowing their commercialisation. Solid-state batteries replace the flammable liquid electrolyte with a safer solid one, this not only improves the safety of existing battery chemistries but also promotes research into high capacity electrodes that have not yet been adopted due to safety risks. Solid-state electrolytes suffer from poor lithium ion conductivity, therefore perform worse at high charge and discharge rates. New battery designs that employ different electrochemical reactions such as lithium sulfur batteries, which utilises an ultra-high capacity cathode that transitions between solid sulfur and lithium sulfide via soluble polysulfide intermediates, offer an alternative to traditional mechanisms but require more optimisation and analysis of issues that degrade materials and shorten battery lifetime.

1.3 Spray deposition

Spray deposition has been used to manufacture materials for fuel cells, supercapacitors, electrolysers, and solar cells alongside some research into its uses for battery electrodes.[11] Spray deposition is a thin film manufacture method that is used to deposit homogenous, discrete layers of material on a substrate. It works by forming an aerosol through atomisation of a suspension of precursor material, then directing the droplets towards a substrate, at which point the solvent is evaporated leaving the solids behind. In the context of energy device manufacturing, spray deposition provides several distinct advantages. Spray deposition is compatible with a wide range of materials and can be scaled up to large areas, making it a useful tool in the testing and commercialisation of new materials. Because of its layer-by-layer deposition method, in contrast to traditional slurry coating practices, precise tuning of layer properties such as porosity, conductivity, and material type can be achieved, allowing for optimisation of electrochemical activity and durability. While there is a great deal of research into spray deposition of battery materials, very little of it utilises this key impact of layer-by-layer deposition, especially in the context of new battery materials.[12,13] By harnessing the intricate control over electrode properties alongside the compatibility of spray deposition with many materials, several key challenges facing new battery materials and chemistries may be tackled, using electrode design to elongate battery lifetime and increase performance.

1.4 Research motivation

There is a global push towards new battery chemistries and materials that will be crucial in tackling the energy storage requirements of portable electronics, renewable energy generation and transport. One method of improving the characteristics of existing materials and the development of new materials is through precise structuring of electrodes. Control over aspects of an electrode such as porosity, conductivity or material choice can improve performance and negate the onset of degradation. Spray deposition represents a highly specific and targeted manufacture method, it gives through-thickness control of electrode structure in a layer-by-layer fashion which is not possible with current slurry-based manufacture methods. Currently spray deposition has been under-utilised in the method, and there is limited research on the properties of thin films made in this way.

This work aims to manufacture battery electrodes using ultrasonic spray deposition, studying the effects of non-homogenous films on battery performance. Novel spray deposition methods will be used to manufacture gradients into battery electrodes to optimise placement of materials to enhance performance and lifespan. This proof-of-concept work aims to demonstrate how spray deposition can be used to manufacture graded electrodes, which can provide benefits towards battery performance. This involves developing a new gradient spray manufacturing technique alongside optimisation of the manufacture process for materials that have not been spray deposited previously. The battery chemistries chosen (lithium sulfur, solid-state and silicon anode) represent a broad spectrum of novel battery technologies. It is hoped that the effectiveness and impact of graded battery electrodes will be furthered to other materials and battery chemistries and the manufacturing approach taken up by the energy storage industry as a viable deposition method.

1.5 Thesis overview

This thesis begins with a review of the literature on spray deposition of battery materials, comprising all the major themes on the manufacture of anodes, cathodes, solid-state electrolytes, and artificial interfaces; focussing on the effect of spray parameters such as temperature, air flow, and atomisation type on the manufactured electrode architecture. The review concludes with the current research into full cell, multiple layer deposition and layered electrodes alongside the current literature on spray deposited gradients.

Following this, a deep dive into the methodology and learnings of the design of the gradient spray manufacture process is presented, including studies into the effects of lesser-researched spray parameters and their subsequent impact on material properties.

The three results chapters encompass three different material gradients, the results of experimental work performed by the author. These comprise of manufacturing gold gradients into lithium sulfur cathodes to improve rate performance, graded composite cathodes for enhanced performance of solid-state polymer electrolyte batteries and, optimisation of silicon placement in graded silicon graphite anodes. These chapters consist of a wide range of new battery materials and chemistries to highlight the effectiveness of graded electrode manufacture and spray deposition in combatting specific issues, and its relevance to energy materials.

This work concludes with a summary discussion of the impact of the graded electrode structure alongside the efficacy of spray deposition and the potential for this methodology in the future, specifically the steps that could be taken to ensure industry involvement and commercial uptake of these designs.

Chapter 2 Literature Review

2.1 Introduction

2.1.1 Overview

Spray deposition is a proven industrial manufacturing method to coat thin films of materials for a wide range of applications; notably in the energy materials field, spray deposition has been used for fuel cell manufacturing.[14] It has been applied to battery materials in a few cases, often for next generation materials or technologies, and has been shown to be useful in both aiding the manufacture and functionality of these materials. Spray deposition can be used to deposit films quickly and easily on a variety of substrates, including existing battery materials, with a range of macro and microstructures available to optimise the material and chemical properties of the final film. The techniques and precise methods of spray deposition vary depending on the desired structure or chemistry of the thin film; parameters such as temperature, solvent, atomisation method and air flow rate can all be used to influence final film structure. This review covers research into spray deposition of battery materials, from cathode and anode to solid-state electrolyte and full cell manufacture, discussing the effect of spray parameters, processability and versatility of the spray process, and the subsequent coating performance.

2.1.2 Broader context

Global battery demand is expected to grow by 25% annually, it is expected that by 2030 electric vehicles will make up 83% of the predicted 2,600 GWh of battery storage by 2030, according to a report in 2019 by the World Economic Forum.[15] The Intergovernmental Panel on Climate Change (IPCC) AR6 report in 2022 clearly highlights that the steep drop in battery costs have increased electric vehicle viability and that batteries could have significant roles to play in rail and heavy goods vehicles, although technology advancements are needed. Batteries are also critical to renewable energy generation, providing frequency regulation, voltage support and smoothing the curve between high peak and low peak usage times. The report also concedes that mineral costs, availability, and mining issues, as well as battery safety and lifetime are key issues surrounding battery technology.[16] Many of these issues are key topics of current battery research, with new battery chemistries such as lithium sulfur aiming to reduce mineral

concerns, solid-state batteries to reduce safety risks and much research aiming to improve performance of existing chemistries.

2.2 Current manufacturing methods of electrodes

Current lithium-ion battery manufacturing concerns the traditional chemistry of a metal oxide cathode paired with a graphite anode coated on metal current collectors with a liquid organic electrolyte. Both the cathode and anode films are usually coated via a slurry-based method; the most used industry technique for this is slot die coating which involves forcing a viscous slurry through a slot onto a substrate, then evaporating the solvent. The coating process itself is quick, compatible with roll-to-roll processing and gives the ability to control thickness.[17] Slot die coating remains a very fast and cheap method of producing large amounts of electrode, therefore it is commonplace in industry, however, there remains some issues surrounding both the deposition process and the structure of the subsequent film, particularly with solvent evaporation.[18]

Slurry-based coating methods require a solvent in which to disperse the battery materials, in industry this is commonly *N*-Methyl-2-pyrrolidone (NMP). NMP is a good solvent for the binder material polyvinylidene fluoride (PVDF) and is excellent at dispersing often hard to work with battery materials. Unfortunately, NMP poses significant safety hazards, both toxicity and flammability, due to this, manufacturing plants are obliged to implement recovery and reuse procedures for NMP which contributes significantly to the cost of manufacturing. NMP has a high boiling point (202 °C), therefore the requirement for extended high temperature drying steps to evaporate the solvent also increase costs of battery manufacture and it is estimated that the recovery process of NMP costs 10 kWh per kg of NMP and that for a factory producing 50 million cells annually, the drying process is 19% of total energy use.[19,20]

2.2.1 Subsequent electrode properties

The long drying time associated with slurry-based coating methods influences the quality of the film; during the evaporation step, components within the slurry can settle and reorganise. As the solvent evaporates from the top of the film, it pulls the binder and conductive carbon with it, therefore leaving a higher proportion of non-active material nearer the electrolyte causing slower lithium diffusion into the bulk of the electrode.[5] The drying step is often the cause of defects within the

electrode as stress develops within the film as the solvent evaporates. This can be the cause of cracks, delamination, and curling, which can decrease performance and safety and increase cost through material wastage.[5] Slot die coating is limited in the complexity of the electrode it can produce as generally it can only be used to make a homogenous film; although bilayer slot die coating is possible it has not been actively researched, and its limitations are unknown.[18]

The goal of electrode coating would be to remove the solvent entirely, this would prevent both the cost of the solvent, recapture, and drying steps as well as potential deformations during drying. There are studies demonstrating this in principle using spray drying and a heated roller, but it is still far from commercialisation.[21]

Other options involve replacement of expensive and dangerous organic solvents like NMP with less toxic organic solvents or water. This reduces manufacturing costs and drying times, however water-based slurries have been proven to form electrodes that are more prone to cracks and deformation.[20]

2.3 Solid-state electrolytes

One of the potential objectives for future batteries is the transition away from liquid electrolytes; this is partially down to the need for higher energy density anodes. Current graphite anodes prioritise safety over energy density, in contrast to a pure lithium metal anode. Lithium metal anodes, with their increased capacity, present a promising proposition to meet the need for higher capacity batteries, but they are hampered by dendrite formation. These dendrites can short the cell which causes a spike in temperature and the possibility of fire. Current liquid electrolytes are highly flammable and only exacerbate the danger when paired with a lithium metal anode. Solid-state electrolytes (SSE) aim to remove this safety risk and, alongside their potential to prevent lithium dendrites, can help the progression towards lithium metal anodes.

True solid-state batteries are not yet a widespread commercial reality although there are a few different materials that are of considerable interest. These include thin films, inorganic ceramic materials and organic polymers, Figure 2-1 demonstrates the main materials used for SSEs and their benefits and

drawbacks. The most studied tend to be the oxide, sulfide and polymer types, and will be the main types discussed here.[22]

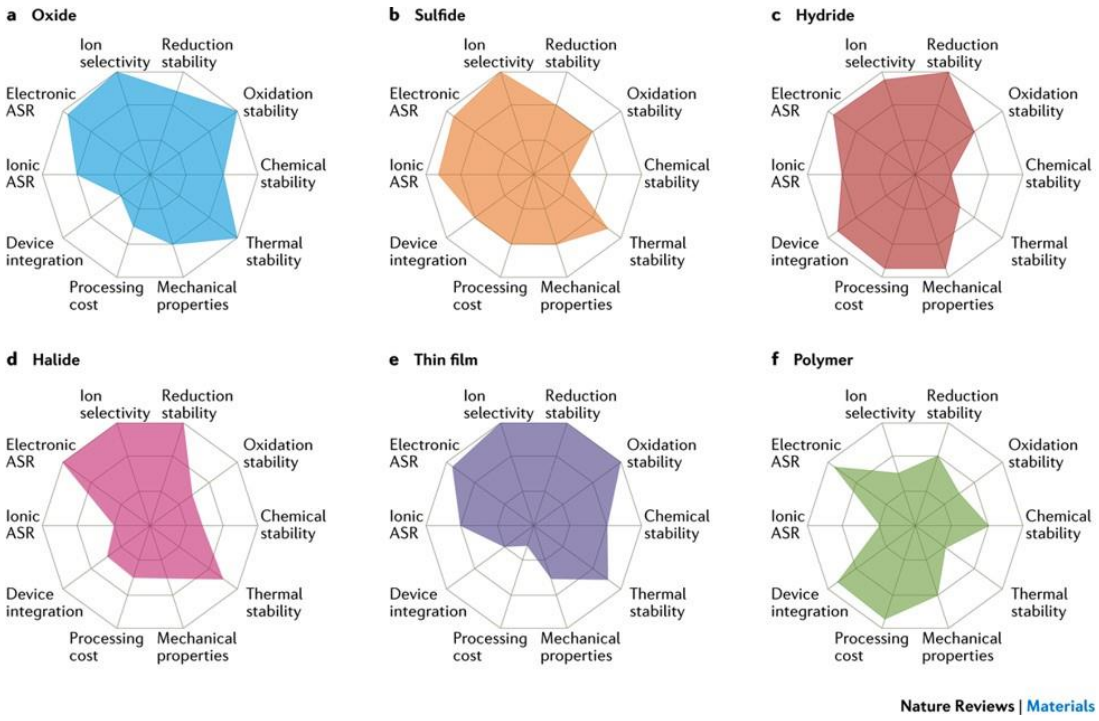

Figure 2-1: *Types of SSE material and their properties. Reproduced from Manthiram et al,.*[22]

Inorganic solid-state electrolytes (SSEs) such as lithium lanthanum zirconium oxide (LLZO) and lithium phosphorous oxynitride (LiPON) boast high Li^+ conductivity and stability, they suffer from complexities in manufacturing, high processing costs and difficulties in device integration, whereas sulfide-based SSEs are cheaper and easier to process but have poor electrochemical stability when paired with lithium.[22] Polymer-based electrolytes or solid polymer electrolytes (SPE's), such as polyethylene oxide (PEO), benefit from cheap slurry-based manufacturing methods but have limited electrochemical stability windows and poorer Li^+ conductivity.[23–27]

One of the key issues with SSEs is the industrial manufacturing cost and feasibility. In research environments, inorganic type SSEs are made by pellet pressing and sintering[28] and thin film SSEs by vapour deposition[29] and atomic layer deposition[30], all of which are expensive and time consuming. Polymer SSEs have the advantage of being both cheap and simple to manufacture.[22] For a battery material to have an impact it needs to have a cheap, scalable manufacture

method and for most current SSE materials, slurry-based processes do not seem appropriate.

2.3.1 Solid-state interfaces

One of the most notable manufacturing issues with SSB's is the interface between the electrolyte and the cathode. The standard method of assembly involves manufacturing the anode, cathode and SSE separately and subsequent assembly, which leads to a large interfacial resistance or gaps between the layers. There has been work on improving this boundary by adding interlayers such as niobium between the electrode and SSE, however this only adds to the complexity and cost of an already difficult manufacture process.[31] Other methods involve co-sintering of the electrode and SSE together to properly fuse the layers; while this does improve the interfacial issues, and it significantly reduces the sintering temperature required it still requires pellet pressing at high pressures of 10 MPa.[32] Other techniques use vapour deposition to form a well contacted thin film of cathode on the surface of the SSE pellet, but this is both costly and slow.[33]. It was found that slurry coating lithium titanate oxide onto a ceramic SSE yielded lower impedance and higher capacities than a clearly defined boundary, thus showing improved interface interactions, but this still required pellet pressing of a ceramic SSE.[28] The ability to manufacture both the cathode and SSE layers sequentially and in situ would allow for the most industrially scalable process

2.4 A detailed explanation of spray deposition

Spray deposition is a broad term that encompasses the use of an air flow to direct solid particles, dispersed in a liquid, towards a substrate. Often the substrate is heated to evaporate the solvent; the pathway from the nozzle to the substrate may also be heated so that the solvent is evaporated before the particles are deposited and this is the procedure for spray drying. The material films are built up slowly over time so that the structure is manufactured in a layer-by-layer fashion which gives significant control over the through-thickness macrostructure as well as the thickness of the final film. There are also a wide range of parameters that can affect the structure of the film, these include: temperature of the substrate or heating method, material flow rate, air flow rate, deposition time, and the voltage difference between nozzle and substrate, alongside many more parameters based around the material dispersion to be sprayed.

In standard solution-based spray deposition, the dispersant in solution is pumped through a nozzle where high pressure air ejects it towards a heated substrate. When this air flow impacts the solution stream it breaks it apart into small droplets, termed atomisation, creating a fine mist of solvent particles containing the material to be coated. While high pressure air is the simplest way to achieve atomisation, other methods can also be used such as ultrasonic vibrations, hydraulic pressure, or potential difference (electrostatic). The droplets then deposit onto a substrate where the remaining solvent is evaporated if it has not already evaporated in flight. Thin films are built up over many layers giving precise control over final film thickness, mass, and area. Because the material is deposited sequentially and not in a one step process like doctor blading or slot die coating there is more control over the composition of the film throughout the thickness of the electrode. However, this also means that spray coating is a slower, more expensive process.[5]

2.4.1 Potential for spray deposition

In response to the issues surrounding slurry-based electrode coating such as the limitations in electrode design, a lack of control over the definite properties of the electrode, cost and issues surrounding solvent evaporation, and difficult manufacturing challenges of SSEs, spray deposition offers a method of directly forming thin films with minimal evaporation time and good precision.

Spray deposition comes in many forms including, pyrolysis,[34] electrostatic,[35] ultrasonic,[36] cold spray,[37] spray drying[38] and powder spray.[21] This review aims to cover how each of these can be used to help solve both manufacturing and materials-based issues surrounding battery anodes, cathodes and SSEs, as well as combinations of these in half or full-cell designs.

2.4.2 Types of spray deposition

There are many variations of spray deposition, depending on the materials and applications. Many differ in terms of atomisation methods and in the spray equipment while other methods rely on changes of material. Figure 2-2 demonstrates schematics of a few of the main types of spray deposition. Furthermore, Table 2-1 compares three types of spray deposition, air spray, ultrasonic and electrostatic on their compatibility with different materials and substrates, control over particle size and therefore porosity and industrial scalability. While air spray is the simplest to scale up and has the broadest

compatibility, ultrasonic and electrostatic provide greater control over particle size, with ultrasonic spray deposition having greater compatibility and scale-up potential than electrostatic.

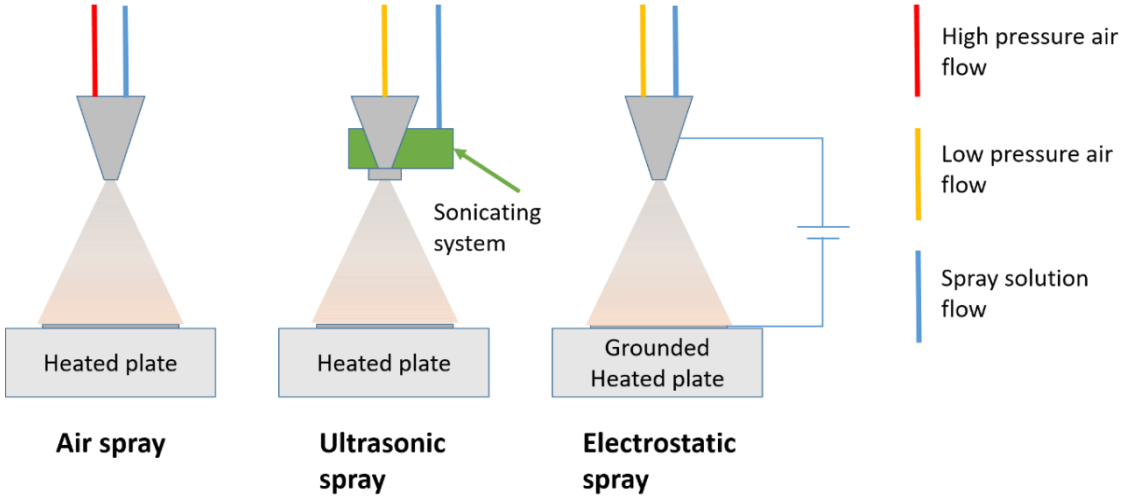

Figure 2-2: *Schematics of air spray, ultrasonic spray, and electrostatic spray deposition*

Table 2-1: *A comparison of three spray deposition types.*

Spray type	Air	Ultrasonic	Electrostatic
Solution compatibility	High	Medium – incompatibly with high viscosity	Low – must be able to hold a charge
Substrate compatibility	High	High	Low – must be conductive
Particle size control	Minimal – broad range of sizes based on air pressure	Medium – based on ultrasonic power	High – based on potential difference
Industrial scalability	High	Medium	Low – more difficult set-up

2.4.2.1 Ultrasonic spray deposition

Ultrasonic spray deposition (USD) uses a sonicating nozzle tip to atomise the solution, which means a lower air flow is needed to direct the particles to the substrate. The sonicating nozzle imparts high frequency sound waves into the liquid which creates standing waves on the surface of the tip, these are ejected from the tip to form droplets.[39] By varying the frequency of the ultrasonic nozzle between 25 kHz and 180 kHz it is possible to change the size of the atomised particles, with a higher frequency giving larger drop sizes, see Figure 2-3. USD gives excellent control over the size of droplet sizes, which can ensure film homogeneity alongside removing the necessity for high pressure airflow which reduces safety risks and improves the control and focus of the spray shape.[39]

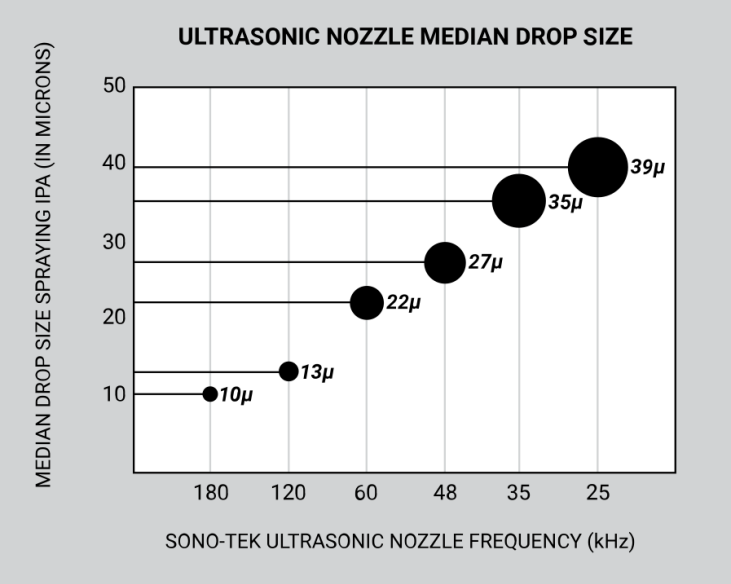

Figure 2-3: *The median droplet size of atomised isopropyl alcohol, at different ultrasonic frequencies. Reproduced from the SONOTEK website.*[39]

2.4.2.2 Electrostatic spray deposition

Electrostatic spray deposition (ESD) uses a voltage difference between the nozzle and the substrate to impart a charge to the solution. A DC voltage between 5-20 kV is applied to induce atomisation at the tip of the nozzle.[40] The charged solution particles repel each other to form droplets that are then attracted to the oppositely charged or grounded substrate, thus forming of an evenly distributed film. Altering the voltage difference can also affect the size of the atomised droplets.[41] The lower limit, or onset voltage of atomisation is usually ~5 kV and

depends on the nozzle substrate distance and the electrical conductivity of the spray solution.[40]

2.4.2.3 Spray drying

Spray drying is used to manufacture nano and microparticles which can then be used directly or separately coated into a film. It follows the same theory as other spray methods but instead of depositing the atomised droplets on a substrate, the solvent is evaporated entirely in flight, often extremely quickly. The speed of evaporation and the size of atomised particles is crucial to control the size and internal structure of the spheres and can be utilised to manufacture hollow particles.[42] Figure 2-4 shows a detailed schematic of a spray dryer.

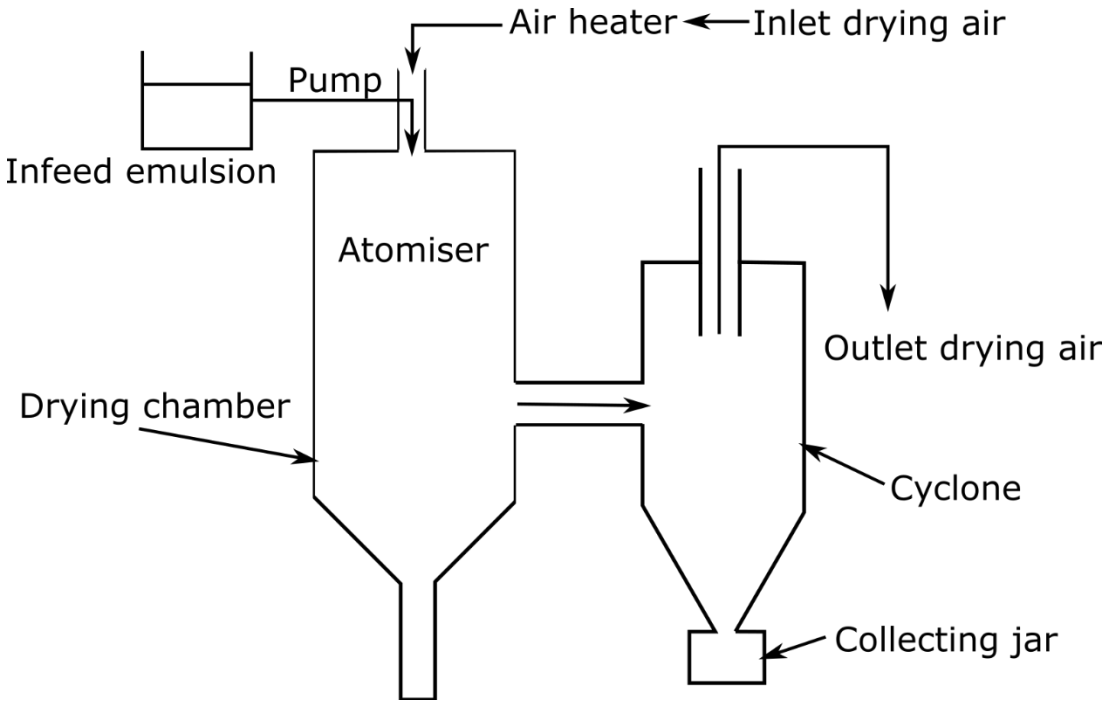

Figure 2-4: *Schematic of spray drying equipment, remade from Nguyen et al.*[43]

2.4.2.4 Other spray methods

Dry powder spray and cold spray are lesser-used methods, although they have great potential for future manufacturing applications. Dry powder spray uses no solvent at all, which cuts industrial costs on solvents and heating/evaporation. It is seen as an ideal future method for manufacturing all solid-state batteries (ASSB's), with many patents being submitted by Toyota in recent years.[44]

Cold spray, or supersonic cold spray, uses high velocity impact of a dispersion onto a room temperature substrate. This not only evaporates the solvent but can

also be used to sinter ceramics in situ, without the need for high temperatures, which may also be crucial for the manufacture of inorganic-type SSEs.[45]

The various methods of spray deposition cover a large area of the requirements for future battery technology such as more intricate design, control over through-thickness structures, reduced solvent toxicity, removal of solvent and the ability to deposit hard to work with materials. The main pitfalls of spray deposition are based around manufacturing time and cost. The layer-by-layer deposition process is still slow and as the optimisation for battery materials is still immature, the cost is higher than traditional slurry coating methods. Hopefully with time and industry involvement, spray deposition can rival slurry-based methods on speed and cost and the additional benefits of this technology can be utilised on a large scale.

2.5 Manufacturing of electrodes with spray deposition

2.5.1 Electrode design

One of the major challenges facing future battery technologies is based around increasing performance while also decreasing cost. 18% of the cost decline of lithium batteries in the last few decades has been associated with the price of cathode materials, alongside a 38% decrease due to better performance and cycle life.[46] The manufacturing step also contributes a significant cost to the cell, with the cost of coating and drying the electrode estimated to be 19% of total cost in a factory producing 50 million cells annually, with this figure rising for smaller factories.[20] New cathode materials tend towards increased surface area, which shortens lithium diffusion time, thus allowing for improved rate performance. Slot die-based slurry coating offers few options in designing 3D architectures, therefore these highly porous structures require a different manufacture technique. Spray deposition is an industrially relevant technique which opens up the possibility of designed electrode materials therefore providing enhanced functionality while maintaining good throughput. While spray deposition is used in fuel cell manufacturing and is considered low cost,[47,48] battery electrodes tend to be thicker and require longer to manufacture therefore the cost of spray deposition is likely to be considerably higher than slot die coating, particularly in its current optimised state.[5]

New materials for anodes are a promising area of research; graphite is the current standard anode for most lithium-ion batteries and acts as an intercalation type electrode. It is becoming apparent that the theoretical capacity of graphite of 372 mAh g^{-1} is too low to match our future storage requirements. Alongside this there are issues related to the solid electrolyte interface (SEI) formation and lithium plating which cause capacity loss and safety issues.[1] While graphite is the industry standard, research into new anode materials aims to raise capacity while maintaining long cycle life. These new anode materials often involve an alternative alloy-based reaction to store lithium, which can offer increased capacity and safety, but requires careful consideration of electrode architecture due to volume expansion upon lithiation.

The literature discussing the manufacturing of anode and cathode materials using spray deposition is focussed predominantly on a few small areas, including new alloy-type materials for anodes, and new structures for both anodes and cathodes. Spray deposition has mostly been used to manufacture novel electrode architectures for alloy-type anodes Si, SiO, SnO, MnO, and others, to combat issues related to volume expansion, irreversible reactions,[49] and poor electronic conductivity.[50]

There has been substantial work on spray deposition of cathode materials, often with an aim similar to the work on anodes; with definable structure[51] and porosity[52] being of key interest. Alongside this there is some literature on the manufacture of thin cathodes for use in micro batteries.[53]

Although spray deposition is unlikely to compete cost wise with industrial slot die coating of current battery electrodes, it can make many aspects of electrode manufacturing more controllable, which is of considerable interest especially for new materials and structures. By altering parameters such as spray temperature, solution flow rate, air flow and deposition time, suitable architectures with controlled porosity, surface area and morphology can be manufactured, which are crucial properties in controlling volume expansion, irreversible reactions, and conductivity.

2.5.2 Temperature effects on sprayed electrode architecture

Perhaps the most important aspect contributing to electrode structure is the rate of solvent evaporation. During the spray, the atomised particles consist of the solid or solvated material inside a small solvent droplet. The dwell time between

this particle reaching the substrate and complete evaporation determines the level of reorganisation of solid material on the substrate, with slower evaporation times allowing the material to move and restructure. The temperature of the substrate and the boiling point of the solvent are the main factors that influence the solvent dwell time; solvent choice is often more limited as it must still be able to effectively disperse or dissolve the material.

Temperature control is therefore one of the most discussed parameters in spray deposition; in work exploring this effect in lanthanum calcium chromite electrodes for solid oxide fuel cells (SOFC's) the influence of on temperature on structure is clear. It was found that below 210 °C, a denser cracked structure (a) is seen, whereas a web-like reticular structure formed at substrate temperatures between 210 °C and 240 °C, (b, c and d), with pore wall thickness decreasing with increased temperature. Above 300 °C a nanowire structure is seen instead (e).[54] Longer solvent dwell times formed more dense structures that were particularly susceptible to crack formation, whereas shorter dwell times formed highly porous 3D structures. The structure of a material is inherent in its properties, particularly electrochemically; surface area, porosity and the 3D macro-architecture all influence performance and lifetime of electrodes, and it is clear here that shortening solvent dwell times introduces porosity into the film. The ability to influence electrode structure with a simple temperature change is of great importance for specific and designed manufacture.

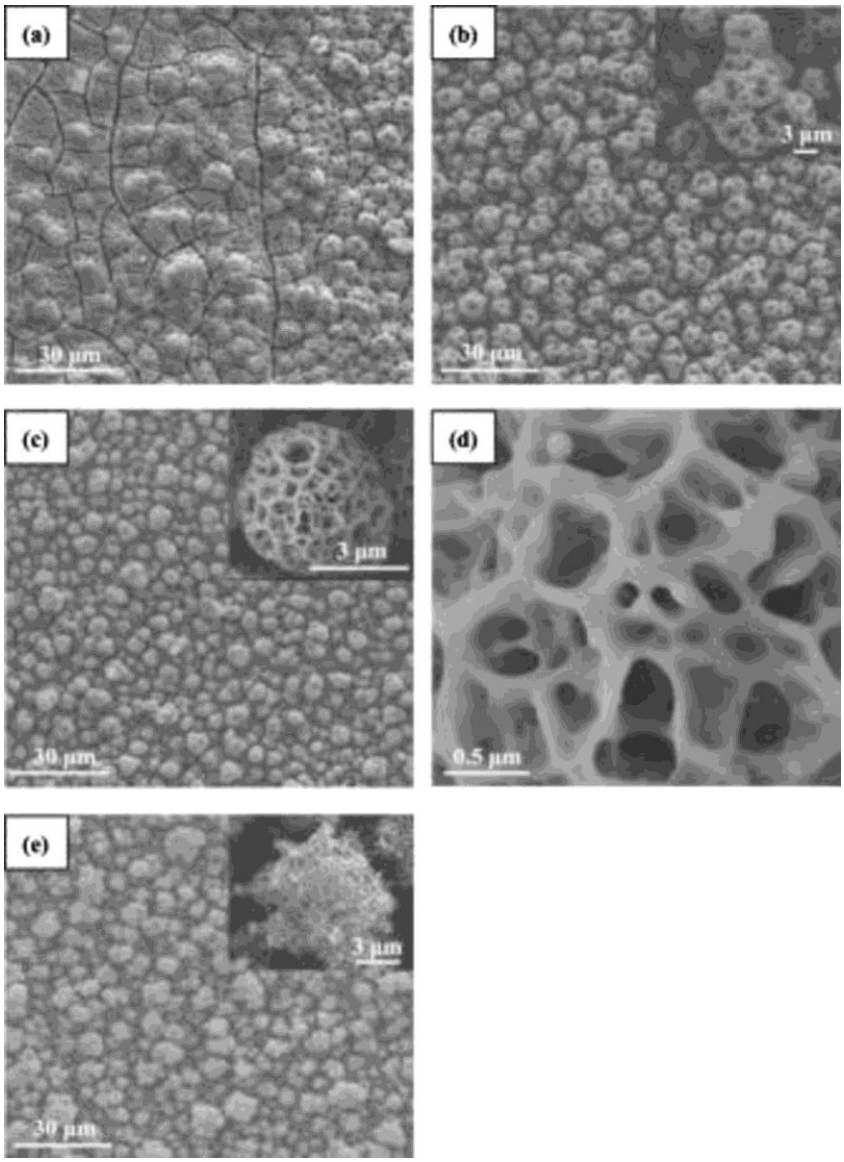

Figure 2-5: *SEM images of LCC thin films deposited on copper substrates at different temperatures: (a) 180 °C, (b) 210 °C, (c and d) 240 °C, and (e) 300 °C. Reproduced from Jiang et al.*[54]

In work on battery materials, temperature effects have been studied for alloy-type anode materials to demonstrate a range of different structure that can be manufactured. These include tree-like SiO_2,[55] hollow Sn-C nanofibers,[56] hydrangea-like SiO,[57]pomegranate-like SiO,[58] 3D nanotube networks[59] and many other reticular structures[34–52]. These reticular structures are characterised by a web-like network which contain large pores between the network in the 10's of μm size range; often the walls themselves contain smaller pores of up to a few μm in size.[73] It is thought that the pores are formed by the evaporation of the solvent after deposition of the droplet; the material reorganises to the edges of

the solvent particles therefore leaving pores in the centre of the droplet. If the temperature is increased, more of the solvent has evaporated prior to collision with the substrate, thus leaving smaller pores, however if the temperature is decreased, the solvent dwells for enough time on the substrate for the solid to reorganise into denser structures. This effect can also be taken advantage of by using a higher boiling point solvent, and much of the work uses a mix of two different solvents to achieve an appropriate boiling point, and therefore a reticular structure.[60,63,64,66,67,69,71–74] Some work suggests that the surface tension of the substrate influences whether the film is reticular. When a copper substrate was used instead of aluminium, the reticular structure changed to cage-like particles, due to the bigger contact angle which is thought to inhibit the size of solution droplets on the substrate.[54] The films precursors may also affect whether the film is reticular or not, with acetate-based precursors forming reticular films and nitrate-based precursors forming denser non-reticular films, however the exact cause of this is unknown.[65,75] The reticular structure has been found to withstand the effects of volume expansion of the alloy material as it allows extra pore space, preventing disconnection and destruction of the anode.[69] This has been shown to improve the cycle life of cells with reports such as 402 mAh g^{-1} after 100 cycles at a current density of 200 mA g^{-1},[70] 507.7 mAh g^{-1} after 100 cycles at a current density of 800 mAh g^{-1},[71] and as high as 1466 mAh g^{-1} after 100 cycles at a current density of 400 mAh g^{-1}.[63] All of which are above the performance of current graphite anodes and provide promising choices for future high capacity, purposefully designed alloy-based anodes.

2.5.2.1 Precursor material spray

Often the material which is sprayed is the same as the one required in the film, this is usually the case for standard materials, where lithium iron phosphate dispersed in a solvent would be sprayed onto a substrate and subsequently assembled in a battery.[76] However, in the case of graphite or nickel manganese cobalt oxide (NMC), these materials are difficult to disperse in a low viscosity solution. The benefit of a heated substrate allows for the formation of the material in situ, from the precursor salts. Much of the research into spray deposited reticular anodes utilises this method, using metal acetates or nitrates to form the final metal oxide compound. Often these precursors are deposited onto stainless

steel substrates at temperatures between 200 °C and 400 °C, before subsequent higher temperature heating steps.[77,78] The additional benefit of this process is the removal of binder from the mix. As the material is synthesised in situ, the structures that form do not require binder to hold them together, thus increasing the active material% and the energy density of the electrode.[77–81] There is also some suggestion of a reduced amount of required conductive additive, although much of the research still includes carbon nanotubes or graphite to enable conductivity.[77,78]

2.5.2.2 Temperature effects on cathodes

Much of the research into spray deposited cathode materials relates to the manufacture of defined 3D structures of lithium (nickel) manganese oxide (LMO[82–89], LNMO[90–93]) from similar nitrate and acetate precursors. Creating high surface area electrodes decreases lithium diffusion time and improves rate performance, with some pseudocapacitive capability observed, which is useful for high power applications.[84,89] However, due to the formation of an electrochemically inactive film on the surface of LMO and LNMO, higher surface area electrodes often have large irreversible capacity loss and large impedance.[83,94]

It was found that USD could be used to manufacture cathodes with columnar-type structures, and that the height and prominence of the columns increases at higher temperatures. At higher temperatures there is less mobility of the particles upon contact with the substrate, so they are more likely to form smaller less cohesive structures. This, combined with the shadowing effect, the idea that the particles are more likely to hit the top face of a pre-existing column leads to this structure formation.[84]

There is also a consideration that during ESD, there is preference for particles to deposit on the top face of columns to remove their charge as quickly as possible.[95] Forming structures in this way provides a method of increasing surface area, therefore improving the rate performance of the cell without changing the chemical composition.

2.5.3 Air flow

When using USD or ESD, which have different atomisation methods, an air flow may be used a means of directing the droplets towards the substrate. There is evidence that this air flow has influence on the final structure of the film.

Increasing the rate of air flow of a water-based spray was found to speed up the evaporation rate of the droplet, with a rate of 60 m s^{-1} causing complete evaporation before the droplet lands. The surface roughness of polymer films was found to decrease between 0 and 15 m s^{-1}, due to the droplet size decreasing as evaporation rate increased. However, at 60 m s^{-1} the roughness was substantially increased, due to the chaotic nature of the high airflow.[41] This creates another avenue for controlling evaporation rate, and subsequently electrode structure, when other parameters such as solvent choice or substrate temperature are impossible to change. This method has been used to manufacture layered graphene oxide electrodes by optimising the airflow rate to ensure each sprayed layer has fully dried before the next layer is coated.[41]

2.5.3.1 Cold spray

Cold spray relies on a much higher air flow rate to remove the need for a heated substrate entirely; with air flow rates between 300 m s^{-1} and 1800 m s^{-1} it is often described as supersonic spray.[45] The sprayed material has enough kinetic energy upon collision to deform the deposited particles and create strong physical, chemical, or mechanical bonds to the substrate, thus improving adhesion of the film. These kinetic force effects have been utilised in battery materials in numerous ways. One example involves using cold spray to induce strain in graphene oxide upon deposition which was found to reduce defects in the final film and helps the graphene to 'self-heal'.[96] Cold spray with an impact velocity of 280 m s^{-1} was used separate out graphite particles into individual graphene flakes upon deposition.[97] Similarly, to manufacture homogenous TiO_2 nanoparticle films for use as an anode, the high air flow spray was used to separate agglomerated TiO_2 which increased the surface area and number of active sites when compared to other TiO_2 deposition methods.[98]

In terms of forming strong mechanical connections, cold spray been used for silicon anodes to ensure good bonding of the silicon to the current collector to prevent delamination caused by volume expansion; the high air flow deforms the silicon and binds the particles to the current collector.[99,100] There is also potential for using cold spray to manufacture inorganic and ceramic films for solid-state electrolytes, thus creating dense well-connected particle structures without the need for high temperature sintering.[37]

2.5.4 Other spray parameters

The type of atomisation process (USD, ESD etc) impacts the droplet size of the atomised liquid. Electrostatic atomisation was found to make more consistent droplet sizes that decreased in size with increased voltage, whereas air spray was less consistent, producing a large range of droplets sizes. Droplets produced through air spray were smaller than in ESD and decreased in size with increased airflow.[41] This means that for deposition processes where homogeneity is crucial, or particle size needs to be controlled, ESD can be utilised effectively, but for speed and increased evaporation rate, air spray may be more suitable.

The solution flow rate was found to influence crack formation and film quality, if the solution flow rate is too high, excess solvent builds up on the film which leads to film shrinkage, reorganisation, and crack formation.[101] This is similar to the effects of low temperature spray, as increased solution flow rate means a longer dwell time on the substrate.

Deposition time/film thickness can influence the films porosity. Throughout the deposition, the substrate/landing points of the droplet's changes from bare substrate to coated material. When spraying onto a metal foil, evaporation occurs quickly and dense layers are formed. This layer is slightly more porous than the foil, which allows for more spreading of the incoming droplets and slower evaporation; this in turn makes the next layer more porous. The through-thickness porosity of a spray deposited $LiCoO_2$ film was found to increase from the foil current collector to the surface of the film due to this phenomenon.[102]

The height of the spray nozzle from the substrate will have some impact, although it is not studied in the literature. The further the distance to the nozzle, the larger the spray shape will be, therefore the thinner the film. It also allows for more time for solvent evaporation, which will affect film porosity and structure.

2.5.5 Solution parameters

The solvent must fulfil many roles, primarily, it must effectively disperse or dissolve the material or precursors, and it must have a suitable boiling point to allow for prompt evaporation. In industrial slurry-based methods, the solvent contributes a significant cost to overall manufacturing. In spray deposition however, although cost is saved on drying time, the volume of solvent required is often much higher to achieve a suitable dispersion and viscosity for effective

deposition. This necessity for more dilute slurries also limits spray deposition somewhat in the choice of material, with larger particle sizes impacting dispersion feasibility. Notoriously hard to disperse materials like graphite or NMC tend to be researched less, due to the requirement for additional surfactants or laborious dispersion techniques such as constant sonication. In slurry-based methods, due to the high viscosity of the slurry, material sedimentation is often much slower than in the dilute solutions required for spray deposition, therefore harder to disperse materials can be coated more easily.

Altering the boiling point of the solvent has the same effect as changing the temperature of the substrate, as it changes the evaporation rate and thus the porosity and structure of the film. Adding more of a low boiling point solvent was found to change the structure of an LMO film from dense to highly porous reticular, as it reduced the solvent dwell time and the ability for the solid to reorganise.[103] This effect is used in the majority of spray deposited anode work to fine tune the evaporation rate to a particular temperature.[60,63,64,66,67,69,71–74]

There is some thought that these bi-solvent systems may impact the structure further. When using an aqueous organic bi-solvent mix, the material to be deposited may be dispersed better in one solvent than the other. TiO_2 nanotubes were found to form a porous structure due to their preferential dispersal in isopropyl alcohol (IPA); the IPA evaporated first, depositing the TiO_2 and leaving droplets of water still on the substrate. When this water evaporates it leaves pores in the film. Due to preferential deposition on the top of existing columns, these pores grow deeper as the film thickness increases.[104]

The concentration of the spray solution is also interlinked with the final film structure. Increasing the concentration of the solution was found to increase the solvent dwell time, therefore requires a higher substrate temperature to prevent cracking and delamination. In an atomised droplet with a high concentration of solid material, some of the material precipitates at the surface of the droplet and thus forms a shell which prevents the contained solvent from evaporating, leading to longer dwell times. [101,105,106] It is also noted that different metal salts decompose at different temperatures, when this occurs during flight, these salts may precipitate at the surface of the droplet, thus causing the same effect.[106]

Additives have been shown to impact the final film structure also; when performing ESD, an acidic spray solution can form denser structures, due to the increased electrical conductivity of the droplet.[103] This work suggests that the

increased conductivity of the droplets is the reason for a homogenous dense coating. This contrasts other research that finds that the charged droplets in ESD are the cause for the formation of columnar structures.[107] In further research the addition of hydrochloric acid (HCL) was found to form a linear tree-like structure during a decomposition SiO_2 spray, whereas in contrast the addition of ammonia formed spherical particles instead.[108]

The ideal goal for future deposition methods is to remove solvent entirely, and while dry spray has been used for some materials, the technique is in its infancy still for battery manufacture.[21,44] Overall, the solvent must effectively disperse the material to be deposited, in the highest concentration possible to reduce the amount of solvent required. Optimisation of the solution parameters can impact evaporation time as well as final structure, however each chemical mixture will require its own research as these parameters are extremely interlinked and complex.

2.5.6 Spray drying

Spray drying has a quite different set-up to spray deposition, but the principles are similar. Instead of the atomised droplets evaporating on the substrate, the solvent is evaporated completely while the droplets are in flight. This method is used to manufacture solid or hollow microparticles and nanoparticles, which are then coated into a film or used directly. The advantages of using tailored microparticles are: better packing efficiency, reduced agglomeration, and in the case of hollow particles, the ability to withstand expansion of active materials during cycling.[109,110] The formation of the hollow particles arises from the preferential precipitation of the solid at the surface of the droplet, with the solvent encapsulated inside, which evaporates to leave a void. The size of the particle is determined by the size of the droplet and the concentration of the solution.[111] Small particles, whether filled, hollow or core-shell, have many uses industrially and have started to be utilised in battery material manufacture, however there is a generally a need for expensive manufacturing steps such as atomic layer deposition (ALD),[112,113] chemical vapour deposition (CVD),[114–116] thermal vapour deposition[117] to manufacture them. Although there are other solution-based methods of manufacturing these particles,[118,119] these methods still require many additional processing steps. Spray drying offers a one-step route to hollow particle manufacture, with the ability to tailor the internal structure of the particle

by varying the temperature, among other parameters, in a cheap and industrially relevant method.

There are two critical factors in determining the inner structure of a spray dried particle, the time required for the droplet to dry, and the time needed for the solid to diffuse through the droplet. If the drying time is slow, dense, filled particles are formed as the solid has time to diffuse through the entirety of the droplet; if the drying time is fast then hollow particles are made.[42,120] Hollow particles increase surface area and lithium ion diffusion rates while also providing space for volume expansion of materials, reducing the likelihood of deformation and cracking which is particularly important for alloy-type anode materials.[120,121]

Another key issue with these alloy-type materials is poor electrical conductivity, which is exacerbated by loss of contact with conductive additives during volume expansion. There are varied approaches in the literature to combat this problem while utilising the advantages of hollow particles. Some work involves spray depositing hollow nanoparticles and then coating with conductive additive with a different method, usually CVD, to ensure adequate conductivity over the entirety of the particle.[109,110,122–126] These anode materials are proven to improve the rate capability of TiO_2 anodes[116] and silicon/graphite anodes, with capacities such as 850 mAh g^{-1} at 0.1 mA cm^{-2},[122] 569 mAh g^{-1} at 0.05 mA cm^{-2} [110] and with some authors reporting extremely high capacities at high rates of 1361 mAh g^{-1} at 3 A g^{-1}.[121] Unfortunately, the combination of spray drying and a CVD coating removes the benefit of spray drying as a one-step, cheap and industrially relevant synthesis. Incorporating a two-step spray which involves a second spray deposition of a protecting layer removes the need for an additional vapour deposition step, this has been demonstrated using a sprayed $LiAlO_2$ layer on a spray-dried lithium titanate anode.[127] These methods make it possible to manufacture hollow bi-layer particles in a one-step process. Hollow spray deposited graphene coated, spray-dried silicon particles were found to perform better in cycle life and rate tests when compared to similar structures made by traditional mixing methods.[128] Figure 2-6**Error! Reference source not found.** shows that spray dried hollow silicon particles that have been subsequently spray coated with few-layer electrochemically exfoliated graphene Si@FL-GB (purple bar), perform better during rate testing than the same materials simply mixed together, without spray drying, Si@FL-GM (green bar). Further it demonstrates

that the secondary spray deposition of carbon materials onto the spray dried silicon particles also improves rate performance, and compares a few different carbon types (graphene oxide, red; bi-layer exfoliated graphene, blue and few layer exfoliated graphene, purple) against uncoated silicon particles (grey). This work demonstrates that spray dried silicon particles perform better than those made by other methods, and that the secondary spray coating of carbon also improves performance.[128]

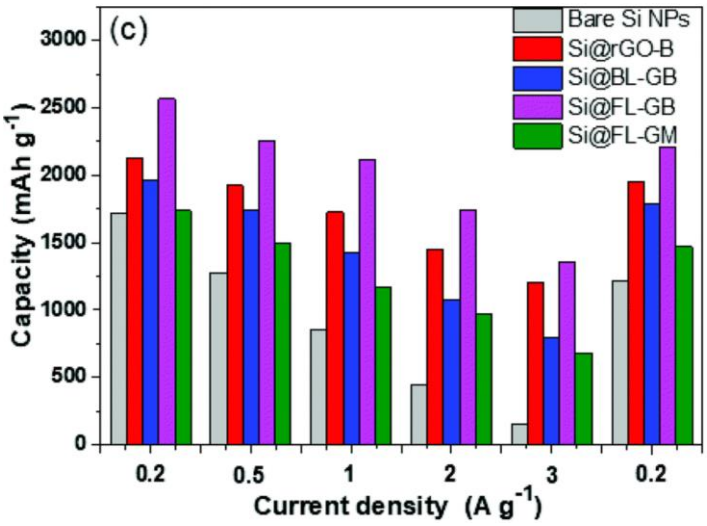

Figure 2-6: *The rate capability of different spray dried silicon graphene hollow nanoparticles. The materials used are (1) bare Si NPs, (2) Si@rGO-B – Graphene oxide, (3) Si@BL-GB – Bilayer electrochemically exfoliated graphene, (4) Si@FL-GB – few-layer electrochemically exfoliated graphene and (5) Si@FL-GM – few-layer electrochemically exfoliated graphene prepared without spray drying method. Reproduced from Jamaluddin et al.*[128]

2.6 Manufacture of artificial SEI and interphase layers

2.6.1 Solid electrolyte interphase

Alkali metals in a non-aqueous solvent are always coated in a thin film caused by the reaction of the metal with the solvent.[129] This solid electrolyte interphase (SEI) is electronically non-conductive but ionically conductive. The SEI forms from the decomposition of the electrolyte until it reaches a thickness that prevent electrons from tunnelling through it. It is beneficial in some ways, as it prevents further degradation of both the metal and the electrolyte, however it is probable that the ionic conductivity of the SEI will be lower than that of the electrolyte and any breakage prompts further degradation of both electrolyte and metal, thus

reducing active material and electrolyte content.[130] To have a highly efficient battery, it is crucial that a stable uniform SEI layer is formed, although this is usually not the case. The SEI is formed of a mix of organic and inorganic compounds, including lithium salts, organic carbonates and polymeric species, based on the composition of the electrolyte. It is quite often inhomogeneous which leads to spots of lower and higher ionic conductivity throughout the layer.[131] This promotes uneven deposition of metals upon the electrode surface instead of the intended alloying or intercalation reaction. These deposits, termed dendrites, form branch-like structures growing slowly through the electrode and can pass through the holes of traditional separator material (Celgard). If the dendrites reach the opposite electrode, they provide a pathway for internal electron transport resulting in a short circuit which heats the battery, potentially expanding the cell and bursting it, creating a fire risk.[132] In addition, any changes with the shape of the electrode surface, occurring from dendrite formation or from volume changes during cycling, have the potential to break the SEI layer and expose new anode material which subsequently reacts and reduces the amount of active material and electrolyte available in the cell.[130] The issues related to SEI growth are often thought to be the main cause of total capacity loss in batteries.[133]

Future anode materials rely on increased capacity compounds such as the alloy-type electrodes which suffer from volume expansion; therefore a stable SEI is significant to maintaining good capacity over multiple cycles.[134] Another future anode material is pure lithium which offers a superior theoretical capacity and energy density and relies on lithium plating and stripping mechanisms during charge and discharge. Pure lithium is highly reactive and its combination with flammable electrolytes and risk of dendrite formation make it quite unsafe. There has been much research into artificially manufacturing or tailoring SEI layers on lithium metal in order to manage the lithium plating and prevent dendrite formation.

2.6.2 Artificial SEI – current methods

Artificial SEI layers target specific properties that promote homogeneity, performance, and stability in the SEI. The key properties an artificial SEI must have are good ionic conductivity, mechanical stability, and chemical stability. One aspect that is often overlooked however is ease of manufacture, the fabrication of these thin layers must be cheap and quick to allow for industry application.

The simplest way of depositing films is by slurry-based methods such as doctor blading, dip coating and drop casting.[135–137] Much of the work in the literature using these methods focusses on flexible, often polymer-based, materials as they are more suited to slurry-based methods than inorganic compounds. These flexible artificial SEIs are more suitable for intercalation type anodes, which do not suffer from volume expansion and therefore do not require an artificial SEI layer with high mechanical strength.[138]

For inorganic artificial SEI layers, other manufacture techniques must be used, these are often costly and time consuming involving high temperatures, pressures, or vacuums. An exception to this is magnetron sputtering, which has been used to manufacture 10 nm to 300 nm thick lithium phosphorous oxynitride (LIPON) directly onto silicon electrodes, which replaced the natural SEI formation and improve the cycle life of the battery.[139,140] Magnetron sputtering is a commonplace and inexpensive process in industry, but it has been noted that it is unlikely to work on thicker, powder-based materials.[138]

Other techniques include CVD, ALD, molecular layer deposition (MLD) and electrodeposition, alongside many others. Table 1 in Fedorov et al, gives an overview of the different techniques that have been used to manufacture artificial SEIs and ranks them in terms of cost, scalability performance and more.[138]

2.6.3 Spray deposition of artificial SEI

Much of the research into artificial SEI and interlayer deposition involves coating a thin layer of material directly onto the cathode or separator films. Spray deposition has the advantage to do this without physically contacting the substrate film. Importantly, it allows for deposition of both low and high tensile strength materials, having been used for polymers and ceramic coatings, on either the anode or the separator.[141,142]

2.6.3.1 Spray deposition of stiff artificial SEI

Spray deposition of artificial SEI layers on pure metal anodes has been done primarily to prevent dendrite formation, by improving the properties of the SEI to ensure homogenous plating and stripping of the metal during cycling. Measurements of the instability in the overpotential of the cell suggest changes in the SEI layer; the SEI is not an ideal ionic conductor, therefore higher overpotentials are required to induce ionic diffusion.[143,144] The thickness of the SEI can be linked with increasing overpotentials. Spray deposited MoO_3 layers

on a lithium film led to overpotentials of 30 mV after 100 hours of cycling compared to 45 mV for bare lithium. The overpotential of protected lithium anodes was found to decrease over time, whereas in bare anodes it increases dramatically.[143] $CsPbI_3$ was used in an equivalent way to reduce the overpotential from 90 mV to 23 mV, although this study specified spray deposition in an inert environment to prevent degradation of the lithium prior to deposition.[145] There is significant improvement in cycle life and capacity loss due to these protecting layers with improvement in coulombic efficiency from 52.1% to 92.8% with a carbon fibre layer on zinc foil for zinc ion batteries.[146] Furthermore a tripling of cycle lifetime was seen with a 5 µm spray deposited stiff layer of Sb_2O_3 which both prevents the nucleation of dendrites and can protect against growth.[141] This layer is especially interesting as it is self-healing, meaning that if cracking of the SEI does occur, it can reseal itself. This is due to a benefit of the layer-by-layer spray deposition; as the initial layers of Sb_2O_3 contact the lithium they are decomposed to form a stiff organic-inorganic composite SEI, with unreacted Sb_2O_3 being subsequently deposited on the surface of the SEI. This reserve of precursors can help deal with large structure changes by filling in gaps or cracks in the formed SEI layer beneath.[141] There is also work on manufacturing a more natural SEI prior to assembling the battery, by spraying standard electrolyte additives such as fluoroethylene carbonate and $LiNO_3$ directly onto molten lithium films which gains more control over the initial formation of the SEI layer. This would only be possible with non-contact manufacturing techniques.[147]

2.6.3.2 Spray deposition of flexible polymer artificial SEI

The volume of work on spray deposition of polymer interphase layers is small and can be divided into two categories. The first is deposition of a layer directly onto the current collector, to aid lithium plating and stripping in anode-free cells.[148,149] The aims of anode free cells is to reduce the mass of excess lithium, therefore improve gravimetric energy density. As there is no excess lithium in the cell it is crucial that minimal SEI growth and dendrite formation occurs during cycling. Polyethylene oxide (PEO) and polyacrylic acid (PAA) nanoparticles were deposited onto bare copper current collector films which were shown to reduce overpotential fivefold. The lithiophilic PEO and abundance of carboxyl groups help create homogenous nucleation sites for lithium plating which reduces dendrite formation, and therefore SEI growth.[149] In a similar method ESD was

used to manufacture red blood cell shaped polyether sulfone particles on the surface of the current collector; this decreases the overpotential from 63 mV to 37 mV compared to bare copper. It is thought that this polymer layer helps the wettability of the current collector which results in more even lithium plating.[148]

The second category of work is in preventing electrode dissolution, and involves polymer spray deposition directly onto electrodes. ESD was used to deposit a 40 nm poly(poly(ethylene glycol) methyl ether methacrylate) or P(PEGMA) on LiV_3O_8 electrodes. This thin layer helps to prevent dissolution of active material into the electrolyte, and it was seen to increase capacity retention from 67% to 85% after 100 cycles.[150] The polymer coating acts as an artificial SEI, allowing ions through it but preventing material dissolution. Another study using spray deposited Nafion found a 73.9% capacity retention compared to 60.7% with a bare electrode due to the decreased cathode dissolution.[151] While both methods are important in improving battery characteristics, spray deposition onto the current collector is likely to produce a more uniform film due to the polished flat nature of the current collector surface. Manufacturing a film onto an existing electrode will be affected by the surface roughness of the material and therefore is impacted greatly by the initial deposition method used for the electrode, alongside the material chosen.

2.6.3.3 Spray deposition on separator

It is possible to spray deposit materials directly onto the separator; this can be to alter the properties of the separator, but in most cases, it is a way to form an SEI layer on the surface of the electrode upon contact with the separator. Nafion and Cl terminated MXene have both been used to form a more stable SEI.[142,152] Film thickness is crucial with thinner Nafion coatings appearing inhomogeneous, leading to breaks in the SEI and subsequently preferential nucleation sites for lithium.[142] Spray deposition on the separator allows for in situ formation of a thicker more even coating which lead to homogeneity in the SEI coating. Spray deposition onto the separator removes the requirement for the inert atmosphere needed for deposition onto lithium.

The other benefit of spray depositing directly onto the separator involves combining effects of SEI formation with that of preventing diffusion through the separator or improving interfacial contact with SSEs.[153,154] A MXene-based film sprayed onto a single side of a glass fibre separator was shown not only to help

prevent dendrite growth in SEI formation but also, due to the attached negative groups, help to prevent positive ions from moving through the separator.[153] An indium tin oxide (ITO) layer deposited on a lithium lanthanum gallium zirconium oxide SSE not only helps homogenous lithium plating but also provides good contact between the SSE and the lithium.[154]

A few studies have modified the properties of the separator using aluminium compounds for other benefits such as thermal resistance and dendrite prevention.[155,156] Modification of a standard Celgard separator was done by spray deposition of organoaluminium compounds, which formed Al_2O_3 on the surfaces of the separator.[155] Interestingly, the thin inorganic layer was formed on both sides of the membrane, and the sprayed droplets penetrated through the separator to deposit Al_2O_3 throughout the thickness. These modified separators showed higher thermal stability and less shrinkage under high temperature conditions, decreasing the likelihood of shorts occurring.[155] Similarly, this technique can be applied to solid electrolytes which can have a low resistance to dendrite formation, particularly in polymer and lower tensile strength materials. Applying an Al_2O_3 film on an interior surface of a PVDF-based SSE, thus forming a sandwich style composite electrolyte can help the tensile strength of the SSE but crucially would provide some barrier to dendrite penetration.[156] This improved the thermal stability of the separators, but was also shown to decrease electrical resistance from 4.3 Ω to 2.9 Ω.[157] When cells were subjected to heat treatment at 150 °C, there were found to maintain a stable voltage, whereas standard Celgard-based batteries shorted.[157]
There is little work on the manufacture of free-standing separators using spray deposition, possibly because spray deposition is unlikely to compete on speed and cost with slurry coating methods for standard separator manufacture. Spray deposition is more suited towards bespoke separator modification for adding specific functionality.

Overall spray deposition onto separator materials is an easy way to modify the properties of the electrodes, the solid electrolyte and the separator itself, depending on which side of the separator is modified. Generally the separator is an inert material which means that spray deposition onto it would be easier than spraying onto electrodes, which may be air or temperature sensitive. This means

that complex and expensive spray deposition requirements such as dry rooms, inert gas or low-temperature (therefore slower) spraying can be avoided.

2.7 Solid-state electrolyte manufacture

When free standing SSEs are often manufactured in pellet form for research purposes, they are then sandwiched between the electrodes and high pressures used to form the contact between the three layers. SSEs do not have the ability to 'wet' the electrode as liquid electrolytes do and rely on physical contact with the surface of the electrode. During cycling, volume expansion or changes in electrode architecture reduces the interfacial contact, increasing polarisation, resistance and the chance of lithium plating.[158] Polymer SSEs are more flexible and therefore more likely to withstand volume expansion, whereas stiffer SSE's are more resistant to dendrite formation. It has been shown that the deposition of a polymer electrolyte directly onto the cathode surface can reinforce the adhesion between a composite cathode and the SSE.[159]

A fundamental requirement for SSEs is the ability to be manufactured easily and cheaply. Most of the research into inorganic type SSEs requires pellet pressing and sintering techniques, which are less scalable and more expensive.[160] The approach is different for polymer-based solid electrolytes / solid polymer electrolytes (SPE's), which can be formed by traditional slurry casting methods, therefore are competitive with liquid electrolytes on cost and scalability.

Spray deposition provides an industrially relevant and scalable manufacture method for direct deposition of inorganic type SSEs directly onto electrodes, which can not only improve interfacial contact, but allow for fewer processing steps during manufacture. Alternatively, spray drying offers an inexpensive route to SSE particle manufacture, a key step in the synthesis of inorganic, high tensile strength SSEs. There are several different inorganic materials that have been spray deposited for SSE purposes, either by spray drying for particle synthesis,[161–163] or direct spray onto electrodes.[103,105,164–167] Due to the easy manufacture process of SPEs, few studies into spray deposition of these materials exist.

2.7.1 Spray drying of inorganic SSEs

Spray drying of SSE inorganic precursors can be used to manufacture ordered and symmetrical particles that can then be sintered and formed into an SSE. This

uniformity of particle size is crucial for good packing density, which in turn affects the ionic conductivity through the electrolyte.[163] Particle size is influenced by solution concentration, solvent boiling point, and temperature of the reactor. In a study on the temperature effects of spray drying, the particle size of $Li_{3.6}Ge_{0.6}V_{0.4}O_4$ SSE decreased from 10 µm to 0.2 µm as the deposition temperature increased from 400 °C to 600 °C.[164]

Other spray parameters can have a substantial effect on the composition of the SSE particles. The pH of the spray solution was found to affect the crystallinity of the final particles of $Li_{1.3}Al_{0.3}Ti_{1.7}(PO_4)_3$ (LATP), where a pH value of 6 was found to produce the highest intensity X-ray diffraction peaks, implying a highly uniform crystal structure; it is likely that a pH of 6 helps to stabilise the precipitating crystalline structure.[168] One crucial aspect that requires consideration is the loss of lithium during spray. This is often a factor during sintering, where lithium loss can occur over 900 °C.[163] Despite the lower required temperature of spray drying, lithium loss may be something to consider; small droplets of quickly evaporating solvent could amplify this issue, and the combination of erratic air flow and large spray-substrate distances could have an impact.

2.7.2 Direct to electrode spray of inorganic SSEs

Spray deposition is useful in manufacturing uniform and order SSE particles but can also be used to deposit the SSE layer directly onto the electrode. This is particularly important when rough electrodes are used, where any voids may not be contacted by a free-standing SSE. Inorganic SSEs often require post sintering to either complete the formation of the crystalline structure, or to bind together separate particles and increase density. This is also the case with spray deposited films, therefore the choice of electrode is limited, as it must be able to survive the high sintering temperatures needed for SSE processing. The choice of electrode material is then restricted to materials such as NiO[165], TiN[166], $LiMn_2O_4$[103], WO_3,[167] and yttria-stabilised zirconia,[105] which have higher melting points than traditional cathode materials of LFP and NMC. This method may be more suited to deposition onto anode materials, particular alloy type anodes which also require sintering, and often are designed to have rough reticular structures. A method of bypassing this issue would be to use cold spray/supersonic spray to deposit the SSE, as the high impact force could sinter

the particles upon deposition, there may be some damage to the electrode structure however.

Many of the standard parameters of spray coating can be used to optimise film characteristics; for example it was found that increasing the solution concentration of various ceramic precursors impacted the crack formation of the subsequent film.[105] In this work, each solution concentration had a minimum deposition temperature to prevent cracking, this minimum deposition temperature increased with increasing concentration and it was found that there was a limit to solution concentration where at the highest concentration there was no suitable deposition temperature to prevent crack formation.[105] Other work found that when the deposition temperature was too high, (600 °C), $La_{0.9}Sr_{0.1}Ga_{0.8}Mg_{0.2}O_3$ formed on the surface of a NiO substrate as small islands, that were disconnected from each other, this is most likely due to the fast evaporation of the solvent and preferential landing of the solid particles. When lowered to 150 °C a denser full coverage film was formed.[165]

Spray deposition is beneficial in coating rough or 3D electrode surfaces, and can compete with vacuum deposition in the manufacture of micro-batteries. Micro-batteries use 3D electrode structure to reduce internal resistance, and shorten the lithium diffusion paths, while remaining lightweight and small. These 'pillar' electrodes are demonstrated in Figure 2-7.

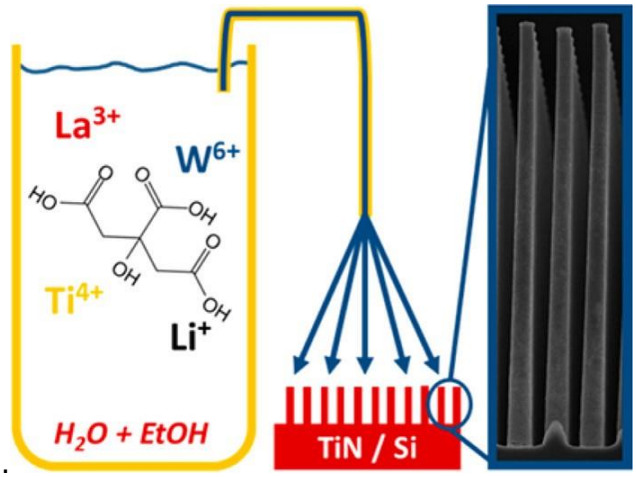

Figure 2-7: *The methodology of coating TiN / Si microcylinders with lithium lanthanum titanate. Reproduced from Ham et al.*[169]

These 3D thin film electrodes tend to consist of pillars in the Z axis, which makes coating them effectively to the base of the pillar quite difficult and requires expensive vacuum techniques. Spray coating can adequately coat these

structures with SSE material if the atomised droplets are small enough to reach the base of the pillars.[167] When the solution concentration is too high the material agglomerates at the top of the pillars, the authors relate this to the size of the droplets, claiming higher concentration is equal to larger droplets, however it may also be due to the fast evaporation providing preferential landing points for solid particles.[166]

One method of removing the limitations placed on electrode material choice by the high temperature sintering step of the SSE is to deposit the electrode material onto the pre-sintered SSE instead.[170,171] This offers the existing benefits of using a wider range of materials and maintaining the good contact between electrode and SSE however it requires the manufacturing of a free-standing SSE layer.

These techniques of spray deposition onto existing electrodes, electrolyte or separator materials are an interesting development in the field of spray deposition. The ability to manufacture different layers on top of each other, potentially using the same technique, leads to the possibility of half or even full cell manufacture in a layer-by-layer deposition method, removing the many separate processing steps required for each individual component.

2.8 Multi-layer spray deposition

Spray deposition has been used to deposit layers of SSE on top of existing electrodes,[166,167,172] to deposit both the electrode and SSE sequentially,[103] and to spray both electrodes onto opposite sides of an existing SSE pellet.[170,171,173] There are some examples of full cell spray deposition, involving consecutive deposition of both electrodes and SSE.[174–176] This method has been promoted as a promising solution for producing unconventional battery shapes, better suited for the future of integrated batteries and smart devices as current industrial techniques support only a limited range of electrode shapes, restricting their integration into next-generation technology.[175]

2.8.1 Full cell spray deposition

There are a few different studies on full cell spray manufacture, but none manage to complete the brief of a spray deposition synthesis of all components. The use of a solid electrolyte removes the requirement for filling with liquid electrolyte, although due to the limitations with SSEs in terms of operational conditions, these are not particularly industrially relevant. One study sprays ASSBs using a combination of ESD and electrospinning to manufacture LFP/PEOs/Sn

multilayers which are then cut and assembled into coin cells, using electrospray to deposit the cathode and anode and electrospinning to deposit the PEO SPE. They found that it performed favourably compared to other PEO-based cells made more traditionally. In post-cycling analysis it is shown that the Sn anode has disintegrated, and no clear layer is seen. Although not mentioned by the authors, there appears to be no current collector deposited on the surface of this Sn electrode, so this disintegration of the Sn into the PEO would be a concern with a lack of current collector to provide electrical connection to the entirety of the anode.[176] When spraying a full electrode/electrolyte/electrode system it is easy to ensure one of the electrodes has a current collector, as this is the substrate for the spray; manufacturing a current collector on the surface of the most recently deposited electrode provides more of a challenge. It would be possible to spray a copper-based current collector, however, an aluminium current collector which is traditionally used in cathodes would present a challenge due to the formation of explosive aerosols with fine aluminium powder.[175] A solution to this is to use carbon nanotubes as a replacement for an aluminium current collector; researchers designed a method to spray deposit an LCO/separator/LTO battery onto any surface by first depositing carbon nanotubes as a current collector onto the substrate. Substrates they have used include glass, stainless steel, glazed ceramic tiles, flexible polymer sheets and curved surfaces which promotes the production of integrated batteries which are structurally designed for their application.[175] This method however does not deposit an SSE, but uses a spray deposited separator, therefore they require filling with liquid electrolyte and then sealing in situ. The substrate material selection is limited due to the need to heat it to at least 90 °C.

This work shows that it is possible to completely manufacture a full battery assembly using spray deposition, which gives the opportunity for specialist designs and substrates for future integrated batteries, using a single manufacture technique. The limitations concern the poor performance of existing SSE technologies thus requiring the need for liquid electrolyte as well as the cell casing, which will be determined by size, shape, and substrate of the battery.

2.8.2 Layered and graded electrodes

Spray deposition has also been used to manufacture individual electrode and SSE films consisting of multiple individual layers or a graduated structure. This

gives the ability to optimise the material and chemical properties through the thickness and on both sides of the film. An electrode of this type can be made using other methods, such as slurry coating, where a doctor bladed bilayer NMC/LFP electrode is shown to impact the rate performance of the cell.[177] While industrially relevant, bi-layer slurry coating has not been studied in detail and also runs the risk of re-dispersing previously deposited materials. There is also a minimum layer thickness limit to slurry-based techniques that prevents the manufacture of many layers in a thin film.

2.8.2.1 Bilayer spray deposition

Using bilayers of different materials can alter the porosity,[178] thermal stability,[88] chemical stability[179] and chemistry[180] of the film, depending on the intended use. These bi-layers can be even layers,[178–180] or thin coatings on top of the primary film[88] in a similar vein to carbon coating of non-conductive materials, or artificial SEIs.

Control of porosity is crucial to optimise battery electrodes for volumetric capacity while retaining high active material utilisation. On this topic a spray deposited bilayer TiO_2 battery anode with higher porosity material nearer to the current collector and denser nanoparticles at the surface of the film was found to help electrolyte wetting nearer the current collector without unnecessary sacrifice of energy density across the whole thickness.[178] This control of porosity could be crucial to solving many issues related to liquid electrolyte-based electrochemical devices, particularly in lithium sulfur batteries where pore blocking by charge and discharge products represents a significant hurdle.[181,182]

Thermal stability of a $LiCoO_2$ cathode can be improved by a 3 wt% layer of $LiMn_2O_4$ on the surface of the electrode.[88] This type of surface modification is similar to the spray deposition of artificial SEI layers and opens the door to a multitude of surface modifications without the need for complex and expensive vacuum deposition techniques.

Chemical properties of materials can be altered using bilayers to impact the reactions on each side of the film. In fuel cell manufacture, two catalyst coated membranes were sprayed into a bilayer with one modified to be hydrophilic and the other hydrophobic to improve the management of water within the cell assembly.[180] This same bilayer property modification technique can be used to modify battery SSE properties which are sandwiched between two different

materials. In order to prevent oxidation of a PEO polymer electrolyte by high voltage cathodes, and the facile formation of lithium dendrites in a poly(N-methyl-malonic amide) (PMA) electrolyte, a bilayer SSE was spray deposited so that the negative properties of each material could be avoided when the film was in contact with both a lithium anode and a $LiCoO_2$ cathode.[179]

The ability to use layered structures to change the surface properties to improve chemical and structural stability has been taken further. In an effort to modify both faces of a film, spray deposition has been used manufacture sandwich structures, in which a central primary material has a thin protecting layer of another material surrounding it.[183,184] In another study on the oxidation of PEO with high voltage cathodes, a PVDF 'skin' was spray deposited on both sides of the SSE, protecting it from degradation due to its low oxidation onset potential.[184] This method was not done using spray deposition and instead involved the formation of three separate SSE films, which then had to be melded together under heat. Spray deposition would allow for a layer-by-layer assembly of these sandwich electrolytes and potentially give better adhesion between the layers. On work related to the volume expansion of silicon anodes, a carbon/silicon/carbon sandwich structure was spray deposited and was found to perform better than bilayer or mixed electrodes. The carbon near the current collector decreased electrical resistance, whereas the carbon at the electrolyte interface protected the silicon from extreme volume expansion and degradation.[183]

2.8.3 Layer-by-layer spray deposition

Layer-by-layer (LBL) deposition is the formation of stacked bilayers on top of each other to provide a structure that offers synergistic characteristics.[185] Much of the energy storage research into this field focuses on electrically or ionically conductive polymers for use as battery electrodes,[186–188] electrolytes[189,190] and fuel cell membranes.[185,191] Each individual bilayer is very thin, often in the nanometre range, and full films can be hundreds of microns thick. The use of spray deposition in this design approach has been adopted as an alternative to the traditional industry method of layer-by-layer dip coating.[189] Layer-by-layer dip coating is a process where a substrate is repeatedly dipped in a solution of material A, rinsed off, dried, and then the process repeated with solution B. The residual material that has adsorbed to the substrate forms a thin dense film that can be built upon to create the final structure. Spray deposition can be used to

replace the dip portion of the process and has been shown to speed up manufacture and decrease individual layer thickness.[185] The focus of the research therefore is on the comparison between spray deposition techniques and the resulting materials, to that of dip coating, particularly focussing on the speed and scalability of the process as well as the functionality of the film.

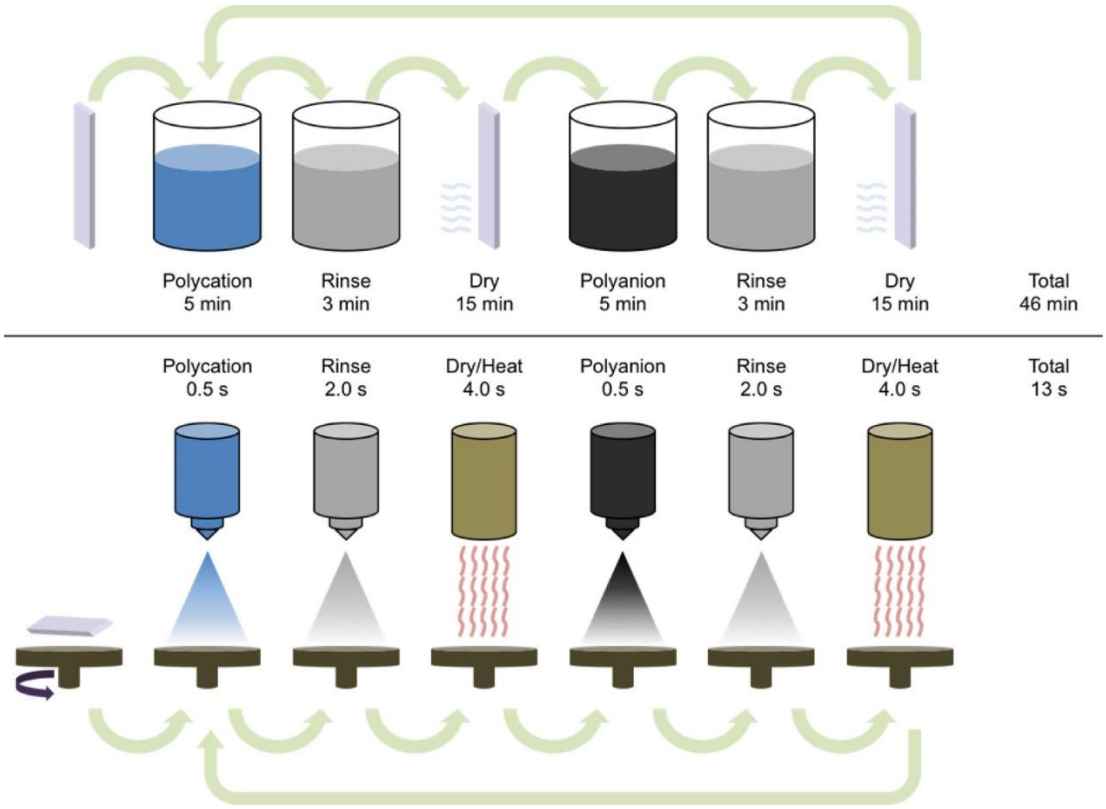

Figure 2-8: *The process of layer-by-layer dip coating (top) and layer-by-layer spin spray coating (bottom) with the time taken for each step. Reproduced from Gittleson et al.*[186]

Figure 2-8 shows the time comparison between a single bilayer manufacture with spray deposition and dip coating for a spin-spray LBL deposition technique, demonstrating the vast improvement in speed.[186] Spray coating can lead to a quicker deposition of bilayers particularly when combined with a method that allows quick in situ draining of excess liquid. This rinsing step removes excess material that would lead to thicker films, and shortens drying time, and techniques such as the spin spray method[186] and a tilted substrate design[189] allow for bilayer manufacture speed improvements of 115 times and 37 times faster compared to dip coating, respectively. Other works suggests that a spray deposition only method can provide a growth rate of 70 times faster that dip coating, without the need for spinning or tilting, but it must be recognised that the measurement they

use is film growth rate, not bilayer manufacture rate; in this case the spray deposited films were 46 nm thick, compared to 9 nm for dip coating. The increase in thickness of their bilayers is responsible for the growth rate increase and does not constitute a significant increase in bilayer manufacture time.[187] Conversely, the methods using a mechanical spin drainage step found the bilayer thickness to be thinner than that of dip coating at 0.8 nm compared to 3.1 nm for dip coating.[186]

This ability to combine spray deposition with other methods, comes from the inherent manufacturing differences between dip and spray deposition. Rather than moving the substrate around to different large deposition and rinsing baths; simply changing the spray solution over a fixed substrate allows for more control and decreases time, complexity, and the possibility of cross contamination of materials.[187] This process has been used to manufacture polymer films such as a polyaniline / poly(acrylic acid) bilayer as a doping-type cathode,[188] Poly(sodium 4-styrenesulfonate) / poly(allylamine hydrochloride) as a solid electrolyte,[189] and various polymer films for anode materials.[186,187] It has also been applied to more standard commercial battery anode materials such as silicon and graphite, where a repeating pattern was found to prevent the agglomeration of silicon nanoparticles and improve rate performance.[192]

2.8.4 Gradient spray deposition

Any film that has different material interactions on the top face compared to the bottom face, will require different properties to match these. This is evidenced in the necessities of the bilayer films, in which the stability and chemistry associated with the top and bottom interfaces are quite separate to each other. This bilayer work also creates another interface in the centre of the film between the two separate layers. Taking this work further requires the removal of this new central interface, creating instead a gradual change between the two distinct materials at the top and bottom face of the electrode.

Figure 2-9: *Illustration of a bilayer (a) and gradient (b) structure of two different porosity materials.*

This method of graduating structures gives even more control over the properties of the through-thickness structure, optimising the materials, porosity, and other properties in every layer of the film, while removing the potential central boundary created by bilayer deposition.[193]

2.8.4.1 Templating gradient manufacture methods

The gradient manufacture technique of battery materials has been demonstrated through methods such as ice,[193] salt,[194] and starch templating,[28] usually in the pursuit of porosity control. Battery electrodes play two key roles, one in providing adequate electrical conductivity, from the current collector, to the active material. The other is allowing for ion movement, therefore ionic conductivity, through the pores of the electrode. Active material needs to be both electronically and ionically connected in order for redox reactions to occur. Generally a battery electrode is a homogeneous structure containing optimised porosity and conductive additive. These values are optimised for the whole structure, therefore are an average of what is required throughout the electrode thickness. It is thought that during cycling, due to the anisotropic nature of the batteries electric field and electrode tortuosity, the lithium ion mobility (ionic conductivity) varies throughout the electrode in a gradient fashion. Furthermore, overpotential gradients are thought to occur due to varying electrode conductivities.[13,195,196] These gradient may impact the electrode performance, particularly at high rates or in thicker electrodes. One method to improve spatial performance and optimise the electrode might be to implement a gradient structure which increases porosity on the top face (near the electrolyte) and increases conductivity at the bottom face (near the current collector). This should provide enhanced performance both electrically and ionically where it is required.

Using templating methods, the porosity has been controlled to manufacture low tortuosity (Li^+ pathway resistance) electrodes, this improves cell performance

compared to homogeneous electrodes, while also reducing the proportion of inactive material and increasing the energy density of the batteries. Graduated $LiCoO_2$ cathodes with an average porosity of 36% were found to have a tortuosity of 3.92, compared to homogenous cathodes that had a similar porosity of 34% and a tortuosity of 6.19. This difference in particularly important at high rates where the graded cathodes had a 54% higher capacity density than non-graded ones.[197]

Gradient structures have particular significance on the ability to make thick electrodes, with most work focussing on ultra-thick cathodes. This is crucial to improving energy density of batteries by increasing the ratio of active material to cell casing, separator, current collector, and other inactive elements. Cathodes with thicknesses of 230 µm,[197] 900 µm,[193] as well as high mass loading anodes[194] have been manufactured using templating, which would prove difficult with conventional slurry casting methods due to the probability of increased crack formation with thickness.[193]

Although providing promising results, templating methods are not yet industrially relevant, many of these techniques require complex methods or equipment, particularly for temperature gradient equipment for directional ice templating,[193] pressure and heat bonding of individually casted electrode layers,[197] or multiple layer slurry coating.[194] While many of these methods involve the combination of multiple layers of electrodes with different porosity, the thin layer-by-layer nature of spray deposited electrode manufacture allows for true gradients to be built without the need for post processing.

2.8.4.2 Spray gradient manufacture methods

There has been little work in the use of spray deposition to manufacture gradients in battery materials, with only the Grant group in Oxford having published on the topic.[12,13] Using precise control of the flow rate of two separate solution inputs they have aimed to grade the conductive content throughout both an LFP cathode and a LTO ($Li_4Ti_5O_{12}$) anode finding that increasing the ratio of carbon nearer the current collector improved rate performance by 520% at 3C in LFP cathodes. This was associated with a decreased polarisation and therefore charge transfer resistance in the electrode.[13]

Graduated electrodes present a pathway to further optimisation in terms of performance and energy density, allowing for thicker electrodes with lower porosity and decreased inactive content. These techniques will only be taken on board by industry if their benefits can be matched by a cheap and scalable manufacture method, while this may be a possibility with multiple layer doctor blading, the technology is not there yet for the extremely thin layers needed for appropriate gradients. Spray deposition, while not commonly used in battery electrode manufacture, has proven itself a viable candidate for the large-scale manufacture of functional electrodes that require little post processing or additional steps.

The ability to form bilayers, sandwich structures, repeated bilayer patterns and gradients only breaks the surface of what is possible in spatial electrode design. Future electrode designs may combine a multitude of these structures, not only in one electrode but across the whole cell, with the potential for variations in structure across the x, y, and z plane. The requirement for the manufacture of such complex materials requires a precise deposition method, of which spray deposition is a suitable candidate and with proper scaling and planning, may prove to be an industrial competitor for large scale manufacturing.

2.9 Conclusions

Spray deposition is a versatile technique with many interesting variations that allow a wide range of structures to be made. By modifying basic parameters such as temperature, solvent, concentration, air flow etc., the drying time of the atomised droplet can be altered thus influencing the final structure of the deposited films. Reticular films made this way can be used to combat issues of volume expansion in alloy type anodes[28,29,58,59–61,88], or columnar structures can increase the surface area of cathode materials for increased rate performance.[84,89]

A further increase in droplet evaporation rate gives rise to spray drying which increases control over the size,[111] shape[213] and internal structure of solid or hollow micro-particles.[120] Most of this research requires further processing of these partials into a film, however there is potential for a direct formation of a hollow particle film using a repeated bilayer pattern of hollow spray dried particles and binder / conductive additives, thus allowing for a one step synthesis.

The inherent ability of spray deposition as an aerosol-based technique means a wide range of substrates can be used, allowing for the direct deposition of artificial SEI layers, separators and SSEs onto cathodes,[157,214,215] anodes, lithium[119,121,122–124] or other battery components.[142,144,152–154] This increases physical contact of these layers and can be used to add protecting or functional interlayers to improve stability and performance of the materials, without the need for additional processing steps. Taken further, the work here shows that spray deposition has been used to manufacture every component in a battery bar the cell casing.[174–176] These ‘paintable’ batteries provide a route to new designs of cell shape and structure, as well as integrated batteries, specific to their application, whether this is microbatteries[88] or novel shapes and casing structures.[175]

Spatial distribution of materials within an electrode or film may be crucial to full optimisation of energy density, porosity, and performance. Graduated electrodes are proven to outcompete homogenous ones made by traditional slurry-based methods and give the ability to manufacture ultra-thick cathodes which vastly increase capacity, with a minimal increase in non-active materials. The potential for precise deposition techniques that do not involve complex machinery or operating conditions to manufacture inherently designed architectures is large, and the choice of industrial deposition method will decide the complexity and properties of the battery materials of the future. While spray deposition remains in its infancy regarding industrial battery manufacture due to speed deficiencies[5] and a lack of commercial standardisation, it remains a promising avenue for future materials manufacture, in both energy storage and beyond.

Chapter 3 Methods

3.1 Spray deposition

Spray deposition is a broad term for thin layer manufacture using aerosol particles, this aerosol can either be a liquid or a solid; liquid deposition is more common and is used in this work therefore will be one discussed here. After initial atomisation of the solution, deposition involves two steps, propelling of the particle towards the substrate and evaporation of the solvent. Generally, both ESD and USD use some additional air flow, termed shaping air, to direct the atomised particles towards the substrate. Evaporation is done usually by applying heat to the substrate although in some cases, such as spray drying, the atomised particles are directed into a heated chamber and the solvent fully evaporated before the particles are deposited.

The spray deposition equipment used in the work is a SonoTek Exactacoat USD system. This technique was chosen due to its broader compatibility in terms of both materials and substrate when compared to electrostatic spray, and for the greater control in atomisation and particle size when compared to air spray. USD uses ultrasonic sound waves which create standing waves in the liquid on the tip of the nozzle, as the liquid leaves the nozzle surface it breaks apart into small droplets of a size dictated by the frequency of the sound waves, see Figure 3-1 (a). The droplets are then directed towards a heated substrate which quickly evaporates the solvent leaving the solid particles deposited.

Spray deposition is used to manufacture electrodes in a layer-by-layer fashion. Each layer deposits a small amount of mass in a thin film of material and the overall thickness is built up slowly. The spray heads therefore must have the ability to raster over the deposition area and are often built onto a gantry that allows movement in the x, y, and z axis. This means that it is easy to manufacture films of specific shape and size.

In this work, to ensure homogeneity throughout the film manufacture, the spray head was rastered over the deposition area 4 times to effectively deposit 1 layer. The distance between the raster lines was set to 4 mm; to prevent gaps between the patterns a second spray was done at a 2 mm offset. Further to this, to prevent raised horizontal lines from occurring two further passes were sprayed again at a 90 ° rotation, see Figure 3-1 (b).

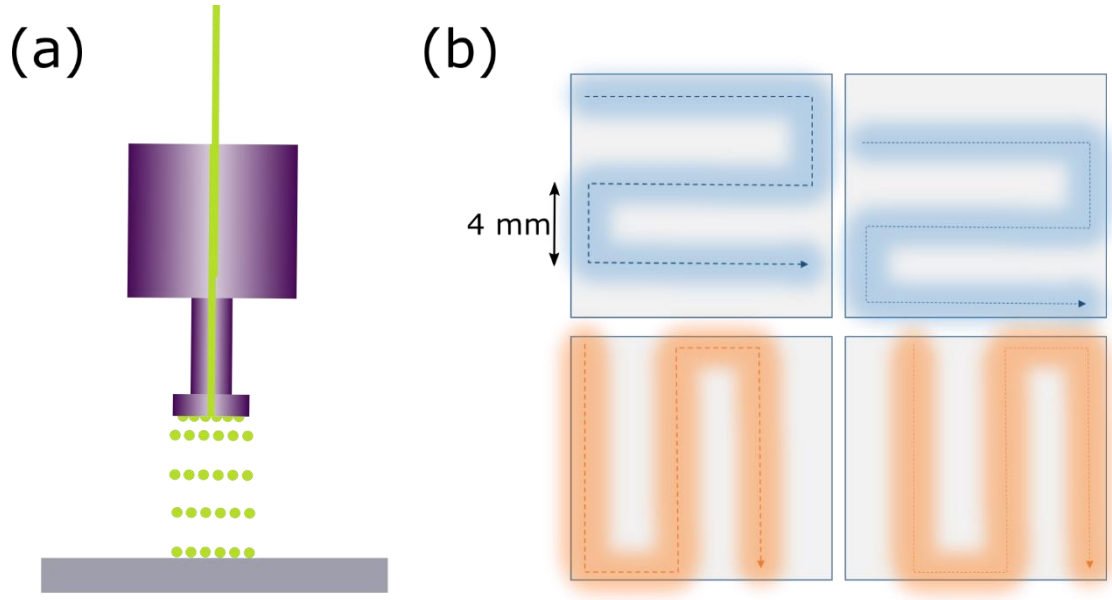

Figure 3-1: *(a) The atomisation of a liquid in an ultrasonic spray nozzle. Ultrasonic sound forms standing waves in a liquid on the surface of the nozzle which then detach to form small uniform droplets.*
(b) The four raster patterns used to build up one layer of deposited material in spray deposition.

The films sprayed in this work vary in thickness from ~10 µm to a few hundred µm, as measured by optical and scanning electron microscopy. To spray different thicknesses of films automatically a program must be created to run the various elements of the spray program in a reproducible yet adjustable way. The general elements of the spray coater are shown in Figure 3-2 (a) and consist of two syringes that are pushed or pulled at a defined rate by syringe pumps. A refill valve controls whether the syringes are connected to a bulk refill solution or to the spray nozzles, when connected to the refill solution the syringe plungers can be pulled back to load the syringes. To spray, the refill valve is closed, and the pumps push liquid towards the isolation valves which act as a stop to prevent liquid flowing through accidentally. The liquid is then pushed through to the nozzles which atomise the solution into droplets which are then directed towards the substrate using the shaping air. The associated parts of the spray coater including the syringes, syringe pump, refill valve and nozzles are showing in Figure 3-2 (b) and (c).

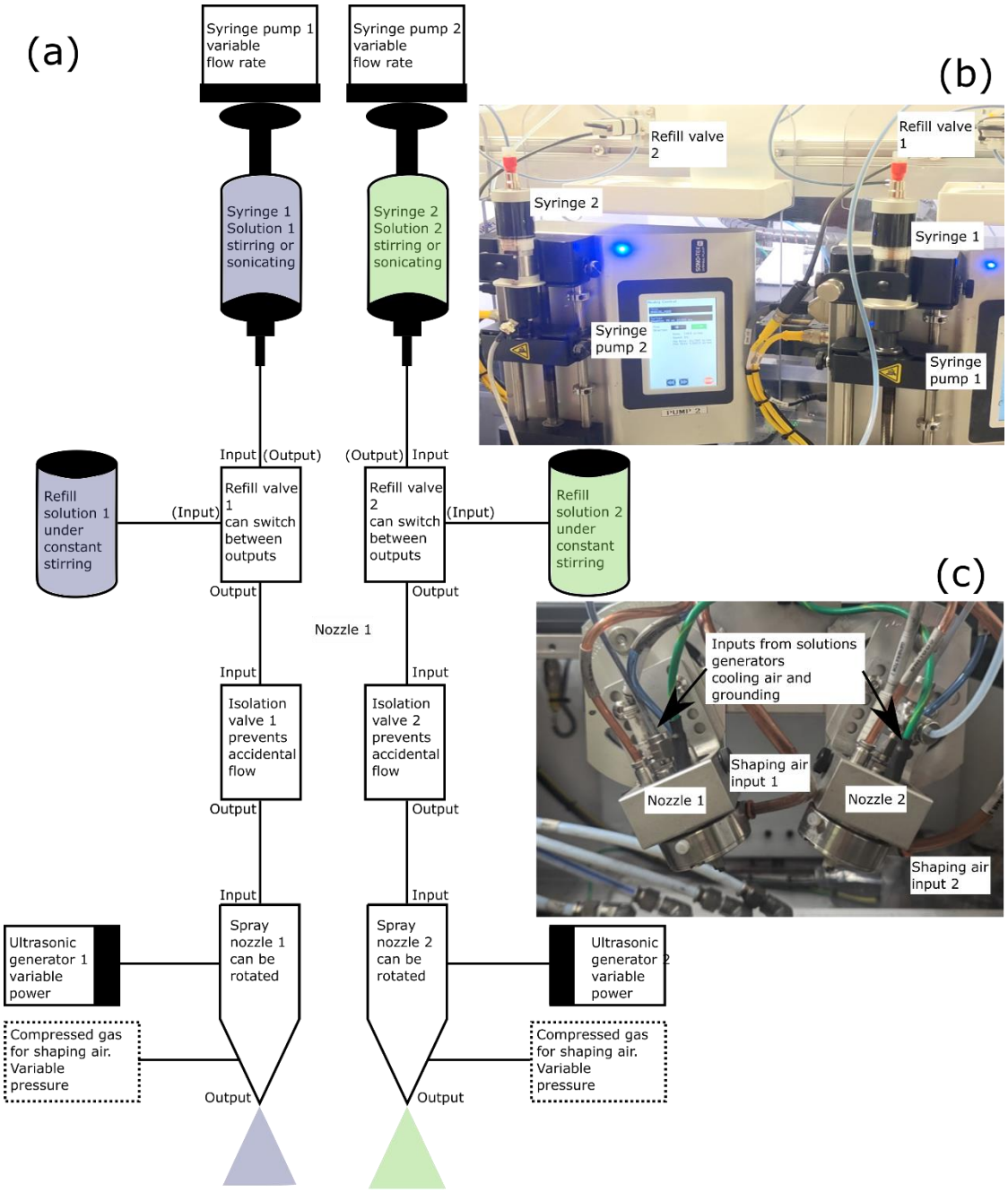

Figure 3-2: *(a) The schematic of the Sonotek Exactacoat spraycoater, including the flow from the syringes to the refill solutions to the spray nozzles and subsequent inputs. (b) Image of the spraycoater showing the syringes, syringe pumps and refill valves. (c) Image of the spraycoater nozzles showing the solution and shaping air inputs.*

The methodology for manufacturing gradients into an electrode involves writing a program that varies the syringe pump rates of the two syringes throughout the course of the spray.

Line	Command	Position	Units	Description
1	Comment	Gradient Spray Bi-Nozzle		Title
2	Comment	Edit lines 5,6,34		Description
3	DMC	RUN_PWR[11]=2	Watts	Setting ultrasonic power of Nozzle 1
4	DMC	RUN_PWR[12]=2	Watts	Setting ultrasonic power of Nozzle 2
5	DMC	RATEINP=0.5	ml min^{-1}	Total flow rate
6	DMC	TOTALCOUNTINP=19		Number of passes
7	DMC	RATE1=RATEINP	ml min^{-1}	Input of syringe 1 initial rate
8	DMC	RATE2=0	ml min^{-1}	Input of syringe 2 initial rate
9	DMC	COUNTER=0		To count pass number
10	DMC	RATE[11]=RATE1	ml min-1	Applying initial rate to syringe pump 1
11	DMC	RATE[12]=RATE2	ml min-1	Applying initial rate to syringe pump 2
12	DMC	#LOOP1		Return position for loop
13	TOOL	1 On		Turning on generator 1, syringe pump 1, isolation valve 1 and shaping air 1
14	TOOL	2 On		Turning on nozzle 2, syringe pump 2, isolation valve 2 and shaping air 2
15	AREA	72.83,99.395,0	mm	XYZ coordinates of three corners of square
16		122.83,99.395,0	mm	
17		122.83,149.395,0	mm	
18	AREA	122.83,99.395,0	mm	90° rotation of square
19		122.83,149.395,0	mm	
20		72.83,149.395,0	mm	
21	AREA	74.83,101.395,0	mm	2mm offset square of square to fill in gaps
22		124.83,101.395,0	mm	
23		124.83,151.395,0	mm	
24	AREA	124.83,101.395,0	mm	90° rotation of offest square
25		124.83,151.395,0	mm	
26		74.83,151.395,0	mm	
27	TOOL	1 Off		Turning off generator 1, syringe pump 1, isolation valve 1 and shaping air 1
28	TOOL	2 Off		Turning off nozzle 2, syringe pump 2, isolation valve 2 and shaping air 2
29	DMC	RATE1=(RATE1-(RATEINP/TOTALCOUNTINP))		Calculating new rate for syringe pump 1, based off TOTALCOUNTINP
30	DMC	RATE2=(RATE2+(RATEINP/TOTALCOUNTINP))		Calculating new rate for syringe pump 2, based off TOTALCOUNTINP
31	DMC	COUNTER=COUNTER+1		Update counter
32	DMC	RATE[11] = RATE1	ml min^{-1}	Setting new rate of syringe pump 1
33	DMC	RATE[12] = RATE2	ml min^{-1}	Setting new rate of syringe pump 2
34	DMC	JP#LOOP1,COUNTER<20		Check if counter limit has been reached and loop command

Figure 3-3: *The code used to operate the ultrasonic spray coater in manufacturing graded films.*

Figure 3-3 shows the code used to manufacture a 0% to 100% gradient of two different materials, using two nozzles. It consists of setting a loop (line 34) that tracks a counter up to a defined number, in this case 20. The total count input (line 6) is set to 19 but the loop counter limit is for 20 passes, this is to account for the final spray pass, which needs to be 100% solution 2, if it were set to 19, the final pass would still have a small input from syringe pump 1. The code sets the initial flow rates for each syringe (lines 10 and 11), then sprays the four raster patterns (area is shown in lines 15 to 26) described above before calculating the new flow rates for each syringe (lines 29 and 30). Before the area code are two tool functions to use for that area: isolation valves, syringe pumps, generators and shaping air. To spray with two nozzles simultaneously, both sets of these be

turned on and off manually before and after the spray patterns (lines 13, 14, 27, 28). When spraying thicker electrodes that require more than one syringe of liquid, the program must also contain refilling instructions which ensures that neither syringe empties entirely throughout the course of the spray. The benefit of using code to automate the gradient is that it is repeatable but also customisable, for example in order to manufacture an 80% gradient rather than a 100% gradient, the starting flow rates can be altered as well as the calculation to work out the new flow rates to ensure that the correct ratio is reached.

In order to ensure good dispersion of materials throughout deposition, the spray coater was fitted with sonicating syringes or stirring syringes where required. The sonicating syringes operated on a schedule of 5 seconds on 5 seconds off, at a power of 3 W, and the stirring syringe operated at 200 rpm. When a bulk refill solution was used the supply bottle was left stirring at 300 rpm.

3.2 Spray solutions

For the majority of this work the precursor solutions for spray deposition followed the same general principle; this involved dispersing micron sized solid particles into a liquid which was then sonicated to prevent sudden sedimentation. The solvent was chosen in terms of its ability to disperse or dissolve the solids, as well as having a sufficiently low boiling point and viscosity. The viscosity of the solvent is crucial when using USD compared to other atomisation methods as higher viscosity liquids is not atomised as easily using sound waves and requires power higher than that of the generator used here. In most of this work, a bi-solvent mixture of IPA and DI-water was used, as there was often solid carbon, graphite or LFP particles which dispersed well in IPA, alongside water soluble polymers such as CMC and PEO which dissolve effectively in water. This bi-solvent system also served to reduce the overall boiling point when compared to water alone which speeds up drying time and therefore increases the max flow rate of solution that can be achieved. The overall speed of spray deposition is determined by the dispersion limits of the solvent alongside its evaporation rate; higher concentration solutions mean that more material can be deposited per pass and therefore fewer passes are needed to achieve the same thickness and faster evaporation rates mean that the total flow rate of solution can also be increased. It must be noted that faster deposition has the potential to reduce film

homogeneity, however. Initially work was done in the lithium sulfur chapter using solution concentrations of 1 mg mL^{-1} but the long deposition times (~12 h) and large solution volumes (~500 mL) proved to be difficult going forward. Eventually, using syringes that provided either additional stirring or sonication, and by shortening the tubes connecting the syringe to the nozzle, the sedimentation time of the solid material was increased beyond that of the time taken for spray deposition and solutions of 10 mg mL^{-1} were used for the remaining work. Solution and material choice was key in reliably manufacturing electrodes using spray deposition; it was found that particle sizes above a few microns were difficult to disperse for longer than a few minutes, and highly viscous liquids capable of dispersing them such as Cyrene, a safer NMP replacement, caused both pumping and atomisation issues. The decision was taken not to add any additional surfactants to the solution mixtures as these would then complicate any electrochemical results and analysis.

3.3 Spray parameterisation

The key parameters that affect the quality and microstructure of spray deposited electrodes are solvent boiling point, temperature of the substrate, solution flow rate, shaping air rate and nozzle height. These all relate to the speed of evaporation of the solvent, and optimisation of all these parameters leads to faster coating times and therefore cheaper manufacturing costs. Solvent boiling point and substrate temperature are self-explanatory and have clear boundaries; the solvent must be able to effectively disperse or dissolve the active materials which limits choice, and the substrate cannot be heated beyond the decomposition temperature of the materials to be deposited. The solvents used in this work are DI water and IPA, which have low boiling points, which allows low substrate temperatures to be used, between 60 °C and 150 °C depending on material.

Shaping air rate, solution flow rate and nozzle height have fewer clear influences on the quality of the spray, therefore a study was designed to analyse their effects on deposition. A 10 mg mL^{-1} LFP (lithium iron phosphate 1.5 µm, MSE supplies) solution in 1:1 IPA:DI water by volume was sprayed for ten seconds onto aluminium foil at 120 °C. Standard parameters were a spray height of 60 mm, flow rate of 1 mL min^{-1} and shaping air of 0.5 psi. Each parameter was altered in

turn to look at the effects on the deposited film which was imaged using optical microscopy (Keyence VHX 7000 at 20 x magnification), see Figure 3-4.

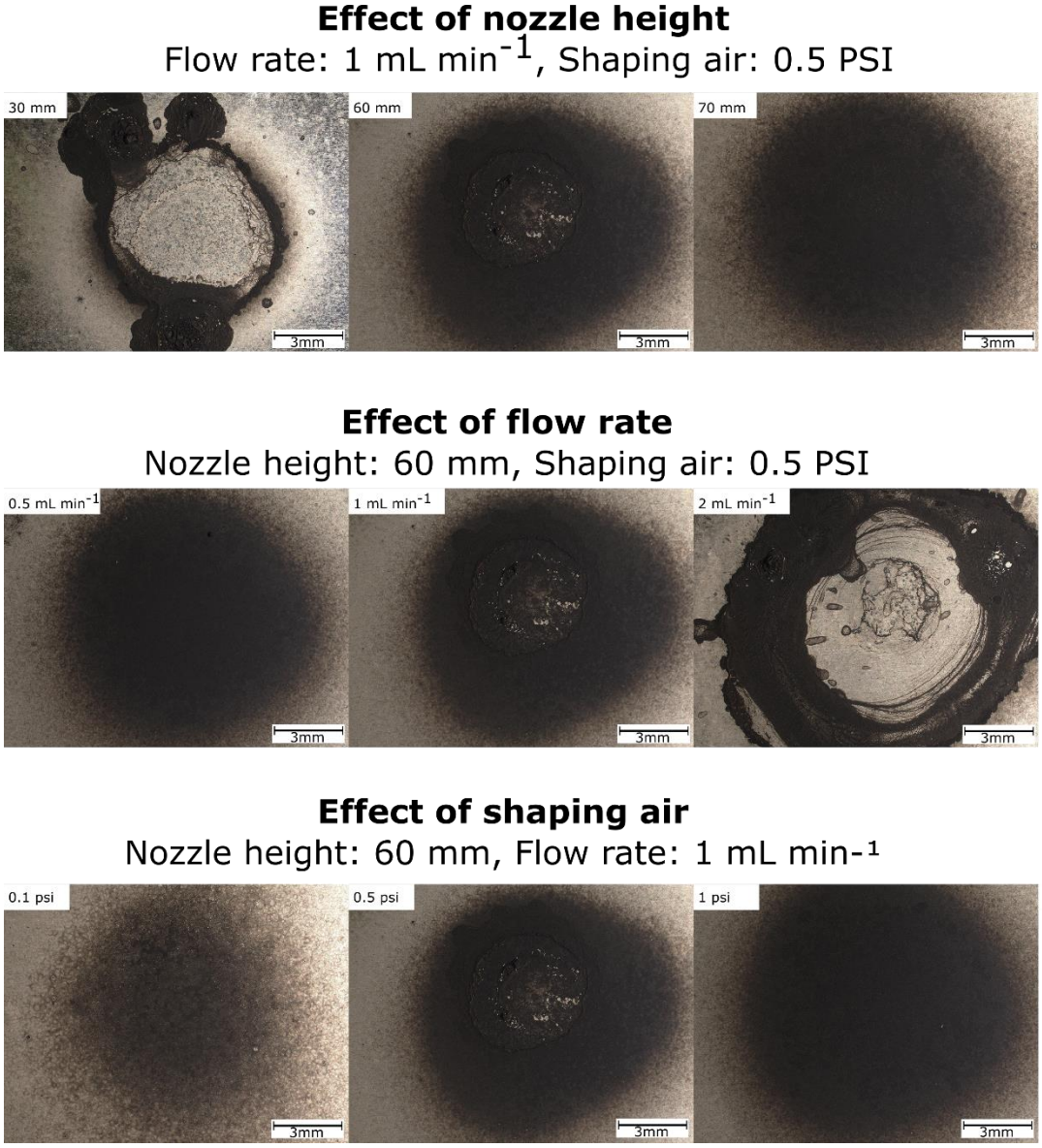

Figure 3-4: *The parameterisation of ultrasonic spray deposition of LFP showing the effect of nozzle height, solution flow rate, and shaping air pressure on a 10 second dot spray. LFP solution was 10 mg mL^{-1} and was sprayed onto aluminium foil at 120°C.*

The quality of the sprayed circle in the nozzle height study shows that at a nozzle-substrate distance of 30 mm a coffee ring pattern is formed. This is a result of the solvent remaining on the surface long enough to be pushed to the edges of the spray area by the shaping air. This coffee ring pattern is very clearly seen at a nozzle height of 30mm. The short nozzle substrate distance does not give the spray enough time to spread out and thin, instead focussing the bulk of the

solution on a small area, leading to solvent build up on the substrate. It was seen at higher nozzle distances of 60 mm that the influence of the shaping air has been reduced, but still some cracks and voids are present in the centre of the dot. This is a cause of self-reorganisation of material in the remaining solvent which allows for preferential deposition leading to inhomogeneity. At higher nozzle heights of 70 mm the film appears even and homogenous with no sign of defects, meaning that the solvent has evaporated quickly.

When flow rate is varied instead, similar patterns are seen. A solution flow rate of 0.5 mL min^{-1} forms a good film, characterised by the homogeneity of the surface. Increasing the flow rate causes central voids at 1 mL min^{-1} and clear redistribution of material at 2 mL min^{-1}. The increase in amount of solvent without an increase in the evaporation rate means the solvent dwell time is too high and reorganisation can occur.

The shaping air pressure was found to have multiple impacts of film quality; firstly, it became clear that shaping air can influence the evaporation rate. Poor quality films were seen at 0.5 psi, with cracking and delamination evident in the centre of the dot spray. Unusually at both 0.1 PSI and at 1 PSI the dot spray shows no evidence of material reorganisation. The film manufactured with low shaping air pressure (0.1 psi) has less deposited material in a less defined shape. It is thought that with a low shaping air pressure, the in-flight droplets are less directed and therefore there are large material losses, alongside a greater deposition area. This would mean less solvent is reaching the desired target area and therefore the slow evaporation rate is sufficient, and no reorganisation occurs. The dot sprayed at 1 PSI shows a much larger area of deposited material, although with no evidence of cracking. It is hypothesised that high shaping air pressures can increase the evaporation rate of solvent through the movement and replacement of air and solvent vapour. From these studies it can be concluded that the optimum spray parameters would be a nozzle height of 60 mm, flow rate of 1 mL min^{-1} and a shaping air of 1 PSI. These parameter settings optimise speed of solution flow while using the increased shaping air to speed up solvent evaporation rate.

In order to study the effects of shaping air further, full films were manufactured comprising of 20 spray passes of 10 mg mL^{-1} LFP in 1:1 IPA:DI water by volume,

at a flow rate of 1 mL min^{-1}, substrate temperature of 120 °C and nozzle distance of 60 mm. Shaping air pressure was adjusted between 0.1 psi and 2 psi and the mass and thickness of the subsequent films was measured, see Figure 3-5.

It was found that shaping air influences the efficiency of the spray, as expected, with lower shaping air pressure resulting in less mass being recorded in the desired spray target area. As the shaping air pressure is increased up to 1 psi, the film mass reached a maximum of ~10 mg. Interestingly the reverse trend is seen with the film thickness, measured using a micrometer, with lower shaping areas producing a film with a larger measured thickness, which continues decreasing up to at least 2 psi. As has been shown previously, a slow evaporation rate leads to inhomogeneity and crack formation within a film, which creates areas of raised material that are abnormally high thickness and are not representative of the average thickness. It is also possible that higher pressure shaping air compresses the material more, which may be the reason for the continued decrease in film thickness between 1 and 2 psi, despite both films appearing fully homogenous. Shaping air is not a parameter that has been studied in the literature before, particularly not for battery materials, but some research has found that varying the nozzle/substrate distance, similar effects can be seen, with larger distances increasing thickness and decreasing mass and vice versa.[223] The principle is similar with larger nozzle/substrate distance leading to decreased air pressures upon deposition. The film density seen with the 2 psi shaping air in Figure 3-5 is around ten times lower than that seen with commercial LFP electrodes made using slot die coating which emphasises the increase in porosity available when using spray deposition as a manufacture method.

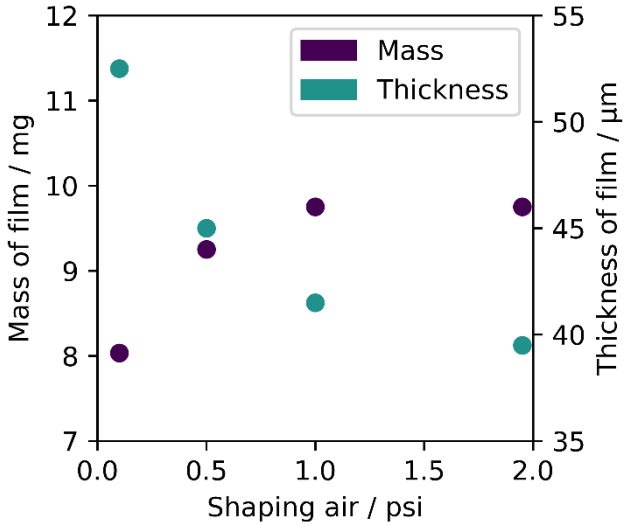

Figure 3-5: *The mass and thickness of LFP films sprayed with different shaping air pressures.*

Although the quality and structure of films manufactured by spray deposition is primarily dependent on the solvent evaporation rate, due to material reorganisation, the number of factors that influence the solvent evaporation mean that spray deposition of new materials requires detailed optimisation to ensure film quality alongside speed of manufacture. All the materials in this work are not common spray deposition materials, therefore they also required optimisation of spray parameters alongside dispersion properties and solvent before sufficient quality films could be manufactured.

For each of the three battery chemistries studied in this work the list of parameters that needed optimising includes: solvent choice, solution concentration, sonicating method and time, additional dispersion techniques (stirring or sonicating syringe), flow rate, nozzle distance, shaping air, substrate temperature, spray shape (raster gap), raster speed, dwell times (additional pause to aid evaporation) and pass count (thickness). This is on top of battery performance optimisation parameters such as: active material/binder/conductive carbon ratio, electrode thickness, conductive carbon type and substrate material. An ideal spray deposition was one that created a good atomisation, without sedimentation of material in the syringe or tubes, created a homogenous film of adequate size, while remaining a relatively quick process <8 hours. In order to optimise all of these parameters a great deal of trial and error manufacturing work took place for each battery chemistry, and as many of these materials had not

been sprayed previously, or not on a similar USD device, the parameterisation had to be done without estimated values.

3.4 Electrode characterisation

Characterisation of the gradients was done either using a scanning electron microscope (SEM), with energy dispersive X-ray spectroscopy (EDX) or with X-ray computed tomography (X-ray CT). SEM EDX was used when gradients were manufactured using a material vastly different from the host material in terms of its characteristic X-rays, discussed further in Section 3.4.1 below, and when particle sizes were too small for X-ray CT, i.e. gold in the graded lithium sulfur cathodes, and silicon in the graded silicon graphite anodes. EDX was performed on through-thickness cross section samples to capture the full gradient, this process comprised cutting the electrode, sealing in epoxy resin and the polishing using a polishing wheel. Where EDX did not show good detail, or there was significant overlap in characteristic X-rays, i.e. for the LFP/PEO solid-state composite cathodes, X-Ray CT was used to demonstrate the difference in density through the thickness of the electrode.

3.4.1 Scanning electron microscopy with energy dispersive X-ray analysis

SEM combined with EDX is an analytical technique for simultaneously examining surface morphology and elemental composition of materials. SEM utilises a focused electron beam to scan the sample surface, producing high resolution images by detecting secondary and backscattered electrons. Secondary electrons are a result of inelastic scattering and primarily originate from the surface of the materials providing detailed surface topography, while backscattered electrons are a result of elastic scattering from a broad region with the material resulting providing good compositional contrast, enabling differentiation based on atomic number.

EDX, when integrated with SEM, allows for the elemental analysis of the sample by detecting X-rays emitted as the electron beam interacts with atoms in the sample. Each element produces characteristic X-ray peaks, enabling precise elemental identification and quantification. SEM EDX offers comprehensive insights into both the structure and composition of materials allowing for precise characterisation and analysis of complex structures.

In this work, secondary electron measurements were performed using an SEM EVO MA10; all samples were dried and mounted onto carbon tape before loading into the SEM. If samples were non-conductive, they were gold sputtered to add a conductive coating of a few nanometres thick. Samples were cut and mounted along the same plane as the electron beam. EDX was utilised over a diagonal line that covered the thickness of the electrode and current collector. The hit count related to each element can then be plotted in relation to the distance along the measurement line. The line was chosen to be diagonal rather than perpendicular to the electrode to increase the total number of measurements across the thickness and therefore reduce the noise.

3.4.2 X-ray computed tomography

X-ray Computed Tomography is an imaging technique that provides high resolution, three-dimensional (3D) representations of the internal structure of a sample. X-ray CT works by rotating an X-ray source and detector around the sample, capturing a series of two-dimensional (2D) radiographs from multiple angles. These images are then computationally reconstructed into a 3D model, which can then be analysed further.

The technique requires differences in X-ray attenuation across materials, with denser structures absorbing more X-rays and appearing with higher contrast in the final image. X-ray CT is particularly useful for characterizing 3D structures without the need for disassembly, therefore is a good option for in-situ characterisation. It is used in the battery electrode field for the study of porosity or defects prior to and during battery cycling, as well as post-failure studies.

The X-ray CT used here was a lab-based micro-CT X-ray instrument (Zeiss Xradia 620 Versa, Carl Zeiss). Further analysis and segmentation were done using Avizo3D 2023.2 software (ThermoFischer) and ilastik software.

3.5 Electrochemical analysis

3.5.1 Electrochemical impedance spectroscopy

Electrochemical impedance spectroscopy (EIS) is an analytical technique used to investigate the impedance of an electrochemical cell over a range of frequencies by applying a small sinusoidal voltage and recording the resulting current response. The impedance data provides insight into various processes

occurring at the electrode/electrolyte interface, such as charge transfer, diffusion, and capacitive behaviour.

In an EIS analysis, the resulting impedance spectra are typically displayed as Nyquist or Bode plots, where different regions correspond to distinct electrochemical phenomena. The standard Nyquist plot usually contains a semicircle profile alongside a steep gradient tail, these give information about the charge transfer resistance of the electrochemical cell. By fitting the experimental data to an equivalent circuit model, quantitative information about resistance, capacitance, and diffusion processes can be extracted, and applied to specific processes occurring within the cell. EIS is a valuable, non-destructive technique widely applied in the characterisation of batteries, although it suffers from being quite sensitive to the experimental design, alongside the subjective nature of equivalent circuit fitting.

The DRT (Distribution of Relaxation Times) transformation and analysis of the real and imaginary impedance was performed using RelaxIS 3 (RHD Instruments). A Gaussian function was applied for data discretization, with a second-order regularization fitting parameter (λ) of 0.0001, and a shape factor of 0.5 used. The software facilitated the determination of peak positions and shifts across cycles during charge and discharge.

In this work, EIS was used simply to determine the overall charge transfer resistance inside the electrochemical cell. In this way, no equivalent circuit is used to deconvolute the plot and the total resistance is used as a comparative tool.

Specific electrode and electrolyte manufacturing methods, alongside coin cell assembly and testing differ for the different battery chemistries and materials researched in this work, therefore will be discussed separately in each chapter.

Chapter 4 Gradient Catalyst Structures in Carbon Cathodes for High-Rate Lithium Sulfur Batteries

4.1 Abstract

Lithium sulfur batteries offer increased capacity and gravimetric density when compared with current Li-ion batteries. They currently suffer from a range of issues which are hindering commercial uptake; these include poor cycle life, rate performance and low active mass loading. Sulfur is non-conductive and exists in the final charged and discharged states as solid S_8 or Li_2S. These sulfur containing deposits can often block electrolyte access to unreacted sulfur contained within in the electrode; this effect is worsened at high current densities.[224] Gold catalysts embedded within the sulfur have been proven to enhance the rate performance and sulfur utilisation, this is thought to be due to an impact on the electronic and lithium conductivities of the electrode.[225] The addition of gold raises the cost and mass of inactive material inside the electrode, therefore ensuring the minimum possible gold amount is optimum for commercialisation; it is thought that the blocking effect of solid sulfur species occurs mainly on the surface of the film therefore the location of gold should be optimised to the electrode surface only.[182] To test the location dependence of gold catalysts on the deposition and removal of solid sulfur charge and discharge products, carbon-based cathodes were manufactured with 5.5 wt% gold added in different gradient formations. Gradient cells with gold either predominantly near the surface or the base of the electrode were tested for rate capability with different sulfur% loadings between 10 wt% and 70 wt%. It was found that the gold catalyst had little effect at lower sulfur loadings, but at 70 wt% sulfur a gradient structure with increased gold at the surface of the electrode was found to reduce capacity loss at higher C-rates and showed higher concentrations of polysulfides in the electrolyte, suggesting better conversion between solid and soluble sulfur compounds.

4.2 Background

Lithium sulfur (Li-S) batteries are a next generation battery technology that is expected to have a large contribution to the clean energy transition. Li-S batteries move two electrons per sulfur atom between the cathode and anode, compared to ≤1 electron per transition metal in Li-ion which greatly increases the potential

charge transfer per mass, particularly when battery mass is a crucial metric towards commercial use.[226] Because of this, sulfur offers a theoretical capacity of 1672 mAh g^{-1}, which is a vast increase on current lithium-ion cathode materials which have a limit of ~300 mAh g^{-1}.[226] Sulfur is also very naturally abundant and non-toxic, which makes it cheaper and safer to work with, and removes many issues related to mining and human rights that are associated with other chemistries such as $LiCoO_2$.[227] Despite these promises, commercial uptake of lithium sulfur has been slow due to sulfurs low-conductivity, high self-discharge and poor rate performance issues that plague the chemistry. While many companies are researching the technology with an aim of commercialisation, there are no companies that currently sell them.

4.2.1 Lithium sulfur electrochemistry

Lithium sulfur batteries contain a sulfur-containing cathode (positive electrode) and a lithium metal anode (negative electrode) in an organic lithium salt containing electrolyte. They differ from traditional intercalation-based Li-ion batteries in the redox reactions that occur during charge and discharge. The main Li-S reaction is shown in Equation 4-1, which demonstrates that each individual sulfur combines reversibly with two lithium ions to form lithium sulfide. Pure elemental sulfur exists as the cyclic octatomic molecule S_8 and the sequence of reactions from solid S_8 to solid Li_2S_8 forms intermediate soluble polysulfides with varying chain length.[228]

$$S + 2Li^+ + 2e^- \rightleftarrows Li_2S \qquad \textbf{Equation 4-1}$$

During discharge lithium ions move from the metal anode to the sulfur containing cathode through the electrolyte, while electrons pass through an external circuit to the cathode. The solid S_8 progresses through longer chain polysulfides to shorter chain ones and eventually to the discharge product Li_2S; the reverse occurs during the charging process. The charge-discharge curve in Figure 4-1 shows two voltage plateaus in the discharge process at 2.3-2.4 V and 2.1 V, which are thought to account for the reduction of solid S_8 and the formation of solid Li_2S which are kinetically slow reactions.[229]

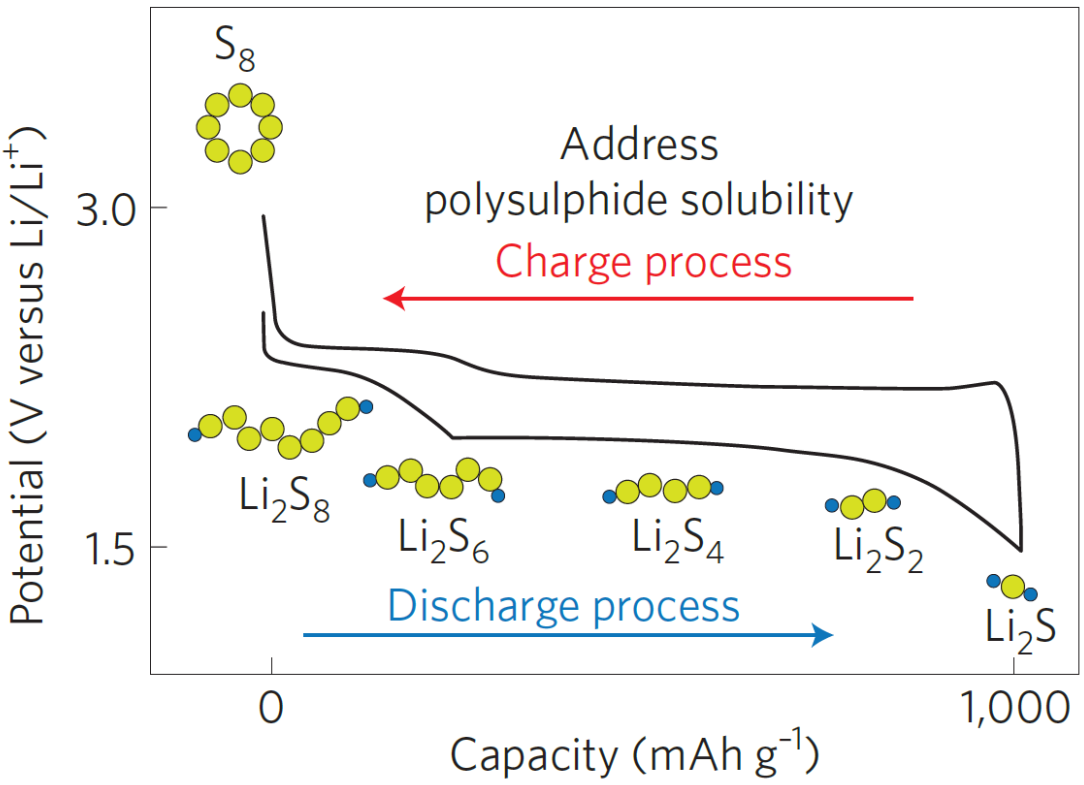

Figure 4-1: *The charge discharge curves of a lithium sulfur cell, showing the associated voltage plateaus and polysulfide intermediates. Reproduced from Bruce et al.*[228]

4.2.2 Limitations and issues surrounding lithium sulfur

There are a range of issues preventing commercialisation of lithium sulfur batteries, these relate to the solubility of the polysulfides and the conductivity of the solid sulfur and its compounds.

The solubility of the polysulfide intermediates means that they can get trapped in the electrolyte and become disconnected from the cathode, leading to active material loss and lowered capacity. This may be taken further with the polysulfide shuttle effect which occurs when longer chain polysulfide intermediates in solution diffuse to the lithium metal anode where they are reduced to shorter chain polysulfides, thus reducing the coulombic efficiency, and causing capacity fade. The parasitically formed short chained polysulfides can then shuttle back to the cathode where they oxidised back into long chained species. This shuttle effect can cause self-discharge, degradation of the anode, cycle life disruption and capacity fade.[230,231]

Elemental sulfur and Li_2S are both non-conductive, therefore, to ensure that electron movement within the sulfur containing cathode is not hindered, a large amount of conductive additive is needed. This conductive additive is usually carbon, and the final composition of the cathode contains sulfur, conductive carbon, and a binder. At the beginning of charge or discharge the solid S_8 or Li_2S at the surface of the electrode in closest contact with the electrolyte will be the first to undergo a solid-liquid transition into soluble polysulfides. This then allows electrolyte access further through the thickness of the cathode to interact with the next available solid sulfur-based material. All sulfur inside the cathode must maintain access to both the conductive carbon and to the electrolyte to be considered active material, and any inactive sulfur will decrease the energy density of the material. Addition of large amounts of carbon and optimisation of cathode porosity can help to ensure effective sulfur utilisation but also risks lowering the energy density of the material by reducing overall active material content. A cathode containing at least 70% active sulfur is considered a reasonable goal to retain a high enough energy density for commercialisation.[231] There is also an issue of volume expansion during discharge. During discharge there is a volume change of ~80% during the conversion from S_8 to Li_2S, this has the potential to crack microstructures and destroy active material and conductive carbon connections.[226]

4.2.2.1 Rate capability

The discharge end point, i.e. the maximum capacity of discharge, should be determined by the maximum quantity of active material available for discharge. It is thought that a large lithium diffusion resistance caused by a build-up of non-conductive Li_2S can block electrolyte access to the remaining active material and terminate the discharge prematurely thus reducing the real capacity of the battery.[182] This pore blocking effect, caused by build-up of Li_2S on the surface of the cathode, happens on the discharge due to the volume/density differences between S_8 and Li_2S.

Lithium sulfur batteries suffer from poor rate capability, that is, the capacity significantly reduces as the rate of charge and discharge increases. This is caused by a low sulfur utilisation, and is potentially due to this pore blocking effect, which is worsened at high rates.

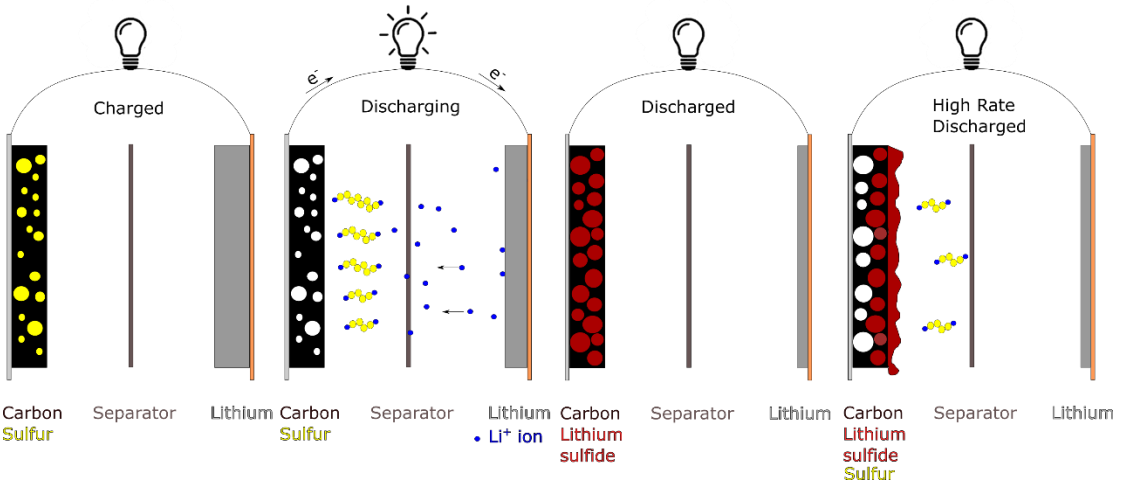

Figure 4-2: *Diagram of the proposed pore blocking effect of high discharge rates.*

Li_2S has been shown to cover the surface of the cathode, and to increase charge resistance, but there are debates as to the exact structure of the Li_2S deposition at different rates. [181,182] It is true that Li_2S will deposit preferentially on the surface of the cathode at higher rates due to a higher polarisation, but the structure of this deposition will determine whether it is pore blocking or not. There are studies demonstrating a thin full coverage across the surface of the cathode at fast discharge rates and larger intermittent particles at slow rates,[232] and another showing the opposite.[233] Another theory suggests that poor rate capability is an aspect of polysulfide mass transfer through the electrolyte rather than a pore blocking effect.[234]

4.2.3 Catalysts for improved rate capability

The deposition of Li_2S and S_8 are kinetically slow reactions, requiring large overpotentials to proceed. This slow deposition of the soluble polysulfides can cause non-uniform deposition of solid sulfur species on the surface of the cathode, which can disconnect or block pores. Control of this deposition is crucial to obtaining ordered and more uniform S_8 and Li_2S products, thus maintaining capacity across cycles. Catalysts can be used to both adsorb the soluble sulfur species to prevent diffusion and the shuttle effect, and to lower the activation energy for deposition. Potential catalysts need to have high electrical conductivity, numerous active sites, structural stability, low cost and, the ability to adsorb the polysulfides, to be effective.[224] Conductive carbon additives cover a lot of these points, but lack the ability to adsorb the polysulfides, instead relying

on mechanical trapping of the polysulfide species. This requires good control of porosity to manufacture a cathode with large enough pores to prevent pore blocking and to counteract the shuttle effect. Many studies exist on hierarchical carbon structures with a range of pore sizes to allow for good electrolyte wetting while retaining high surface area containing mechanically trapping micro and nanopores.[235–237] These carbons can be further doped with nitrogen or phosphorous which allow them to adsorb polysulfides.[238] Alternatively, metal oxides form thiosulfate groups in situ which also adsorb the polysulfides and lower the activation energy of the reduction process thus fulfilling the requirements for an effective catalyst.[239]

The experimental research in this chapter is based on work done by Marangon et al., who incorporated 3 wt% gold nanopowder into sulfur prior to manufacturing of the electrode.[225] This was a development of an idea that gold enhances the reaction kinetics of S_8 deposition and potentially for Li_2S_8 also.[240] The 3 wt% gold doped sulfur electrodes studied by Marangon et al., were shown to have a decreased sheet and Warburg resistance and a corresponding increase in capacity, see **Error! Reference source not found.**. The gold nanopowder was f ound to increase the electronic and ionic conductivities with a small amount of additive compared to the 15 wt% used previously in tin and nickel additive studies.[225,240] The previous work on nickel and tin had shown that the tin, which formed large metal clusters, was beneficial to rate capability, whereas the nickel, which was more homogenous, improved cycle life.[240] Gold catalysts allowed for a reduced catalyst content while providing both benefits.

Table 4-1: *The resistance and discharge values of different wt% loadings of gold in sulfur. Reproduced from Marangon et al.*[225]

Material	Sheet resistance (Ω/□)	Warburg resistance (O)	Discharge capacity (mAh g_S^{-1})
S	56.6 ± 0.9	25.1 ± 0.5	920 ± 90
S:Au 97:3 w/w	34.8 ± 0.8	24.2 ± 0.5	1000 ± 100
S:Au 85:15 w/w	25.2 ± 0.7	15.1 ± 0.6	1200 ± 100

The study incorporated X-ray CT to observe the movement of sulfur and gold during cycling and this clearly shows the agglomeration of the gold nanopowder

which forms clusters inside the electrode. Figure 4-3 shows the X-ray CT cross sections and volume rendering of these electrodes before and after one cycle. The agglomeration of the gold (magenta) can clearly be seen. One additional interesting note is that these cathodes were coated onto a thick carbon felt current collector to aid X-ray imaging. It is clear from (c) and (d) that the current collector contains sulfur and is therefore acting as an additional carbon matrix. This will improve the sulfur utilisation and reduce the energy density of the electrode. The addition of gold also increases the cost and weight of the lithium sulfur battery which conflicts the benefits of the technology.

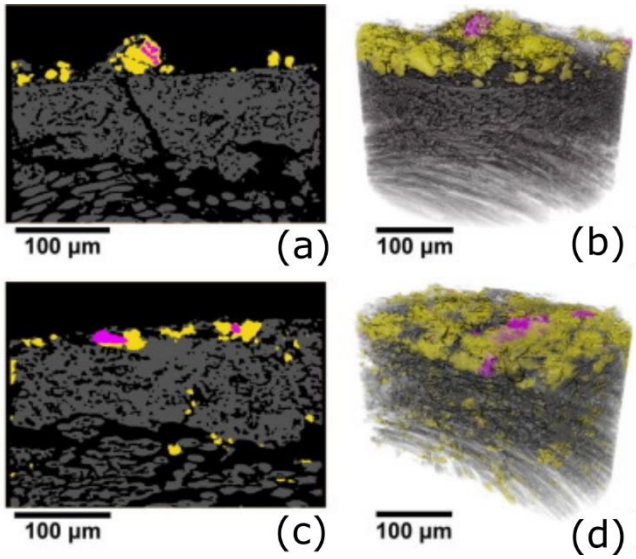

Figure 4-3: *X-ray CT imaging of 3 wt% gold electrodes before (a,b) and after (c,d) one cycle. (a,c) showing cross sectional four phase segmented slices showing gold in magenta, sulfur in yellow and carbon in grey. (b) and (d) show the four-phase segmented volume rendering. Reproduced from Marangon et al.*[225]

The work in this chapter aims to study the effect of fixed gold particles and the impact of their location within the cathode on the rate capability of lithium sulfur batteries. By using a novel gradient spray approach for manufacture of Li-S cathodes, a gold gradient can be incorporated into the through-thickness axis and the effect on rate capacity studied. This gives the ability to optimise the amount and placement of catalysts and prevent the agglomeration to increase the coverage.

4.3 Methodology

Carbon and binder containing electrodes were manufactured by spray deposition followed by a sulfur impregnation using a polysulfide solution. Sulfur was impregnated post carbon-based cathode manufacture due to concerns of contamination of the spray coater due to the low sublimation temperature of sulfur, and the need for a heated substrate in the spray deposition method. Sulfur content was calculated as a % of total coating mass, with common wt% used of 10%, 50% and 70% sulfur. Where standard electrodes were used these were Nanomyte BE-70 (NEI). A gradient spray system was used to manufacture gold catalyst gradients into the carbon matrix. Polysulfide solution was either drop casted onto the cathode or added into the electrolyte. Post sulfur impregnation the cathodes were constructed into coin cells and tested for rate capability.

4.3.1 Spray solution methodology

The materials used for cathode manufacture were carbon black (Super C65, C-NERGY Imerys), CMC binder (sodium carboxymethylcellulose, Sigma-Aldrich), sulfur (Sigma-Aldrich) and 60 wt% gold supported on Vulcan XC-72 (Fuel Cell Store).

The CMC binder was dissolved in water to a solution of 1 wt% and stirred overnight. The binder solution was added dropwise to a stirring solution of carbon black in 1:1 deionised water:isopropyl alcohol (IPA). A 1:1 DI water:IPA solution was chosen based on the dispersion tests shown in Figure 4-4, which demonstrate that a 1:1 DI water:IPA solution, labelled as 5 showed greater dispersion based on the darkness of the solution; it also maintained dispersion for longer/had a slower sedimentation time, which matches previous literature.[104] The final solution was 1 mg mL^{-1} in total solid concentration with a 5:1 ratio of carbon to CMC binder. For electrodes containing gold, some carbon black was substituted for gold carbon to give 5.5 wt% of gold to carbon. The solids were dispersed prior to spray deposition using a sonic horn (Fisherbrand 505) at a power of 40% and a pulse of five seconds for 10 minutes. During spray, the refill bottle was under continuous stirring, and a sonic syringe was used to keep the material in the tubes well dispersed.

Figure 4-4: *Dispersion test of 1 mg mL^{-1} carbon black in different ratios of water and IPA. Each number on the vials represents a 10 wt% increase in IPA.*

4.3.2 Polysulfide solution

A 10 M (in terms of atomic sulfur) solution of Li_2S_8 polysulfide solution was used for both drop casting and electrolyte impregnation of sulfur into the pre-prepared carbon matrices. The methodology employed is based on that by Dibden et al.[241] In an Ar-filled glovebox, 0.574 g of lithium sulfide (Alfa Aesar) and 2.81 g of elemental sulfur (Sigma Aldrich) were added to 10 mL mixture of 1,3-dioxolane (DOL, anhydrous, Sigma-Aldrich) and 2-dimethoxyethane (DME, anhydrous, Sigma-Aldrich) at a ratio of 1:1 DOL:DME by volume. This was left stirring at 60 °C for 72 hours, the heat then removed, and stirred for a further 48 h. The as used polysulfide solution was then separated from the powder cake (excess material).

4.3.3 Electrolyte manufacture

Electrolyte manufacture was done according to the Lithium Sulfur Technology Accelerator (LiSTAR) guide, which is the Faraday Institution work program for lithium sulfur batteries and has written a standardised methodology for electrolyte manufacture based on the work by Agostini et al.[242] Molecular sieves were dried at 220 °C and transferred to a glove box while still hot; once cooled they were added to DOL and DME (anhydrous, Sigma Aldrich) and left for 3 days. Bis(trifluoromethane)sulfonimide lithium (LiTFSI, Sigma Aldrich) and lithium nitrate (Sigma Aldrich) were dried under vacuum at 120 °C for 3 days and added to a 1:1 by volume mix of DOL:DME to make a 1M LiTFSI and 0.8 M $LiNO_3$ solution.

4.3.4 Spray methodology

The solution was sprayed onto carbon coated aluminium foil (MTI) at 120 °C over an area of 25 cm^2 using a raster pattern. The flow rate of the solution was

1 mL min^{-1} with a shaping air of 1.2 PSI and a nozzle sonication power of 2 W. The sonic syringe used a power of 2 W for 5 seconds every ten seconds. The spray head used was an AccuMist (SonoTek) nozzle with spray diameter of ~2 cm. Initial studies used an Impact nozzle (SonoTek) which allowed for a spray diameter of up to 15 cm, but this produced an inhomogeneous coating that increased the amount of wasted material.

To manufacture a gradient, two solution inputs are required; to prevent contamination of the second nozzle, the two syringe inputs were connected to a single nozzle and the solutions mixed a few seconds prior to atomisation, as opposed to using two individual nozzles. This made the programming of the spray coater more difficult, and a complicated program was written which manually operated the valves, nozzle power, shaping air, syringe pump rate and refill programs separately.

For non-gold, and non-graduated gold containing electrodes, a single solution was sprayed with 100 spray passes comprising each film. For gold containing graduated electrodes, two syringes were used, one comprising only carbon and binder and the other with 11 wt% gold compared to carbon. Gradient spray manufacture was achieved by altering the flow rates of the syringes throughout the spray process.

4.3.5 Polysulfide deposition

Electrodes were cut into 15 mm diameter disks and dried under vacuum overnight at 40 °C then transferred into an Ar-filled glovebox. For removal of sulfur from standard NEI cathodes, the cathode disks were heated under vacuum at 120 °C for a week and weighed regularly until no further mass change was seen. Polysulfide solution was used to impregnate sulfur into the electrodes by drop casting and evaporation or by direct addition to the electrolyte. For drop casting, the required ratio of polysulfide solution was dropped onto the carbon matrix and left to evaporate in the glovebox; for electrolyte impregnation, some of the electrolyte was substituted with the required ratio of polysulfide solution which was introduced between the separator and cathode layers.

4.3.6 Coin cell manufacture

The construction of the coin cells differed slightly to other battery chemistries discussed, the CR2032 coin cell parts used were from MTI, and two 0.5 mm thick spacers used, see Figure 4-5. Polysulfide solution was added between separator

and cathode (positive electrode), and electrolyte added on to the separator. The total volume of electrolyte and polysulfide solution was 80 µl. A 16 mm diameter Celgard 2400 separator and a 0.12 mm thick 14 mm diameter lithium disk (Goodfellow) anode were used.

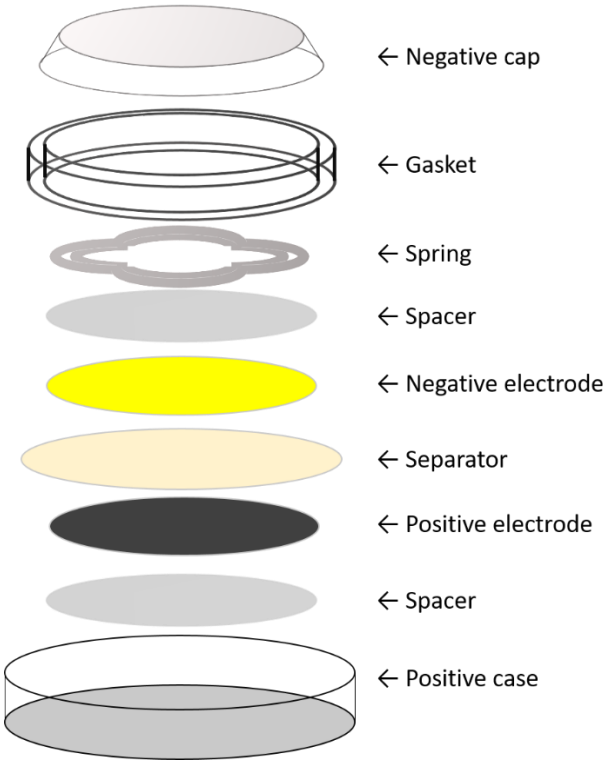

Figure 4-5: *Schematic of coin cell construction for Li-S cathode testing.*

4.3.7 Cell testing

Cells were tested on a BCS-805 battery cycler (BioLogic) and were first left to rest for 2 hours, then subjected to two formation cycles at C/50 with charge and discharge limits of 2.6 V and 1.8 V vs open circuit voltage (OCV) respectively; cells were rested for 1 hour between each charge and discharge. The real capacity from these formation cycles was used to dictate the C-rate for rate testing. Cells were then subjected to rate testing with 5 cycles each at C/20, C/10, C/5, C/2, 1C and C/20.

Repeats of all lithium sulfur batteries were manufactured and cycled using the same methodology each time. It was found that for sulfur loadings of 50 wt% and above there was a high failure rate with cells either failing in the initial discharge, or at higher rates. This failure was due to the cells inability to pass the required current, likely due to prohibitively high resistance caused by the non-conductive nature of S_8 and Li_sS. This is further supported by the increased failure rate of the

50 wt% and 70 wt% sulfur loading batteries, which represent comparatively high active material loadings. This prevented substantial complete repeats from being obtained and in these cases only one battery is presented for analysis.

4.3.8 Characterisation

SEM EDX was performed for electrode characterisation to determine the presence of a gold gradient. The accelerating voltage was set to 20 kV to ensure that it was suitably above the required level needed for gold X-ray emission ($L_{\alpha 1}$ of ~10 keV). However, it was found that the hit count for gold was still too low, therefore the M_{α} emission line at 2.12 keV was chosen instead. The magnification was 1476 x.

4.4 Results

Li-S cathodes were manufactured as described in the methodology, using carbon black and CMC binder to make the conductive carbon matrix prior to sulfur impregnation. To determine the optimal sulfur impregnation method two different techniques were tested: (1) drop casting of a polysulfide solution and (2) addition of polysulfide solution to the electrolyte. Method (1) was quickly abandoned due to a curling of the electrode when THF was used as the solvent, and a DOL polymerisation reaction occurring when a 1:1 DOL:DME solution was used leading to solidification of the drop casted solution on the surface of the electrode. To compare the effects of method (2), standard sulfur containing cathodes (NEI Nanomyte BE-70) were heated under vacuum at 120 °C until all the sulfur had been removed, they were then assembled into coin cells with a partial replacement of the electrolyte by a polysulfide solution and the cycling profile compared to unmodified electrodes.

Figure 4-6 shows that the unmodified NEI cathode had a higher initial capacity at low C-rates, and this decreased over the five cycles at each rate, which suggests a loss of sulfur to the electrolyte.[231] The addition of the sulfur in the electrolyte gave a lower capacity at C/20, which was due to the loss of sulfur instantly to the electrolyte, capacity drop across the five cycles at each rate was reduced compared to the unmodified electrode. It is likely that the sulfur in this instance was deposited only in places that are accessible to the electrolyte, therefore it remained active throughout the duration of cycling. Despite the poorer performance at lower C-rates the 1C and C/2 cycles appear similar, if not better

than the standard NEI cathode in terms of discharge capacity, therefore it was concluded that this sulfur impregnation method was suitable and would not interfere with experimental results going forward. The reasoning behind the use of this sulfur loading method was due to issues with contamination of the spray coater, which would affect the material composition of other films manufactured using it. Industrially it could potentially benefit the speed and cost of manufacture to spray deposit the sulfur as there would be no risk of cross-contamination for a spray machine that is solely used for Li-S cathode manufacture.

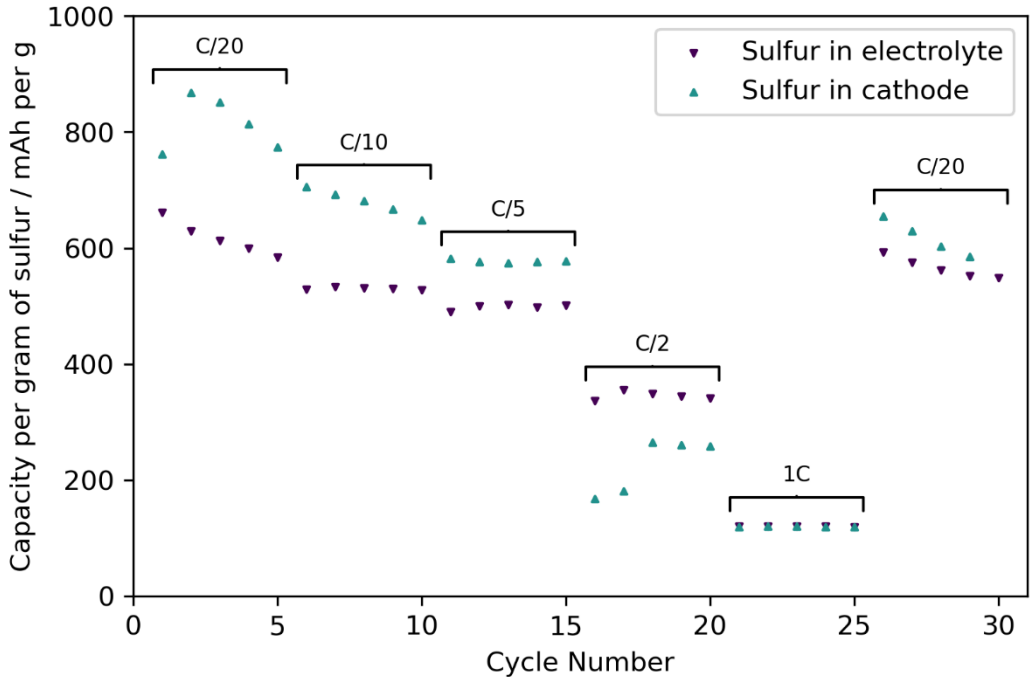

Figure 4-6: *Capacity per gram of sulfur at different rates of a standard NEI electrode with sulfur in the cathode, and with the sulfur removed and re-added in the electrolyte.*

The addition of polysulfide solution into the electrolyte adds some additional variables; one being whether an initial charge or discharge would better deposit the sulfur into the carbon matrix. The polysulfide solution used contained Li_2S_8 chains specifically, so the cell overall was closer to being charged than discharged upon assembly. It was assumed that charging first would allow less time for diffusion of the highly soluble longer chain polysulfides through to the anode and that this would retain more active material, although upon testing, no real difference was found between the two.

Another factor that must be considered is the effect of the change in concentration of the electrolyte. The mass of sulfur added into the electrolyte is proportional to the mass of conductive carbon in the film, which varies from sample to sample. Therefore, as the polysulfide solution does not contain the additional lithium nitrate and LiTFSI salts, the concentration of these varies between different sulfur wt% electrodes.

4.4.1 Effect of sulfur loading on rate capability of spray deposited cathodes

The sulfur loading of cathodes is crucial to the commercial viability of the Li-S chemistry but higher sulfur loading often leads to more inactive sulfur and a lower sulfur utilisation. The spray deposited cathodes were tested for rate performance at different sulfur loadings to examine this phenomenon.

Spray deposited conductive carbon electrodes were manufactured with different volumes of polysulfide solution in the electrolyte, from 10 wt% to 70 wt% sulfur with respect to the mass of the electrode, see Figure 4-7 (a). When a lower sulfur wt% was used, a higher sulfur utilisation was seen, represented as a higher capacity per gram of sulfur. This is particularly significant at lower C-rates; at C/20 10 wt% sulfur loadings obtained almost twice the capacity per gram of sulfur of 70 wt% electrodes, ~700 mAh g^{-1} compared to 400 mAh g^{-1}. This increased capacity at lower sulfur loadings is due to the higher ratio of conductive carbon to sulfur, which allows more surface area for the conversion between the charge and discharge products. It is clear however that this increased sulfur utilisation caused by low sulfur loadings does not last long, as the final C/20 cycles at all three sulfur loadings showed a much smaller spread of capacities. There was a significant capacity drop for the 10 wt% loading from ~800 mAh g^{-1} in the initial C/20 cycles to ~ 500 mAh g^{-1} in the final ones, whereas the 50 wt% loading remained the same at ~500 mAh and the 70 wt% loading increased from ~400 mAh g^{-1} to ~450 mAh g^{-1}. This convergence of all three mass loadings to between 400 and 500 mAh g^{-1} suggests that the carbon black used in this study cannot reliably utilise sulfur loadings above 50 wt%, likely due to limited volume of surface area or areas of inactive electrode which are not contacted by electrolyte.

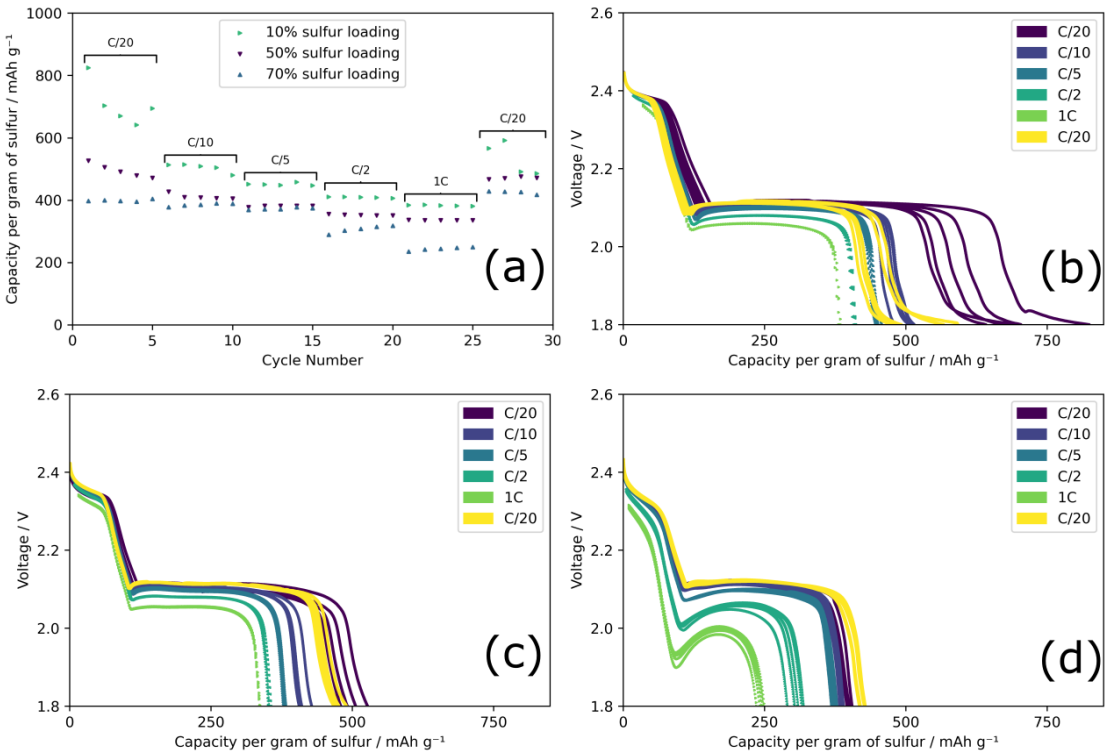

Figure 4-7: *The discharge capacity per cycle of the three different sulfur loadings during rate testing (a) and the discharge curves of three different wt% loadings of sulfur cathodes. (b) 10 wt%, (c) 50 wt%, (d) 70 wt%*

A capacity drop is seen for all the sulfur loadings as the rate increases. This is thought to be the result of pore blocking due to a high proportion of sulfur in the electrolyte and a strong polarisation caused by the high current. Between C/10 and C/2 the capacity drops by similar amounts for all the electrodes. At 1C the 70 wt% sample drops significantly more than the other sulfur loadings, to ~230 mAh g^{-1} compared to 10 wt% sulfur at ~400 mAh g^{-1}. This is likely due to the increase in Li_2S surface coverage and therefore pore blocking at the cathode, with higher currents promoting surface deposition and higher sulfur loadings increasing coverage. The difference in actual current density in the testing due to the use of relative C-rates may also have an impact; rather than setting a consistent current for all wt% electrodes the cells were tested at a C-rate appropriate to their theoretical capacity, therefore a 1C discharge for the 70% loading cell had a current 7 times higher than that of the 10% cell, which increases the polarisation effect. Testing with proportional current rates, i.e. 1 mA cm^{-2}, was considered but this would make it difficult to compare sulfur utilisation between different sulfur loadings as 1 mA cm^{-2} may be the equivalent of C/15 for the 70 wt% loading and

2C for the 10 wt% loading. Additionally using C-rate as a method of determining rate capability ensures that the insights are more industrially relevant, as this is generally the terminology used in commercial applications.

Figure 4-7 (b-d) show the discharge curves of the same three cells: (b) 10 wt% sulfur, (c) 50 wt% sulfur and (d) 70 wt% sulfur. The extra capacity in the first few cycles of the 10 wt% cell was seen as long tails at low voltage. There are a few possible explanations for this: one is that the tails are due to the full utilisation of sulfur; the end of discharge is determined not by the pore blocking of the cathode but from the full utilisation of sulfur in the cell. These tails may be caused by the slow but complete utilisation of sulfur as it diffuses across the cell.

Another explanation is that the long tails are caused by the reduction of lithium nitrate, which is added to help form a stable SEI layer on the anode.[243] This reduction of lithium nitrate would show up as extra capacity especially in slower cycling. The cause of this effect in the 10 wt% only cells may be down to the final composition of the electrolyte; the same total electrolyte content was kept consistent between all electrodes but the amount of electrolyte that was substituted by polysulfide solution varied between electrodes, meaning that the actual concentration of LiTFSI and $LiNO_3$ was not consistent, see Table 4-2 for estimated $LiNO_3$ and LiTFSI values.

Table 4-2: *Showing the estimated $LiNO_3$ and LiTFSI concentrations at different sulfur loadings*

Sulphur loading %	LiTFSI (M)	$LiNO_3$ (M)
10	0.96	0.77
30	0.86	0.69
50	0.69	0.55
70	0.32	0.26

A higher sulfur loading requires more substitution of electrolyte with polysulfide solution and therefore creates a lower lithium nitrate and LiTFSI concentration, with the actual concentration of $LiNO_3$ dropping to 0.26 M at 70 wt% sulfur loadings. Due to the saturated nature of the polysulfide solution, it was not possible to dissolve the lithium salt and additive alongside the polysulfides. It was found that this lower dilution of electrolyte salts did not impact the rate performance, but this was only tested using standard NEI cathodes, which are 70 wt% sulfur. It may be that at lower sulfur loadings, and therefore a higher lithium nitrate concentration, the reduction of lithium nitrate is the cause of the long tails. The fact that these tails are shorter in the final C/20 cycles of the 10 wt% cell supports this as there would be a lower concentration of lithium nitrate remaining in the electrolyte after cycling.

Another clear observation is the large dip in voltage at the end of the first plateau occurring at ~100 mAh g^{-1} of sulfur. The first plateau is associated with the formation of soluble polysulfides from solid S_8, therefore, at the end of this plateau all the active sulfur is in the electrolyte. The solvation of polysulfides causes an increase in viscosity of the electrolyte which in turn increases the resistance by reducing ionic mobility. This increase in resistance is seen as a decrease in voltage at the end of the first plateau.[244] In Figure 4-7 (d), 70 wt% loading, this effect is most visible, and the voltage drop exacerbates as the rate, and sulfur loading, increase. The 70 wt% sulfur loading results on a high sulfur concentration electrolyte, leading to an increased viscosity and therefore higher resistance and a larger voltage drop.

4.4.2 Graduated catalyst cathodes

As shown previously by Marangon et al, metal catalysts can aid the deposition and removal of solid charge and discharge products by decreasing interphase resistance and increasing electronic and ionic conductivity.[225]

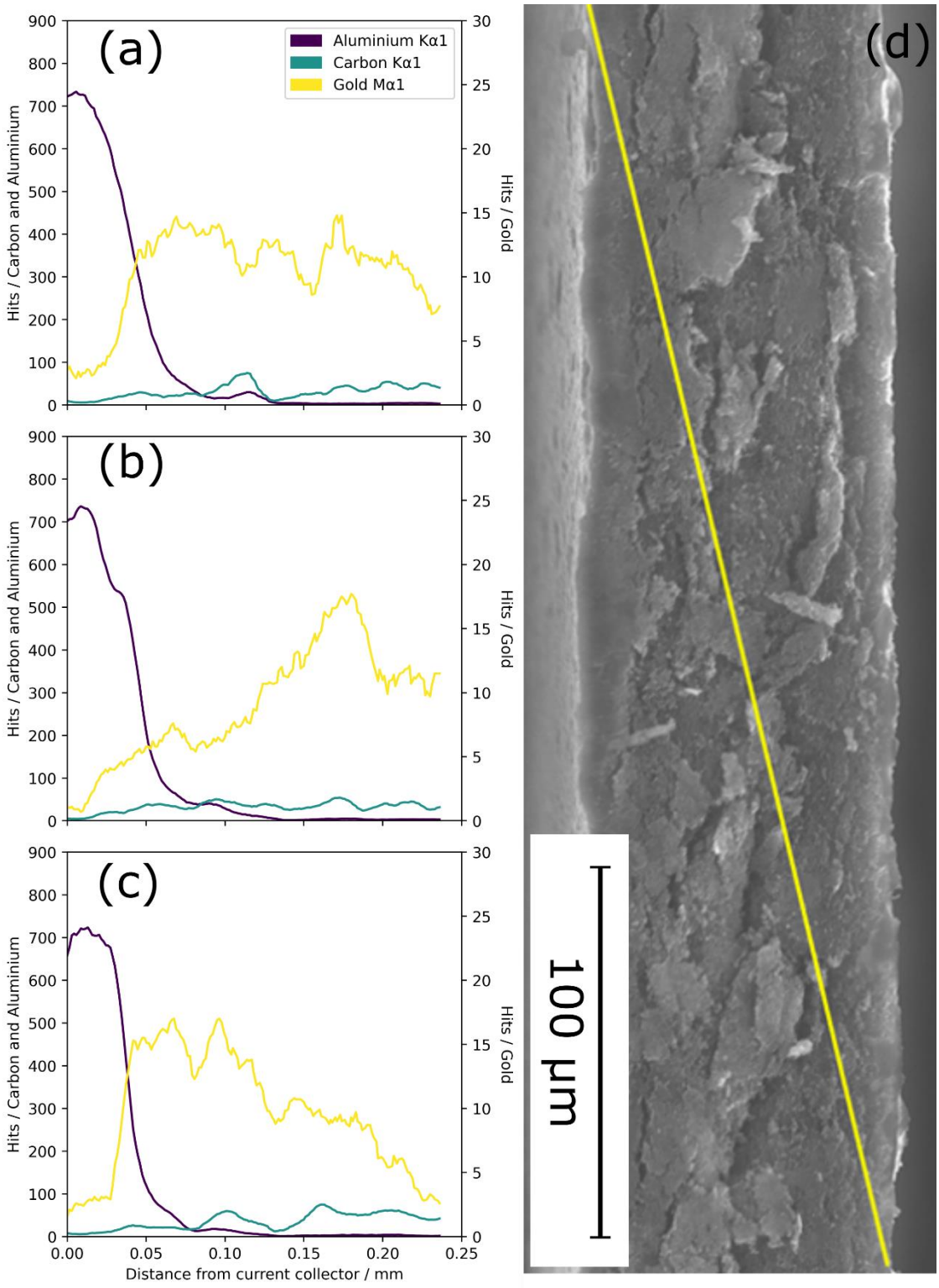

Figure 4-8: *The cross section EDX and corresponding SEM of graduated gold carbon electrodes. (a) a homogenous mix of gold, (b) a gradient of increasing gold from the current collector to the top, (c) a gradient of gold increasing towards the current collector. (d) The SEM image for the homogenous gold electrode demonstrating the line in which EDX measurements were taken.*

To optimise and test this theory further, gold coated carbon was introduced into the spray deposited conductive carbon electrodes, at a ratio of 5.5 wt% compared to the mass of the carbon and binder. Gold coated carbon was used as a method to prevent agglomeration which clearly occurs in the work done by Marangon et al.[225] Gold gradients were manufactured into the electrode to optimise the placement of gold and further test the theory that catalysts can improve the deposition and removal of solid sulfur charge and discharge products.

Figure 4-8 shows the EDX and associated SEM cross section images of the non-graduated (a), and graduated electrodes, (b) and (c). Two gradients were manufactured: one with gold content increasing away from the current collector towards the surface of the electrode (b) and, one with increasing gold towards the current collector (c). The EDX of all the electrodes show a layer of aluminium current collector and then differences in the hit count of gold. (a) shows an unchanging gold hit count, while (b) shows a steady increase towards the surface of the electrode; (c) shows the opposite behaviour with high gold hit counts at the current collector which decreases towards the surface of the electrode.

Cells containing different sulfur loadings were made from these gold containing cathodes. Figure 4-9 shows the cycling data of some of the gold gradient electrodes, specifically, the electrodes where the gold content is highest near the electrode surface at sulfur loadings of 50 wt% and 70 wt%. At most discharge rates, the gold electrodes had a lower capacity than the control. This is because the sulfur loading is based on the total film mass, including both carbon and gold, meaning the gold electrodes therefore had a higher sulfur to carbon ratio, lowering the carbon surface area available to the sulfur. Sulfur loading was calculated this way as lowering sulfur content goes against the motivation behind this work and is not industrially relevant, if sulfur loading were reduced for these electrodes, any comparison to control electrodes would be biased.

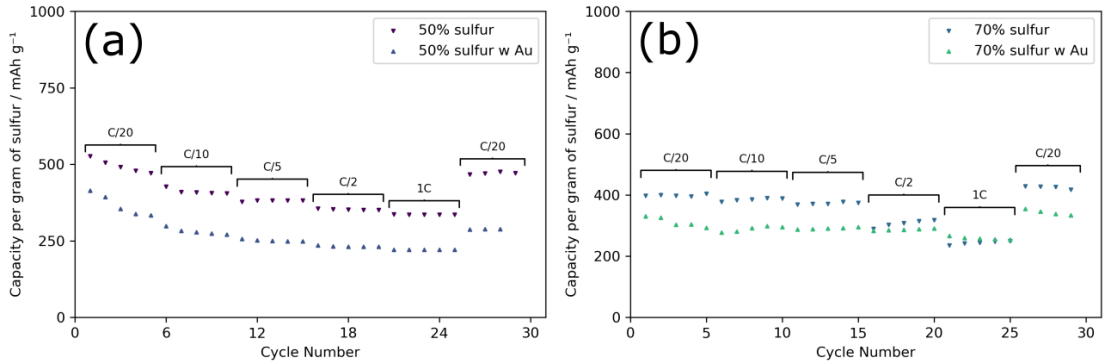

Figure 4-9: *The discharge capacity at different rates of (a) 50 wt% sulfur cathodes with and without a gold gradient and (b) 70 wt% sulfur cathodes with and without a gold gradient. The gold gradient is specifically with increasing gold content towards the electrode surface.*

There seems to be no other obvious differences in capacity with 50 wt% sulfur loading, with and without gold, and both had similar drops in capacity as rate increased. With 70 wt% loading (b) however, the gold gradient sample showed higher or the same capacity than the control at 1C and C/2, therefore rate induced capacity loss is reduced. This is likely due to the influence of gold catalysts promoting more active material utilisation under high current loads and sulfur loadings. The exact influence of the gold on the electrochemical behaviour can be observed further from the voltage capacity curves of the two 70 wt% sulfur electrodes, see Figure 4-10.

The voltage versus capacity discharge curves of the 70 wt% sulfur cathodes showed a bigger first plateau voltage dip with the gold gradient, (b), compared to without (a). This suggests a more saturated electrolyte solution which would occur from a greater conversion of solid sulfur to polysulfides. The improved capacity seen in the gold gradient electrode is evident in the extended length of the second plateau, where most of the capacity is usually seen. This improvement is seen more clearly in (c) where the first derivative of the capacity curve showed an increased second plateau length but a decreased first plateau length for the gold graded cathode. The extended second plateau explains the capacity increase as it is associated with the formation of solid discharge products, which may be being catalysed by the gold. The decreased first plateau length however remains a mystery; it can only be assumed that the large voltage dip, caused by the increased viscosity of the electrolyte is impacting the shape of the discharge curve, and making the first plateau appear shorter. Alternatively, due to the high

sulfur concentration of the electrolyte in the 70 wt% loading cells, the dissolution kinetics may be reduced thus minimising the proportion of S_8 that can be dissolved.

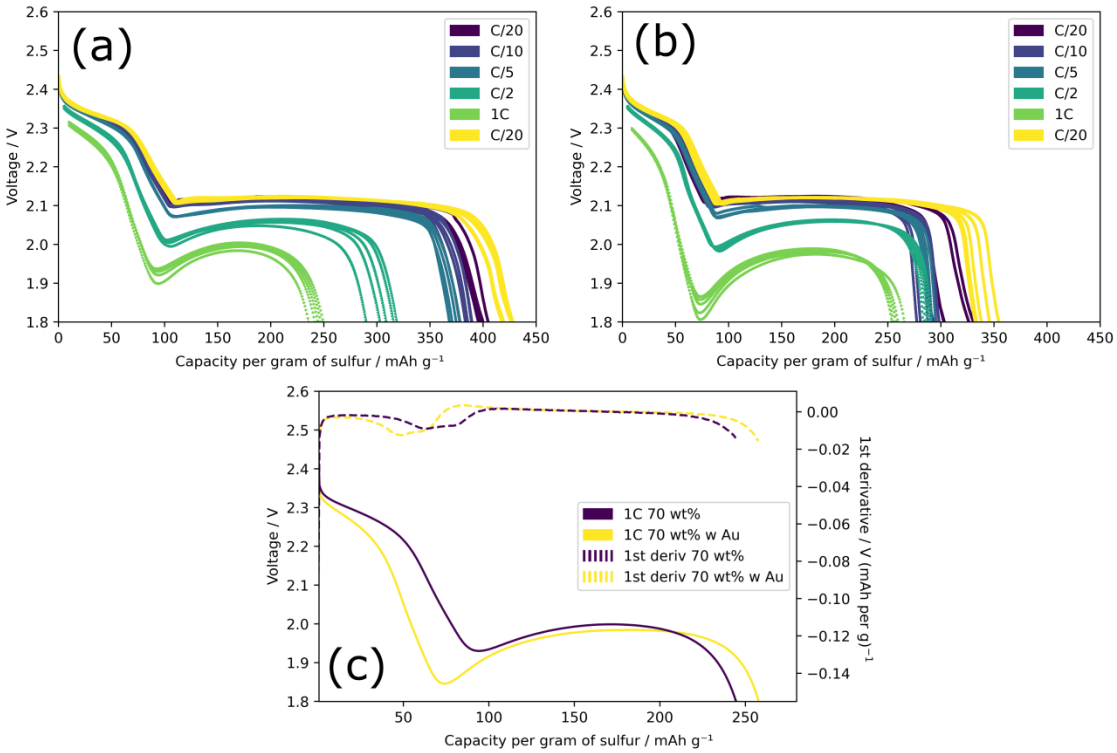

Figure 4-10: *The rate capability discharge curves of 70 wt% sulfur electrodes with increasing gold gradient away from the current collector (b) and without (a). (c) shows the first derivative of a 1C cycle from (a) and (b).*

The ungraded gold electrodes and opposite gradient electrodes (gold content increasing towards the current collector) discharged at lower capacities than the control electrodes at all rates, see Figure 4-11 which shows the rate performance of both gradients and the ungraded cathode at 70 wt% sulfur loading. The difference in performance at 1C is clear with the ‘Gold bottom’ and ‘Gold mix’ electrodes delivering less capacity than ‘Gold top’ and ‘No gold’.

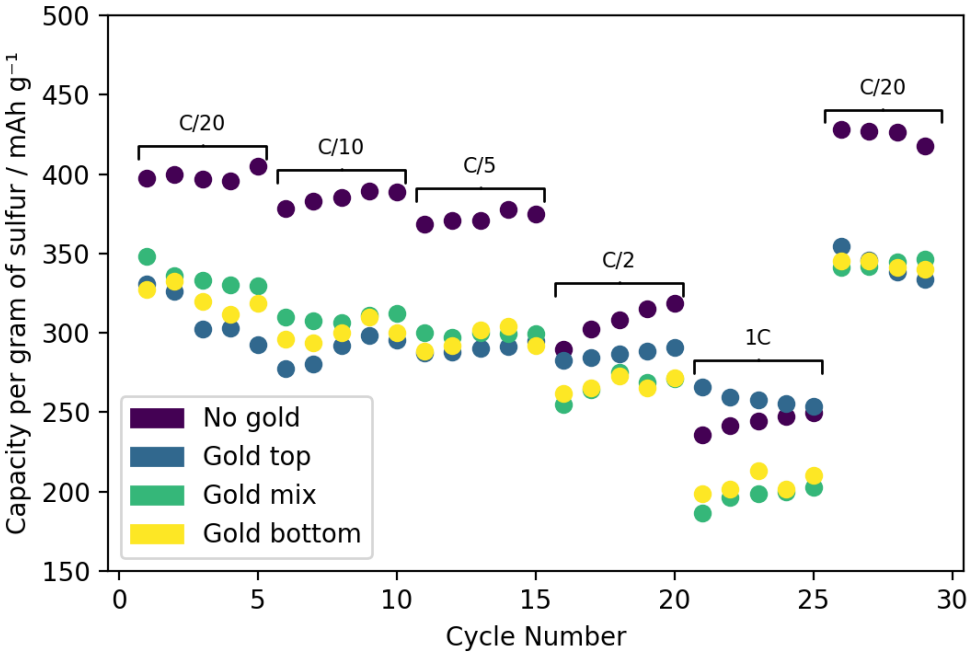

Figure 4-11: The capacity per gram of sulfur per cycle of 70 wt% loading sulfur carbon cathodes with and without gold gradients at different C-rates. Gold top refers to a gold gradient increasing towards the top surface of the electrode, gold mix refers to a homogenous ungraded gold catalyst mix, gold bottom refers to a gold gradient that increases towards the bottom surface of the electrode.

This suggests that the effects of gold are only relevant near the surface of the electrode. Comparable results were seen for the 10 wt% and 50 wt% sulfur loadings for both gradients and mixed electrodes. This suggests that the gold only has a catalysing effect under high sulfur loadings when the risk of pore blocking is highest. This work acknowledges golds activity as a catalyst of the deposition and re-dissolution of solid products, helping to prevent the pore blocking which occurs under high rate, high loading, cycling conditions. Unfortunately, the difference seen is minimal, and only makes a difference in extreme circumstances. Gold electrodes were also consistently lower capacity at all other sulfur loadings and rates; therefore, gold does not counteract the loss of conductive carbon. The increase in mass and cost of the electrode when using gold must also be considered when considering the method for commercial use. The results seen here differ to those in Marangon et al., in which low sulfur loadings were used and large increases in capacity seen when using gold

catalysts. It was hypothesised that the difference in these results to those of Marangon et al. were due to the type of gold used; gold carbon was used here versus gold nanoparticles in their study. The methodology of this study was repeated for gold nanoparticle clusters, but it was found that a working 70 wt% sulfur cell could not be manufactured due to the prohibitively high resistance. The methodology was also repeated for ruthenium-based catalysts, and similar issues were found.

4.5 Conclusions

The methodology for manufacturing catalyst gradients in carbon matrices for lithium sulfur batteries was proven to be successful, with clear gradients of low mass ratio gold and proven impacts of gradients on the electrochemistry of the cell. The use of spray deposition opens possibilities of intricate through-thickness electrode design which can be easily transferred to other battery electrodes, energy storage devices or thin films in general. It has been shown that while a gold gradient towards the surface of the electrode does increase polysulfide concentration in the electrolyte and can improve sulfur utilisation at high sulfur loadings and current loads, it does not improve the overall energy density of the chemistry, and would ultimately increase the cost of production, both in materials and method. This research showed that the only instance that gold improved the capacity of the cathode was when gold was graded towards the top of the electrode, and tested at high rates (1C) and at high sulfur loadings 70 wt%, see Table 4-3.

This raises questions about the work shown by Marangon et al. as either the type of gold, integration method or cell assembly must be the reason for the differing results.[225] As the work by Marangon et al. was intended to be imaged via X-ray CT, the 70 wt% sulfur film was coated onto a carbon felt current collector, as a metal current collector would impact the quality of the scan. Figure 4-3 (c and d) show the thin (~50 µm) film coated onto a thick (~150 µm) carbon felt; even after one cycle some sulfur can already been seen integrated into the carbon felt current collector, which is not intended to be a sulfur host. This means that the real sulfur wt% of the overall electrode is lower than intended. This could be a reason for the higher capacity seen in their studies (920 mAh g^{-1} of sulfur) and the reason for the significantly higher increase in capacity with the addition of gold, between 80 and 200 mAh g^{-1}. Thicker electrodes may benefit more from the

increase in conductivity of gold, especially near the surface of the overall electrode (current collector + coating) which is where the gold is located. While thick electrodes would be beneficial for future lithium sulfur batteries, they need to be concurrent with a high sulfur loading.

Table 4-3: *Comparison of capacity at 1C of different gold gradients with different sulfur loadings.*

Cathode type	Capacity at 1C / mAh g^{-1}
50% S no gold	~330
50% S gold top	~220
70% S no gold	~240
70% S gold top	~260
70% S gold mix	~200
70% S gold bottom	~215

4.5.1 Future work

This research would greatly benefit from additional characterisation of both the gradient and the specific structure of the gold carbon. Although the EDX data shown in Figure 4-8 does clearly show a gradient, the data is quite noisy and EDX data is can vary across the sample. Further gradient characterisation could involve X-Ray Photoelectron Spectroscopy (XPS) depth profiling, which utilises an ion beam to remove the surface layer of a sample each time XPS is performed, therefore gaining insight into the chemical composition of a sample throughout the thickness.

Gaining a greater insight into the specific structure of the gold carbon is crucial to determining the mechanism of the gold in improving the electronic or ionic conductivity of the electrode. Transmission electron microscopy could be used to determine the size of the gold particles, both before and after cycling, which would be useful in determining any degradation or reorganisation of the gold. This could be combined with sheet resistance and impedance studies which would give the conductivities of the samples throughout cycling.

The potential for lithium sulfur cathodes is great enough that solving the issues surrounding it remains an important topic of research. With conductive cathode structures the optimisation of the porosity, structure, placement, and quantity of additives is vital to help bring down inactive material content, allow for thicker

cathodes and improving the energy density, rate performance and cycle life of the chemistry, past that of current lithium-ion cells. Spray deposition may provide a route to manufacture of these bespoke designed electrodes, perhaps in terms of specifying porosity or pore size throughout the thickness; manufacture of hierarchically porous carbon matrices could issues surrounding Li-S, particularly those related to the polysulfide shuttle effect. Ultimately both Li-S and spray deposition have great potential for optimisation and commercial viability with the right direction, and work should continue on new electrode designs.

Chapter 5 Gradient Deposition of Composite Cathodes for Improved Performance of Solid Polymer Electrolyte Batteries

5.1 Abstract

In solid-state batteries, planar interface resistances can occur from the boundary between composite cathode and solid electrolyte. Graded composite cathodes were manufactured to increase the proportion of solid electrolyte near the surface of the electrode to remove this interface boundary. Graded LFP/PEO composite cathodes were compared with ungraded homogenous LFP/PEO electrodes in rate and cycle life testing. It was found that graded electrodes reduced impedance which led to increased cycle life and enhanced rate performance when compared to ungraded electrodes. It is thought that the gradient removes or reduces the planar boundary between cathode and electrolyte which increases contact and removes areas of high resistance thus preventing further degradation of this interface and subsequent capacity loss.

5.2 Background

The ether or carbonate-based electrolyte commonly used in Li-ion batteries is highly flammable and if heated and exposed to air can catch fire or explode. This can happen during a short-circuit or with damage to the cell casing. As battery technology improves with the adoption of lithium metal anodes, high capacity cathodes or new chemistries, the safety of the electrolyte only becomes more important. Solid-state electrolytes (SSEs) are less flammable and significantly reduce the risk of explosion and fire. SSEs also pave the way towards high-capacity electrodes, ultra-thin electrolytes and new shapes and designs of cell architecture. SSEs currently suffer from issues that are hampering their wide-scale commercialisation including manufacturing complexity, low material stability, poor ionic conductivity, limited cycle life and high cost and much of the research goes towards resolving these issues.[22]

There are different materials that are actively researched as SSEs, and these can be categorised as inorganic SSEs and polymer-based SSEs. Inorganic SSEs for lithium-ion batteries were born from the discovery of LiPON and the category now contains various other materials such as ceramic, perovskite, sulfide and garnet type.[22] Meanwhile, the realisation of poly(ethylene oxide) (PEO) as a functional

electrolyte led to the field of solid polymer electrolyte (SPE) research.[245] These two material types have differences in their manufacturing methods, functionality, and properties. Inorganic SSEs are usually dense hard structures, often requiring sintering of small particles to form a strong and dendrite resistant material[160] and lithium mobility is due to defects throughout the crystalline structure. SPE's are often much more flexible, providing better interfacial contact with the cathode but are softer and have less resistance to dendrite formation. Lithium-ion mobility in SPE's occurs through the non-crystalline portions of the polymer chain, where lithium ions can move to different coordinating sites using polymer chain movement.[160]

5.2.1 Polymer solid electrolytes

There are three main forms of SPE: gelled, solvent free and composite. The standard form of SPE is solvent free, consisting of only the polymer or polymers and a lithium containing salt. The first and most researched polymer is polyethylene oxide, which conducts lithium ions using coordination from the ether groups in PEO. A ratio of 6:1 of ether groups to lithium ions shows the highest ionic conductivity due to the formation of a double helix structure which coordinates the lithium cation in a tunnel-like structure separately (without the anion), using the ether groups, see Figure 5-1. Other ratios like 1:1 and 3:1 form zigzag and single helix structures with lower numbers of coordinating ether groups.[246]

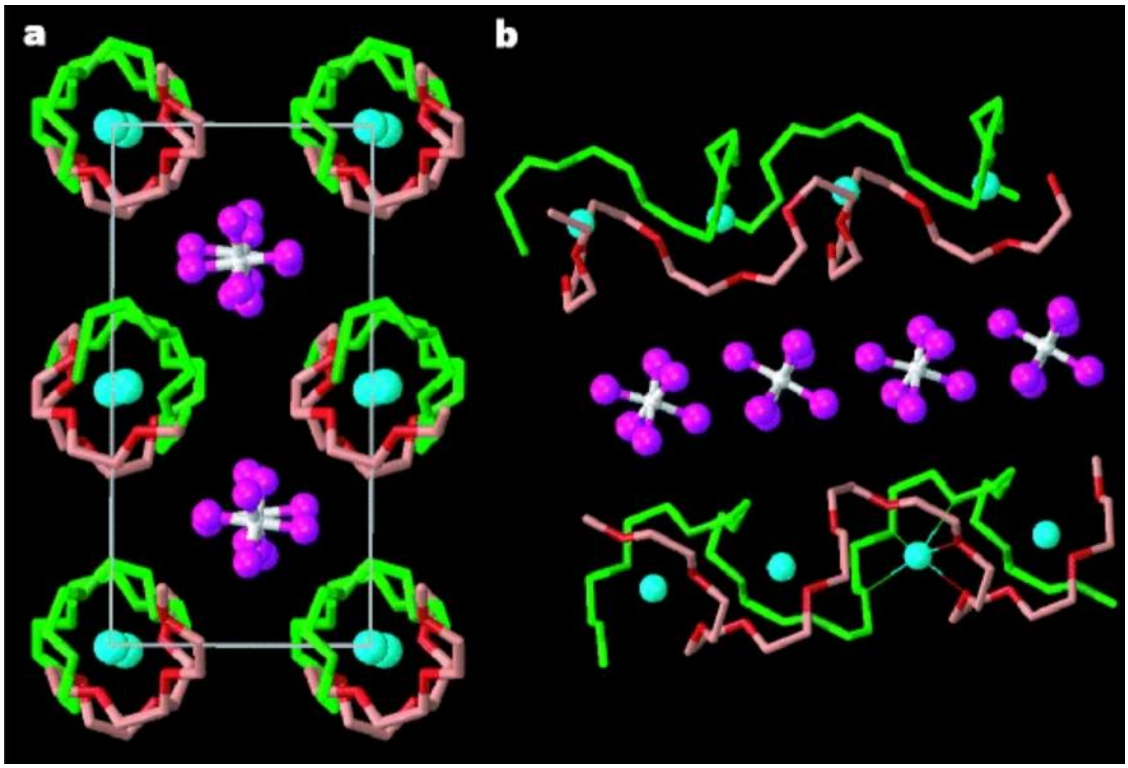

Figure 5-1: *(a) Vertical view of the PEO_6:$LiAsF_6$ structure showing rows of Li^+ ions perpendicular to the page. Blue spheres, lithium; white spheres, arsenic; magenta, fluorine; light green, carbon in chain 1; dark green, oxygen in chain 1; pink, carbon in chain 2; red, oxygen in chain 2. (b) View of the structure showing the relative positions of the chains and their conformations. Thin lines indicate coordination around the Li^+ cation. Reproduced from MacGlashan et al.*[246]

PEO remains the most prominent material in SPE research, due to its reasonable electrochemical stability against lithium, good solubility towards lithium salts and its low glass transition temperature, which is crucial to the ionic conductivity of the polymer as lithium-ion movement only occurs in the amorphous regions of the polymer. PEO with a molecular weight of 5 x 10^6 has a glass transition temperature (T_g) of ~60 °C and a bulk crystallinity of 70-84% at room temperature, therefore much of the research with PEO electrolytes is done at temperatures between 50 °C and 100 °C in order to decrease the crystallinity and improve ionic conductivity.[247]

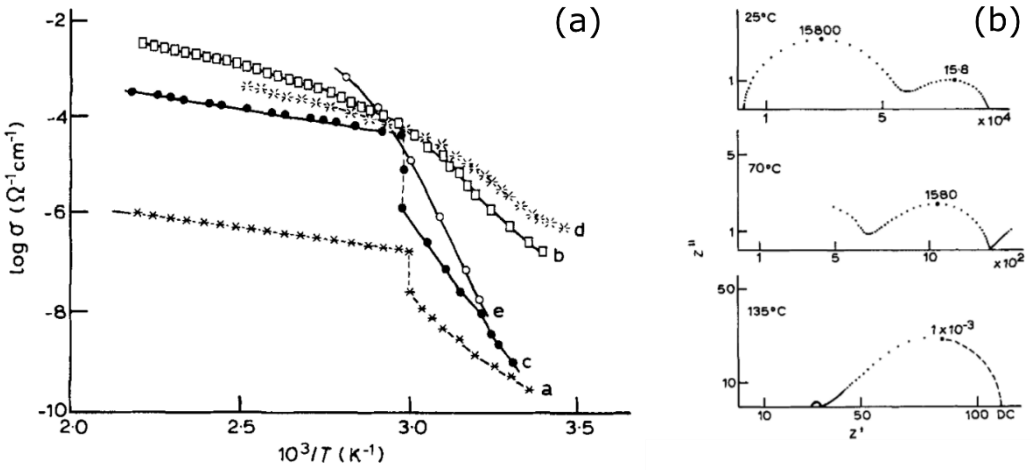

Figure 5-2: *(a) The ionic conductivity of $(PEO)_n.MeClO_4$ electrolytes. a is pure PEO; b is M = Li; c is M = Pb; d is M = Cu; e is M = Hg. (b) The impedance spectra of an $Li/PEO_8.LiClO_4/Li$ cell at increasing temperatures. Reproduced from Magistris et al.*[247]

Due to the high crystallinity at room temperature the ionic conductivity can be as low as 10^{-9} S cm^{-2}, whereas it needs to be closer to 10^{-3} S cm^{-2} to compete with liquid electrolytes. The ionic conductivity is therefore very dependent on temperature, see Figure 5-2, and increases rapidly with temperature up to the T_g of the polymer; above this point it remains more stable at ~10^{-4} S cm^{-2} (a). There are methods of improving the ionic conductivity of solvent free SPE's such as crosslinking, hyperbranching, co-polymerisation and blending with another polymer with the aim of reducing the crystallinity.[248]

Gelled polymer electrolytes (GPE)'s utilise a polymer matrix filled with liquid electrolyte, often called a plasticiser. This retains the benefit of a solid electrolyte and an ionically conductive liquid electrolyte. Unfortunately, a high quantity of plasticiser is often needed for GPE's to compete with liquid electrolytes, and this reduces the safety and strength of the GPE.[249]

5.2.1.1 Composite polymer electrolytes

Composite polymer electrolytes (CPE's) combine multiple different materials; the most defining of these is the inorganic/organic CPE which contains a bulk polymer alongside an inorganic material. The addition of inorganic solids to polymer electrolytes disrupts the polymer chains and can increase the amorphous fraction of PEO thus raising the ionic conductivity, this is especially

important in reducing the necessary operating temperature of SPE's.[250] These inorganic filler materials can be inert or ion conducting. Inert fillers include small particles of metal oxides such as SiO_2 and TiO_2[251] and, in general, a 10 wt% loading of particles smaller than 10 µm in size provide the highest increase in ionic conductivity, see Figure 5-3.[252]

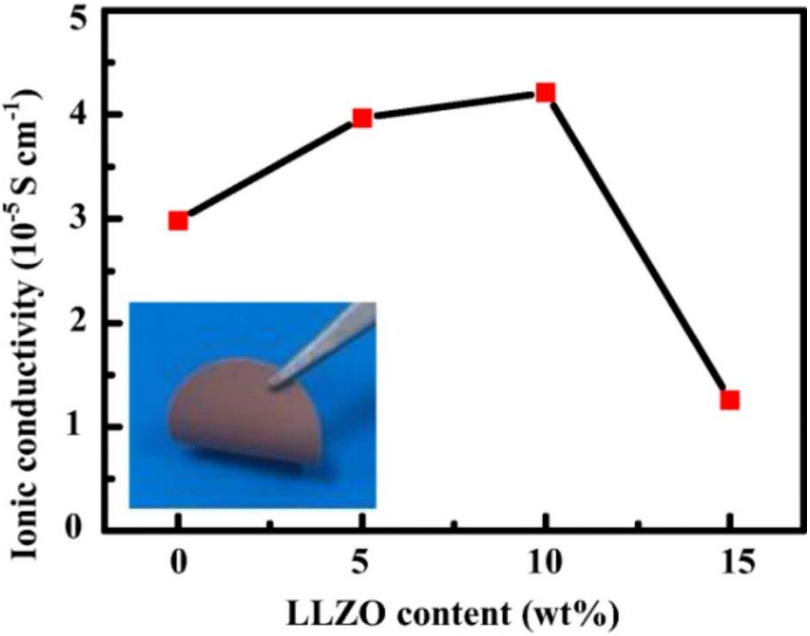

Figure 5-3: *The ionic conductivity of a PEO electrolyte with increasing LLZO filler content. Reproduced from Li et al.*[253]

Ion conducting fillers such as LLZO also create this effect while providing extra pathways for lithium movement although the exact method of this movement is debated; some research suggests the cause is the amorphous polymer shell that forms around the filler,[254] while others suggest it is through the particle itself.[255] The addition of inorganic filler not only increases ionic conductivity, but it also increases the material strength of the electrolyte, which offers extra protection against dendrite formation.[256] Pure PEO has a low mechanical strength of between 1 MPa and 15 MPa, whereas Al-doped LLZO SSEs have a strength of ~150 GPa,[257] which makes them much more dendrite resistant. Techniques such as crosslinking, blending and the addition of filler can be used to increase the strength of the polymer.[258]

5.2.1.2 Composite cathodes

SPE's and CPE's are not wetting electrolytes; they do not fill the pores of the cathode and therefore can only contact the surface of the electrode. This limits

the ionically active portion of the electrode to the area in contact with the electrolyte. To resolve this issue, composite cathodes are often manufactured with the electrolyte combined into them, to ensure full contact throughout the thickness of the film. This decreases the energy density of the cathode but increases the utilisation of active material, therefore a balance must be found to optimise both.

5.2.2 Issues with PEO-based SPE's

For PEO-based SPE's, a majority of work is focussed on the degradation of the polymer at high voltages, which is crucial when working with cathode materials like NMC which have an upper voltage limit of around 4.2 V. Most studies suggest that the decomposition of PEO takes place above 3.8 V although the actual voltage limit is debated. It is thought that the lithium salt can impact the oxidation, therefore the voltage limit may vary with composition which may be the reason for a variety of reported oxidation voltages.[23–26]

For inorganic type SSEs the electrode-electrolyte contact is crucial; due to the rigid nature of the inorganic films good contact with the electrode is not assumed and any changes in the electrode structure, through volume expansion or architecture degradation, can worsen this contact.[259] This, alongside the formation of SEI layers can increase interfacial resistance with prolonged cycling. Polymer electrolytes are more flexible to electrode structure changes although any oxidation of the polymer at high voltages can form highly resistive interfacial layers.[260] The total resistance of an SSE or SPE battery is made up of individual interface and bulk combinations. The interfaces that can contribute to the resistance are between the current collector and composite cathode, between the active material particles and the electrolyte inside the composite cathode; between the composite cathode and the electrolyte layer, and the interface between the electrolyte and the anode. Figure 5-4 (b) shows the location of all potential interfaces throughout a PEO-based composite cathode cell and the contribution of the cathode and anode interfaces on the impedance profile of a full cell (a), thus demonstrating how the total cell resistance is built up by individual SPE interfaces.[261]

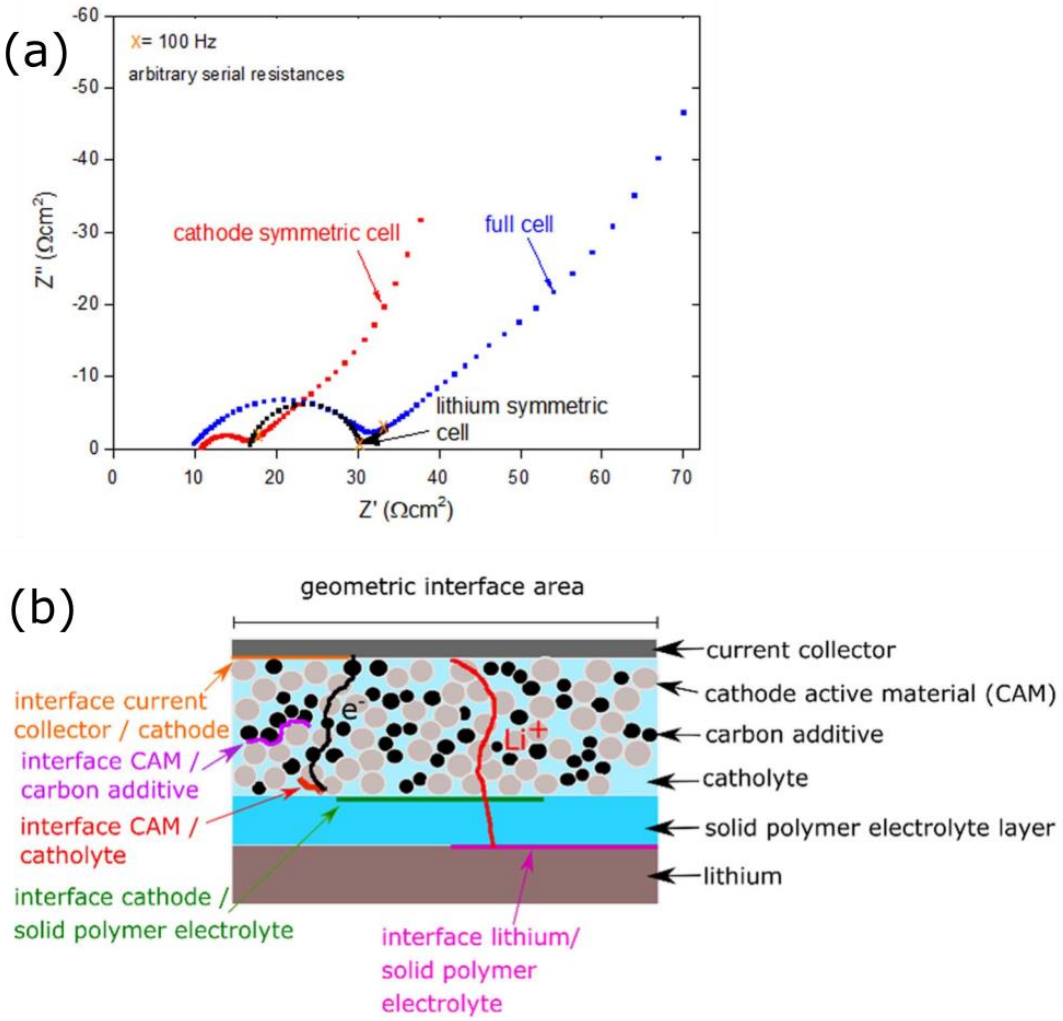

Figure 5-4: *(a) The Nyquist EIS plot of an LFP composite cathode/PEO/Lithium cell showing the contributions from cathode and anode. (b) Diagram of full composite cathode/SPE/lithium cell showing the locations of interfaces. Reproduced from Wurster et al.*[261]

5.2.3 Literature summary

The research discussed in this chapter aims to improve the performance of a PEO-based SPE and elucidate mechanisms that occur at the interface between the composite cathode and the electrolyte. Composite cathodes have only been manufactured as homogenous mixes of electrolyte and active material. To optimise both ionic and electrical conductivity throughout the composite cathode it follows that an increase in conductive material at the base of the film alongside higher electrolyte content nearer the top of the film would be beneficial. Specifically, lower interfacial resistance should be seen with improved cathode / electrolyte contact, and cathode / current collector contact.[249] A gradient-based

spray approach is used to manufacture graduated LFP/PEO composite cathodes; the cycle life, rate performance and electrochemical properties provide evidence of improved performance and reduced degradation when compared to ungraded electrodes.

5.3 Methodology

Ultrasonic spray deposition was used to manufacture LFP/PEO composite cathodes, ungraded and graded, and a PEO-based SPE. The composite cathode was sprayed directly onto stainless steel disks placed on a heated bed with the SPE layer deposited on top immediately afterwards. Gradients were manufactured by altering the flow rates of two different solutions sprayed out of two nozzles. The composite cathode/SPE films were then incorporated into coin cells and tested for rate performance, cycle life and impedance. Characterisation was performed with X-Ray CT and optical microscopy.

5.3.1 Spray solutions

The solution for spray deposition of inorganic type SSEs was a 10 mg mL^{-1} solution of Al-doped lithium lanthanum zirconium oxide (500 nm Ampcera) in DI water. 15 wt% CMC (sodium carboxymethylcellulose, Sigma-Aldrich) was added for the binder studies.

For PEO-based composite cathodes the overall composition of the films is shown in Table 5-1 and is based on previous literature work, where the active material to electrolyte ratio has been optimised.[261]

Table 5-1: *The expected weight % of the final composition of both graded and ungraded composite cathodes.*

LFP	Carbon black	PEO	LiTFSI
66.8%	3.4%	18%	11.8%

For the manufacture of LFP/PEO composite cathodes, two solutions were manufactured; 14.04 mg mL^{-1} LFP (lithium iron phosphate 1.5 µm, MSE supplies) and carbon black (Super C65, C-NERGY Imerys) in 1:1 ratio of IPA and DI water by volume; a 5.96 mg mL^{-1} of PEO (100,000 M_V Sigma Aldrich) and LiTFSi (Bis(trifluoromethane)sulfonimide lithium salt, Sigma Aldrich) in a 1:1 ratio of IPA (isopropyl alcohol, Sigma Aldrich) and DI water by volume. These solutions were used to manufacture both graded and ungraded composite cathodes.

The PEO-based SPE layer was manufactured using a 13.15 mg mL^{-1} solution of PEO, LiTFSI and optional LLZO (Al-Doped Lithium Lanthanum Zirconate Garnet, 500 nm, Ampcera) in DI water in the quantities shown in Table 5-2, which gives a $[Li^+]$:[EO] ratio of 1:10, which is optimal based off literature studies.[262]

Table 5-2: The weight % of the final composition of the SPE electrolyte

PEO	LiTFSI	LLZO
76.0%	15.6%	8.4%

The solids were dispersed prior to spray deposition using a sonic horn (Fisherbrand 505) at a power of 40% and a pulse rate of five seconds for 10 minutes. During the spray, a 300 rpm stirring syringe was used to maintain dispersion within the syringe.

5.3.2 Spray deposition

To manufacture the composite cathodes, the LFP and PEO solutions were spray deposited using two AccuMist (SonoTek) nozzles and stirring syringe inputs according to the methodology described previously. The nozzles were rotated to -24 ° and 24 ° respectively at a height of 60 mm to ensure overlap of the two spray shapes, see Figure 5-5 for an image and schematic of the rotated nozzles.

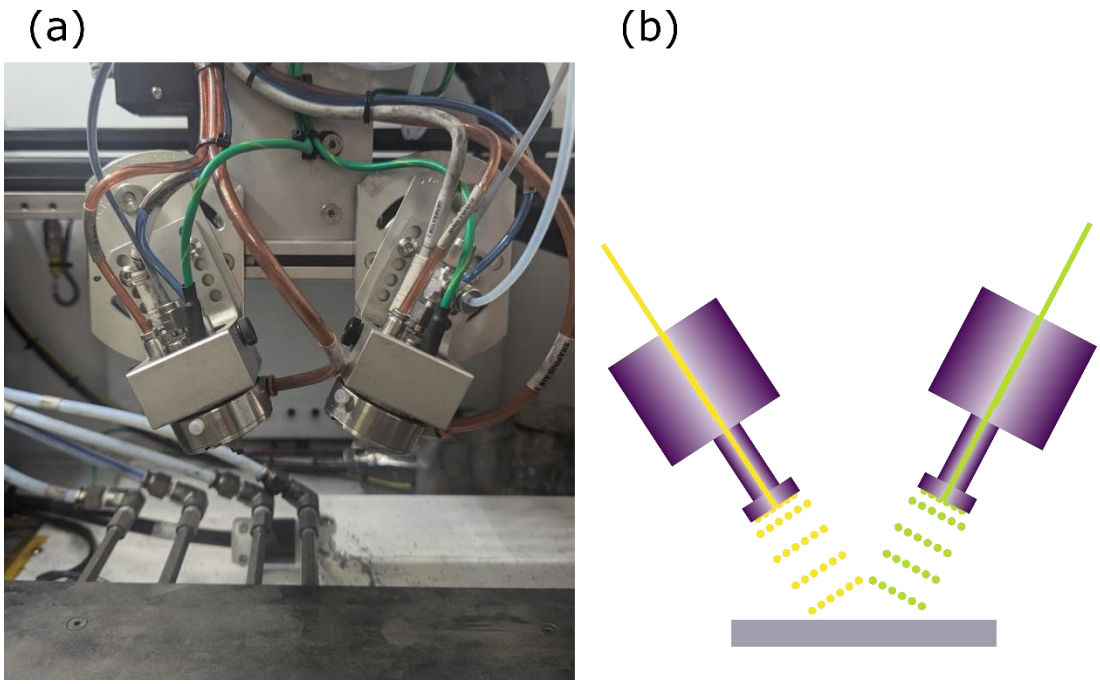

Figure 5-5: *Image and schematic of the bi-nozzle spray system with nozzles rotates to 24° and -24° respectively. (a) Image of the two rotated nozzles, (b) schematic of the two rotated nozzles.*

The heated bed was set to 60 °C and the films were sprayed onto 1 mm thick stainless-steel disks at a combined nozzle flow rate of 0.25 mL min^{-1} with flow rates of the LFP and PEO solutions being kept consistent at 0.125 mL min^{-1} for the ungraded electrodes and a program to vary the flow rates between 0 and 0.25 mL min^{-1} used for the graded electrodes. The shaping air was limited to 2 psi to ensure the spacers did not move and to improve atomisation; 80 sets of 4 spray passes comprised each cathode.

The SPE layer was sprayed directly onto the previously coated composite cathode at the same conditions using one AccuMist nozzle over 80 sets of 4 spray passes. After spray deposition the films were cooled and dried under vacuum at room temperature overnight before being transferred to an Ar-filled glovebox.

5.3.3 Coin cell manufacture

Coin cells were manufactured according to Figure 5-6 using CR2032 coin cell parts (Hohsen). An additional 1 mm thick stainless spacer and a 0.12 mm thick 14 mm diameter lithium disk (Goodfellow) anode were used.

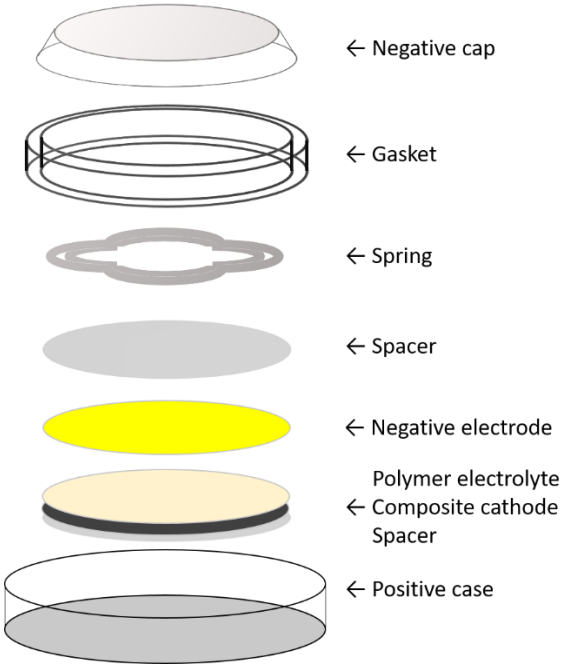

Figure 5-6: *The schematic of coin cell construction for SPE composite cathode testing*

5.3.4 Cell testing

Coin cells were tested on a Biologic VMP-300 (Biologic) at 60 °C in a Binder KB23 cooling incubator (Binder); this temperature was chosen due to the need for higher temperatures for acceptable ionic conductivity with PEO and the concerns of damage to cell holders and the coin cell gasket above 65 °C. Theoretical capacities were calculated from mass measurements of the stainless-steel disks before and after spray deposition; quoted C-rates are proportional to the cells theoretical capacity. Cells were tested for cycle life performance at C/10 and for rate performance at rates between C/10 and 2C; initially all cells were formed for two cycles at C/20. All cycling was performed between 2.5 V and 3.65 V, and no voltage hold was used. EIS was performed after every charge and discharge post a one-hour OCV rest period. EIS was performed between 10 mHz and 7 MHz, 20 points per decade and an amplitude of 10 mV.

5.3.5 Optical microscopy and X-ray CT

For characterisation, composite cathodes with and without an SPE layer were deposited onto Al foil of ~20 µm thickness and cut and sealed perpendicularly in an epoxy block. After drying under vacuum the cross-section epoxy samples were polished using a polishing wheel (SMARTLAM 2.0, Kulzer Technik) and imaged using a Keyence VHX-7000 optical microscope.

X-ray computed tomography (X-ray CT) was performed on a lab-based micro-CT X-ray instrument (Zeiss Xradia 620 Versa, Carl Zeiss). 1601 projections were taken with an exposure time of 5 seconds, magnification of 20 x, a source operating voltage of 80 kV and source current of 125 µA with a tungsten emission and a pixel size of 381 nm. Reconstruction was done using a cone beam filtered back projection algorithm using commercial software (Reconstructor Scout-and-Scan, Zeiss, Carl Zeiss). The data was cropped using Avizo3D 2023.2 software (ThermoFischer) and segmented using ilastik software using the methodology in Dawson et al.[263,264]

5.4 Results

5.4.1 Inorganic type SSEs

Initially an inorganic type of SSE was chosen for study for its higher ionic conductivity, however it was found that while films could be manufactured, no ionic conductivity could be measured. The gradient composite cathode was intended to enhance the cathode/SSE contact, particularly during volume expansion over cycling, which is a major problem in stiff inorganic type SSE material. LLZO was chosen as a suitable inorganic material due to its better stability in air than other SSE materials.[265] LLZO was difficult to disperse in solution, possible due to its high density, although the addition of 15 wt% CMC binder dispersed the material better. Although LLZO films could be spray deposited, no ionic conductivity was obtained, despite the film being sufficiently electronically resistive. It was concluded that without sintering the particles of LLZO were not in adequate contact to transfer lithium ions. Due to the direct on cathode spray deposition any sintering process would involve sintering a combined cathode/SSE system which would damage the LFP. This was still attempted and the LFP was seen to change colour from black to red, a clear degradation of the material, see Figure 5-7. Due to the need for sintering with inorganic type SSEs a suitable polymer was chosen instead, and gradient composite SPE type cathodes were studies for the remainder of this project.

Figure 5-7: *The colour change of LLZO coated LFP after 600 ^{o}C sintering. Red, LFP; White, LLZO.*

5.4.2 Optimisation of PEO spray

PEO was chosen as a suitable SPE as it is the most widely researched and understood, can be easily dispersed in water, and has adequate ionic conductivity at higher temperatures.

The molecular weight of PEO affects its melting point and glass transition temperature (T_g), Table 5-3 indicates the PEO available for purchase and its subsequent melting point.

Table 5-3: *showing the molecular weight and melting point of different PEO polymers, all information sourced from Sigma Aldrich*.

Molecular Weight	Melting point (°C)
M_n 300	15
M_n 400	4 – 8
M_n 600	20 – 25
M_n 1,305-1,595	43 – 46
M_n 2,050	52 – 54
M_v ~8,000	60 - 63
M_v 100,000	65
M_v 600,000	65

It was found that when dispersed in DI water at 1 mg mL^{-1} the 600,000 M_v polymer, which is closer in mass to those normally used in literature, made a solution that did not seem viscous but when atomised by the sonicating nozzle it did not form discrete small droplets (~ 13 µm); instead a sputtering spray was seen with large droplets (~ 1 mm) formed at all flow rates and nozzle power which did not lead to a homogenous film.

To evaporate the solvent the substrate needs to be heated; higher temperatures allow for faster flow rates and therefore shorter overall spraying times. Lower molecular weight PEO films did not have sputtering issues but were likely to melt after deposition due to the heated substrate. A balance was found with the 100,000 M_v PEO, which could be sprayed at sufficient flow rates without sputtering while maintaining a substrate temperature of 60 °C which was below the melting point of the polymer.

5.4.3 Optimisation of PEO electrolyte

LLZO was included in the PEO electrolyte mix as it has been proven to increase ionic conductivity and provide resistance to dendrite formation.[256]

The ionic conductivity of PEO was measured with and without 10 wt% LLZO at different temperatures, see Figure 5-8. These values fitted well with similar structures in literature, and the log of the ionic conductivity was seen to increase linearly with temperature.[262] Above the melting point of PEO the ionic conductivity plateaus, therefore, with limits of temperature dictated by the cycling equipment, a temperature of 60 °C was used for all experiments. Interestingly the addition of LLZO did not show an increase in ionic conductivity as expected, perhaps LLZO would have more of an impact above the melting point of the PEO, where the crystallinity of the polymer chains is at a minimum and no longer the main factor in determining ionic resistance.[253]

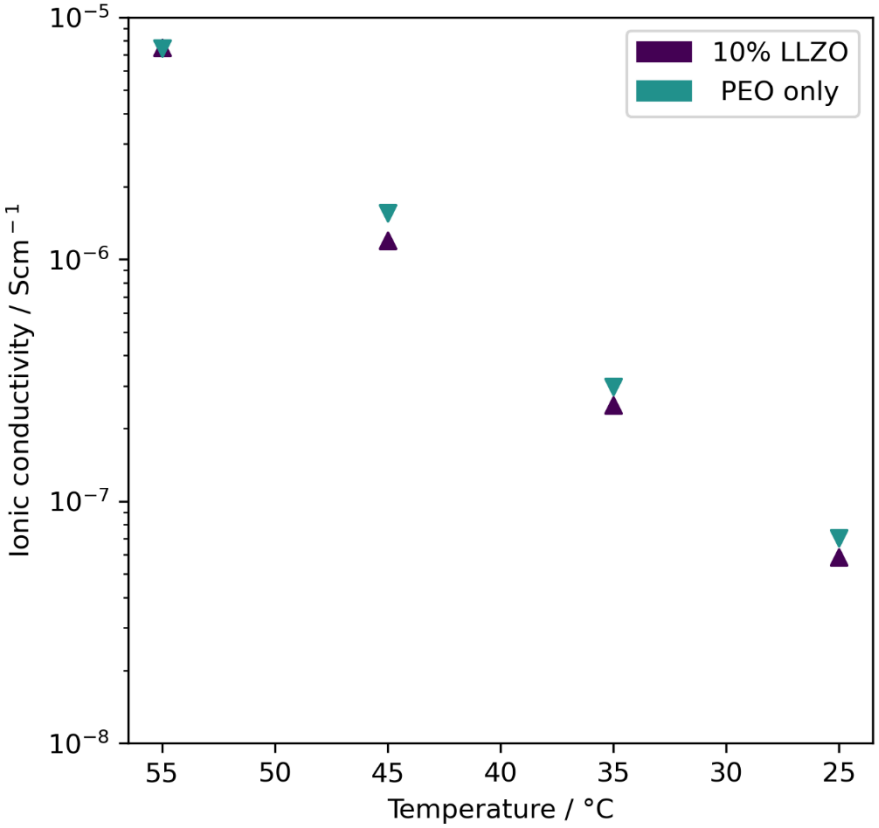

Figure 5-8: *The ionic conductivity of PEO/LiTFSI SPE's with and without 10 wt% LLZO at increasing temperatures.*

5.4.4 Effect of LLZO on cycling performance

LFP composite cathodes were manufactured with an LFP/PEO/LiTFSI/carbon black ratio of 66.8/18/11.8/3.4 by mass. To study the effect of LLZO on cycling behaviour, LFP/PEO/Lithium cells were cycled with and without the addition of 10 wt% LLZO. Figure 5-9 shows the charge curve of three variations of these cells at 20 µA of current. The use of single layer of PEO (80 counts of 4 spray passes at 0.25 mL min^{-1} flow rate), causes the voltage to drop after ~10 hours and reach 0 V after ~40 hours suggesting that an internal short-circuit has occurred. While shorting is a known consequence of dendrite formation, which is a common issue with PEO-based batteries due to their low mechanical strength[26], a dendrite-induced failure on the first charge is unlikely. Instead, it is possible that upon heating to near the melting point of PEO, the polymer no longer has the structural integrity to withstand the internal cell pressure resulting from the wave spring and is displaced, allowing the two electrodes to touch. When a PEO electrolyte that is twice as thick (160 passes)

was used, the cell drops in voltage after ~20 hours and reaches 0 V after 60 hours. The increase in thickness therefore delays the pressure induced displacement of PEO but not sufficiently enough to operate the cell. The addition of LLZO however, even in the single layer PEO, shows no voltage drop even after the full 60 hours of charge and as is shown for the remainder of this work, allows for repeated cycling even at high current rates. The harder LLZO material is thought to prevent internal short-circuiting through physical blocking, and even though there was no significant improvement in ionic conductivity, is a valuable additive to the SPE mix.

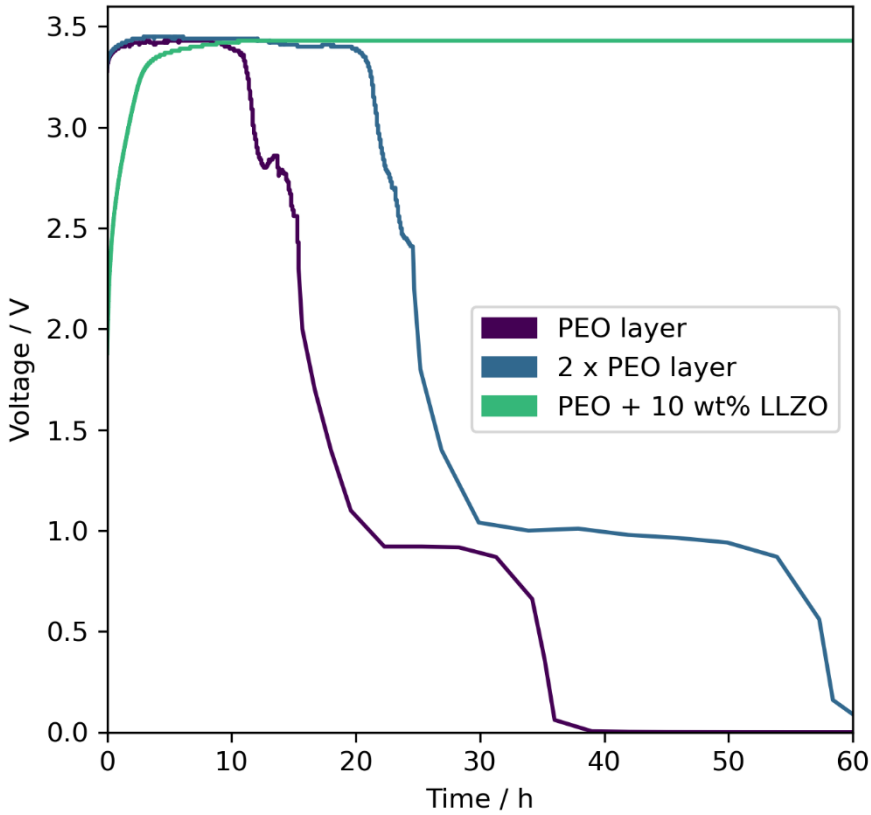

Figure 5-9: *The voltage vs time plots of spray deposited LFP composite/PEO/Lithium cells charging at 20 µA for 60 hours.*

5.4.5 Gradient composite cathodes

Gradient composite cathodes of LFP and PEO were manufactured using the gradient spray system as previously described, using one solution of PEO and LiTFSI and one of LFP and carbon. To manufacture a gradient from 100% LFP at the current collector to 100% PEO at the top of the film, while maintaining a

total PEO ratio of 66.8 wt% two different concentration precursor solutions were required (LFP: 14.04 mg mL^{-1}, PEO: 5.96 mg mL^{-1}). Figure 5-10 shows the expected solution and mass flow rates of the two solutions through the spray coater: (a) demonstrates the change in flow rate of the two solutions over the course of 80 passes (~9 mL). The total flow rate remains consistent at 0.25 mL min^{-1} which means that the spray shape and evaporation rate remains unchanged, despite the two changing inputs. (b) shows the solid mass flow of the two different concentration solutions, where a higher mass flow of LFP is seen for much of the spray, and the total mass flow lowers as the spray progresses. The impact of this can be seen in (c) where the plot of cumulative mass deposited shows the gradient of each material through the thickness of the film is a curve and not a straight line. This is an effect of using two different concentration solutions and requiring a material ratio that is not 1:1. This effect could be resolved by reprogramming of the flow rates in (a), using a curved program rather than a linear one although this was deemed to be unnecessary as the actual change in structure would be minimal.

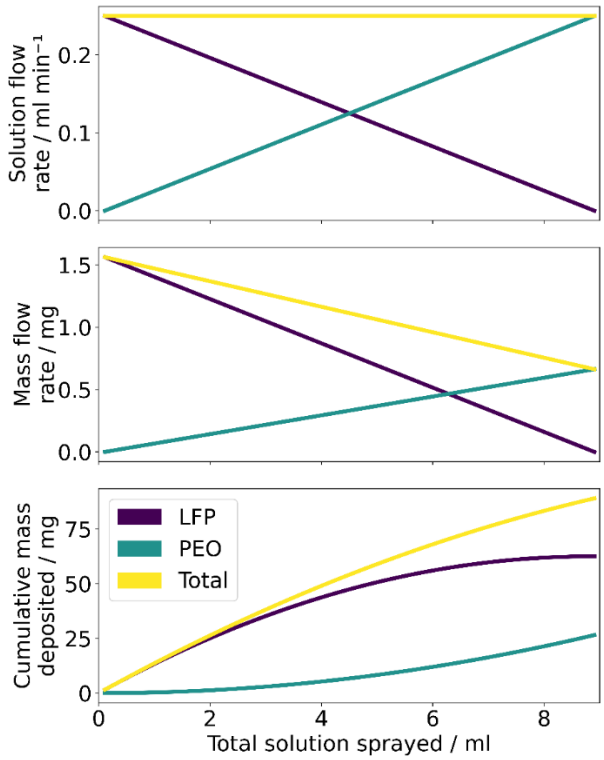

Figure 5-10: *Showing the spray parameters and estimated solution and mass flow rates of the LFP and PEO solutions. (a) The solution flow rates through the spray coater over the course of the full spray. (b) The associated mass flow*

of the two different concentrations solutions. (c) The cumulative deposited mass of each material.

5.4.6 Characterisation of graded composite cathodes

Characterisation of the graded films was done with optical microscopy and X-ray CT. Figure 5-11 shows the cross section optical microscopy image of the ungraded and graded composite cathodes, coated with a layer of PEO SPE.

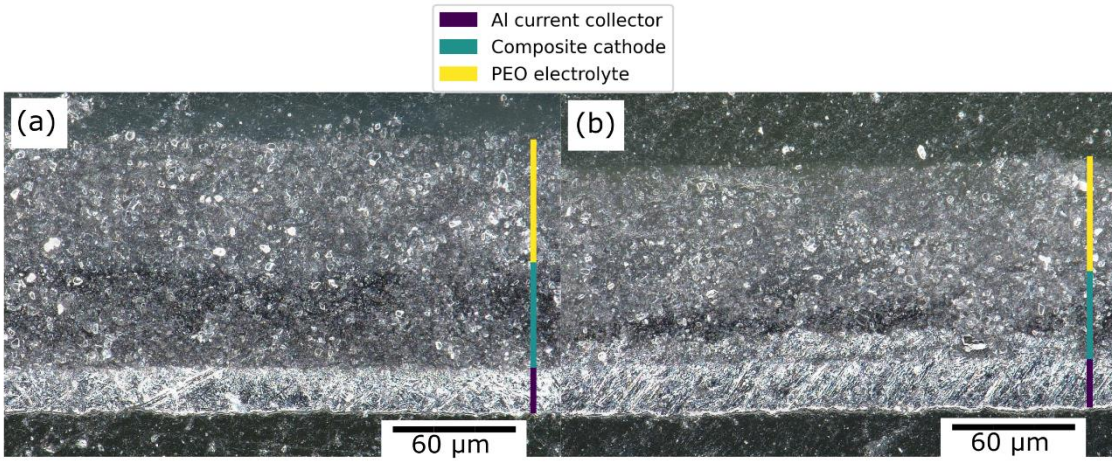

Figure 5-11: *The cross-sectional optical microscopy images of composite LFP cathodes with PEO electrolyte on top, coated onto foil. (a) An ungraded composite cathode and (b) a graded composite cathode from LFP to PEO. Both have the same thickness of PEO electrolyte on top.*

There is a clear difference between the two structures; the ungraded sample (a) shows three distinct layers; the aluminium current collector, the composite cathode and the SPE. Whereas in (b), the composite cathode layer varies from bottom to top; the middle similar to the ungraded composite cathode which is expected. The graded PEO SPE layer appears thicker, but this would be because it blends in with the top of the composite cathode, hence demonstrating a gradient.

Figure 5-12 shows the X-ray CT characterisation of graded and ungraded composite cathodes. (a) shows a demonstration of the graded spray manufacture. Figure 5-12(b) shows the through-thickness LFP % of the ungraded and graded composite cathodes from the current collector to the surface of the

electrode as calculated from the segmented X-Ray CT scans in Figure 5-12(c), using image analysis of the X-Ray CT slices to determine the LFP ratio.

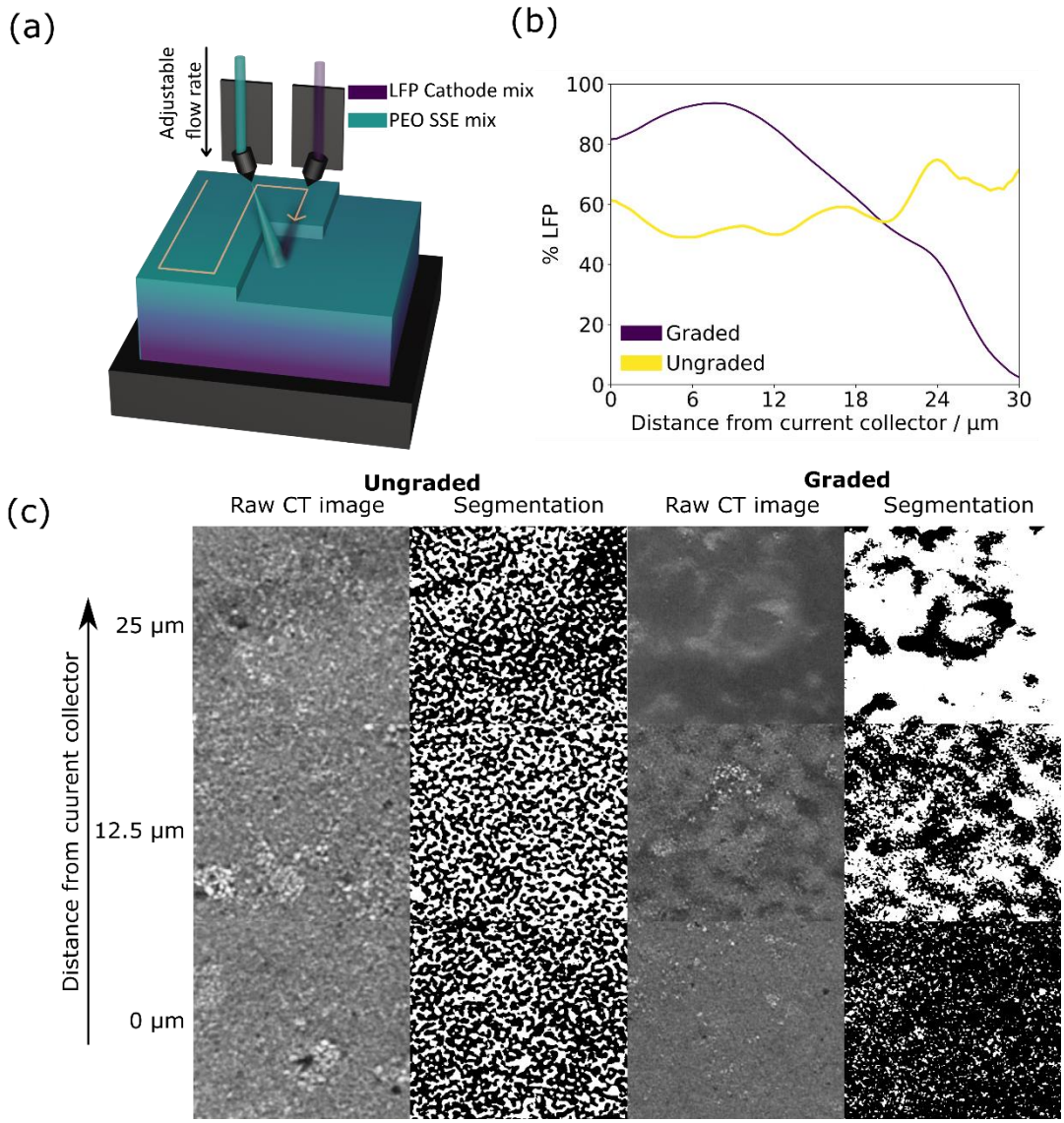

Figure 5-12: *The manufacturing methodology and characterisation of graded and ungraded LFP/PEO composite cathodes. (a) Schematic of the rastering two spray nozzle set-up and the subsequent gradient film. (b,c) The characterisation of graded and ungraded composite cathodes using X-ray CT with (b) experimental results showing the % of LFP measured throughout the thickness of the electrodes as calculated using the segmentations shown in (c) which shows three of the raw X-ray CT slices and corresponding segmentations at different distances from the current collector, in the segmented column white indicates PEO and black indicates LFP.*

There is a clear steady drop in LFP % in the graded composite cathode from ~100% to 0% over the 30 µm thickness, whereas the LFP % in the ungraded cathode remains stable at ~60%. The slight increase in LFP % in the graded cathode between 0 and 10 µm is thought to be due to some settling of the molten PEO during spraying which displaced some LFP. The raw X-Ray CT slices and associated segmentations shown in Figure 5-12(c) demonstrate the density difference of the materials at distances from the current collector of 0 µm, 12.5 µm and 25 µm in an electrode of ~30 µm thickness. The associated segmentation was done based on the greyscale value of the raw slices, with highly dense LFP appearing lighter in the raw slices and darker in the segmented ones. The change in density throughout the graded electrode is clear with the 0 µm slice of the graded cathode appearing as a dense LFP structure and the 25 µm slice containing mostly polymer. By contrast, the ungraded electrode shows the same ratio and structure of LFP and PEO at 0 µm, 12.5 µm and 25 µm, thus demonstrating the effectiveness of one-step spray deposition in manufacturing true gradients in electrodes.

5.4.7 Cycle life performance of graded composite cathodes

The graded and ungraded composite cathodes were tested for capacity loss during long term cycling at a rate of C/10. At cycling temperatures of 25 °C the cells functioned poorly with charge and discharge cut-off voltages often hit within a few seconds of applied current thus proving the necessity for an amorphous polymer for lithium-ion movement. At 60 °C both composite cathode structures cycled normally without shorting at C/10. The graded and ungraded composite cathodes were tested for capacity loss during long term cycling at a rate of C/10 and graded composite cathodes suffered less capacity loss over 80 cycles than ungraded ones. Figure 5-13 (a) displays the capacity per cycle of the graded and ungraded cathodes. Here and across multiple repeats, see Appendix Figure 8-1(a) and (b) the graded electrodes maintained capacity after extensive cycling significantly better than the ungraded even though the ungraded electrodes had higher initial discharge capacity (~100-120 mAh g^{-1}) than the graded ones (~80 mAh g^{-1}). The initial lower capacity for the graded composite cathode is thought to be due to the reduced amount of PEO near the current collector which limits ionic conductivity near the base of the electrode and creates areas of less active LFP. Capacity loss in the ungraded cathode is quite significant, decreasing from

~100 mAh g^{-1} to almost zero after 80 cycles; by contrast, the graded cathodes retained high capacity remaining at ~80 mAh g^{-1} after 80 cycles, thus negating the impact of the lower initial capacity.

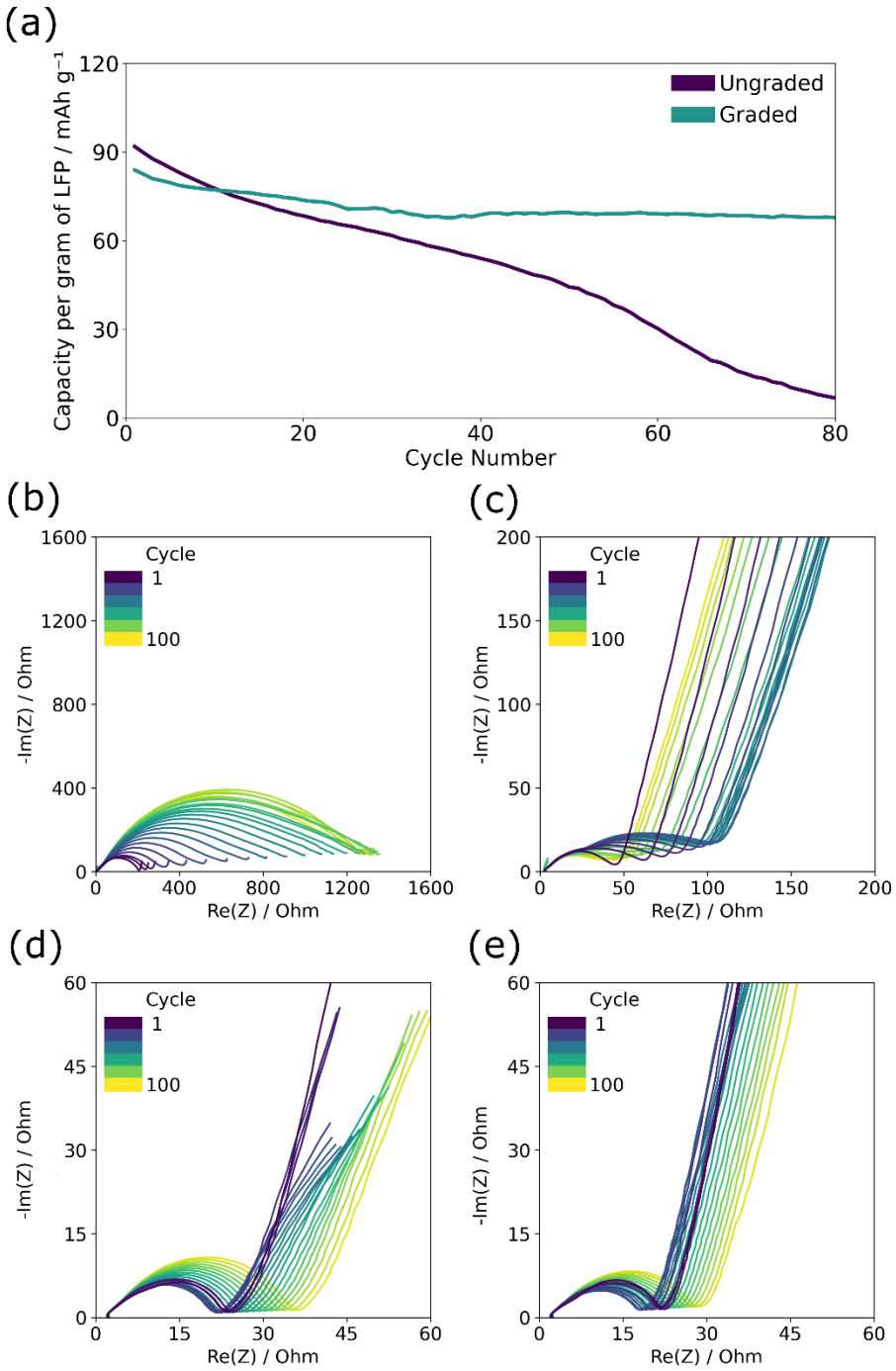

Figure 5-13: *The cycle life performance and charge and discharge EIS of graded and ungraded composite LFP/PEO cathodes against lithium metal at C/10. (a): the discharge capacity per gram of LFP. (b-e): EIS of graded and ungraded cathodes every 10th cycle in either the charged or discharged state with: (b) ungraded charged, (c) ungraded discharged, (d) graded charged, (e) graded discharged.*

The electrochemical impedance spectroscopy shown in Figure 5-13(b-e) demonstrates the difference in the charge transfer resistance across the cell for the two different structures throughout cycle life testing. The total resistance can be observed by the size of the semicircle along the x-axis and is made up of overlapping semicircles of the bulk PEO ionic resistance and two main planar interface resistances, one for the cathode/electrolyte interface and the other for the anode/electrolyte interface.[261] The graded composite cathode had a lower initial resistance on the first cycle (~20 Ω in both states) compared to the ungraded cathode (160 Ω in the charged state and 50 Ω discharged). The impedance of the ungraded composite cathode after the first charge, Figure 5-13 (b), of ~160 Ω is much higher than that of the discharge (c) ~50 Ω. It has been shown that the resistance of the discharged state should be lower than that of the charged, partially due to the intrinsic differences in lithium-ion diffusion coefficient in $LiFePO_4$ and $FePO_4$.[261,266] Furthermore, throughout the 80 cycles, the graded composite cathode has a smaller increase in resistance than the ungraded one, particularly in the charged state with resistance after the final charge of ~1400 Ω for the ungraded composite cathode and ~40 Ω for the graded. The initial lower resistance alongside the smaller increase in resistance of the graded composite cathode suggests that the charge transfer in either the bulk PEO or the planar interfaces of the graded composite cathode is improved and suffers less damage with cycling. The higher increase in resistance after 80 cycles with the ungraded composite cathode may explain the significant deterioration in capacity, due to degradation of the cathode/electrolyte interface. As the material composition of the bulk PEO is the same in both composite cathodes it is assumed that the graded composite cathode provides and maintains better interfacial contact with the SPE layer due to the lack of a clear boundary between the surface of the composite cathode and the PEO based SPE. This is also thought to be the reason for minimal capacity loss or resistance increase during cycling as separation of these two layers is much more unlikely to occur as there is no clear plane in which disconnection can occur. To resolve greater detail in the EIS analysis, distribution of relaxation times (DRT) analysis of the spectra was performed, allowing overlapping relaxation processes to be resolved into a series of local maxima linked to specific time constants (τ).[267] In the DRT analysis, the charge transfer peak in the charged ungraded composite cathode, Figure 5-14(a), can be seen

to have grown in size and shifted from ~10^{-3} s^{-1} to ~10^{-1} s^{-1} over 80 cycles, suggesting that charge transfer both increased in resistance and became slower with cycle induced degradation; this would account for the distinct loss in capacity. By contrast, there was very little change in the charge transfer peak over the course of cycling in the graded composite cathode, Figure 5-14(c). As the material composition of the bulk PEO is the same in both SPE layers, it is assumed the charge transfer resistance between the composite cathode and the bulk PEO SPE is the primary cause of degradation. With the graded composite cathode, capacity loss or resistance increase during cycling is more unlikely to occur as there is no clear plane between the two layers in which disconnection can take place.

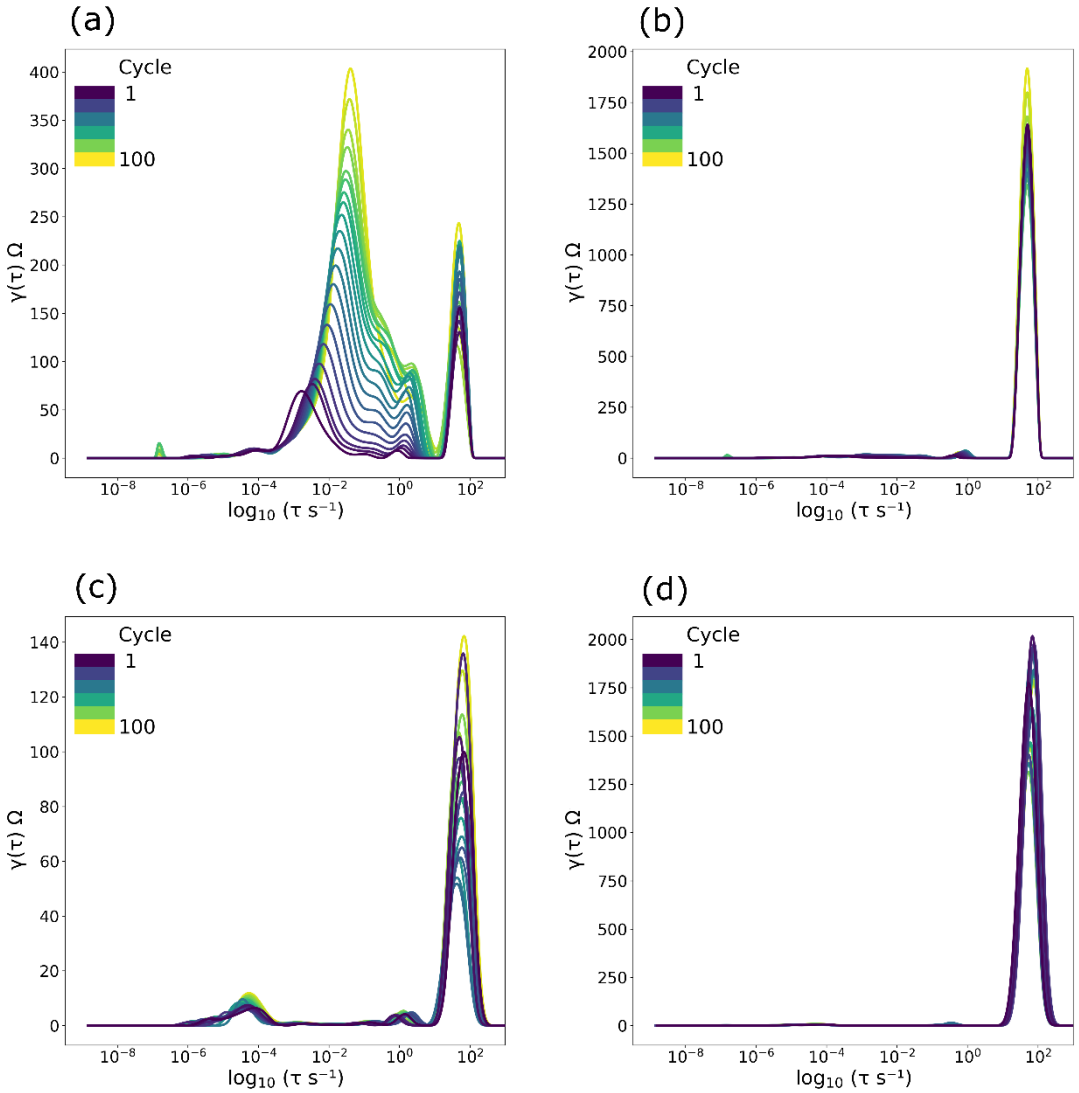

Figure 5-14: *EIS distribution of relaxation times (DRT) of graded and ungraded composite LFP/PEO cathodes against lithium metal. (a-d): EIS DRT spectra of graded and ungraded cathodes measured every 10th cycle at C/10 in either the charged or discharged state with (a) ungraded charged, (b) ungraded discharged, (c) graded charged, (d) graded discharged.*

5.4.8 Rate performance of graded composite cathodes

Graded and ungraded composite cathodes were tested for rate performance between C/10 and 2C and the typical corresponding discharge capacity and EIS plots are shown in Figure 5-15. While ungraded cathodes had higher capacity at C/10, similar to cycle life testing, at all rates above C/10 the graded composite cathodes performed better. The capacity of the ungraded composite cathodes

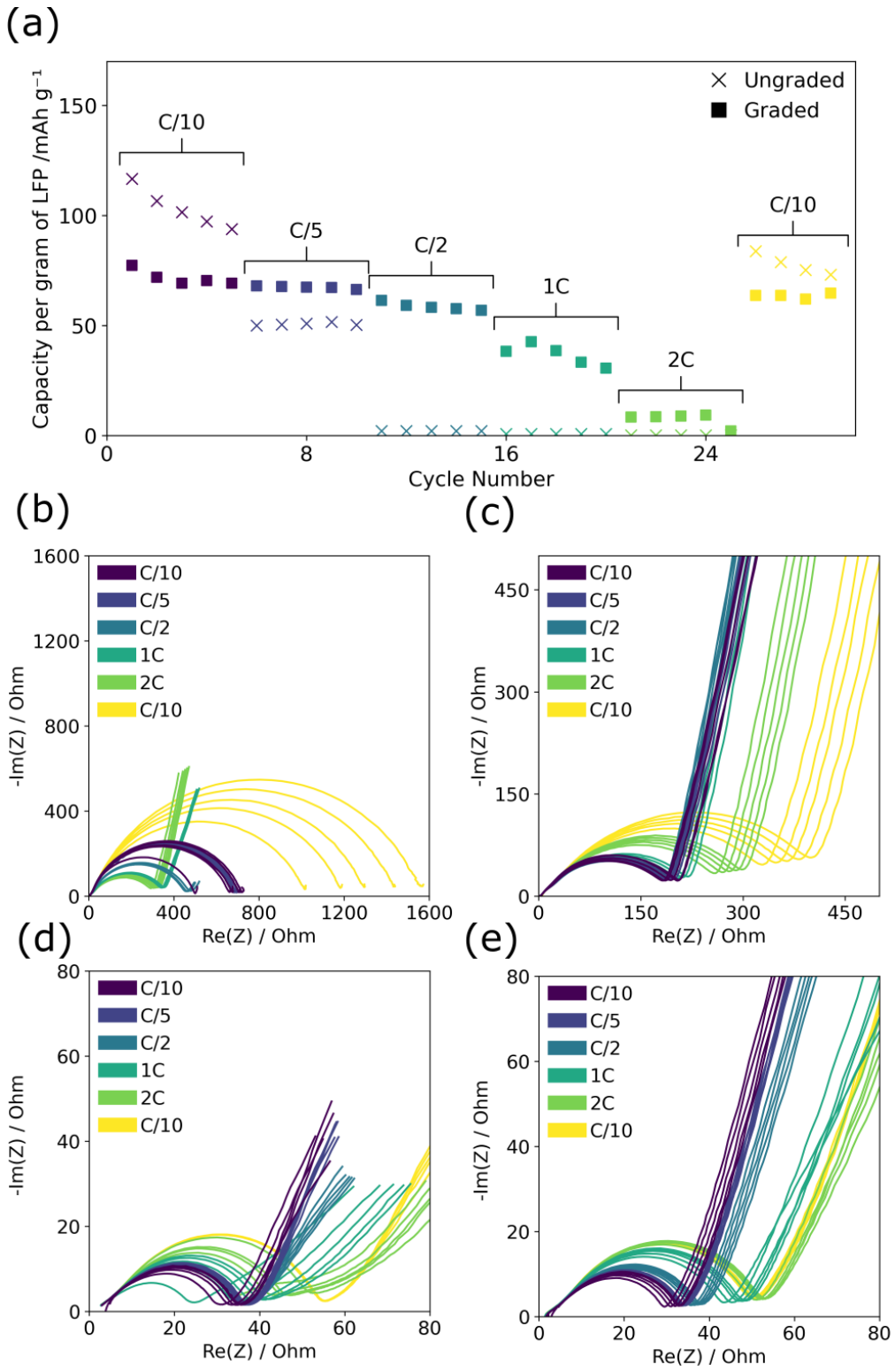

Figure 5-15: *The rate performance and charge and discharge EIS of graded and ungraded composite LFP/PEO cathodes against lithium metal. (a) voltage vs capacity plot at increasing rates of both graded and ungraded cathodes. (b –d) EIS of graded and ungraded cathodes per cycle in either the charged or discharged state with (b) ungraded charged, (c) ungraded discharged, (d) graded charged, (e) graded discharged.*

dropped from ~100-120 mAh g^{-1} in the initial C/10 to 50 mAh g^{-1} at C/5 and then to ~0 mAh g^{-1} at C/2, 1C, and 2C. Based on the recovery of the capacity in the final C/10 cycles back to ~80 mAh g^{-1}, this significant capacity loss can be attributed to poor rate performance and not solely to cycle life degradation. The graded composite cathodes maintained a relatively stable capacity up to 1C of between 50 and 80 mAh g^{-1}, ~30-40 mAh g^{-1} at 1C and, then to ~10 mAh g^{-1} at 2C. Graded cathodes consistently achieved higher capacity than the ungraded cathodes at rates above C/10 across repeats, see Appendix Figure 8-1 (c) and (d), demonstrating improved rate performance despite the initially lower capacity.

Similarly to cycle life testing, the total resistance of the graded cathodes was substantially lower than ungraded cathodes at all points (graded between 20 Ω and 60 Ω and ungraded between 170 Ω and 1600 Ω), see Figure 5-15 (b-e). In all cases except for the ungraded charged EIS (b), the measured resistance increased with rate and the final C/10 cycles show around twice the resistance of the initial C/10 cycles. This suggests that there was some permanent degradation that occurred with high rate cycling. The DRT analysis of the charged states in Figure 5-16(a, c) shows that the charge transfer resistance peak for the final C/10 cycles was higher than for the initial C/10 cycles with a higher increase in resistance for the ungraded composite cathode which further suggests permanent degradation of the PEO SPE/composite cathode interface.

The ungraded charged EIS showed slightly different behaviour as the resistance decreased with rate from C/2 onwards and then increased by a significantly larger proportion for the final C/10 going from ~300 Ω to ~1600 Ω. The 2C resistance value of ~400 Ω and EIS profile showing a longer diffusion tail was similar to that of the discharged state which suggests that at high C-rates full lithiation had not taken. The DRT analysis in Figure 5-16(a) shows a high diffusion peak (~10^2 s^{-1}) during 1C and 2C testing for the ungraded charged state which confirms that there was minimal lithiation due to the lack of diffusion throughout the PEO structure. This was confirmed by the low capacity recorded for the ungraded cells between C/2 and 2C and may also explain the high capacity seen in the final C/10 cycles. At high rates, limited lithiation has occurred therefore there is minimal cycling-induced degradation to the structure and the capacity remains abnormally high, although in repeats the recorded capacity of the final C/10 cycles varies,

see Appendix Figure 8-1(c) and (d). This phenomenon was not present in the graded cathodes which indicates that a more complete lithiation has occurred at high C-rates. The DRT peak at ~10^2 s^{-1} associated with lithium diffusion in the charged graded composite cathode, Figure 5-16(c), follows an opposite trend to the charged ungraded composite cathode as peak height decreased with increased C-rate. This demonstrates that in the graded composite cathode, diffusion does not contribute as significant a proportion of impedance at higher rates, unlike the graded composite cathode in which the increase in diffusion-based impedance prevents any real lithiation from occurring. The improved lithium diffusion in the graded composite cathodes is therefore thought to be a major factor in their superior rate performance and must be due to the changes in the PEO SPE/composite cathode interface.

Overall, the graded cathodes have lower resistance than the ungraded cathodes with smaller resistance increases at higher rates demonstrating the stability of the graded composite cathode structure to maintain good lithium mobility under high current densities. This could be due to the improved electrolyte pathways through the cathode created by the gradient which are less constricted with lower tortuosity and therefore promote fast lithium movement and reduce charge transfer resistance which manifests as superior rate performance and the ability to pass higher current loads. Alongside this, the lack of a distinct electrolyte/electrode boundary promotes ionic contact and reduces rate-based degradation of the interface.

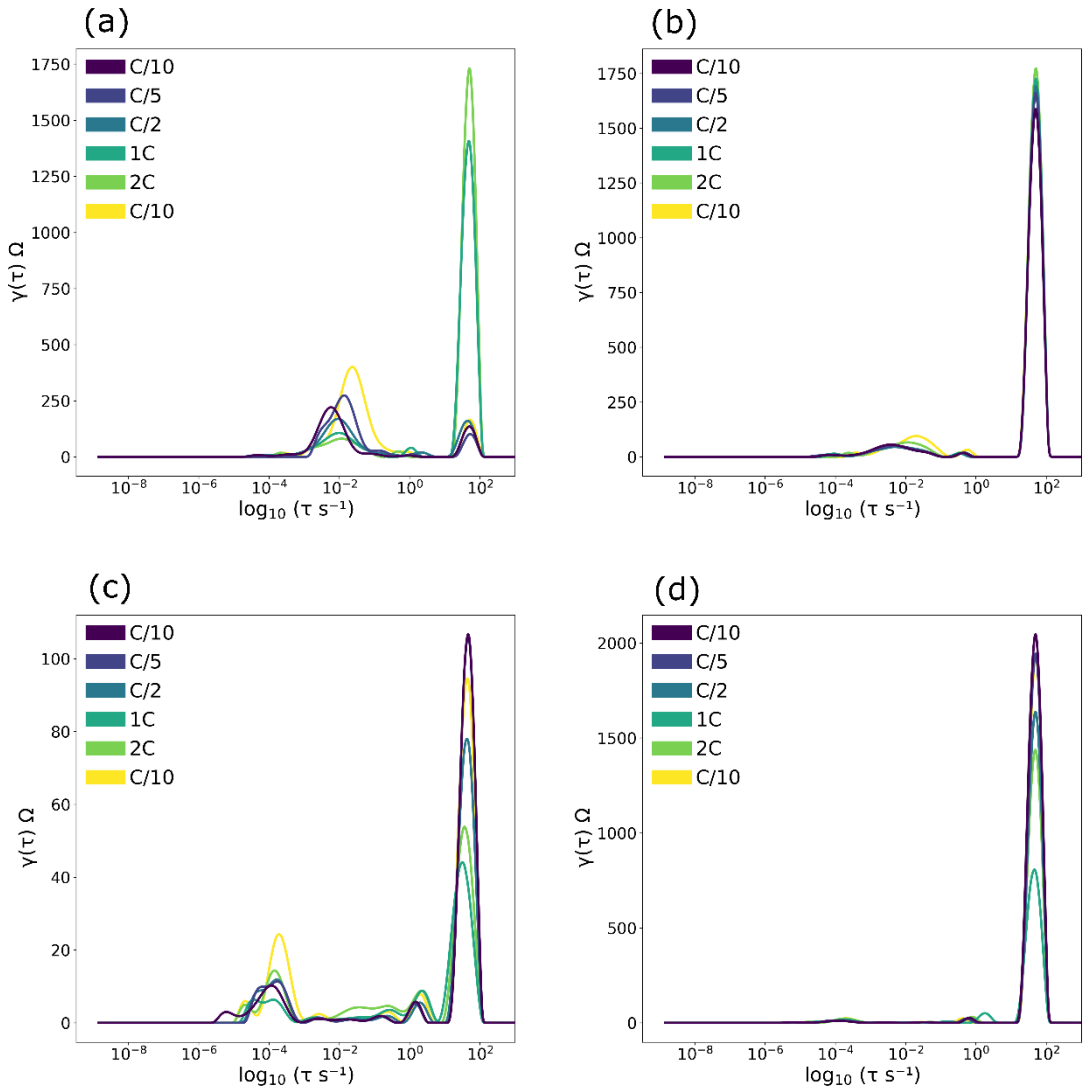

Figure 5-16: *EIS distribution of relaxation times (DRT) of graded and ungraded composite LFP/PEO cathodes against lithium metal during rate performance. (a-d): EIS DRT spectra of graded and ungraded cathodes measured at each rate in either the charged or discharged state with (a) ungraded charged, (b) ungraded discharged, (c) graded charged, (d) graded discharged.*

5.4.9 Charging issues

A well-documented and crucial drawback of PEO is its small oxidation window. There are contrasting upper voltage limits that have been reported for PEO-based electrolytes up to a maximum of 5 V vs Li/Li$^+$.[23–27] The accepted voltage of PEO degradation is 3.9 V vs Li/Li$^+$,[23,25,27] this is the value seen with a carbon-based high surface area electrode, whereas a flat blocking electrode raises the oxidation voltage.[27] It is thought that above 3.9 V the chain of PEO is oxidised to form

esters, which still provide acceptable Li^+ conductivity; above 4.2 V however the polymer breaks down further and this significantly impacts the performance of the electrolyte. The oxidation voltage in turn is affected by the oxidising nature of the cathode material with highly oxidising cathodes such as $LiCoO_2$ exacerbating PEO degradation.[25] Altogether this promotes the idea that stable cycling, without electrolyte oxidation, can be obtained by using low voltage and less oxidising cathodes such as LFP.

The graded composite cathodes manufacture here revealed unexpected charge profiles, see Figure 5-17; while the discharge profiles maintain consistency in the general shape, the charge profiles exhibit two additional behaviours. The first is seen in the cycle life testing (a) as a noisy voltage profile, only appearing after ~40 cycles. The second is seen in rate testing (b) at rates above C/2 as a flat line infinite charge at ~3.45 V. This behaviour was not seen in the ungraded cathodes, which suggests that the cause is due to the nature of the composite cathode. There are two potential explanations for this charge behaviour: electrolyte oxidation below that of the literature voltage limit and dendrite formation/shorting, these effects are summarised below.

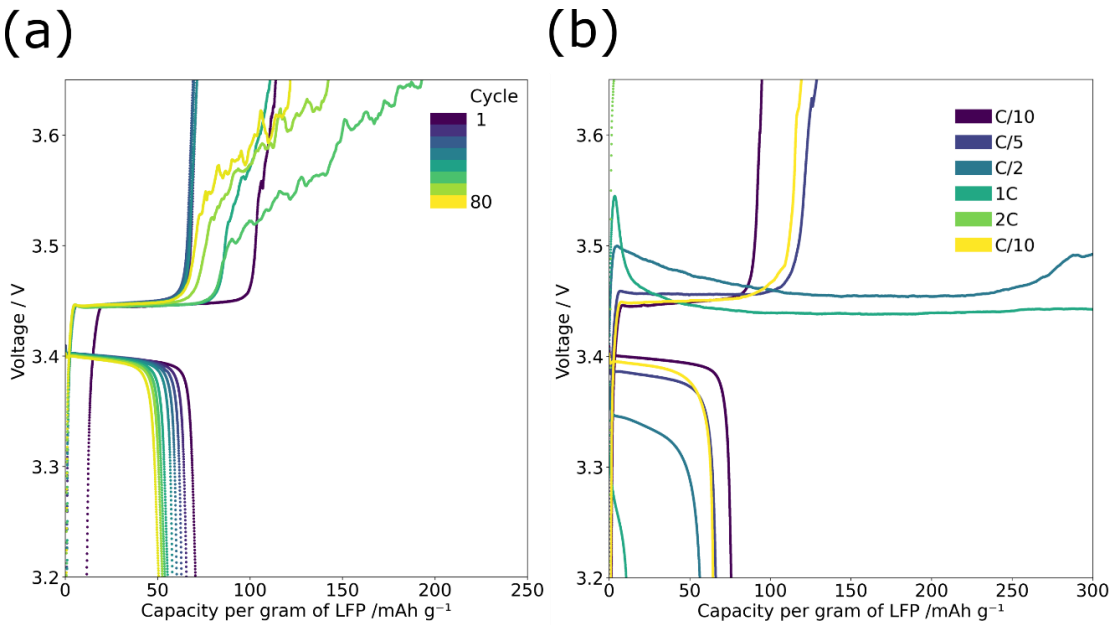

Figure 5-17: *The charge and discharge profiles of graded composite cathodes showing every 5th cycle in (a) cycle life studies at C/10 and (b) rate testing.*

5.4.9.1 Electrolyte oxidation

Despite the consensus that PEO oxidation occurs above 3.9 V which is well above higher voltage limit in this study of 3.65 V, there is some literature that supports this hypothesis of degradation. An in-depth study of PEO oxidation by Seidl et al. highlights flaws in cyclic voltammetry experiments used previously to determine the upper voltage limit and uses EIS to study resistance increases from PEO degradation. They found that oxidation initially occurs at 3.2 V with the terminal OH groups, and further degradation of the chain begins at 3.6 V which was supported by infrared spectroscopy studies.[24] This means that the infinite charge seen at high rates may be due to electrolyte oxidation as the voltage of 3.45 V is in this range. Most of the research into PEO use long chain length (600,000 M_w and above) whereas Seidl et al. use 200,000 M_w and the work reported here uses 100,000 M_w which increases the ratio of terminal OH groups and therefore the significance of the oxidation at 3.2 V. This does not explain the difference in charge profiles between the graded and ungraded composite cathodes, however. It is possible that the gradient structure places fewer LFP particles on the surface of the electrode and that this impacts the spatial distribution of the electrochemical reactions within the electrode. It is known that there is a reaction rate gradient in an electrode, based on lithium-ion diffusion, with the surface of the electrode closest to the electrolyte experiencing faster reaction rates than the material adjacent to the current collector.[268,269] When this effect is combined with the gradient of active material within the cathode it places a large current density on the few LFP particles near the surface which would raise the potential difference in these localised areas to a point at which the oxidation of PEO ensues. This effect is intricately linked to current density therefore would be amplified at higher rates; this is evident by Figure 5-17 (b) in which the effect did not appear in the cycling behaviour until C/2 when a noisy voltage profile was seen. At rates above C/2 the voltage profile changed further, and an infinite charge was recorded, this suggests that oxidation is interminable with higher current densities, due to localised potential differences. In ungraded cathodes the high Li^+ flux at the electrode surface is more evenly distributed across more particles therefore the localised potential difference may remain below the oxidation limit.

To determine the onset voltage of PEO oxidation, linear scan voltammetry studies were done on gradient composite cathode cells post rate testing, see Appendix

Figure 8-2, and no significant peaks were observed in the range of the normal battery cycling. The LSV showed a gradual increase in current from 20 mA to 500 mA between 2 V and 4 V; similar LSV studies in literature show current ranges of less than 1 mA, even at higher voltages, therefore this high current suggests a potential short in this cell despite its ability to discharge after the LSV was performed. This suggests instead that the infinite charge is not due to PEO oxidation but instead a micro-short that appears on charge; it is also possible that the high current seen here is masking any potential oxidation peaks.

5.4.9.2 Dendrite formation and micro-shorts

When manufacturing the graded and ungraded composite cathode coin cells, a considerable proportion of the graded cells shorted during the initial heating step prior to the formation cycles, this behaviour was not seen in the ungraded cells. Homann et al. study 'voltage noise failure' which they find occurs with LFP and NMC cathodes and only on charge.[26] They eliminated the possibility of electrolyte oxidation by studying the voltage that an 'infinite' plateau was observed; tests on multiple cathode materials and different PEO chain lengths found that all the cells had a significant oxidation plateau at 4.6 V vs Li/Li^+. The failure of the cells they reported on occurred randomly and at various voltages with all types of cathode material. They determined therefore that the source of the noisy charge profile is micro-shorts or soft shorts, dendrites that form weak connections between the lithium metal anode and the cathode during charge and allow for excess current to be passed without de-lithiating the cathode or raising the voltage past the experimental limits. As separating the cell to search for physical proof of dendrites is difficult, they concluded that increasing the thickness of the PEO or trading the lithium metal anode for a graphite one less likely to form dendrites would prove the existence of these micro-shorts.[26] These methods, along with others were attempted in resolving the charging issues, see Table 5-4 for the fixes and results.

Table 5-4: *The attempted fixes and subsequent results on resolving the charging issues in graded LFP/PEO composite cathodes.*

Attempted fix	**Result**
2 x thick PEO SPE	No change
3 x thick PEO SPE	No change
Graphite anode	Instant short
50% gradient	Noisy voltage, no infinite charge

2 x LLZO % in SPE	No change
Celgard Separator	Poor performance, similar to that of ungraded

In the graded composite cathode, both a thicker PEO layer and a graphite anode did not prevent the infinite charge or noisy voltage profile, with thick PEO cells performing similarly to standard thickness cells and graphite anodes shorting on manufacture. Other fixes were attempted such as a 50% gradient (reducing the intensity of the gradient by half), increasing the amount of LLZO in the electrolyte (this was a proven fix for shorting with pure PEO SPE's), and the addition of a Celgard separator as a block for dendrite formation, see Appendix Figure 8-3 for cycling results. The 50% gradient showed the same characteristics as the fully graded composite cathode, with noisy voltage profiles at rates above C/2, although no infinite charge was seen which suggests a minor improvement. Increasing the LLZO fraction showed both infinite charging alongside noisy voltage profiles and the addition of a Celgard separator merely raised the resistance to a level that prevented any usable discharge capacity at rates above C/5, showing similar results to that of the ungraded cathode with poor rate performance but no infinite charge.

The charge profile at high rates in Figure 5-17 (b) does not resemble a noisy voltage curve as seen in Homann et al. therefore it is not due to micro-shorts or dendrite formation, the long plateau is more like the oxidation profiles seen at 4.6 V vs Li/Li^+ seen in the same work. Alongside this, the inability of thicker SPE layers or additional LLZO in resolving these issues also suggests that they are not due to dendrite formation. However, many more of the graded composite cathodes shorted during or before the formation cycles and the high current seen in LSV scans on post rate testing cells suggests that the cells have shorted at least during and post charge. Both PEO oxidation and dendrite formation are issues which plague the performance and adoption of SPE-based electrolytes and have been studied in detail, and it is assumed that both effects are impacting the charge processes of the graded composite cathodes. It is interesting to note that none of these effects were seen with ungraded cathodes; it may be that partial grading of the cathode, either grading only the cathode/electrolyte interface, or the cathode/current collector interface may reduce the occurrence of

noisy and infinite charge profiles, and this may be an interesting research direction in the future.

Overall, while this is impractical for implementation of these battery types the decreased resistance and improved LFP/PEO contact are desirable qualities which lead to greater performance on discharge in both cycle life and rate-performance studies. While electrolyte oxidation and dendrite formation are issues related to the PEO system, there are potential solutions such as adding protective interlayers or coatings or by adaptation of the SPE by substitution of the terminal groups of PEO.[23] Alongside this there is much research in the literature[23–27,270–272] on other prevention methods such as adding fillers,[270] sacrificial electrolyte additives[271] and cathode coating.[272]

5.5 Conclusions

Graded composite cathodes of LFP and PEO were manufactured using spray deposition and shown to perform better than ungraded composite cathodes in both cycle life and rate performance studies. The resistance of graded cathodes was consistently an order of magnitude less than that of ungraded cathodes and it is thought that this is due to the improved cathode/SPE interface. Graded cathodes maintained good capacity after 80 cycles at C/10 whereas ungraded cathodes failed to provide any significant capacity. Graded cathodes functioned at all rates whereas ungraded cathodes provided no capacity at any rate higher than C/5.

While PEO has a limited electrochemical stability window and is hampered by dendrite formation and oxidation the gradient technique here is not limited to PEO as a material choice. This technique could be employed to a range of solid-state materials with which solid-solid interfaces are of crucial importance in optimising battery performance and lifetime. Gradient structures can remove these physical interfaces and improve connection between active material and electrolyte thus improving ion conductivity and adding resilience to volume changes within the cathode.

Chapter 6 Optimisation of Silicon Location in Through-Thickness Gradient Silicon Graphite Anodes

6.1 Abstract

Silicon boasts a high theoretical capacity and is commonly added in small quantities to commercially available graphite anodes. Upon lithiation, silicon forms an alloy and experiences substantial volume expansion, this can crack or dismantle the electrode architecture leading to loss of active material through disconnection and loss of electrolyte though SEI formation. Recent research has found that layering silicon and graphite in an attempt to contain silicon within the bulk of the electrode helps to prevent capacity degradation.[273,274] Spray deposition can therefore be used to manufacture both layered and graded silicon graphite anodes in greater detail to determine the specific location dependencies of silicon in composite anodes.

Graded silicon graphite anodes were manufactured using spray deposition to study the effect of through-thickness silicon location on cycle life. It was found that prioritising silicon placement closer to the current collector extended the lifetime of the anodes through buffering of the volume expansion of the silicon particles. To further optimise speed and cost of the manufacturing process, layered silicon graphite anodes were manufactured using a combination of slurry-based doctor blading and spray deposition. This dual technique manufacturing approach to electrode production sped up production 10 times while also providing the precision required for novel electrode design.

6.2 Background

Graphite anodes represent a low cost, conductive and long-lasting electrode for lithium-ion batteries; graphite's low surface area and chemical stability is crucial to stabilising SEI formation and extending the lifespan of the electrode. The need for higher capacity batteries and subsequent push for new cathode materials has necessitated an increase in the lithium storage capacity of the anode to match. Among the potential new anode materials are alloy-type anodes, which, unlike a graphite-type intercalation storage mechanism, form a metallic alloy with lithium upon discharge. Silicon is the most heavily researched of these alloy-type anodes and has a theoretical capacity of ~3579 mAh g^{-1} at room temperature with around

4 lithium atoms per silicon atom and a final discharge structure of $Li_{15}Si_4$; in comparison graphite can only hold 1 lithium atom per 6 carbons, leading to a theoretical capacity of 372 mAh g^{-1}.[275] Alongside this, it's abundance, ecological properties, and low redox potential[276], make silicon an ideal candidate for future anode materials.[277]

6.2.1 Challenges with silicon

Pure silicon anodes would provide the highest theoretical energy density, but they suffer from extremely poor cycle life; this is primarily due to the issue of volume expansion although the low conductivity of silicon is also a factor. Silicon, like many alloy-type anodes suffers from a large volume expansion on lithiation, up to 300%; this can cause cracks and microstructure breakdown leading to isolation of active material and subsequent capacity loss.[277] Alongside this, any change in structure would cause the formation of new electrically insulating SEI, which further isolates active material and decreases the lithium and electrolyte stock.[278] This issue can be lessened by using silicon oxides, which decreases the volume expansion to 160% but also brings down the theoretical capacity. Figure 6-1**Error! Reference source not found.** shows the crack formation of a silicon electrode during cycling, and it is clear from (c) that after just 50 cycles the electrode structure has been destroyed.

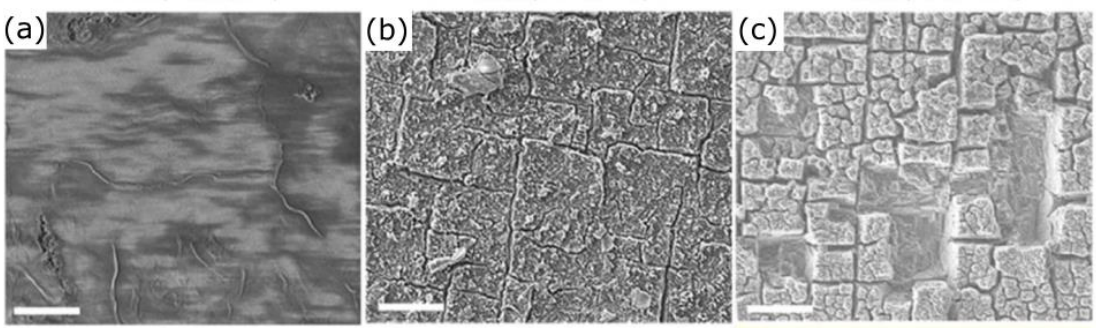

Figure 6-1: SEM images of *cracking of silicon(100) electrodes cycled between 2 V and 0.01 V at (a) 3 cycles, (b) 8 cycles and (c) 50 cycles. Scale bar = 20 µm. Reproduced from Shi et al.*[279]

As a result of the volume expansion of silicon, a composite cathode is required to withstand particle swelling and maintain the electrode structure. Silicon or silicon oxides are often combined in small ratios with carbon or graphite with a 10% mass ratio of silicon giving theoretical capacities of ~twice that of graphite alone. A balance needs to found between the capacity and the cycle life as higher

mass ratios of silicon give higher capacities but degrade faster, see Figure 6-2. Conductive carbon materials such as carbon black have a higher surface area than graphite which in turn means more area for SEI formation and therefore greater electrolyte decomposition, it also is an inactive material, whereas graphite has the benefit of contributing to the capacity while also improving the properties of the silicon. For these reasons, the use of graphite as a composite in silicon batteries remains the optimal target.

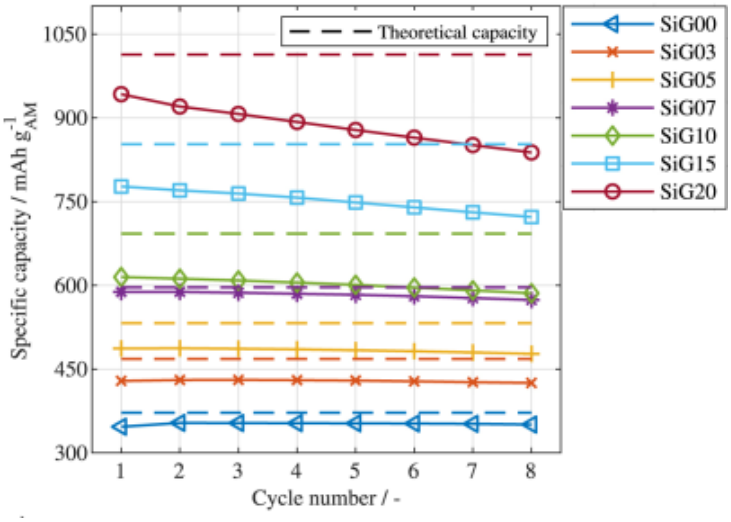

Figure 6-2: *The capacity per gram of active material per cycle of different silicon/graphite ratios, SiG00 is 0 wt% silicon, SiG03 is 3 wt% silicon etc. Reproduced from Moyassari et al.*[280]

6.2.2 Methods for improving silicon performance

While composite cathodes help mitigate the destructive effects of the volume expansion, they do not prevent them entirely; often the increased capacity of silicon is only obtainable for a few cycles before the capacity drops to either the same level or below that of just graphite. In some cases, the capacity can decrease well below that of graphite alone; Figure 6-3 shows how the capacity of a 15 wt% silicon graphite electrode decreases below that of a stable graphite electrode after ~100 cycles. This is due to a destruction of the graphite architecture with repeated expansion of silicon particles.[281]

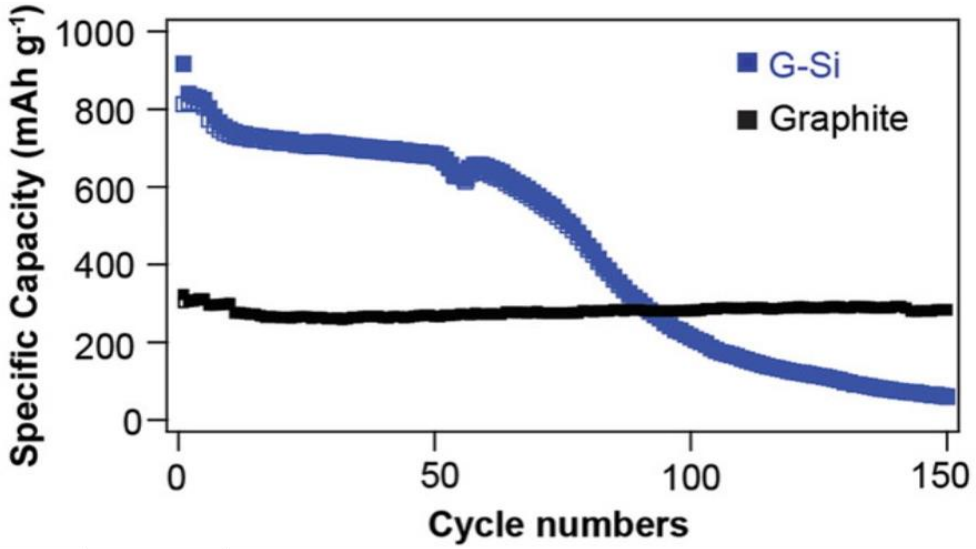

Figure 6-3: *Comparison of 15 wt% silicon in graphite and graphite electrodes in terms of capacity per gram of active material per cycle. Reproduced from Son et al.*[281]

Within silicon graphite anodes there are additional methods of stabilising silicon particles, these include: changing the design of the silicon, whether forming nanostructures or utilising silicon oxides[282]; protective coating of silicon either in core shell structures[276,283,284] or full electrode coating[274]; careful selection of binders in terms of strength and flexibility[285]; electrolyte additives to form more stable SEI layers[286] and artificial SEI manufacture.[287] When considering mitigation strategies for volume expansion, ease of manufacture must be considered as techniques that require complex methodology are unlikely to be industrially relevant.

6.2.2.1 Impacts of conductive additive

Simply mixing with graphite is not enough to ensure good cycling stability of silicon as there is poor interface adhesion between silicon and graphite which becomes particularly significant with smaller silicon particles due to a size incompatibility.[277] Carbon can act as an interface between the graphite and silicon, and, with a vast number of different carbon structures and pore sizes available the carbon additive can influence the porosity, conductivity, and flexibility of the electrode. A good example of one such structure is a Si/graphite/C particle formed by spray drying,[283,284,288] of which the methodology is shown in

Figure 6-4; this structure disperses small SiO particles in a graphite and carbon microsphere matrix.

Common carbon additives are carbon black or carbon nanotubes, which promote a decrease in electrical resistivity when compared to electrodes without added carbon.[289] The carbon type plays a crucial role dependent on its structure with carbon nanotubes found to increase electrical conductivity, whereas larger carbon black materials create porosity for electrolyte wetting and room for volume expansion.[283]

Often the carbon additive is introduced in the form of a pitch which is a material which is pyrolysed into a carbon source in situ; in the case of Figure 6-4 the pitch is asphalt.[288] The benefit of using pitch, or in some cases a sugar, is that it acts as a binder and conductive additive, and importantly, pitch is also generally much cheaper than other carbon sources.[283]

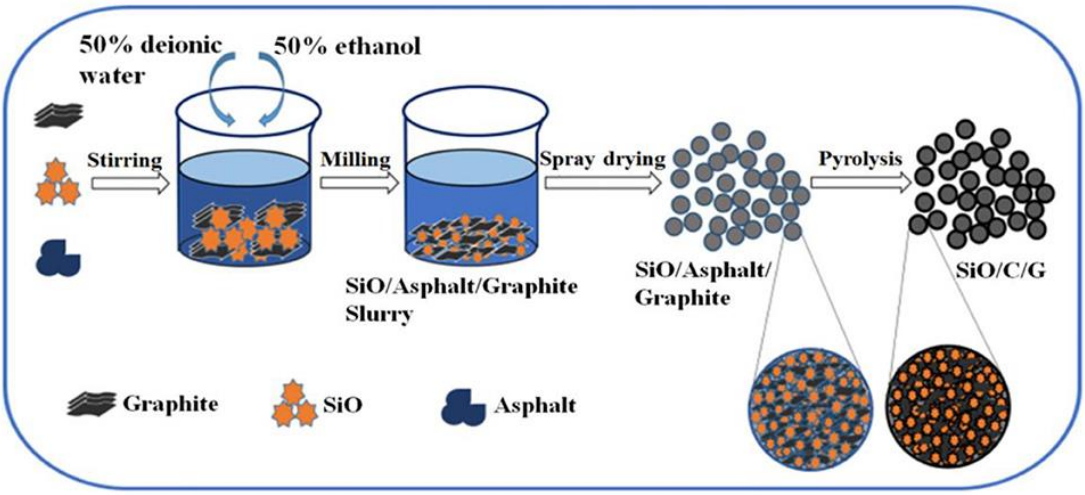

Figure 6-4: *The spray drying methodology for manufacturing Si/C/graphite particles. Reproduced from Long et al.*[288]

6.2.2.2 Impacts of binder

The binder plays a crucial role in the interconnectedness of silicon and graphite, holding the particles together and retaining the structure of the electrode despite repeated volume expansion and contraction. A binder must possess good mechanical strength, flexibility and adhesion, while also remaining compatible with current manufacture methods. While PVDF is the most common binder in traditional graphite anodes, a comparative study of four binders found that the PVDF had the lowest ultimate tensile strength and Young's modulus which translates to irreversible deformation upon silicon expansion.[285] Binder elasticity

is crucial to long lasting electrodes with the highest elastic recovery seen with low Young's moduli binders such as poly(amide imide).[285] This suggests that a binder that is both flexible and strong is needed to tackle the extreme volume expansion of silicon which has led to research into hybridisation and co-polymerisation of binders with different properties to create the optimal mechanical characteristics.[285,290] This discussion of the binder's structural and mechanical properties is disputed however with some authors claiming the binder's chemistry as the crucial aspect for long lasting silicon. Figure 6-5 shows a comparison of CMC and PVDF-based binders in graphite and silicon graphite anodes. Whereas PVDF performs better in graphite only anodes, when silicon is introduced a severe loss of capacity is seen in the first few cycles, representing a destruction of the anode, CMC on the other hand shows a greater stability in silicon containing anodes; this is thought to be due to a chemical bond between the CMC and the silicon.[291]

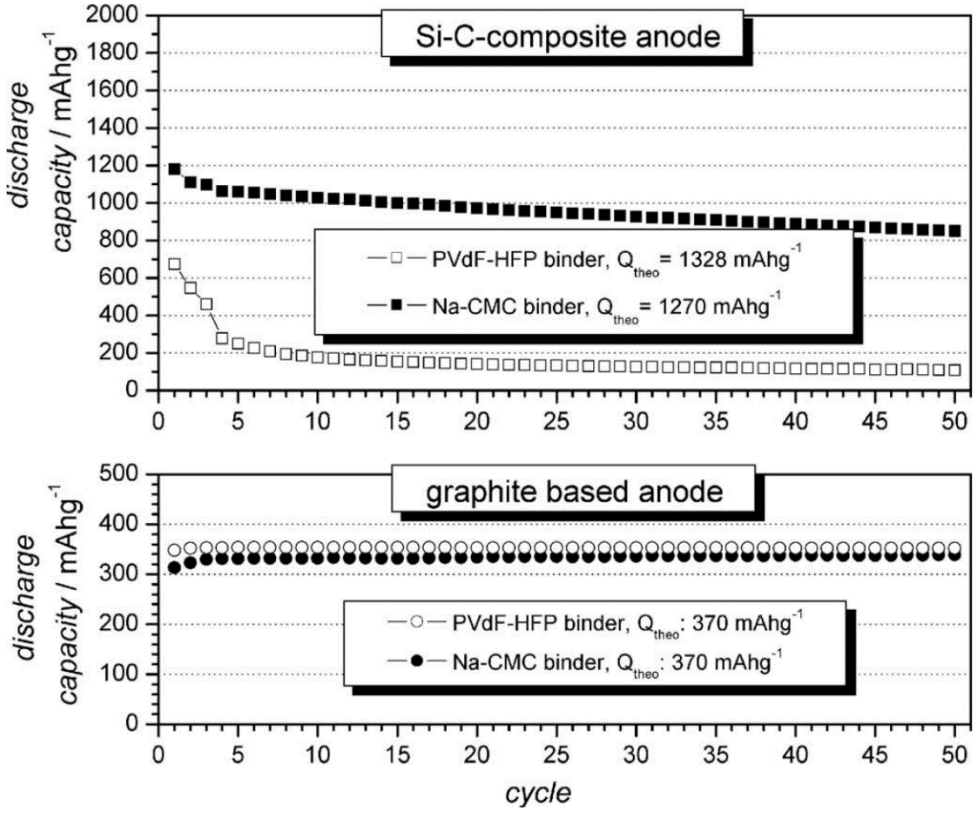

Figure 6-5: *A comparison of PVdF and CMC binders in Si-C and graphite anodes in terms of discharge capacity per cycle. Reproduced from Hochgatterer et al.*[291]

6.2.2.3 Impacts of the electrolyte

With repeated expansion and structure change comes constant SEI disruption and exposure of new electrode surface; the formation of new SEI consumes lithium and electrolyte and causes increased electrical resistance in the electrode leading to isolation of active material. Electrolyte additives such as fluorinated ethylene carbonate (FEC), propylene carbonate (PC) and vinyl carbonate (VC) can assist the formation of a more stable SEI layer.[292] The SEI is formed of a mix of organic and inorganic compounds, but it is thought that the inorganic compounds adhere more weakly to silicon, therefore making them less likely to sustain damage during volume expansion. $LiPF_6$ was found to reduce into a LiF-based SEI more readily in ether-based solvents which reduced overpotentials during cycling, which are a sign of a more stable SEI, and cells with ether-based electrolyte retained 80% capacity after 100 cycles compared to 4.5% capacity retention with traditional EC/DMC-based electrolyte.[293] Whether silicon is directly in contact with the electrolyte is crucial to SEI formation; coating of silicon particles with carbon showed different differential capacity curves compared with bare silicon due to the separate SEI reactions. These carbon coated silicon electrodes had 12% less irreversible capacity loss in the first cycle due to improved SEI formation.[294] Other methods of SEI stabilisation include the formation of artificial siloxane networks which form directly on the silicon surface to protect it.[293]

6.2.3 Electrode structure

The ionic and electronic conductivity throughout an electrode is not homogenous; the electronic conductivity reduces with increased distance from the current collector, and poor electrolyte wetting and long lithium diffusion pathways further from the surface of the electrode decreases ionic conductivity.[295] Because of this, the local lithium-ion concentration varies throughout the electrode and is highest at the electrode-electrolyte interface. For silicon on the surface of the electrode, this implies that both the SEI formation and volume expansion will be faster, causing disintegration of the silicon particles alongside an unstable SEI. Silicon that is set in the bulk of the graphite should be more protected as the graphite helps to buffer the volume changes and limit the electrolyte contact. Simply removing the silicon from the surface would decrease the overall capacity of the cell, whereas a gradient throughout the electrode would offer the benefit of

retaining maximum silicon content while removing the 'at risk' silicon particles. This idea has been realised in the form of layered structures which manufacture different regions of either Si-graphite or graphite on top of each other. These studies found that the optimal performance was with a sandwich structure in which the middle of the electrode, containing silicon, was sandwiched between two graphite or carbon only layers.[273,274] These studies differ in the manufacture approach using either thin-layer doctor blading[273] or spray deposition[274] but show comparable results. Figure 6-6 shows the rate and cycle life performance of spray deposited (a) and doctor bladed (b,c) layered Si-C electrodes. The clear difference between the two is the capacity at low C-rates/current densities; the doctor bladed electrodes are a composite of silicon and graphite whereas the spray deposited ones are silicon and carbon black which have a much lower ratio of active material and therefore a lower capacity. Homogenous/blended electrodes show the poorest performance in both capacity and rate capability and sandwich structures show the best performance. In (a) however, the sandwich structure starts with the highest capacity but then drops below that of the Top C structure after ~70 cycles; therefore, the optimal layer orientation is not entirely clear.[273,274]

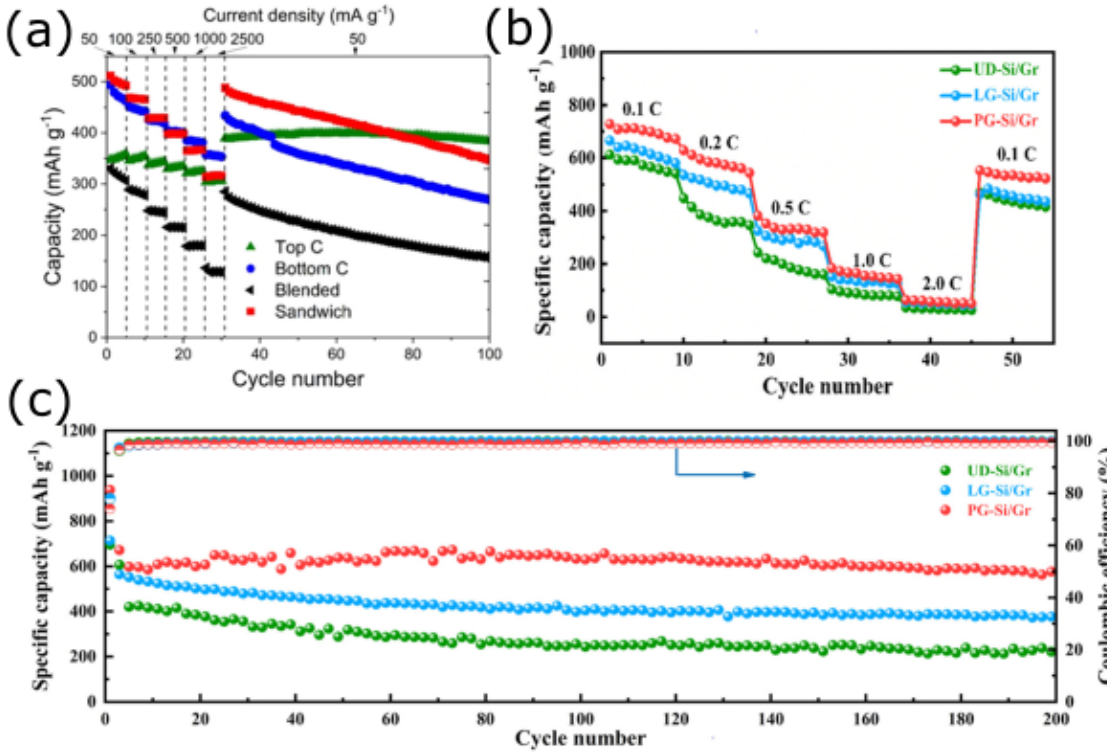

Figure 6-6: *Comparison of layered silicon-C electrodes in rate capability and cycle life studies. (a) spray deposited layered electrodes of silicon and carbon*

black at different current densities, the legend refers to the location of the carbon only layer, with sandwich indicating a silicon containing layer between two carbon layers. Reproduced from Huang et al.[274]*; (b, c) doctor bladed layered silicon-graphite electrodes with UD-Si/Gr representing a homogenous mix of silicon and graphite; LG-Si/Gr representing silicon layer near the surface of the electrode; PG-Si/Gr representing the sandwich structure with silicon in the middle. (b) is the rate capability of these cells, and (c) the cycle life at 0.2C.*

6.2.4 Literature summary

The research in this chapter aims to further the concept of layered silicon/graphite electrodes by spray depositing true gradients into the anode in different combinations, building on the layered Si/C electrodes manufactured previously by Huang *et al*.[274] The concept of containing the silicon within the bulk of the electrode shows promise in extending the life of the silicon while the use of graphite rather than carbon as a silicon host allows for maximised active material content and a lower surface area for SEI formation. Spray deposition can be used to manufacture full true gradient anodes without the need for toxic chemicals or multi-step manufacture. By elucidating the optimal silicon configuration in the electrode, current high performing silicon nanomaterials can be improved further through a simple change in manufacturing process thus pushing the technology forwards towards high capacity, long lasting silicon containing anodes.

6.3 Methodology

Graphite dispersion and binder-related film properties were studied using optical microscopy. Silicon graphite anodes were manufactured using a combination of spray deposition and doctor blading. Coin cells were then assembled and tested for cycle life performance. Silicon graphite electrodes were characterised using a combination of optical microscopy and SEM EDX.

Ultrasonic spray deposition was used to manufacture graded silicon graphite, to add thin silicon layers onto doctor bladed graphite anodes as well as in graphite dispersion mass measurements. In all cases, dispersions of graphite and/or silicon in a water/IPA solvent was spray deposited onto a substrate, this was either copper foil for anode manufacture, commercial or in-house slurry casted

graphite anodes when manufacturing layered silicon graphite anodes or a small petri dish when performing mass measurements.

Chemicals and materials used in the manufacture of silicon graphite electrodes were: 15 µm graphite (Artificial graphite for battery anode, MTI), 5 µm graphite (xGnP M-5 graphene nanoplatelets, XG sciences), silicon nanopowder (<100 nm, >98% trace metals basis, Sigma Aldrich), CMC binder (sodium carboxymethylcellulose, Sigma-Aldrich), styrene-butadiene rubber (SBR, BM-451B, TOB Machine), IPA (isopropyl alcohol, Sigma Aldrich, carbon black (Super C65, C-NERGY Imerys) and DI water. Additional binders used for the binder study were tannic acid (Sigma Aldrich), polyvinylpyrrolidone (PVP, M_w ~1,300,000, Sigma Aldrich), Poly(3,4-ethylenedioxythiophene) polystyrene sulfonate (PEDOT:PSS, high conductivity grade, 3.0-4.0% aqueous dispersion, Sigma Aldrich), Polyacrylic acid (PAA, M_V 1,250,000, Sigma Aldrich) and polyvinylidene difluoride (PVDF, Solef, Solvay Specialty Polymers). Additional chemicals used for doctor blading of graphite anodes were battery grade graphite (S360 E-3, BTR) and Super C45 carbon black (C45, MSE supplies).

Electrodes for the binder study were manufactured using a single solution and single nozzle spray using a mixed silicon/graphite/carbon black/binder solution. The ratio of materials in the solution were: 15 µm graphite; 0.7, silicon; 0.1, carbon black; 0.1, binder; 0.1. Solutions were 1 mg mL^{-1} and were sprayed onto copper foil (10 µm thick, Targray) over 100 passes at a flow rate of 1 mL min^{-1}, shaping air of 1 psi and substrate temperature of 150 °C.

To manufacture graded silicon anodes, two spray solutions were used alongside two nozzles and associated syringe pumps: a 10 mg mL^{-1} 5 µm graphite/carbon/binder solution and a 1 mg mL^{-1} silicon/carbon binder solution. Both solutions were manufactured to be 0.8/0.1/0.1 ratio by mass of active material/binder/conductive carbon, respectively. These were sprayed simultaneously onto the same area using rotated nozzles. The total flow rate of the two solutions was 0.5 mL min^{-1}; for mixed/homogenous silicon graphite electrodes the flow rates of the two solutions were fixed at 0.25 mL min^{-1} for the duration of the spray, for graded silicon graphite electrodes the flow rates increased/decreased in a stepwise fashion between 0 mL min^{-1} and 0.5 mL min^{-}

[1]. Solutions were spray deposited onto copper foil at an area of 25 cm^2 shaping air of 1 psi and substrate temperature of 150 °C.

Graphite dispersion studies were performed using 10 mL of 1 or 10 mg mL^{-1} graphite (5 µm and 15 µm) in different solvents: DI water/IPA, acetonitrile (ACN, 99.9%, Sigma Aldrich), N-Methyl-2-pyrrolidone (NMP, 99.0%, Sigma Aldrich). Prior to spray deposition and some graphite dispersions studies, solutions were sonicated using a sonic horn (Fisherbrand 505) at a power of 40% and a pulse rate of five seconds for 10 minutes.

For combined spray and slurry coating layered silicon graphite studies, 1 mg mL^{-1} silicon/binder/carbon solution was spray deposited onto either commercial graphite-based anode sheets (LiFUN), or homemade graphite anodes. For deposition onto commercial anodes, the silicon solution was spray deposited at 0.5 mL min^{-1} for between 10 and 40 passes at a substrate temperature of 150 °C and shaping air of 1 psi. For manufacture of graphite anodes a 49.5 wt% slurry with materials ratios of BTR graphite; 0.9525, C45; 0.01, CMC (3 wt% in water); 0.015, SBR; 0.0225 and DI water, was mixed in a non-planetary centrifugal mixer (Thinky ARE-250, Intertronics) at 500 rpm for 7 minutes and 2000 rpm for 15 minutes. After mixing the slurry was doctor bladed onto copper foil using an (Elcometer 3600/4) and draw down coater (Elcometer 4340) and dried on a hotplate at 60 °C for at least 1 hour.

All anode films were cut into 12 mm diameter electrodes and dried under vacuum at 80 °C before being transferred into an Ar-filled glovebox.
Coin cells were manufactured according to Figure 6-7 using CR2032 coin cell parts (Hohsen). One 1 mm thick stainless spacer and a 0.12 mm thick 14 mm diameter lithium disk (Goodfellow) anode were used alongside a 19 mm diameter Celgard separator. 100 µL of electrolyte (1 M $LiPF_6$ in a solvent consisting of a 30 : 70 wt% ethylene carbonate : ethyl methyl carbonate mixture with 2 wt% vinylene carbonate, E-Lyte) was added onto the separator and the cells were crimped using a hand crimper (Hohsen).

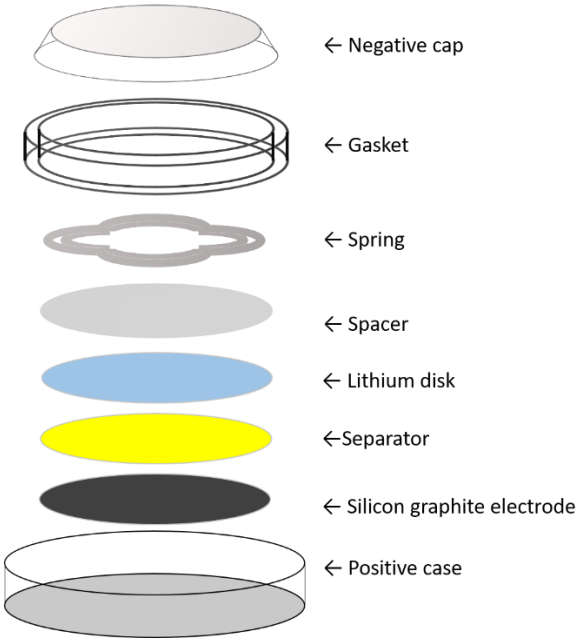

Figure 6-7: *Schematic showing the construction of the coin cells used for silicon graphite anode experiments.*

Cells were tested on a BCS-805 battery cycler (BioLogic) and were first left to rest for 2 hours, then subjected to two formation cycles at C/20 or at a current of 100 µA with charge and discharge limits of 1.5 and 0.01 V vs OCV respectively; cells were rested for 1 hour between each charge and discharge. Cells were then tested for cycle life at C/10 or at a current of 200 µA.

Characterisation of the graded silicon electrodes was done using SEM EDX. The magnification was set to 1056 x and the accelerating voltage was 10 kV. Graphite dispersion studies were performed using a Dino-Lite AM7515MT1A Digital Coaxial Illumination Microscope at a magnification of 115 x. Binder studies optical microscopy was done using a Keyence VHX-7000 at a magnification of 80 x.

6.4 Results

6.4.1 Binder studies

Multiple different binders have been suggested as beneficial for silicon stability; these include tannic acid[296], PVP[297–299], CMC[297,300], PEDOT:PSS[297], SBR[301], PAA[302] and PVDF[303]. As so many studies differ on which binder is optimal for silicon graphite electrodes, it is likely that the manufacture method is crucial in determining the binder's functionality. Spray deposition is not a common method of graphite electrode manufacture therefore the optimal binder material is even

more uncertain. To elucidate this, some of the commonly used binders were tested with 10% silicon graphite electrodes manufactured using spray deposition. The electrodes were all manufactured using battery grade graphite of size 15 µm and nanosize silicon, with either 10 wt% or 20 wt% of binder. It is clear from the optical microscopy of the films in Figure 6-8 that the binder effects the macrostructure of the electrode. Figure 6-8 shows varying structures from cracked and peeling electrodes with CMC and PVDF binders, to pitted structures with CMC/Sbr, PAA and tannic acid. Only PVP and PEDOT:PSS binder-based electrodes showed fully homogenous film structures. The cracking and peeling of CMC and PVDF-based electrodes suggest poor adhesion of the binder to both the silicon/graphite mix and the current collector, whereas the pitted structures may be due to the bi-solvent effect of preferential binder solubility in either water or IPA which can cause the formation of through-thickness pores.[104] In this case the binder may be localised to IPA and the remaining water droplets deposit disconnected material which can be blown away by the next spray pass.

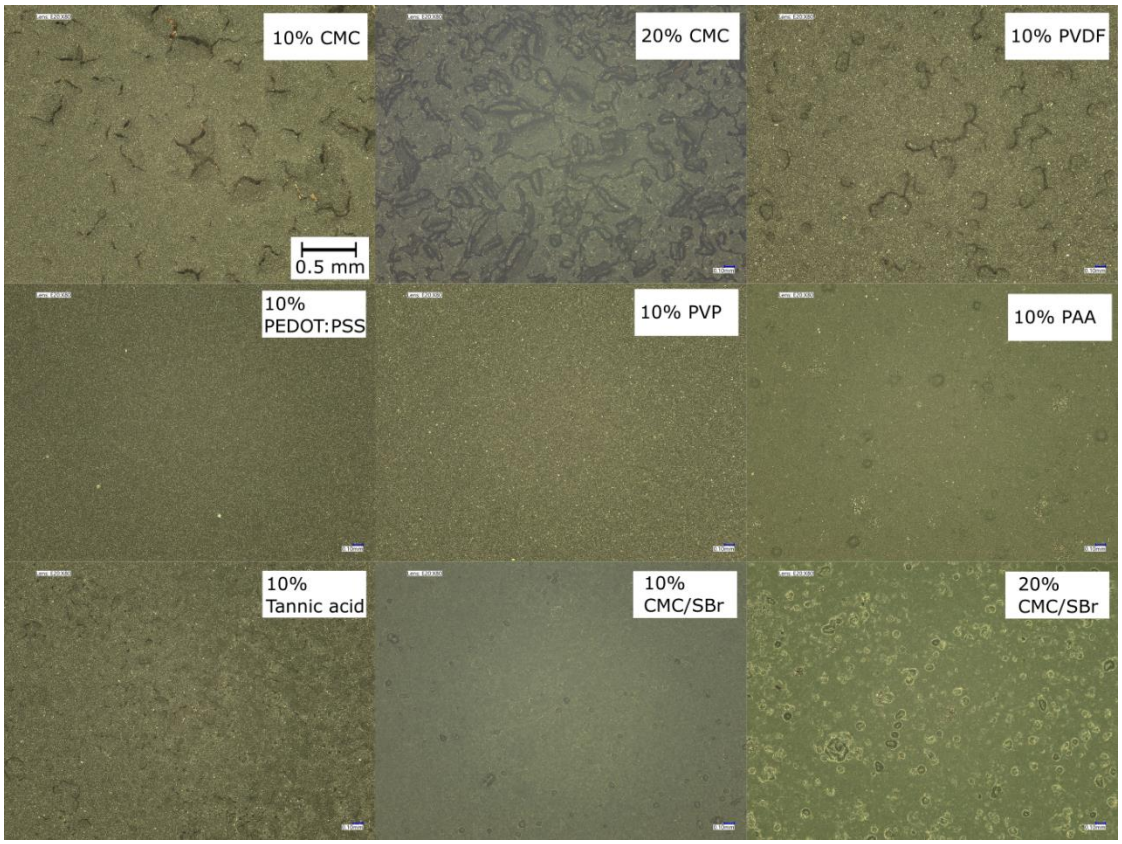

Figure 6-8: *Optical microscopy images of 10 wt% silicon graphite anodes with different binders and binder ratios.*

Figure 6-9 shows the cycling data of the 10% silicon graphite anodes with the different binders. The theoretical capacity of graphite is 372 mAh g^{-1} and the sample with no silicon remains steady at ~300 mAh g^{-1} for 100 cycles after an initial higher capacity in the first cycle due to SEI formation. Most of the silicon containing anodes have an initial capacity that is exceptionally high (up to ~1200 mAh g^{-1}) when compared to its theoretical capacity of (512 mAh g^{-1}), suggesting good utilisation of silicon and potential side reactions such as SEI formation during formation. Within 100 cycles all the silicon containing electrodes lose capacity to a point much lower than pure graphite, due to silicon expansion and destruction of the electrode framework.[281] The only binders to show capacity higher than that of graphite after 10 cycles were 10% tannic acid and 10% CMC/Sbr which both showed a pitted structure. 10% CMC/Sbr shows an unstable capacity that rose from ~400 mAh g^{-1} to ~800 mAh g^{-1} after 25 cycles which is a behaviour seen in multiple studies and is assumed to be due to reorganisation of material within the electrode which randomly reconnects silicon particles with the conductive matrix thus initiating a heightened capacity. A subsequent degradation of the electrode structure is seen between cycles 25 and 50 which demonstrates the destruction of the electrode architecture. Based on the performance of the electrodes in the binder study, 10% CMC/Sbr was taken to be the optimal binder for studying gradient silicon graphite anodes and is the binder used in all further studies.

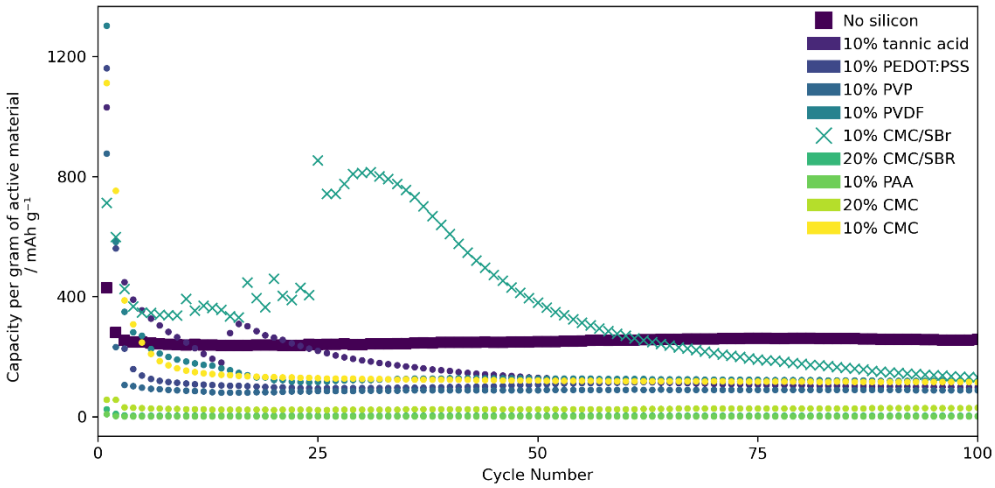

Figure 6-9: *The discharge capacity per gram of active material of 10% silicon graphite anodes with different binders, cycled at C/10 of the theoretical*

capacity. Sample with no silicon has 10% CMC/Sbr binder. The first two cycles are at C/20.

6.4.2 Graphite dispersion

A key feature of the capacity seen in Figure 6-9 is that many of the silicon containing electrodes failed to provide any significant capacity even in the first few cycles, this is unusual as if the silicon is not active, and the graphite should still provide a baseline capacity of ~300 mAh g^{-1}. This lack of active graphite cannot be blamed on destruction of the electrode architecture due to silicon expansion either, as the silicon has also remained inactive. This suggests that there was an issue with the graphite in spray deposited electrodes. To test this, each component was spray deposited individually into a petri dish and the mass of deposited material was compared to the expected mass. The first 5 dual bars of Figure 6-10 (as indicated by the blue square) demonstrate the expected versus actual deposited masses of the graphite (15 µm size), conductive carbon, silicon, and binder. While there are some small losses of material with the silicon and binder due to disrupted spray shape and large nozzle-substrate distance, there is almost no graphite being deposited which cannot be explained away by normal manufacturing losses. Graphite is particularly difficult to disperse in solutions, and often researchers resort to exfoliating graphite into graphene in order to suspend it.[304] On further inspection it was found that the graphite was sedimenting in the syringe input and was therefore not entering the spray system, leaving films of only silicon, carbon and binder which would have a theoretical capacity of 3579 mAh g^{-1} of active material. To study this further a microscope system was used to study the settling of graphite in different solvents.

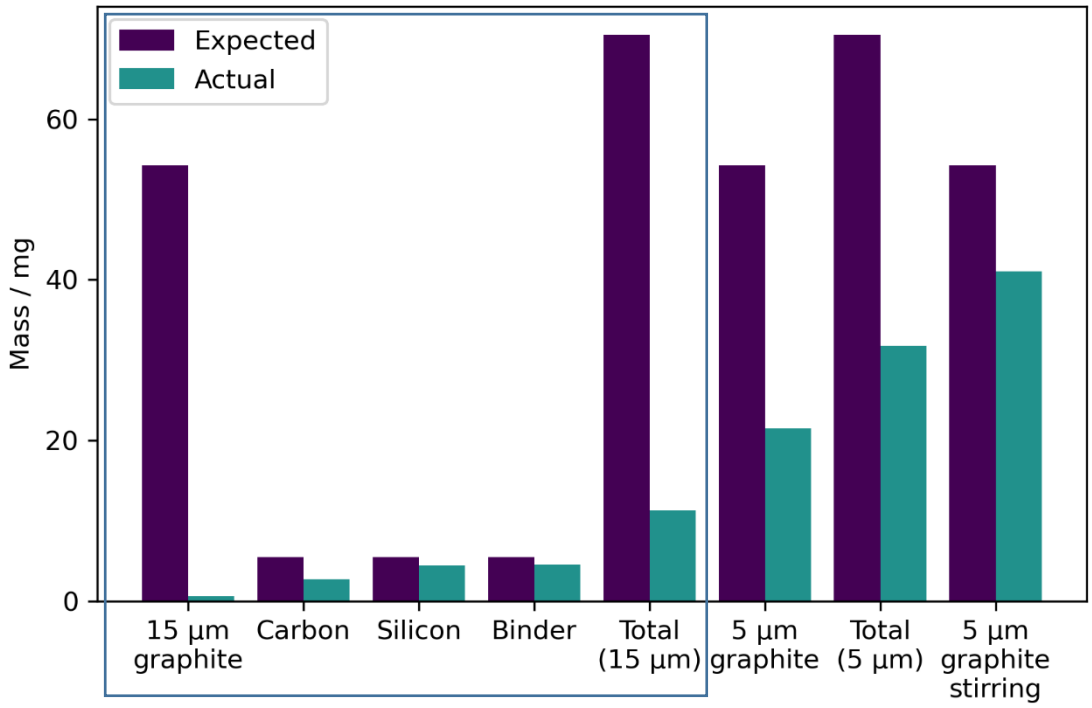

Figure 6-10: *Bar chart of expected and actual mass of anode components after spray deposition. Blue square showing the individual components and total used for the binder studies. Total indicates all components (carbon, silicon, graphite, and binder).*

Figure 6-11 shows the sedimentation of graphite in different solvents; it is clear from (a) and (b) that in 1:1 DI water:IPA by volume a 1 mg mL^{-1} dispersion of graphite settles very quickly with the sediment layer growing from 0 mm to 0.7 mm in 4 minutes. For slurry-based coating methods the solvent of choice is usually NMP or acetonitrile (ACN), (c) shows the sediment build-up of 1 mg mL^{-1} graphite in these solvents and in low concentrations they form worse dispersions of 15 µm graphite. When sonicated it was found that the sedimentation layer formed at the same speed or quicker which was unexpected, but the solution remained black after leaving for an hour, whereas without sonication it became clear and fully sedimented. This is due to sonication induced graphite exfoliation which forms more easily dispersible graphene. Methods of better dispersing graphite include exfoliation into graphite or the addition of surfactants, however this would both reduce the effectiveness of lithium intercalation between individual graphene layers and incorporate additional non-active materials into the electrode structure.[305]

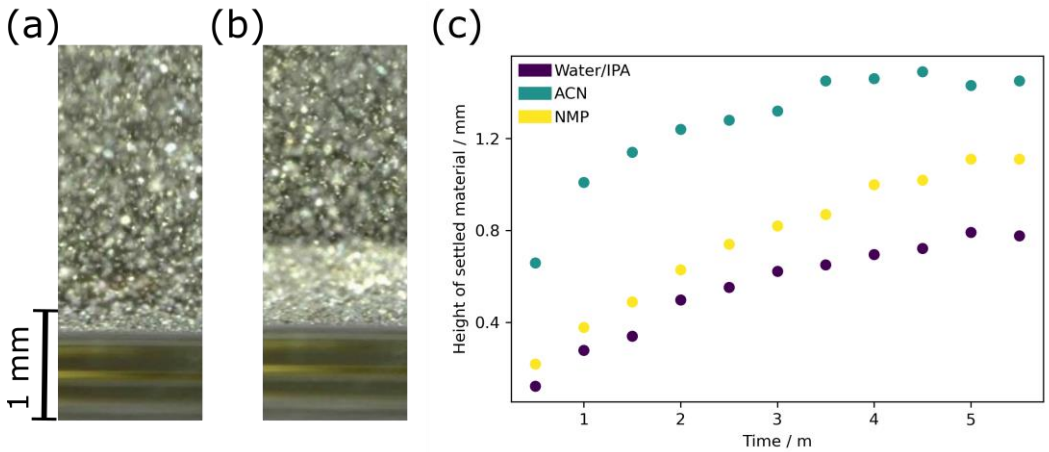

Figure 6-11: *The sedimentation of 15 µm graphite in different solvents with: (a), (b) showing the growth of the sediment layer of 15 µm graphite at 1 mg mL^{-1} in 1:1 DI water:IPA by volume after 30 seconds and 4 minutes, respectively. (c) shows the growth over time of 15 µm graphite sediment in DI water, ACN and NMP.*

The graphite used in this study is 15 µm diameter which is particularly large for dispersion in solution, from practice it has been noted that particles above 1-2 µm diameter cannot be dispersed. To study the effect of particle size, 5 µm graphite particles were tested in the same dispersion tests. It was found that the density of these particles was so low that at higher concentrations of 10 mg mL^{-1} the solution forms an equilibrium of partially sedimented graphite; although this does compact over time it was a significantly lower sedimentation speed than with large diameter graphite. Figure 6-12 shows the syringe and tubing of with different concentrations of 5 µm graphite. (b-d) show the tubing with 1, 3 and 10 mg mL^{-1} graphite concentrations, respectively. These show that clearly the graphite is now dispersed well enough to enter the tubing more easily than the 15 µm graphite, and the 10 mg mL^{-1} (d) tubing clearly showed movement of the graphite particles at a flow rate of 0.5 mL min^{-1} and minimal deposition of graphite inside the tubing. This is thought to be due to the low density of the graphite which allows it to flow with the solution even with low flow rates. Figure 6-10 shows the expected and actual mass recorded after spray with 5 µm graphite; there is a marked increase in actual mass recorded of graphite in both the graphite only and total studies, demonstrating the better dispersive properties of the smaller graphite particles.

Figure 6-12 (a) shows the syringe during the total (5 µm graphite, carbon, silicon, and binder) study, and a separation of the materials can clearly be seen with a lighter brown colour appearing nearer the top of the syringe and more black material near the bottom. The silicon (lighter brown material) disperses very well in water/IPA whereas the graphite settles causing the two materials to separate out in the syringe. When a stirring function was added to the syringe the actual mass of graphite deposited was increased again, see the final bar in Figure 6-10. For these reasons, for all experiments involving the spray deposition of graphite onwards, 5 µm graphite was used, alongside a stirring syringe, to ensure that the actual mass deposited is as close to the expected as possible.

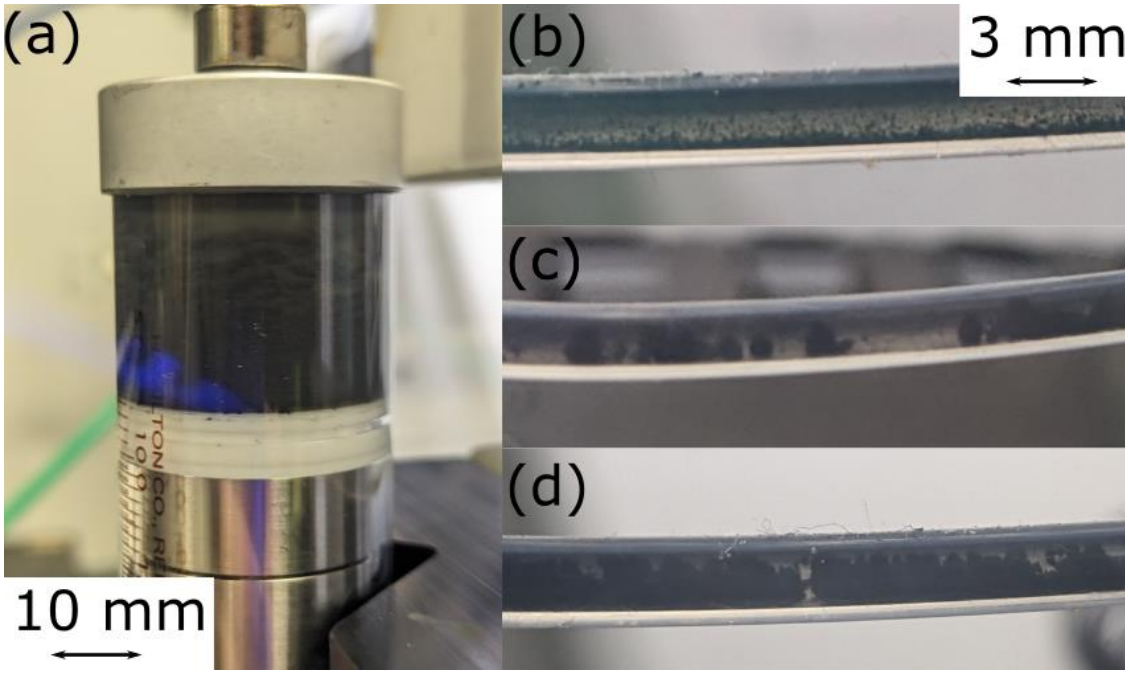

Figure 6-12: *(a) The separation of silicon and carbon without stirring in the syringe. (b-d) The solution flow tubes at different concentrations of 5 µm graphite at different concentrations and a flow rate of 0.5 mL min^{-1}. (b) 1 mg mL^{-1}, (c) is 3 mg mL^{-1}, (d) is 10 mg mL^{-1}.*

6.4.3 Gradient silicon graphite electrodes manufactured using spray deposition

Using the methodology explained previously, silicon gradients were manufactured into graphite electrodes using a one-step spray deposition process. The specific placement of silicon within the electrode may provide protection of the electrode macrostructure by prevention of architecture breakdown due to the expansion of silicon. In order to study the optimal

placement of silicon within the electrode, three different structures were manufactured: a homogenous 10 wt% mix of silicon nanoparticles in a graphite electrode, a gradient from 20 wt% of silicon at the base of the electrode to 0 wt% at the surface, and a gradient from 0 wt% silicon at the base of the electrode to 20 wt% at the top. Figure 6-13 shows the EDX and associated cross section SEM image of these three structures. The EDX in (a) and (c) show clearly an increase in silicon at the base/surface of the electrode respectively, with peaks between 30 and 40 hits, whereas (b) shows a relatively consistent hit count for silicon of around 20 throughout the thickness of the electrode. SEM EDX is a very precise measurement, with the line in the SEM images showing the location of EDX measurement, due to this the results can be quite dependent on the specific points chosen, therefore the EDX plots shown here do not show a perfect gradient but do show the general trend of the entire electrode.

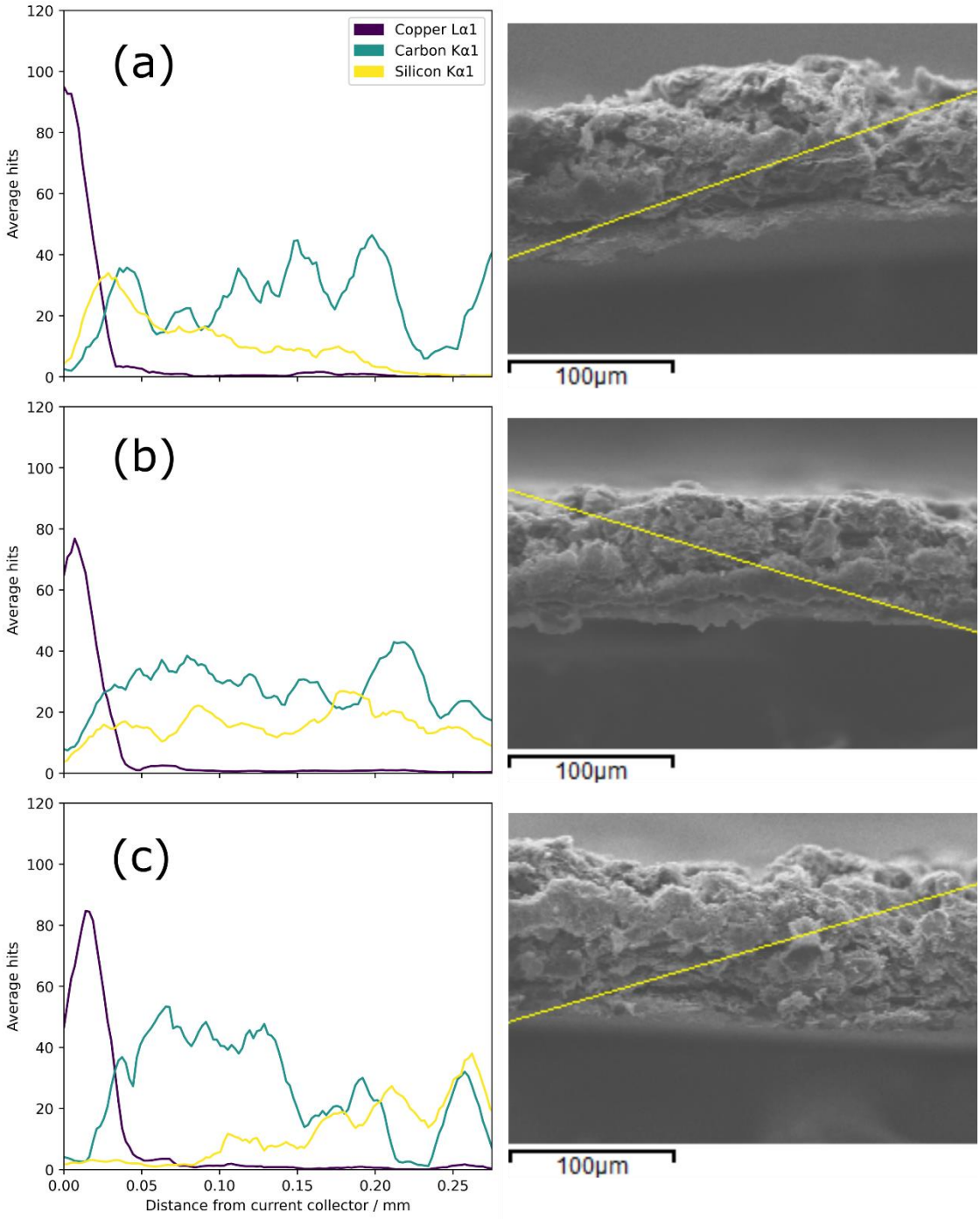

Figure 6-13: *The EDX hits and associated SEM image with EDX measurement line of silicon, carbon and copper through the thickness of graded silicon electrodes with (a) bottom graded silicon, (b) ungraded silicon and (c) top graded silicon.*

6.4.4 Performance of graded silicon graphite and silicon carbon electrodes.

Spray deposited graded silicon graphite electrodes were tested at a rate of C/10 of their estimated theoretical capacity. Two different thicknesses were manufactured, thin electrodes comprised of 10 spray passes and were 50 µm

and thick electrodes comprised of 20 spray passes and were 100 µm. To further study the effect of placement of silicon, electrodes were manufactured replacing the graphite with carbon black, which is inactive in terms of lithium intercalation and therefore removes the additional capacity of graphite from the results and allows for less convoluted analysis. Figure 6-14 shows the mean capacity per cycle of graded silicon/graphite and silicon/carbon electrodes in three different silicon configurations: silicon content increased near the base of the electrode – Bottom, a homogenous mix of silicon throughout the electrode – Mixed, and silicon content increased towards the surface of the electrode – Top, as demonstrated in Figure 6-13.

In all three electrode designs, the Si Bottom electrode recorded the highest capacity with Si Top performing the worst over 80 cycles. The thin Si/graphite electrodes provided higher capacity per gram of active material, suggesting that increasing the thickness of the electrode reduces the silicon/graphite utilisation, which is a well-known issue for battery electrodes. The silicon/carbon electrode removes the influence of the graphite on the cycling performance, and the Si Bottom configuration remains the best performing, indicating that the placement of silicon is key in determining both utilisation and stability during cycling. It is thought that the Si Bottom structure prevented the internal stress/strain caused by silicon volume expansion which minimised cracking and disintegration of the electrode architecture.[273] The surface covering of carbon above the silicon acts as a mechanical buffer preventing full disconnection of silicon and breakdown of the carbon/graphite matrix.[274]

The capacities of the first few cycles is especially high, reaching ~ 1200 mAh g^{-1} in the Si/graphite electrodes and ~ 800 mAh g^{-1} in the Si/carbon electrodes. This is primarily due to solid electrolyte interface formation on both the graphite and silicon material surfaces, consuming electrolyte and lithium in an electrochemical reaction.[306,307] Alongside this, irreversible reactions during the oxidation of silicon can elongate the first few discharge profiles.[308] The discharge plots of the 1st, 2nd and 5th cycle in Appendix Figure 8-4 demonstrate a long plateau at ~0.2 V that shortens as the cycle number increases, indicating the effects of these two influences on the initial cycling behaviour of silicon/graphite anodes.

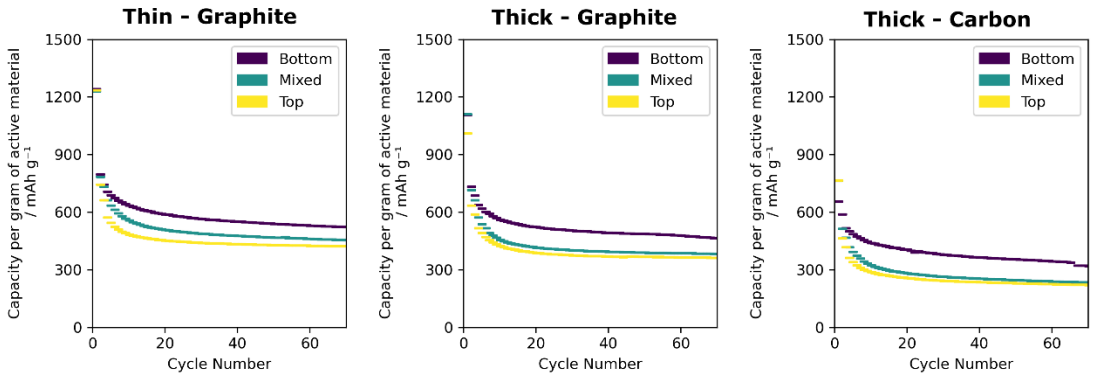

Figure 6-14: *The mean cycle life (C/10) performance of spray deposited graded silicon graphite and silicon carbon electrodes. Each plot shows the mean performance of cells that have been graded with either silicon near bottom of the electrode, a homogenous mix of silicon throughout the electrode, or silicon near the top. The three plots are indicated as to whether the electrodes were thick or thin, and whether the electrode was silicon/graphite or silicon/carbon.*

There was considerable variety in the repeatability of the cycling results seen with the graded silicon/graphite electrodes, particularly with the thin electrodes. Figure 6-15 shows the minimum, maximum and mean capacities recorded over 5 repeats of the thin and thick graded Si/graphite electrodes. There is a disparity of ~400 mAh g^{-1} between the minimum and maximum capacities in the thin Si Bottom anode, and ~200 mAh g^{-1} difference in the thick Si Bottom anode. Similar differences occur in both the Si Mixed and Si Top anodes, demonstrating that with a thin electrode of 50 µm and large graphite particle sizes (5 µm) there is less certainty and reliability in the designing and manufacturing of a graded electrode. It is likely that due to the large size of graphite particles, the thin electrodes varied considerably in structure and specific placement of silicon, therefore there was a wide range of useable capacity and degradation. When thickness was increased to 100 µm this variability was reduced, the thick electrodes were manufactured using 20 spray passes compared to 10 passes for the thin electrodes; each pass may not be entirely even therefore homogeneity is built up by manufacturing electrodes over many passes, this is most likely the explanation for differences in reproducibility between the thin and thick electrodes. There were variations in the repeatability of electrodes between the three gradient structures also, with the homogenous mix design providing the

smallest range, and Si Bottom providing the largest. It is likely that the high concentration of silicon (20 wt%) near the current collector is the cause for this variability in capacity, these areas will be much more dependent on graphite architecture and more sensitive to subtle changes between electrodes. The homogenous mix electrode has a consistent 10 wt% of silicon, therefore there is more resilience to electrode differences.

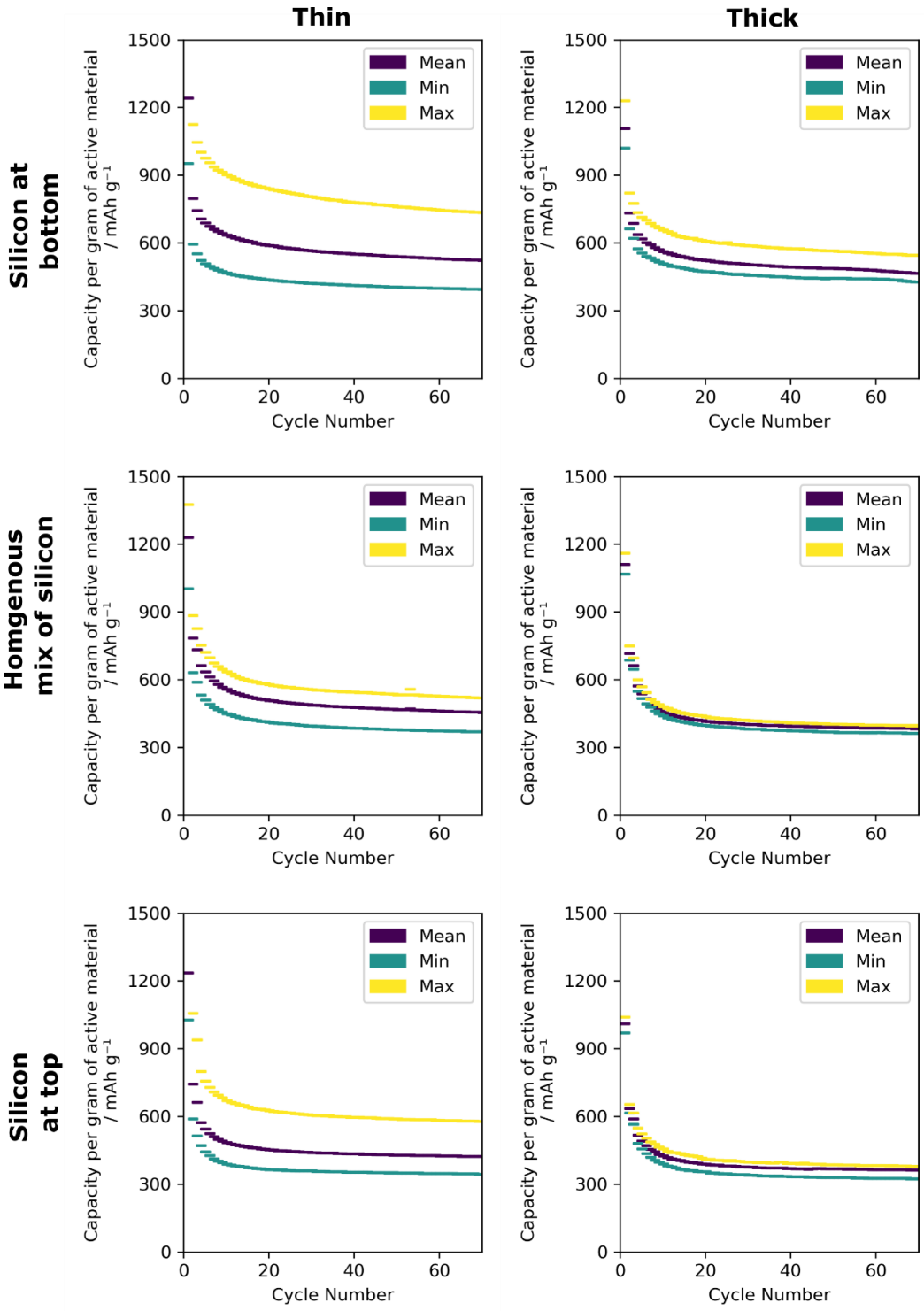

Figure 6-15: *The minimum, maximum and mean capacities recorded for graded silicon/graphite cells during cycle life testing at C/10. The two columns indicate whether the electrode was thin or thick, and the rows dictate the type of gradient.*

This work demonstrates the location specific nature of silicon performance, which is a known phenomenon in the literature.[273,274,295] While previous research has

focussed on the deposition of discrete silicon layers, here, true gradients are manufactured throughout the electrode in a one-step deposition process. It is shown that, much like in layered films, embedding silicon deeper into an electrode protects the silicon from the high Li^+ concentrations seen at the anode surface, preventing degradation upon excessive volume expansion.[274] This work builds upon the layered Si/C spray deposited anodes manufactured by Huang *et al.* by demonstrating the performance of graded rather than layered electrodes, and by successfully spray depositing graphite, thus increasing the overall energy density of the anode.

6.4.5 Combining spray deposition with slurry coating for Si/graphite electrode manufacture

Spray deposition is not commonly used in industry for manufacturing battery electrodes due to the time and cost associated with layer-by-layer deposition.[5] Manufacturing layered or graded materials is challenging with current slurry coating methods, therefore in order to commercialise these new electrode designs industrial manufacturing methods must be taken into account.[18] With the desire for greater energy density comes increased electrode mass loading and thickness. When this is combined with a slow layer-by-layer deposition method, manufacture time is increased thus inflating the total cell cost. The thick 20 pass silicon/graphite electrode manufactured here was ~100 µm thick, and took ~1 hour to manufacture a 25 cm^2 electrode, whereas industry is currently targeting manufacturing speeds of 90 m min^{-1}, showing clearly that spray deposition has a long way to go to compete.

In order to further improve the manufacture speed of location specific silicon electrodes, spray deposition was combined with more traditional slurry coating methods. As the combination with slurry coating makes gradient manufacture deposition difficult, layered silicon/graphite electrodes were manufactured instead. While some literature research has focussed on entirely slurry coated, or spray deposited silicon/graphite anodes, there is little research into combined spray/slurry coating methods.[273,274]

To study the viability of this bi-technique manufacturing method, commercial graphite anodes were used as a substrate for silicon spray deposition, thus producing layered silicon/graphite electrodes.

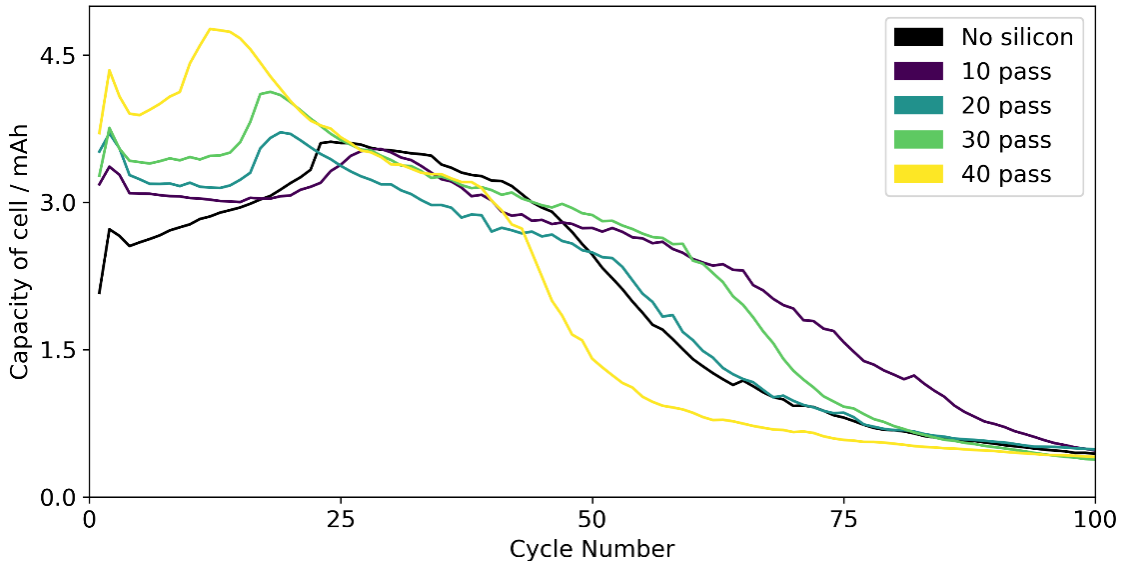

Figure 6-16: *The capacity of batteries made with Li-FUN graphite electrodes with different amounts of spray passes of silicon on top. 10 spray passes is roughly equal to 0.22 mg cm^{-2} electrode.*

Commercial Li-FUN graphite anodes were used as a substrate for silicon deposition, and coated with different mass loadings of silicon nanoparticles, combined with binder and conductive carbon. Figure 6-16 shows the capacity per cycle of these silicon/Li-FUN graphite cells. The mass of silicon deposited over ten passes is roughly 0.22 mg cm^{-2}, although due to fluctuations in the mass of the Li-FUN graphite electrode the total mass of silicon per electrode is difficult to quantify. What is initially clear is the capacity difference during the initial 25 cycles that coincides with increased pass number of silicon deposition. Cell capacity increased with silicon pass number; on the fourth discharge the respective capacities were: No silicon; 2.59 mAh, 10 pass; 3.09 mAh, 20 pass; 3.23 mAh, 30 pass; 3.41 mAh and 40 pass; 3.89 mAh. This demonstrates that a thin layer of silicon coating on a slurry coated electrode can be used to increase electrode capacity.

The cycling data of the bare Li-FUN electrode, indicated as ‘No silicon’, shows typical graphite behaviour during the early stages of cycling, with capacity increasing steadily for the first 25 cycles. This is due to the combined effects of SEI formation, which takes place over multiple cycles and artificially extends cycling profiles, as well as increasing utilisation of the electrode, with parts of the graphite that were previously not ‘wetted’ by the electrolyte or were inactive becoming useable for lithium ion intercalation.[306–309] This effect was replicated in

all the silicon coated electrodes, with peaks in discharge capacity occurring between cycle 15 and 30 due to more complete electrode activation. After 25 cycles however there is a decrease in capacity seen in all the tested electrodes, and after 100 cycles there is <0.1 mAh seen with all electrode configurations. This dramatic decrease in capacity is unusual in graphite electrodes, especially commercial Li-FUN electrodes, which suggests an issue with cell manufacture or cycling parameters for the sudden deterioration in performance. Despite this the promising increase in capacity for the initial 25 cycles of cells with spray deposited silicon coatings suggests potential for bi-technique manufacture of layered silicon/graphite anodes. While spray depositing thin silicon layers onto commercial cathodes provides a route to surface coated graphite electrodes, previous results have indicated that silicon location within the thickness of the electrode is important in determining silicon's longevity and cycle life performance. In order to study this, slurry coated graphite electrodes were manufactured in-house with silicon layers sprayed before and after graphite deposition.

Three different combinations of layered silicon graphite electrodes were manufactured in order to study the effect of silicon location. Each electrode comprised 40 passes of silicon (0.88 mg cm^{-2} of silicon). 'Silicon bottom' comprised of 40 passes of silicon directly onto the copper current collector, the graphite electrode was then coated on top. 'Silicon top and bottom' comprised of 20 passes of silicon onto the current collector, then doctor bladed graphite, and finally a further 20 passes of silicon on top. 'Silicon top' involved spraying 40 passes of silicon on top of a doctor bladed graphite electrode. Figure 6-17 shows the mean capacity per cycle of the layered silicon graphite electrodes compared to a control graphite-only electrode. All the silicon-containing electrodes have a higher initial capacity of 4-5 mAh per cell than the control electrodes (~3 mAh). The 'silicon top' electrode has the highest initial capacity, likely due to the reaction rate gradient that exist inside electrodes which means that material near the surface of the electrode is lithiated first, and any inactive material is more likely to be near the current collector.[268,269] As expected from previous results the 'silicon top' electrode capacity drops quickly from ~5 mAh to 4 mAh within 10 cycles, whereas the 'silicon top and bottom' and 'silicon bottom' electrodes maintained a more stable capacity of ~4 mAh for 20 cycles, with silicon bottom

electrodes performing marginally better out of the two over the 20 cycles. Both ‘Silicon top’ and ‘Silicon bottom’ graphite electrodes degraded in performance towards the control ‘no silicon’ electrode eventually dropping below it after 37 cycles while ‘Silicon top and bottom’ retained capacity better. Unexpectedly the ‘silicon bottom’ electrode performance deteriorated quickly after ~cycle 15 and the ‘silicon top and bottom’ electrode showed the highest capacity from cycle 20 onwards. This suggests that the degradation in the layered ‘silicon bottom’ electrode is worse than a graded silicon bottom electrode. This may be due to the distinct boundary which exists between the sprayed silicon layer and the doctor bladed graphite which could be a source of disconnection with repeated volume expansion during cycling. Furthermore spray deposition of a pure silicon layer onto the current collector prior to doctor blading may impact the stability of the electrode, increasing the risk of delamination. The ‘silicon top and bottom’ electrode has a thinner layer of silicon between the graphite and current collector which may prevent delamination or disconnection with cycling. In the same manner, grading silicon graphite electrodes reduces the existence of a silicon graphite boundary thus minimising the chance of planar disconnection due to volume expansion.

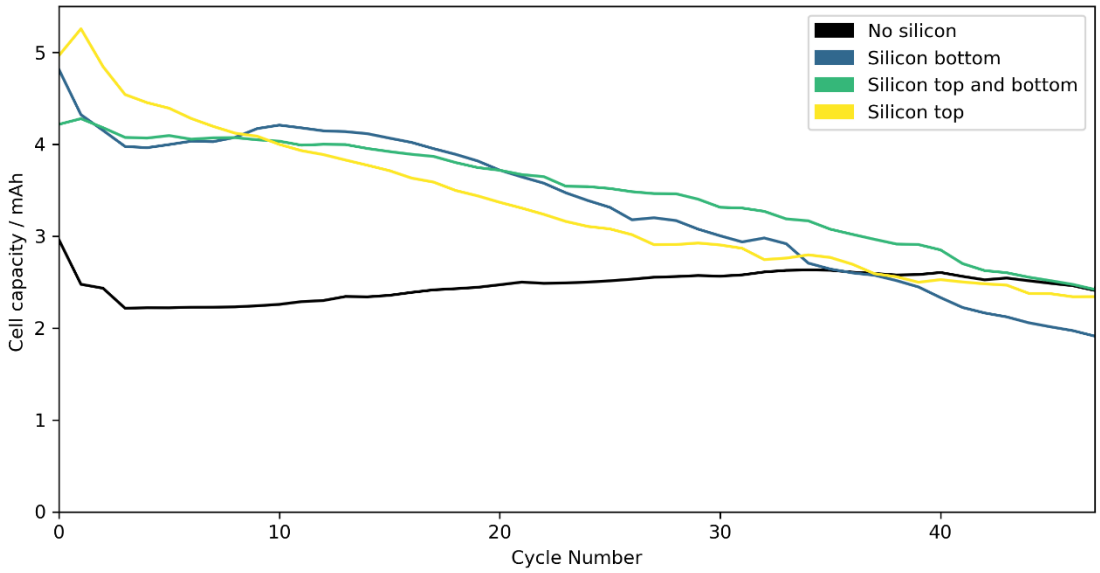

Figure 6-17: *Mean capacity per cycle of combined doctor bladed-spray deposited layered silicon graphite anodes with different locations of silicon. 3 repeats make up each line.*

6.5 Conclusions

Spray deposition was used to manufacture silicon graphite electrodes for use as lithium-ion battery anodes. Graphite dispersion was optimised finding that 15 µm graphite precipitated too quickly for spray deposition, but 5 µm graphene flakes gave the highest spray efficiency. Binder studies concluded that 10 wt% 1:1 CMC:SBR silicon graphite anodes gave the highest capacity. Graded silicon graphite anodes were manufactured in order to study the effect of silicon location on electrode cycle life and stability. Bottom graded silicon graphite electrodes (with higher silicon content near the current collector) gave the highest capacity, and thicker (100 µm) electrodes produced more repeatable cycling results. Table 6-1 shows the average capacity of the different gradients, both thin and thick, of the silicon/graphite and silicon/carbon electrodes, taken from Figure 6-14 and demonstrates that a gradient that prioritises silicon near the base of the electrode, has a higher average capacity than other gradients and of pure graphite (286 mAh g^{-1}) over 70 cycles.

A combination spray deposited/doctor bladed method was studied as a method of improving the commercial viability of spray deposition, allowing for shorter spray times. A simple silicon spray deposition step either before or after slurry coating methods reduced spray deposition time by at least 10 times, from ~2 hour to 20 minutes, while maintaining the benefit of precise location-based silicon placement. It was found that spraying silicon on the surface of the electrode had the highest initial capacity loss, likely due to the fast degradation of the silicon particles. Interestingly, in comparison to graded electrodes spray deposition of silicon underneath a graphite electrode also showed fast degradation, it is thought that this is due to delamination of the electrode. The exact placement of layered silicon on commercial electrodes is not clear, a study using commercial silicon, graphite electrode material would be useful in further examining the impact of silicon location.

Table 6-1: *The average capacities of graded silicon/graphite and silicon carbon electrodes at different thicknesses. Thin is 50 µm and thick is 100 µm*

Experiment type	Average capacity mAh g^{-1}

	Si Bottom	Si Mix	Si Top
Si/Graphite - thin	532	482	413
Si/Graphite – thick	480	392	366
Si/Carbon – thick	373	249	235

6.5.1 Future work

Further characterisation of both the gradient and the specific sulfur/graphite particles would be useful in determining the method of degradation in these cells. X-Ray Photoelectron Spectroscopy (XPS) depth profiling, would give a more specific, volume-focussed, insight into the silicon graphite gradient. In situ X-ray CT would further help to characterise the gradient, and would also be useful in analysing the degradation mechanisms of the electrode, whether this is through particle cracking and architecture destruction or delamination. In order to characterise the exact nature of the silicon graphite mix, TEM could be utilised to examine particle morphology, again both before and after testing. This insight into the exact particle structure might help explain some of the poorer performance, as the silicon and graphite may not be appropriately mixed and may require further preparation before electrode deposition, such as ball milling. Furthermore future work should focus on methods of combining spray deposition with roll-to-roll coating methods such as doctor blading, see Figure 7-2. Alongside this, repetition of this work but more non-standard and state-of-the-art materials might help to bring the capacity of the batteries closer to industrially relevant ones. Similar layered electrode work using lab-made Si/SiO_x nanoparticles in Si/carbon electrodes produced batteries which achieved a peak of 511 mAh g^{-1} which is significantly higher than the 373 mAh g^{-1} average achieved with silicon/carbon electrodes here.[183]

Chapter 7 Conclusion and Recommendations

7.1 Conclusions

Spray deposition is a new manufacture technique for battery electrode production which has potential to be useful for multiple different aspects. The introductory chapters demonstrate the different fields in which spray deposition has been utilised for the manufacture of battery anodes and cathodes, solid electrolytes, interphases and finally for novel layered and gradient structures. A requirement for more intricate design in battery materials in tackling chemistry specific issues which impact battery performance prompts the use of layer-by-layer spray deposition as a manufacture method to influence and optimise final material structure. The work here demonstrates one potential electrode design using spray deposition to manufacture gradients into three separate battery chemistries: lithium sulfur, solid polymer electrolyte and silicon graphite anodes.

In Chapter 4, gold catalysts were introduced into a carbon-based cathode for lithium sulfur batteries using a gradient spray deposition process. Gold was graded throughout the electrode structure in order to optimise the placement of gold throughout the thickness, thus reducing the overall quantity of gold required without compromising on performance. It was discovered that gold had the most effect when graded towards the top surface of the electrode, with increased rate performance seen when compared to other gradients and non-catalyst containing electrodes. Gold near the surface of the electrode was found to increase the concentration of polysulfides in the electrolyte during discharge, suggesting greater conversion of solid sulfur therefore a higher sulfur utilisation. These effects were only seen under extreme circumstances of high sulfur loading (70 wt%) and high rate (1C), and in all other instances the impact of gold was negated by the loss of conductive, high surface area carbon, which reduced the overall sulfur utilisation. This study demonstrates one use for the gradient spray manufacture technique in location-specific deposition of small wt% catalyst materials, and illuminates how optimisation of often expensive catalyst materials could be used to minimise catalyst content thus decreasing cost and increasing energy density of battery materials.

Chapter 5 discusses the potential for spray deposition in solving electrode/electrolyte contact issues in solid-state batteries. With repeated cycling,

resistance of a solid-state battery can increase due to SEI growth or loss of contact between the composite cathode and SSE layer. Spray deposition was used to manufacture graded LFP/PEO composite cathodes which are designed to remove the planar boundary at the electrode/SSE interface. Graded composite cathodes were found to have greater capacity retention and lower resistance than ungraded cathodes in cycle life testing. Furthermore during rate testing, graded composite cathodes functioned at all C-rates up to 2C whereas ungraded composite cathodes failed to deliver any usable capacity at rates higher than C/5. This work is one of the only demonstrations of the spray deposition of a polymer electrolyte and paves the way towards more design in graded composite cathodes for SSB's. Spray deposition also allowed for a one step synthesis of these composite cathodes alongside further facile deposition of the subsequent SPE layer. This process is also easily scalable to larger electrode designs and other materials, providing a method of direct deposition of SSE and SPE materials onto electrodes, ensuring good contact between the two. This promotes the easy manufacture of designed SSB's which is crucial to the full commercial deployment of safer, higher capacity batteries.

Chapter 6 applies the gradient electrode manufacture process to silicon graphite anodes which are hampered by the poor cycle life and stability of silicon. Furthering current research of layered silicon carbon electrodes, and the understanding that the silicon location influences its stability, graded silicon graphite anodes were manufactured in order to optimise this placement and compare with layered electrodes. Despite difficulties in spray depositing graphite, it was found that gradients that increased silicon placement near the current collector led to improved capacity retention. One major issue for commercialisation of this manufacturing technology is the speed of electrode fabrication, with current slurry coating techniques achieving high throughput of material. A combined slurry coating/spray depositing approach was designed and the results generally matched those of the spray-only electrodes, with silicon placement near the surface of the electrode performing the worst. This chapter not only highlights another battery chemistry which can be improved/optimised using spray deposited gradients but also demonstrates the combination of slurry deposition techniques with spray deposition for greater commercial implementation.

7.2 Future perspectives

7.2.1 This work

To further improve and build on this work, a greater array of characterisation tools should be employed to study both macro and microstructure. In order to explore the gradient in greater detail, methods such as X-ray Photoelectron Spectroscopy (XPS) depth profiling, which can be used to remove surface material while also performing elemental analysis would provide data on gradient homogeneity and coverage. Furthermore, if the densities of the graded materials are suitably different, X-ray CT could be used to get a comparison of the material ratio slice-by-slice through the electrode thickness. These characterisation methods would help remove noise and uncertainty that arises during the line-scan EDX cross section measurement used in Chapters 4 and 6.

Other characterisation would help to investigate the electrochemical and material reasons behind the improved performance. Techniques that can be used to examine particle or interface microstructure, before and after cycling would be beneficial in determining exact methods of degradation, or changes in electrode architecture. These techniques could include transmission electron microscopy (TEM) and X-ray CT (either ex situ or in situ through use of a synchrotron). Chapter 4 would benefit from detailed examination of LiS and S_8 deposition. This would help to characterise the effects of the gold catalyst. Operando Atomic Force Microscopy (AFM) would be useful in observing the size and location of deposited sulfur particles, thus further supporting the idea of pore-blocking, particularly at high charge rates. Chapter 5 would benefit from in situ X-ray CT, as this may provide further evidence towards the disconnection of the composite cathode and SPE layers. Examining the difference between these interfaces in graded and ungraded composite cathodes may help to clarify the benefits of gradient electrode. Chapter 6 would benefit from TEM studies of the silicon graphite composite particles, both before and after cycling to compare the difference in architecture breakdown between the different gradient electrodes. TEM would help show the volume expansion of silicon particles, and therefore a comparison between surface or bulk silicon could be made, thus exploring the bulk carbon’s role in protecting and accommodating the silicon expansion.

7.2.2 Applications of graded spray deposited materials

The work in this thesis shows the extent of applications in which graded electrodes can be used to solve real issues within existing and next generation battery chemistries. The materials and topics shown here were chosen in order to demonstrate this breadth of potential implementation, from catalysis to battery performance and safety, across liquid-state and solid-state batteries. This does not represent the limit of applications of this technique and work done by this author using this method has been undertaken on proton exchange membrane fuel cells and membranes for active CO_2 pumping. Therefore there are a multitude of potential applications for gradient spray deposition both within energy storage and materials engineering collectively. Future research into this method should continue to demonstrate the efficacy of gradient spray deposition for other materials, utilising gradient structures to help resolve material issues in other battery chemistries.

7.2.3 Enhanced graded structures with spray deposition

The work in this thesis demonstrates the development and implementation of a spray deposition manufacture method that creates gradients within thin films. This gradient is generally quite simple: either increasing the wt% of a single material through the thickness of the electrode, or inversely changing the wt% of two materials through-thickness. This technique has the potential to be taken further, this is demonstrated with the subsequent spray deposition of a PEO SSE layer directly onto a graded composite cathode in Chapter 5. In future research, methods which involve increasing the complexity of the gradient could be attempted, such as an ABA structure or an ABC structure, similar to the bi-layer or sandwich structures discussed in 2.8.2 but with the added benefit of graded interfaces which could provide substantial benefit to electrode design. The ABA structure could be achieved easily with the current experimental design in this work and is demonstrated in Figure 7-1 (a, c) where (a) shows the necessary flow rates and subsequent material deposition per spray pass required to manufacture an ABA structure and (c) shows the schematic of the currently used bi-nozzle spray coater. Taking this further, an ABC structure could be achieved through the addition of a third spray nozzle and solution input, this would create a graded tri-layer structure which could be useful for battery electrodes that require different surface and bulk properties but suffer from poor adhesion of these layers. Figure

7-1 (b, d) represent the required solution flow rates and subsequent deposition alongside a schematic of the tri-nozzle spray machine required for the manufacture of ABC graded electrodes.

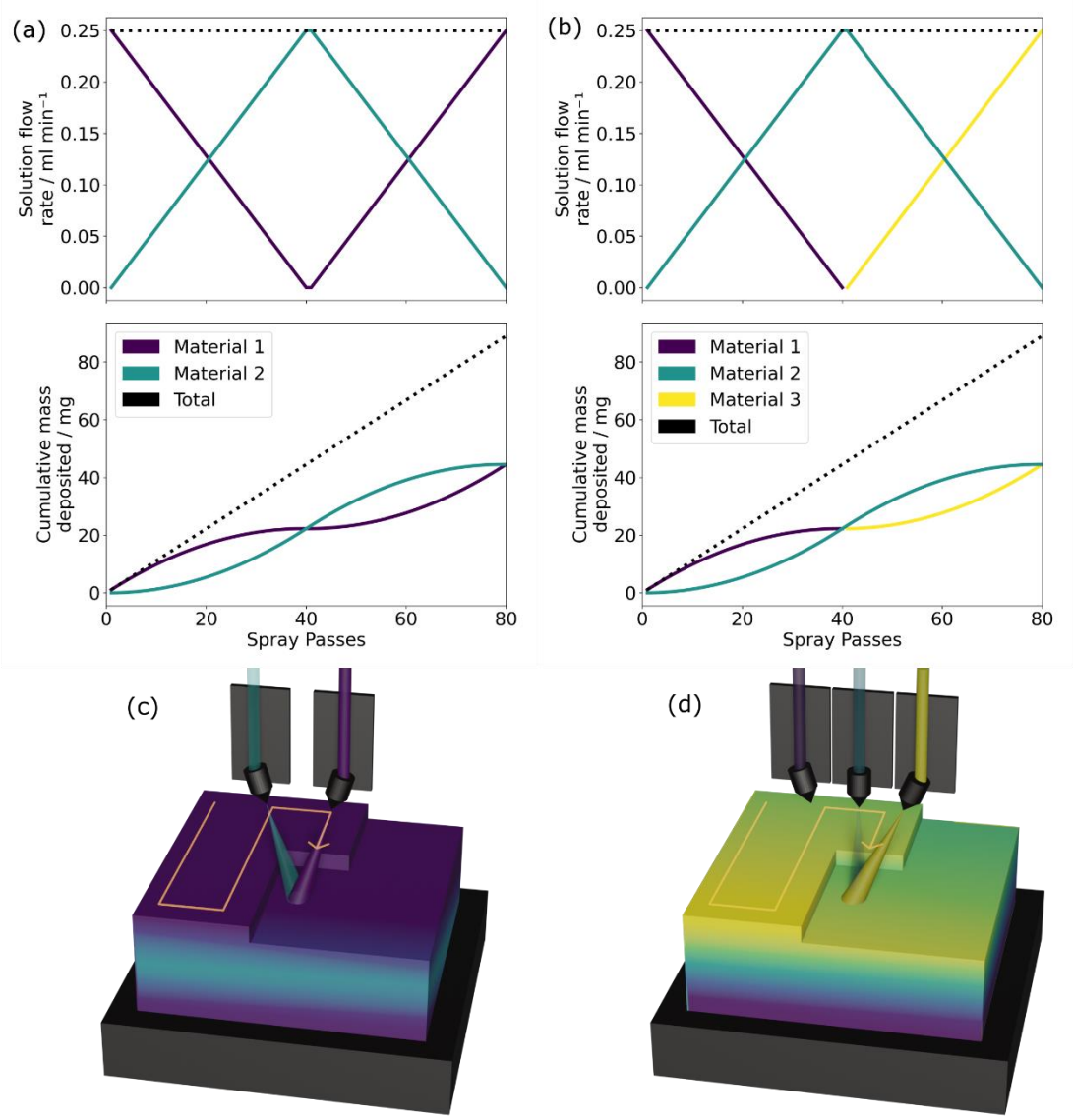

Figure 7-1: *Future perspectives for graded spray deposition with ABA spray (a,c) and ABC (b,d) showing the solution flow rates and cumulative mass plots of the ABA (a) and ABC (b) graded films. (c,d) demonstrate the schematic of the bi-nozzle and tri-nozzle spray coaters needed to manufacture these graded films.*

7.2.4 Combining spray deposition with industry manufacture methods

Some of the work in Chapter 6 of this thesis focuses on increasing the commercial viability of spray deposition in battery electrode manufacture. This work uses a layered two-step doctor blading-spray deposition manufacture approach in order

to retain some electrode design while speeding up fabrication. The gradient work contained here in this thesis focuses on electrode design throughout the entire thickness of the electrode, however in most cases this is not necessary and specific electrode design is often only needed on the surfaces. Combining an industry slurry-based technique such as slot-die coating and a fast processing method (roll-to-roll) printing with spray deposition means that the bulk of the electrode can be manufactured quickly but specific spray deposited design can remain on the surfaces of the film. Figure 7-2 demonstrates a schematic of what this could look like; applying a thin spray coated film to a slurry coated electrode before drying has occurred would ensure some mixing of the two layers, increasing adhesion and also blurring the planar boundary between them, introducing some form of gradient. If this is not required the spray step could be enacted post electrode drying, this would ensure specificity in the two layers and not add some level of unknown into the boundary structure. This would be an excellent introduction into the use of spray deposition as an industrial manufacture technique, providing a level of complexity in electrode design, without constricting speed or cost of manufacture.

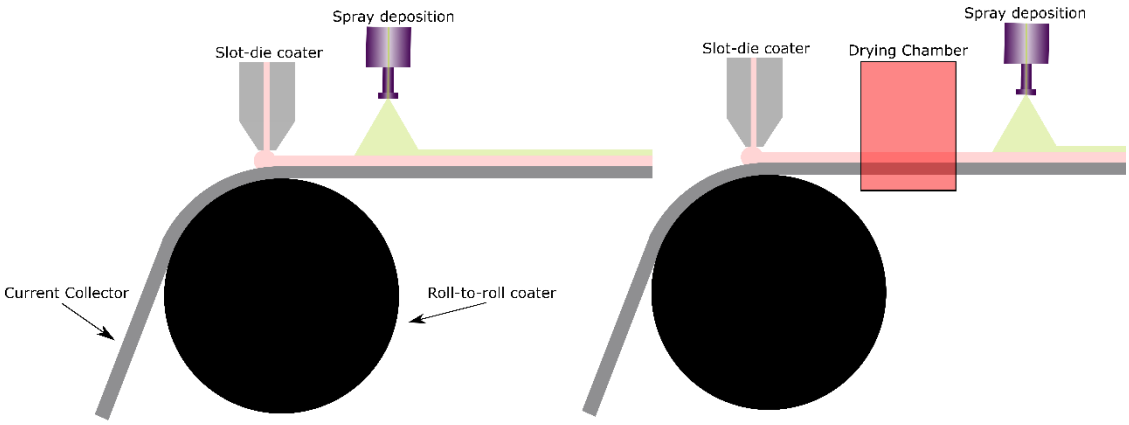

Figure 7-2: *Schematic of a combined roll-to-roll slot-die coater/spray deposition industrial technique with and without drying chamber.*

Chapter 8 Appendix

8.1 Appendix A Information Sheet

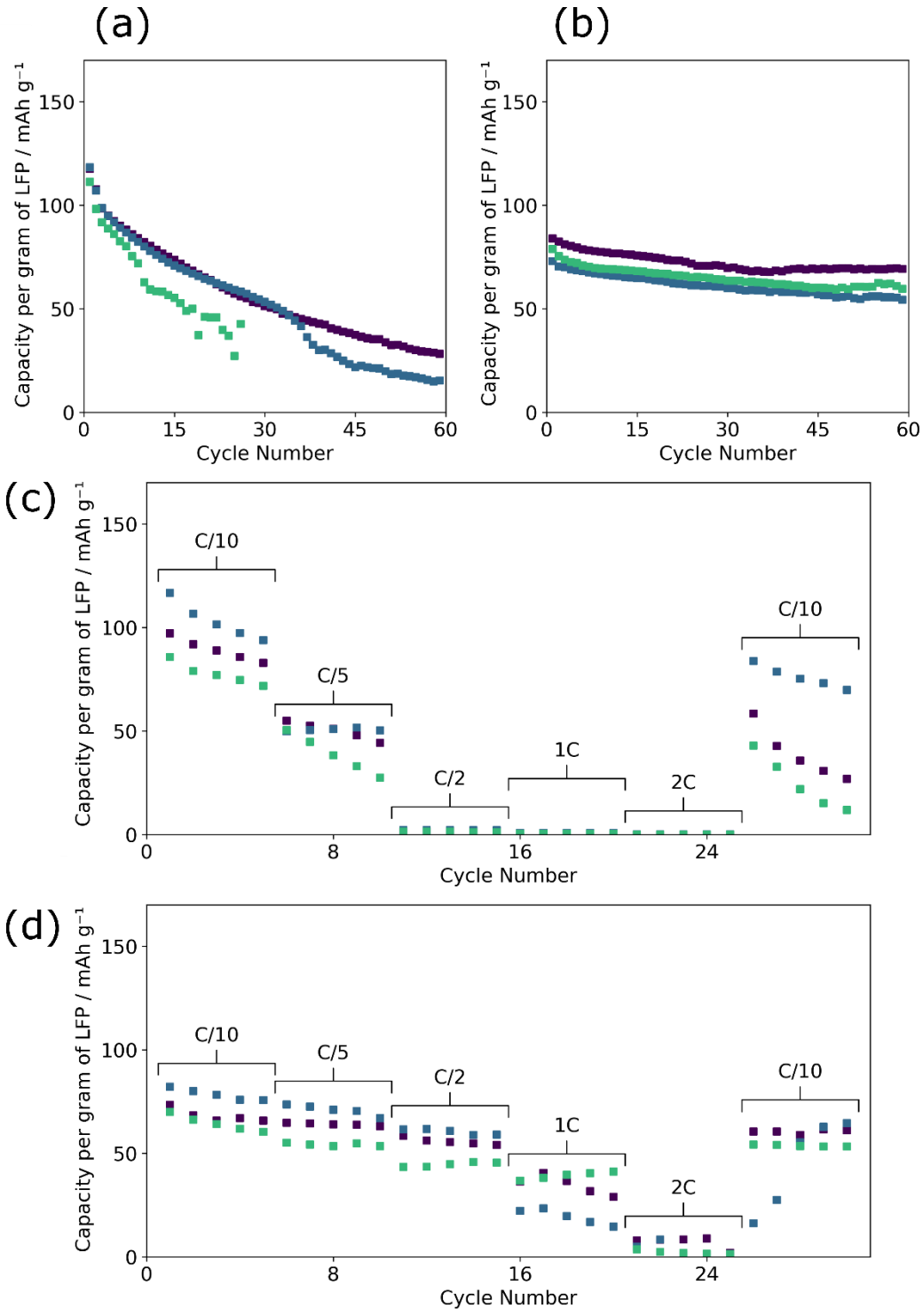

Figure 8-1: *The repeats of ungraded and graded LFP/PEO composite cathodes in C/10 cycle life and rate capability measurements. (a) ungraded cycle life (b) graded cycle life (c) ungraded rate performance (d) graded rate performance*

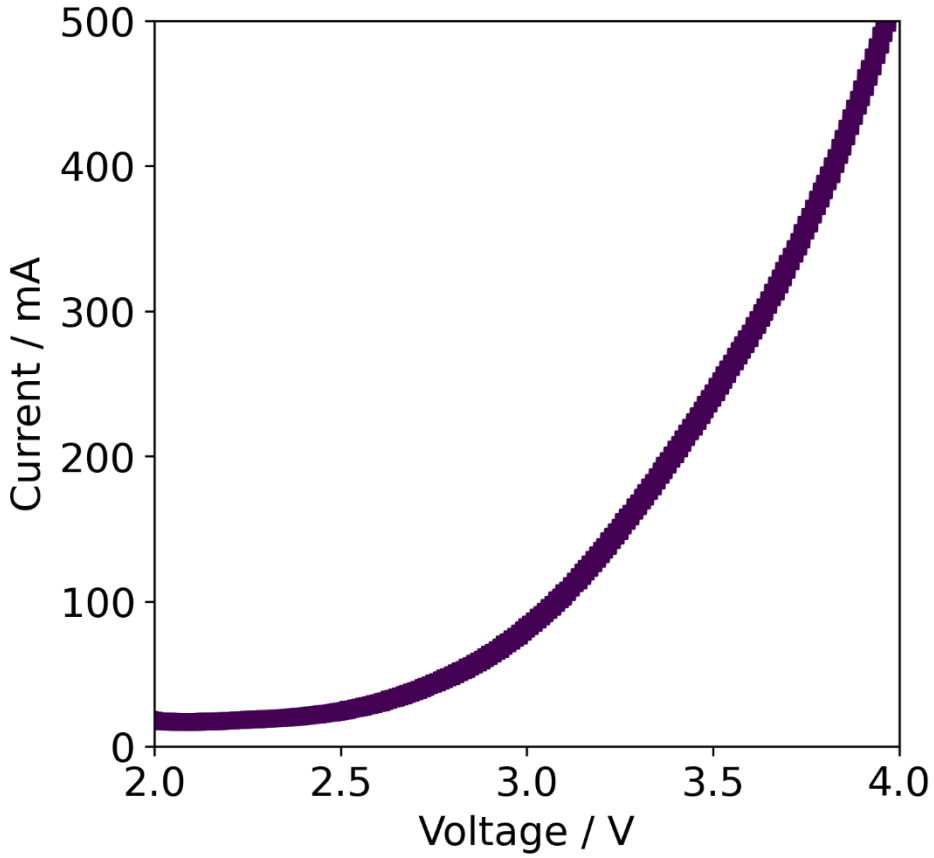

Figure 8-2: *Linear scan voltammetry of a graded LFP/PEO composite cathode*

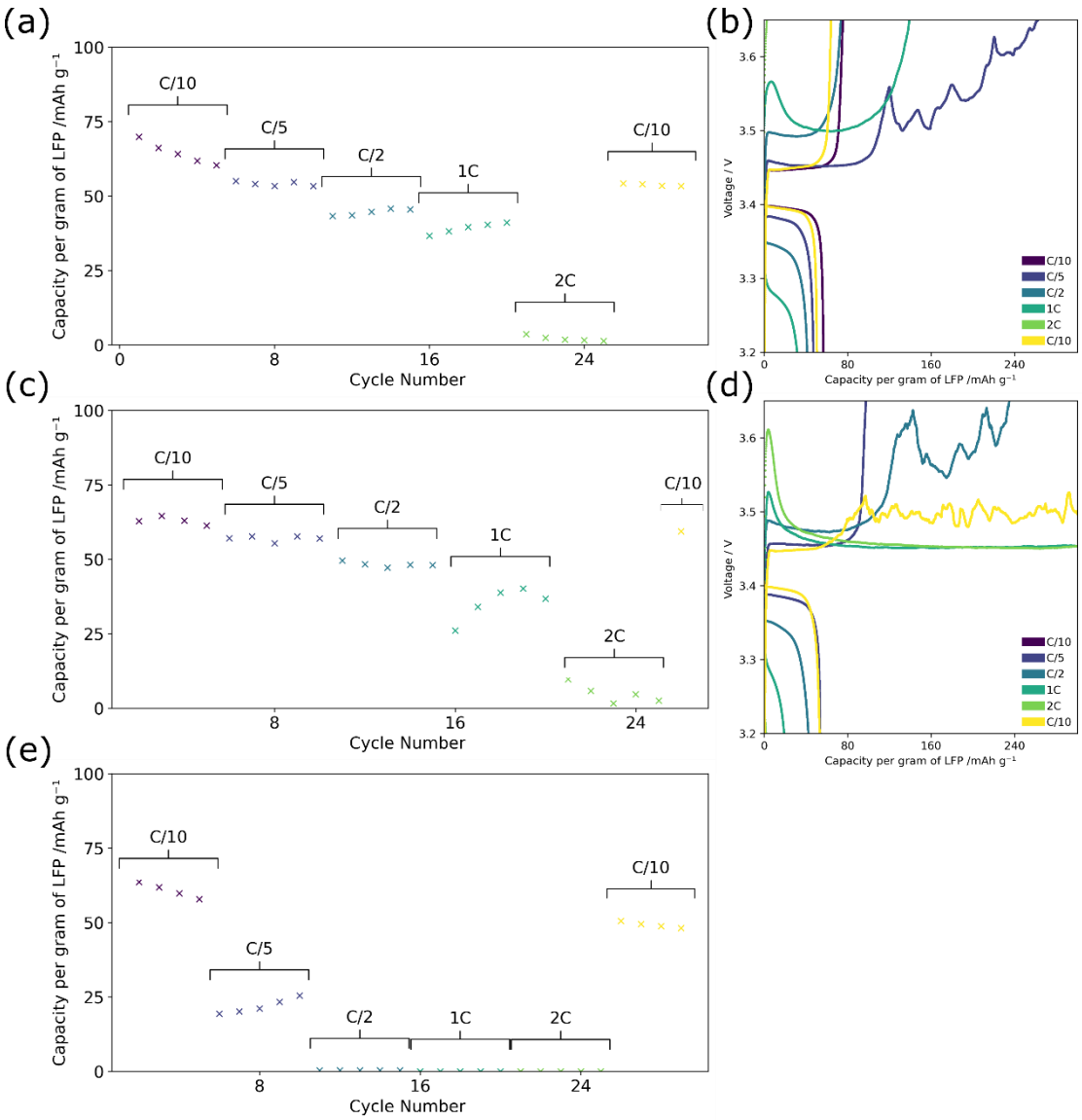

Figure 8-3: *The capacity/cycle number and voltage/capacity graphs of graded LFP/PEO composite cathodes with: (a-b) 50% graded LFP/PEO cathodes, (c,d) triple LLZO cathodes, (e) cells with celgard separator.*

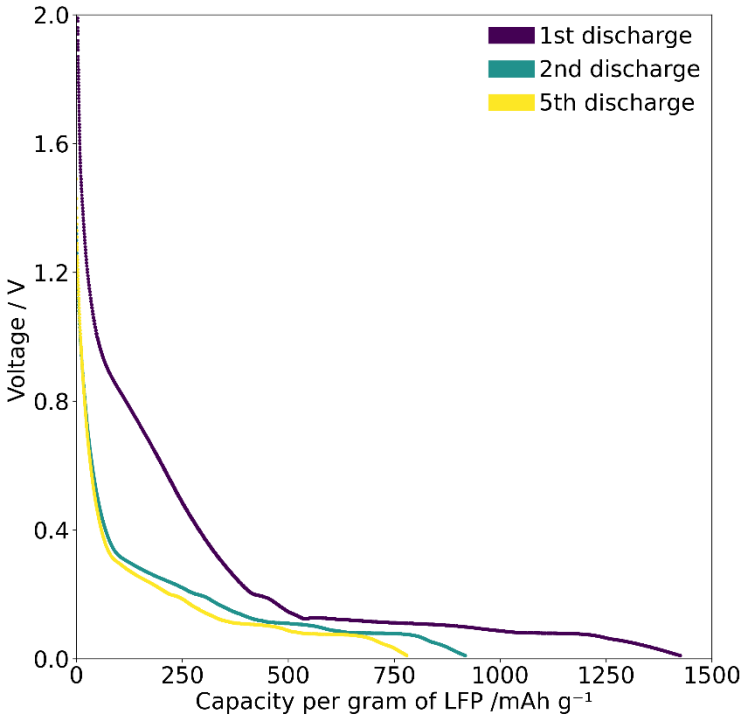

Figure 8-4: *The 1st, 2nd and 5th discharge plots of a 10% silicon graphite anode/lithium cell.*

Figure 8-5: *Left: The author of this work with every coin cell used for these studies. Right: Close-up of the coin cells, estimated ~500 of them.*

References

1 P. U. Nzereogu, A. D. Omah, F. I. Ezema, E. I. Iwuoha and A. C. Nwanya, *Appl. Surf. Sci. Adv.*, 2022, **9**, 100233.

2 P. S. Grant, D. Greenwood, K. Pardikar, R. Smith, T. Entwistle, L. A. Middlemiss, G. Murray, S. A. Cussen, M. J. Lain, M. J. Capener, M. Copley, C. D. Reynolds, S. D. Hare, M. J. H. Simmons, E. Kendrick, S. P. Zankowski, S. Wheeler, P. Zhu, P. R. Slater, Y. S. Zhang, A. R. T. Morrison, W. Dawson, J. Li, P. R. Shearing, D. J. L. Brett, G. Matthews, R. Ge, R. Drummond, E. C. Tredenick, C. Cheng, S. R. Duncan, A. M. Boyce, M. Faraji-Niri, J. Marco, L. A. Roman-Ramirez, C. Harper, P. Blackmore, T. Shelley, A. Mohsseni and D. J. Cumming, *J. Phys. Energy*, 2022, **4**, 42006.

3 P. Molaiyan, S. Bhattacharyya, G. S. dos Reis, R. Sliz, A. Paolella and U. Lassi, *Green Chem.*, 2024, **26**, 7508–7531.

4 D. Kong, H. Lv, P. Ping and G. Wang, *J. Energy Storage*, 2023, **64**, 107073.

5 W. B. Hawley and J. Li, *J. Energy Storage*, 2019, **25**, 100862.

6 M. S. Whittingham, *Prog. Solid State Chem.*, 1978, **12**, 41–99.

7 K. Mizushima, P. C. Jones, P. J. Wiseman and J. B. Goodenough, *Mater. Res. Bull.*, 1980, **15**, 783–789.

8 US4668595A, *Asahi Kasei Corp*, 1986.

9 Y. Miao, P. Hynan, A. von Jouanne and A. Yokochi, *Energies*, 2019, **12**, 1074.

10 P. Roy and S. K. Srivastava, *J. Mater. Chem. A*, 2015, **3**, 2454–2484.

11 B. Joshi, E. Samuel, Y. Kim, A. L. Yarin, M. T. Swihart and S. S. Yoon, *Adv. Funct. Mater.*, 2021, **31**, 2008181.

12 C. Cheng, R. Drummond, S. R. Duncan and P. S. Grant, *J. Power Sources*, 2019, **413**, 59–67.

13 C. Cheng, R. Drummond, S. R. Duncan and P. S. Grant, *J. Power Sources*, 2020, **448**, 227376.

14 J. J. Conde, P. Ferreira-Aparicio and A. M. Chaparro, *ACS Appl. Energy Mater.*, 2021, **4**, 7394–7404.

15 World Economic Forum and Global Battery Alliance, *A Vision for a Sustainable Battery Value Chain in 2030*, 2019.

16 *Climate Change 2022 - Mitigation of Climate Change: Working Group III*

Contribution to the Sixth Assessment Report of the Intergovernmental Panel on Climate Change, Cambridge University Press, Cambridge, 2023.

17 M. Schmitt, M. Baunach, L. Wengeler, K. Peters, P. Junges, P. Scharfer and W. Schabel, *Chem. Eng. Process. Process Intensif.*, 2013, **68**, 32–37.

18 M. Schmitt, Karlsruher Institut für Technologie (KIT), 2016.

19 S. Ahmed, P. A. Nelson, K. G. Gallagher and D. W. Dees, *J. Power Sources*, 2016, **322**, 169–178.

20 S. N. Bryntesen, A. H. Strømman, I. Tolstorebrov, P. R. Shearing, J. J. Lamb and O. Stokke Burheim, *Energies*, 2021, **14**, 1406.

21 B. Ludwig, Z. Zheng, W. Shou, Y. Wang and H. Pan, *Sci. Rep.*, 2016, **6**, 23150.

22 A. Manthiram, X. Yu and S. Wang, *Nat. Rev. Mater.*, 2017, **2**, 16103.

23 W. Hou, Y. Ou and K. Liu, *Chem. Res. Chinese Univ.*, 2022, **38**, 735–743.

24 L. Seidl, R. Grissa, L. Zhang, S. Trabesinger and C. Battaglia, *Adv. Mater. Interfaces*, 2022, **9**, 2100704.

25 J. Qiu, X. Liu, R. Chen, Q. Li, Y. Wang, P. Chen, L. Gan, S.-J. Lee, D. Nordlund, Y. Liu, X. Yu, X. Bai, H. Li and L. Chen, *Adv. Funct. Mater.*, 2020, **30**, 1909392.

26 G. Homann, L. Stolz, J. Nair, I. C. Laskovic, M. Winter and J. Kasnatscheew, *Sci. Rep.*, 2020, **10**, 4390.

27 Y. Xia, T. Fujieda, K. Tatsumi, P. P. Prosini and T. Sakai, *J. Power Sources*, 2001, **92**, 234–243.

28 J. van den Broek, S. Afyon and J. L. M. Rupp, *Adv. Energy Mater.*, 2016, **6**, 1600736.

29 K. Kanehori, Y. Ito, F. Kirino, K. Miyauchi and T. Kudo, *Solid State Ionics*, 1986, **18**–**19**, 818–822.

30 T. Aaltonen, M. Alnes, O. Nilsen, L. Costelle and H. Fjellvåg, *J. Mater. Chem.*, 2010, **20**, 2877–2881.

31 T. Kato, T. Hamanaka, K. Yamamoto, T. Hirayama, F. Sagane, M. Motoyama and Y. Iriyama, *J. Power Sources*, 2014, **260**, 292–298.

32 S. Ohta, J. Seki, Y. Yagi, Y. Kihira, T. Tani and T. Asaoka, *J. Power Sources*, 2014, **265**, 40–44.

33 S. Ohta, T. Kobayashi, J. Seki and T. Asaoka, *J. Power Sources*, 2012, **202**, 332–335.

34 C. Guild, S. Biswas, Y. Meng, T. Jafari, A. M. Gaffney and S. L. Suib, *Catal.*

Today, 2014, **238**, 87–94.

35 J. L. Shui, G. S. Jiang, S. Xie and C. H. Chen, *Electrochim. Acta*, 2004, **49**, 2209–2213.

36 K. Y. Choi, K. Do Kim and J. W. Yang, *J. Mater. Process. Technol.*, 2006, **171**, 118–124.

37 K. Ma and C. X. Li, *CHINA Surf. Eng.*, 2020, **33**, 26–50.

38 B. Vertruyen, N. Eshraghi, C. Piffet, J. Bodart, A. Mahmoud and F. Boschini, *Materials (Basel).*, 2018, **11**, 1076.

39 SonoTek, How Ultrasonic Nozzles Work, https://www.sono-tek.com/ultrasonic-coating/how-ultrasonic-nozzles-work/, (accessed 6 June 2024).

40 C. H. Chen, E. M. Kelder, M. J. G. Jak and J. Schoonman, *SOLID STATE IONICS*, 1996, **86**–**8**, 1301–1306.

41 M. J. Divvela, R. Zhang, Y. Zhmayev, S. Pinge, J. H. Lee, S. W. Kim and Y. L. Joo, *Soft Matter*, 2019, **15**, 6485–6494.

42 N. Tsapis, D. Bennett, B. Jackson, D. A. Weitz and D. A. Edwards, *Proc. Natl. Acad. Sci.*, 2002, **99**, 12001–12005.

43 T. T. T. Nguyen, T. V. A. Le, N. N. Dang, D. C. Nguyen, P. T. N. Nguyen, T. T. Tran, Q. V. Nguyen, L. G. Bach and D. Thuy Nguyen Pham, *J. Food Qual.*, 2021, **2021**, 5525879.

44 Y. Li, Y. Wu, Z. Wang, J. Xu, T. Ma, L. Chen, H. Li and F. Wu, *Mater. Today*, 2022, **55**, 92–109.

45 S. An, B. Joshi, A. L. Yarin, M. T. Swihart and S. S. Yoon, *Adv. Mater.*, 2020, **32**, 1905028.

46 M. S. Ziegler, J. Song and J. E. Trancik, *Energy Environ. Sci.*, 2021, **14**, 6074–6098.

47 I. Fouzai, M. Radaoui, S. Díaz-Abad, M. A. Rodrigo and J. Lobato, *ACS Appl. Energy Mater.*, 2022, **5**, 2138–2149.

48 T. Bayer, H. C. Pham, K. Sasaki and S. M. Lyth, *J. Power Sources*, 2016, **327**, 319–326.

49 T. Yuan, Y. Jiang, Y. Li, D. Zhang and M. Yan, *Electrochim. Acta*, 2014, **136**, 27–32.

50 A. Jamaluddin, B. Umesh, F. M. Chen, J. K. Chang and C. Y. Su, *Nanoscale*, 2020, **12**, 9616–9627.

51 Y. Wang, W. Chen, Q. Luo, S. Xie and C. H. Chen, *Appl. Surf. Sci.*, 2006,

252, 8096–8101.

52 J. L. Shui, G. S. Jiang, S. Xie and C. H. Chen, *Electrochim. Acta*, 2004, **49**, 2209–2213.

53 K. Dokko, N. Anzue, Y. Makino, M. Mohamedi, T. Itoh, M. Umeda and I. Uchida, *ELECTROCHEMISTRY*, 2003, **71**, 1061–1063.

54 Y. Jiang, Y. Yu, W. Sun, C. Chen, G. Meng and J. Gao, *J. Electrochem. Soc.*, 2007, **154**, E107.

55 X. F. Li, A. Dhanabalan, X. B. Meng, L. Gu, X. L. Sun and C. L. Wang, *MICROPOROUS MESOPOROUS Mater.*, 2012, **151**, 488–494.

56 A. Dhanabalan, Y. Yu, X. F. Li, K. Bechtold, J. Maier and C. L. Wang, *MICRO- Nanotechnol. SENSORS, Syst. Appl. II*, 2010, 7679.

57 K. Lim, H. Park, J. Ha, Y.-T. Kim and J. Choi, *J. Ind. Eng. Chem.*, 2021, **101**, 397–404.

58 J. B. Li, W. J. Liu, Y. J. Qiao, G. C. Peng, Y. R. Ren, Z. W. Xie and M. Z. Qu, *Front. Chem.*, 2020, **8**, 568919.

59 C. Zhu, P. Kopold, P. A. van Aken, J. Maier and Y. Yu, *Adv. Mater.*, 2016, **28**, 2409–2416.

60 J. J. Yuan, C. H. Chen, Y. Hao, X. K. Zhang, R. Agrawal, W. Y. Zhao, C. L. Wang, H. J. Yu, X. R. Zhu, Y. Yu, Z. Z. Xiong and Y. M. Xie, *J. Alloys Compd.*, 2017, **696**, 1174–1179.

61 Y. Yu, L. Gu, A. Dhanabalan, C. H. Chen and C. L. Wang, *Electrochim. Acta*, 2009, **54**, 7227–7230.

62 Y. Matsushima, T. Yamazaki, K. Maeda, T. Noma and T. Suzuki, *J. Ceram. Soc. JAPAN*, 2006, **114**, 1121–1125.

63 J. J. Yuan, S. Y. Gao, W. D. Lai, S. L. Zheng, J. X. Meng, X. K. Zhang, X. R. Zhu, H. J. Yu and X. K. Li, *J. Mater. Sci. Electron.*, 2019, **30**, 16008–16014.

64 T. Z. Yuan, Y. Z. Jiang, Y. Li, D. Zhang and M. Yan, *Electrochim. Acta*, 2014, **136**, 27–32.

65 Y. Yu, C. H. Chen, J. L. Shui and S. Xie, *Angew. CHEMIE-INTERNATIONAL Ed.*, 2005, **44**, 7085–7089.

66 X. Zhu, Z. Guo, P. Zhang, G. Du, R. Zeng, Z. Chen and H. Liu, *ChemPhysChem*, 2009, **10**, 3101–3104.

67 C. H. Chen, R. Agrawal and C. L. Wang, *ENERGY Harvest. STORAGE Mater. DEVICES, Appl. VII*, 2016, **14**, 9865.

68 A. Henriques, A. Rabiei Baboukani, B. Jafarizadeh, A. H. Chowdhury and C. Wang, *Materials (Basel).*, 2022, **15**, 9086.

69 J. Zhang, L. B. Chen, C. C. Li and T. H. Wang, *Appl. Phys. Lett.*, 2008, **93**, 264102.

70 J. J. Yuan, X. K. Zhang, C. H. Chen, Y. Hao, R. Agrawal, C. L. Wang, W. Li, H. J. Yu, Y. Yu, X. R. Zhu, Z. Z. Xiong and Y. M. Xie, *Mater. Lett.*, 2017, **190**, 37–39.

71 Y. Z. Jiang, T. Z. Yuan, W. P. Sun and M. Yan, *ACS Appl. Mater. Interfaces*, 2012, **4**, 6216–6220.

72 A. Dhanabalan, X. F. Li, R. Agrawal, C. H. Chen and C. L. Wang, *NANOMATERIALS*, 2013, **3**, 606–614.

73 A. Dhanabalan, Y. Yu, X. F. Li, W. Chen, K. Bechtold, L. Gu and C. L. Wang, *J. Mater. Res.*, 2010, **25**, 1554–1560.

74 L. Wang, H. W. Xu, P. C. Chen, D. W. Zhang, C. X. Ding and C. H. Chen, *J. Power Sources*, 2009, **193**, 846–850.

75 R. Kun, P. Schlee, E. Pal, M. Busse and T. Gesing, *J. Alloys Compd.*, 2017, **726**, 664–674.

76 Z. B. Han, Y. F. Xiong, Y. C. Feng, W. R. Zhang and W. Z. Zhang, *Manuf. Lett.*, 2023, **35**, 152–159.

77 C. Zhu, P. Kopold, P. A. van Aken, J. Maier and Y. Yu, *Adv. Mater.*, 2016, **28**, 2409–2416.

78 A. Dhanabalan, Y. Yu, X. Li, W. Chen, K. Bechtold, L. Gu and C. Wang, *J. Mater. Res.*, 2010, **25**, 1554–1560.

79 A. Henriques, A. Rabiei Baboukani, B. Jafarizadeh, A. H. Chowdhury and C. Wang, *Materials (Basel).*, 2022, **15**, 9086.

80 J. Yuan, S. Gao, W. Lai, S. Zheng, J. Meng, X. Zhang, X. Zhu, H. Yu and X. Li, *J. Mater. Sci. Mater. Electron.*, 2019, **30**, 16008–16014.

81 A. Rabiei Baboukani, E. Adelowo, R. Agrawal, I. Khakpour, V. Drozd, W. Li and C. Wang, *ECS Trans.*, 2018, **85**, 331–336.

82 R. Kun, P. Schlee, E. Pal, M. Busse and T. Gesing, *J. Alloys Compd.*, 2017, **726**, 664–674.

83 D. Shu, K. Y. Chung, W. Il Cho and K.-B. Kim, *J. Power Sources*, 2003, **114**, 253–263.

84 Y. Wang, W. Chen, Q. Luo, S. Xie and C. H. Chen, *Appl. Surf. Sci.*, 2006, **252**, 8096–8101.

85 M. Mohamedi, D. Takahashi, T. Itoh, M. Umeda and I. Uchida, *J. Electrochem. Soc.*, 2002, **149**, A19.

86 S. N. Karthick, S. Richard Prabhu Gnanakan, A. Subramania and H.-J. Kim, *J. Alloys Compd.*, 2010, **489**, 674–677.

87 S. Koike and K. Tatsumi, *J. Power Sources*, 2005, **146**, 241–244.

88 W.-S. Yoon, K. Y. Chung, K.-W. Nam and K.-B. Kim, *J. Power Sources*, 2006, **163**, 207–210.

89 T. Z. Yuan, Y. Z. Jiang, Q. T. Wang, B. Pan and M. Yan, *CHEMELECTROCHEM*, 2017, **4**, 565–569.

90 F. Ffff, R. Yu, Y. Sun, B.-K. Zou, M.-M. Deng, J.-Y. Xie and C.-H. Chen, *J. Power Sources*, 2017, **340**, 258–262.

91 R. Yu, Y. Sun, B.-K. Zou, M.-M. Deng, J.-Y. Xie and C.-H. Chen, *J. Power Sources*, 2017, **340**, 258–262.

92 T. Li, Z. Chen, F. Bai, C. Li and Y. Li, *J. Energy Chem.*, 2023, **81**, 404–409.

93 K. Dokko, N. Anzue, Y. Makino, M. Mohamedi, T. Itoh, M. Umeda and I. Uchida, *ELECTROCHEMISTRY*, 2003, **71**, 1061–1063.

94 A. Du Pasquier, A. Blyr, P. Courjal, D. Larcher, G. Amatucci, B. Gérand and J. Tarascon, *J. Electrochem. Soc.*, 1999, **146**, 428.

95 J. Maršálek, J. Chmelař, J. Pocedič and J. Kosek, *Chem. Eng. Sci.*, 2015, **123**, 292–299.

96 D.-Y. Kim, S. Sinha-Ray, J.-J. Park, J.-G. Lee, Y.-H. Cha, S.-H. Bae, J.-H. Ahn, Y. C. Jung, S. M. Kim, A. L. Yarin and S. S. Yoon, *Adv. Funct. Mater.*, 2014, **24**, 4986–4995.

97 M. Nasim, T. Q. Vo, L. Mustafi, B. Kim, C. S. Lee, W.-S. Chu and D.-M. Chun, *Comput. Mater. Sci.*, 2019, **169**, 109091.

98 E. Samuel, J.-G. Lee, B. Joshi, T.-G. Kim, M. Kim, I. W. Seong, W. Y. Yoon and S. S. Yoon, *J. Alloys Compd.*, 2017, **715**, 161–169.

99 J. Song, H. Li, X. Chu, M. Jiang, C. Wan, Q. Zhang, Y. Chen, J. Zhang, X. Wu and J. Liu, *J. Therm. Spray Technol.*, 2023, **32**, 1203–1219.

100 D. Lou, H. Hong, M. Ellingsen and R. Hrabe, *Appl. Phys. Lett.*, 2023, **122**, 23901.

101 D. Beckel, A. Dubach, A. R. Studart and L. J. Gauckler, *J. Electroceramics*, 2006, **16**, 221–228.

102 C. Chen, E. M. Kelder, P. J. J. M. van der Put and J. Schoonman, *J. Mater. Chem.*, 1996, **6**, 765.

103 C. H. Chen, E. M. Kelder and J. Schoonman, *J. Power Sources*, 1997, **68**, 377–380.

104 S. H. Lee, A. Mahadevegowda, C. Huang, J. D. Evans and P. S. Grant, *J. Mater. Chem. A*, 2018, **6**, 13133–13141.

105 G. Tsimekas, E. Papastergiades and N. E. Kiratzis, *ECS J. Solid State Sci. Technol.*, 2017, **6**, P553–P560.

106 S. B. Weber, H. L. Lein, T. Grande and M.-A. Einarsrud, *Surf. Coatings Technol.*, 2013, **221**, 53–58.

107 J. Marsálek, J. Chmelar, J. Pocedic and J. Kosek, *Chem. Eng. Sci.*, 2015, **123**, 292–299.

108 X. Li, A. Dhanabalan, X. Meng, L. Gu, X. Sun and C. Wang, *Microporous Mesoporous Mater.*, 2012, **151**, 488–494.

109 X. Feng, J. Yang, Y. Bie, J. Wang, Y. Nuli and W. Lu, *Nanoscale*, 2014, **6**, 12532–12539.

110 W. Ren, Z. Zhang, Y. Wang, Q. Tan, Z. Zhong and F. Su, *J. Mater. Chem. A*, 2015, **3**, 5859–5865.

111 J. Ren, H. Ming, Z. Jia, Y. Zhang, J. Ming, Q. Zhou and J. Zheng, *Energy Technol.*, 2017, **5**, 1680–1686.

112 I. D. Scott, Y. S. Jung, A. S. Cavanagh, Y. Yan, A. C. Dillon, S. M. George and S.-H. Lee, *Nano Lett.*, 2011, **11**, 414–418.

113 Y. S. Jung, A. S. Cavanagh, L. A. Riley, S.-H. Kang, A. C. Dillon, M. D. Groner, S. M. George and S.-H. Lee, *Adv. Mater.*, 2010, **22**, 2172–2176.

114 M. L. Marcinek, J. W. Wilcox, M. M. Doeff and R. M. Kostecki, *J. Electrochem. Soc.*, 2009, **156**, A48.

115 D. Deng and J. Y. Lee, *J. Mater. Chem.*, 2010, **20**, 8045–8049.

116 L. Cheng, J. Yan, G.-N. Zhu, J.-Y. Luo, C.-X. Wang and Y.-Y. Xia, *J. Mater. Chem.*, 2010, **20**, 595–602.

117 M. Yoshio, H. Wang, K. Fukuda, T. Abe and Z. Ogumi, *Chem. Lett.*, 2003, **32**, 1130–1131.

118 K. Shin, D.-J. Park, H.-S. Lim, Y.-K. Sun and K.-D. Suh, *Electrochim. Acta*, 2011, **58**, 578–582.

119 J.-H. Lee, W.-J. Kim, J.-Y. Kim, S.-H. Lim and S.-M. Lee, *J. Power Sources*, 2008, **176**, 353–358.

120 Y. Yang, J. Li, D. Chen and J. Zhao, *J. Electrochem. Soc.*, 2017, **164**, A6001–A6006.

121 A. Jamaluddin, B. Umesh, F. Chen, J.-K. Chang and C.-Y. Su, *Nanoscale*, 2020, **12**, 9616–9627.

122 Z. Yan and J. Guo, *Nano Energy*, 2019, **63**, 103845.

123 A. H. Jo, S. Y. Kim, J. H. Kim, Y. A. Kim and C.-M. Yang, *Int. J. Energy Res.*, 2023, **2023**, 1–13.

124 Z. Zhang, X. Liu, Y. Wu, H. Zhao, B. Chen and W. Xiong, *J. Electrochem. Soc.*, 2015, **162**, A737–A742.

125 Z. Zhang, Y. Wang, W. Ren, Z. Zhong and F. Su, *RSC Adv.*, 2014, **4**, 55010–55015.

126 S. Zhao, L. Dong, B. Sun, K. Yan, J. Zhang, S. Wan, F. He, P. Munroe, P. H. L. Notten and G. Wang, *Small*, 2020, **16**, 1906131.

127 L. Wang, Y. Jiao, Z. Qiao, J. Qin, Y. Wang and D. Ruan, *J. Alloys Compd.*, 2023, **966**, 171574.

128 A. Jamaluddin, B. Umesh, F. Chen, J.-K. Chang and C.-Y. Su, *Nanoscale*, 2020, **12**, 9616–9627.

129 E. Peled and H. Yamin, *Isr. J. Chem.*, 1979, **18**, 131–135.

130 R. Fong, U. von Sacken and J. R. Dahn, *J. Electrochem. Soc.*, 1990, **137**, 2009.

131 K. Xu, *Chem. Rev.*, 2004, **104**, 4303–4418.

132 S. Wei, S. Choudhury, Z. Tu, K. Zhang and L. A. Archer, *Acc. Chem. Res.*, 2018, **51**, 80–88.

133 M. B. Pinson and M. Z. Bazant, *J. Electrochem. Soc.*, 2013, **160**, A243.

134 Y. Jin, B. Zhu, Z. Lu, N. Liu and J. Zhu, *Adv. Energy Mater.*, 2017, **7**, 1700715.

135 Y. Liu, D. Lin, P. Y. Yuen, K. Liu, J. Xie, R. H. Dauskardt and Y. Cui, *Adv. Mater.*, 2017, **29**, 1605531.

136 N.-W. Li, Y.-X. Yin, C.-P. Yang and Y.-G. Guo, *Adv. Mater.*, 2016, **28**, 1853–1858.

137 G. Wang, C. Chen, Y. Chen, X. Kang, C. Yang, F. Wang, Y. Liu and X. Xiong, *Angew. Chemie Int. Ed.*, 2020, **59**, 2055–2060.

138 R. G. Fedorov, S. Maletti, C. Heubner, A. Michaelis and Y. Ein-Eli, *Adv. Energy Mater.*, 2021, **11**, 2101173.

139 J. Li, N. J. Dudney, J. Nanda and C. Liang, *ACS Appl. Mater. Interfaces*, 2014, **6**, 10083–10088.

140 A. Reyes Jiménez, R. Nölle, R. Wagner, J. Hüsker, M. Kolek, R. Schmuch,

M. Winter and T. Placke, *Nanoscale*, 2018, **10**, 2128–2137.

141 Z. Tang, S. Li, Y. Li, H. Xu, Y. Yu, Y. Huang and J. Li, *Nano Energy*, 2020, **69**, 104399.

142 T. Yan, F. Li, C. Xu and H.-T. Fang, *Electrochim. Acta*, 2022, **410**, 140004.

143 R. Paste, S. A. Abbas, A. Singh, H.-C. Lin and C. W. Chu, *J. Power Sources*, 2021, **507**, 230306.

144 G. Lin, X. Zhou, L. Liu, H. Li, D. Huang, J. Liu, J. Li and Z. Wei, *RSC Adv.*, 2023, **13**, 6453–6458.

145 N. Kaisar, A. Singh, P.-Y. Yang, Y.-T. Chen, S. Li, C.-W. Pao, S. Jou and C.-W. Chu, *J. Mater. Chem. A*, 2020, **8**, 9137–9145.

146 Y. Du, C. Liu, Y. Liu, Q. Han, X. Chi and Y. Liu, *Electrochim. Acta*, 2020, **339**, 135867.

147 S. Liu, X. Xia, S. Deng, D. Xie, Z. Yao, L. Zhang, S. Zhang, X. Wang and J. Tu, *Adv. Mater.*, 2019, **31**, 1806470.

148 M. Cao, X. Huang, M. Zhao, Z. Zuo, L. Sheng, X. Xie, D. Li, X. Gao, T. Wang and J. He, *Ionics (Kiel).*, 2022, **28**, 4251–4260.

149 T. Liu, X. Wu, S. Zhu, F. Lorandi, L. Ni, S. Li, M. Sun, B. P. Bloom, D. H. Waldeck, V. Viswanathan, J. F. Whitacre and K. Matyjaszewski, *ACS Appl. Energy Mater.*, 2022, **5**, 3615–3625.

150 S. H. Cho, S. W. Hwang, B. H. Kim, K. Y. Bae, H. Yoon, S. S. Yoon and W. Y. Yoon, *J. Nanosci. Nanotechnol.*, 2016, **16**, 10607–10612.

151 K. Y. Bae, M. Kim, B. H. Kim, S. H. Cho, S. S. Yoon and W. Y. Yoon, *Solid State Ionics*, 2019, **331**, 66–73.

152 B. Zhang, W. Zou, Z. Ju, S. Qi, J. Luo, C. J. Zhang, X. Tao and L. Du, *ACS Nano*, 2023, **17**, 22755–22765.

153 J. Zhou, Z. Zhang, W. Jiang, S. Hou, K. Yang, Q. Li, L. Pan and J. Yang, *J. Alloys Compd.*, 2023, **950**, 169836.

154 M. Gao, Z. Gong, H. Li, H. Zhao, D. Chen, Y. Wei, D. Li, Y. Li, L. Yang and Y. Chen, *Adv. Funct. Mater.*, 2023, **33**, 2300319.

155 M. Imai, T. Kubota, A. Miyazawa, M. Aoki, H. Mori, Y. Komaki and K. Yoshino, *Cryst. Res. Technol.*, 2023, **58**, 2200203.

156 J. T. Zhou, X. N. Jiao, B. Yu, Y. L. Ren and W. M. Kang, *Chem. J. CHINESE Univ.*, 2017, **38**, 1018–1024.

157 W. Xiao, L. Zhao, Y. Gong, S. Wang, J. Liu and C. Yan, *RSC Adv.*, 2015, **5**, 34184–34190.

158 Y. An, X. Han, Y. Liu, A. Azhar, J. Na, A. K. Nanjundan, S. Wang, J. Yu and Y. Yamauchi, *Small*, 2022, **18**, 2103617.

159 X. Chen, W. He, L.-X. Ding, S. Wang and H. Wang, *Energy Environ. Sci.*, 2019, **12**, 938–944.

160 J. Janek and W. G. Zeier, *Nat. Energy*, 2023, **8**, 230–240.

161 R. Djenadic, M. Botros, C. Benel, O. Clemens, S. Indris, A. Choudhary, T. Bergfeldt and H. Hahn, *Solid State Ionics*, 2014, **263**, 49–56.

162 J. Li, C. Liu, M. He, S. Nie, C. Miao, S. Sun, G. Xu and W. Xiao, *Electrochim. Acta*, 2023, **439**, 141549.

163 Z. Kou, C. Miao, Z. Wang and W. Xiao, *Solid State Ionics*, 2019, **343**, 115090.

164 L. Hoffart and D. M. Schleich, *Ionics (Kiel).*, 1995, **1**, 482–487.

165 K. Tomomichi, K. Sasaki, Y. Endo, K. Kikai and T. Terai, *ECS Trans.*, 2013, **53**, 175–180.

166 E. J. van den Ham, S. Gielis, M. K. Van Bael and A. Hardy, *ACS Energy Lett.*, 2016, **1**, 1184–1188.

167 E. van den Ham, G. Maino, G. Bonneux, W. Marchal, K. Elen, S. Gielis, F. Mattelaer, C. Detavernier, P. Notten, M. Van Bael and A. Hardy, *Materials (Basel).*, 2017, **10**, 1072.

168 Z. Kou, C. Miao, P. Mei, Y. Zhang, X. Yan, Y. Jiang and W. Xiao, *Ceram. Int.*, 2020, **46**, 9629–9636.

169 E. J. van den Ham, S. Gielis, M. K. Van Bael and A. Hardy, *ACS ENERGY Lett.*, 2016, **1**, 1184–1188.

170 X. M. Wu, S. Chen, Z. Q. He, S. Bin Chen and R. X. Li, *Thin Solid Films*, 2015, **589**, 574–577.

171 Y. Kobayashi, *Solid State Ionics*, 2002, **152**–**153**, 137–142.

172 E. van den Ham, G. Maino, G. Bonneux, W. Marchal, K. Elen, S. Gielis, F. Mattelaer, C. Detavernier, P. Notten, M. Van Bael and A. Hardy, *Materials (Basel).*, 2017, **10**, 1072.

173 X. M. Wu, J. L. Liu, R. X. Li, S. Chen and M. Y. Ma, *Russ. J. Electrochem.*, 2011, **47**, 917–922.

174 J. D. Evans, Y. Sun and P. S. Grant, *ACS Appl. Mater. Interfaces*, 2022, **14**, 34538–34551.

175 N. Singh, C. Galande, A. Miranda, A. Mathkar, W. Gao, A. L. M. Reddy, A. Vlad and P. M. Ajayan, *Sci. Rep.*, 2012, **2**, 481.

176 S. Hafner, H. Guthrey, S.-H. Lee and C. Ban, *J. Power Sources*, 2019, **431**, 17–24.

177 E. C. Tredenick, S. Wheeler, R. Drummond, Y. Sun, S. R. Duncan and P. S. Grant, *J. Electrochem. Soc.*, 2024, **171**, 60531.

178 C. Huang, N. P. Young, J. Zhang, H. J. Snaith and P. S. Grant, *Nano Energy*, 2017, **31**, 377–385.

179 W. Zhou, Z. Wang, Y. Pu, Y. Li, S. Xin, X. Li, J. Chen and J. B. Goodenough, *Adv. Mater.*, 2019, **31**, 1805574.

180 B. Zhao, L. Sun, R. Ran and Z. Shao, *Solid State Ionics*, 2014, **262**, 313–318.

181 T. Danner, G. Zhu, A. F. Hofmann and A. Latz, *Electrochim. Acta*, 2015, **184**, 124–133.

182 Y.-C. Chien, A. S. Menon, W. R. Brant, D. Brandell and M. J. Lacey, *J. Am. Chem. Soc.*, 2020, **142**, 1449–1456.

183 C. Huang, A. Kim, D. J. Chung, E. Park, N. P. Young, K. Jurkschat, H. Kim and P. S. Grant, *ACS Appl. Mater. Interfaces*, 2018, **10**, 15624–15633.

184 Q. Ye, H. Liang, S. Wang, C. Cui, C. Zeng, T. Zhai and H. Li, *J. Energy Chem.*, 2022, **70**, 356–362.

185 J. L. Lutkenhaus and P. T. Hammond, *Soft Matter*, 2007, **3**, 804–816.

186 F. S. Gittleson, D. J. Kohn, X. Li and A. D. Taylor, *ACS Nano*, 2012, **6**, 3703–3711.

187 S. R. Kwon, J.-W. Jeon and J. L. Lutkenhaus, *RSC Adv.*, 2015, **5**, 14994–15001.

188 J.-W. Jeon, S. R. Kwon, F. Li and J. L. Lutkenhaus, *ACS Appl. Mater. Interfaces*, 2015, **7**, 24150–24158.

189 A. Izquierdo, S. S. Ono, J.-C. Voegel, P. Schaaf and G. Decher, *Langmuir*, 2005, **21**, 7558–7567.

190 D. M. DeLongchamp and P. T. Hammond, *Chem. Mater.*, 2003, **15**, 1165–1173.

191 A. Wolz, S. Zils, M. Michel and C. Roth, *J. Power Sources*, 2010, **195**, 8162–8167.

192 J. Wu, X. Qin, H. Zhang, Y.-B. He, B. Li, L. Ke, W. Lv, H. Du, Q.-H. Yang and F. Kang, *Carbon N. Y.*, 2015, **84**, 434–443.

193 C. Huang, M. Dontigny, K. Zaghib and P. S. Grant, *J. Mater. Chem. A*, 2019, **7**, 21421–21431.

194 W. Deng, W. Shi, Q. Liu, J. Jiang, X. Li and X. Feng, *ACS Sustain. Chem. Eng.*, 2020, **8**, 17062–17068.

195 G. B. Less, J. H. Seo, S. Han, A. M. Sastry, J. Zausch, A. Latz, S. Schmidt, C. Wieser, D. Kehrwald and S. Fell, *J. Electrochem. Soc.*, 2012, **159**, A697.

196 Y. Dai and V. Srinivasan, *J. Electrochem. Soc.*, 2016, **163**, A406.

197 E. G. Sukenik, L. Kasaei and G. G. Amatucci, *J. Power Sources*, 2023, **579**, 233327.

198 J. Yuan, X. Zhang, C. Chen, Y. Hao, R. Agrawal, C. Wang, W. Li, H. Yu, Y. Yu, X. Zhu, Z. Xiong and Y. Xie, *Mater. Lett.*, 2017, **190**, 37–39.

199 A. Dhanabalan, Y. Yu, X. Li, K. Bechtold, J. Maier and C. Wang, *MICRO-Nanotechnol. SENSORS, Syst. Appl. II*, 2010, **7679**, 76792I.

200 J. Yuan, C. Chen, Y. Hao, X. Zhang, R. Agrawal, W. Zhao, C. Wang, H. Yu, X. Zhu, Y. Yu, Z. Xiong and Y. Xie, *J. Alloys Compd.*, 2017, **696**, 1174–1179.

201 A. Dhanabalan, X. Li, R. Agrawal, C. Chen and C. Wang, *Nanomaterials*, 2013, **3**, 606–614.

202 X. Li, A. Dhanabalan and C. Wang, *J. Power Sources*, 2011, **196**, 9625–9630.

203 Y. Jiang, T. Yuan, W. Sun and M. Yan, *ACS Appl. Mater. Interfaces*, 2012, **4**, 6216–6220.

204 L. Wang, H. W. Xu, P. C. Chen, D. W. Zhang, C. X. Ding and C. H. Chen, *J. Power Sources*, 2009, **193**, 846–850.

205 C. Chen, R. Agrawal and C. Wang, *ENERGY Harvest. STORAGE Mater. DEVICES, Appl. VII*, 2016, **9865**, 986507.

206 Y. Jiang, Y. Yu, W. Sun, C. Chen, G. Meng and J. Gao, *J. Electrochem. Soc.*, 2007, **154**, E107.

207 J. Zhu, T. Yang, L. Mei, H. N. Zhang, X. Z. Yu, Q. H. Li and T. H. Wang, *Cryst. Res. Technol.*, 2013, **48**, 51–54.

208 J. Zhang, L. B. Chen, C. C. Li and T. H. Wang, *Appl. Phys. Lett.*, 2008, **93**, 264102.

209 X. Zhu, Z. Guo, P. Zhang, G. Du, R. Zeng, Z. Chen and H. Liu, *ChemPhysChem*, 2009, **10**, 3101–3104.

210 Y. Yu, L. Gu, A. Dhanabalan, C.-H. Chen and C. Wang, *Electrochim. Acta*, 2009, **54**, 7227–7230.

211 Y. Yu, C. Chen, J. Shui and S. Xie, *Angew. Chemie Int. Ed.*, 2005, **44**,

7085–7089.

212 Y. MATSUSHIMA, T. YAMAZAKI, K. MAEDA, T. NOMA and T. SUZUKI, *J. Ceram. Soc. Japan*, 2006, **114**, 1121–1125.

213 J. Mao, X. Hou, H. Chen, Q. Ru, S. Hu and K. Lam, *J. Mater. Sci. Mater. Electron.*, 2017, **28**, 3709–3715.

214 J. Ni, L. Gao and L. Lu, *J. Power Sources*, 2013, **221**, 35–41.

215 S. Niu, W. Lv, G. Zhou, H. Shi, X. Qin, C. Zheng, T. Zhou, C. Luo, Y. Deng, B. Li, F. Kang and Q.-H. Yang, *Nano Energy*, 2016, **30**, 138–145.

216 B. Liu, Y. Zhang, Z. Wang, C. Ai, S. Liu, P. Liu, Y. Zhong, S. Lin, S. Deng, Q. Liu, G. Pan, X. Wang, X. Xia and J. Tu, *Adv. Mater.*, 2020, **32**, 2003657.

217 K.-W. Sung, D.-Y. Shin and H.-J. Ahn, *J. Alloys Compd.*, 2021, **870**, 159404.

218 D. Zhu, J. Li, F. Ren, Y. Liu, J. Ren and Y. Xiong, *J. Colloid Interface Sci.*, 2023, **651**, 504–513.

219 W. Yang, Z. Wang, L. Chen, Y. Chen, L. Zhang, Y. Lin, J. Li and Z. Huang, *RSC Adv.*, 2017, **7**, 33680–33687.

220 A. Wang, J. Li, M. Yi, Y. Xie, S. Chang, H. Shi, L. Zhang, M. Bai, Y. Zhou, Y. Lai and Z. Zhang, *Energy Storage Mater.*, 2022, **49**, 246–254.

221 W.-F. Liu, K.-H. Kim and H.-J. Ahn, *J. Alloys Compd.*, 2023, **954**, 170106.

222 J. Li, C. Liu, M. He, S. Nie, C. Miao, S. Sun, G. Xu and W. Xiao, *Electrochim. Acta*, 2023, **439**, 141549.

223 S. Khandanjou, M. Ghoranneviss and S. Saviz, *J. Theor. Appl. Phys.*, 2017, **11**, 225–234.

224 L. Zhou, D. L. Danilov, F. Qiao, J. Wang, H. Li, R.-A. Eichel and P. H. L. Notten, *Adv. Energy Mater.*, 2022, **12**, 2202094.

225 V. Marangon, D. Di Lecce, D. J. L. Brett, P. R. Shearing and J. Hassoun, *J. Energy Chem.*, 2022, **64**, 116–128.

226 A. Manthiram, Y. Fu, S.-H. Chung, C. Zu and Y.-S. Su, *Chem. Rev.*, 2014, **114**, 11751–11787.

227 J. T. Williams, A. Mambu Vangu, H. Balu Mabiala, H. Bambi Mangungulu and E. K. Tissingh, *Lancet Planet. Heal.*, 2021, **5**, e327–e328.

228 P. G. Bruce, S. A. Freunberger, L. J. Hardwick and J.-M. Tarascon, *Nat. Mater.*, 2012, **11**, 19–29.

229 A. Kawase, S. Shirai, Y. Yamoto, R. Arakawa and T. Takata, *Phys. Chem. Chem. Phys.*, 2014, **16**, 9344–9350.

230 Y. V Mikhaylik and J. R. Akridge, *J. Electrochem. Soc.*, 2004, **151**, A1969.

231 S. S. Zhang, *J. Power Sources*, 2013, **231**, 153–162.

232 F. Y. Fan, W. C. Carter and Y.-M. Chiang, *Adv. Mater.*, 2015, **27**, 5203–5209.

233 S.-Y. Lang, Y. Shi, Y.-G. Guo, D. Wang, R. Wen and L.-J. Wan, *Angew. Chemie Int. Ed.*, 2016, **55**, 15835–15839.

234 T. Zhang, M. Marinescu, S. Walus, P. Kovacik and G. J. Offer, *J. Electrochem. Soc.*, 2018, **165**, A6001.

235 J. T. Lee, Y. Zhao, S. Thieme, H. Kim, M. Oschatz, L. Borchardt, A. Magasinski, W.-I. Cho, S. Kaskel and G. Yushin, *Adv. Mater.*, 2013, **25**, 4573–4579.

236 C. Liang, N. J. Dudney and J. Y. Howe, *Chem. Mater.*, 2009, **21**, 4724–4730.

237 G. He, S. Evers, X. Liang, M. Cuisinier, A. Garsuch and L. F. Nazar, *ACS Nano*, 2013, **7**, 10920–10930.

238 J. Wang, K. Jiang, B. Shen and M. Zhen, *ACS Sustain. Chem. Eng.*, 2020, **8**, 749–758.

239 X. Liang, C. Hart, Q. Pang, A. Garsuch, T. Weiss and L. F. Nazar, *Nat. Commun.*, 2015, **6**, 5682.

240 V. Marangon, D. Di Lecce, F. Orsatti, D. J. L. Brett, P. R. Shearing and J. Hassoun, *Sustain. Energy Fuels*, 2020, **4**, 2907–2923.

241 J. W. Dibden, J. W. Smith, N. Zhou, N. Garcia-Araez and J. R. Owen, *Chem. Commun.*, 2016, **52**, 12885–12888.

242 M. Agostini, J.-Y. Hwang, H. M. Kim, P. Bruni, S. Brutti, F. Croce, A. Matic and Y.-K. Sun, *Adv. Energy Mater.*, 2018, **8**, 1801560.

243 M. J. Lacey, A. Yalamanchili, J. Maibach, C. Tengstedt, K. Edström and D. Brandell, *RSC Adv.*, 2016, **6**, 3632–3641.

244 Z.-X. Chen, Q. Cheng, X.-Y. Li, Z. Li, Y.-W. Song, F. Sun, M. Zhao, X.-Q. Zhang, B.-Q. Li and J.-Q. Huang, *J. Am. Chem. Soc.*, 2023, **145**, 16449–16457.

245 D. E. Fenton, J. M. Parker and P. V Wright, *Polymer (Guildf).*, 1973, **14**, 589.

246 G. S. MacGlashan, Y. G. Andreev and P. G. Bruce, *Nature*, 1999, **398**, 792–794.

247 A. Magistris and K. Singh, *Polym. Int.*, 1992, **28**, 277–280.

248 J. Yu, X. Yan, M. Zhaofei, M. Ping, X. Wei, Y. Qinliang and Z. Yan, *Polymers (Basel).*, 2018, **10**, 1237.

249 D. Zhou, D. Shanmukaraj, A. Tkacheva, M. Armand and G. Wang, *Chem*, 2019, **5**, 2326–2352.

250 W. Wieczorek, K. Such, H. Wyciślik and J. Płocharski, *Solid State Ionics*, 1989, **36**, 255–257.

251 P. Yao, H. Yu, Z. Ding, Y. Liu, J. Lu, M. Lavorgna, J. Wu and X. Liu, *Front. Chem.*, 2019, **7**, 450022.

252 C. C. Tambelli, A. C. Bloise, A. V Rosário, E. C. Pereira, C. J. Magon and J. P. Donoso, *Electrochim. Acta*, 2002, **47**, 1677–1682.

253 J. Li, K. Zhu, Z. Yao, G. Qian, J. Zhang, K. Yan and J. Wang, *Ionics (Kiel).*, 2020, **26**, 1101–1108.

254 S. Kalnaus, A. S. Sabau, W. E. Tenhaeff, N. J. Dudney and C. Daniel, *J. Power Sources*, 2012, **201**, 280–287.

255 J. Zheng, M. Tang and Y.-Y. Hu, *Angew. Chemie Int. Ed.*, 2016, **55**, 12538–12542.

256 L. Chen, W. Li, L.-Z. Fan, C.-W. Nan and Q. Zhang, *Adv. Funct. Mater.*, 2019, **29**, 1901047.

257 S. Yu, R. D. Schmidt, R. Garcia-Mendez, E. Herbert, N. J. Dudney, J. B. Wolfenstine, J. Sakamoto and D. J. Siegel, *Chem. Mater.*, 2016, **28**, 197–206.

258 T. Sudiarti, D. Wahyuningrum, B. Bundjali and I. Made Arcana, *IOP Conf. Ser. Mater. Sci. Eng.*, 2017, **223**, 12052.

259 Y. Zhu, X. He and Y. Mo, *J. Mater. Chem. A*, 2016, **4**, 3253–3266.

260 C. Sångeland, G. Hernández, D. Brandell, R. Younesi, M. Hahlin and J. Mindemark, *ACS Appl. Mater. Interfaces*, 2022, **14**, 28716–28728.

261 V. Wurster, C. Engel, H. Graebe, T. Ferber, W. Jaegermann and R. Hausbrand, *J. Electrochem. Soc.*, 2019, **166**, A5410.

262 G. B. Appetecchi, F. Croce, J. Hassoun, B. Scrosati, M. Salomon and F. Cassel, *J. Power Sources*, 2003, **114**, 105–112.

263 W. J. Dawson, A. R. T. Morrison, F. Iacoviello, A. M. Boyce, G. Giri, J. Li, T. S. Miller and P. Shearing, *Batter. Supercaps*, 2024, **7**, e202400260.

264 S. Berg, D. Kutra, T. Kroeger, C. N. Straehle, B. X. Kausler, C. Haubold, M. Schiegg, J. Ales, T. Beier, M. Rudy, K. Eren, J. I. Cervantes, B. Xu, F. Beuttenmueller, A. Wolny, C. Zhang, U. Koethe, F. A. Hamprecht and A.

Kreshuk, *Nat. Methods*, 2019, **16**, 1226–1232.

265 Y. Eatmon, J. W. Stiles, S. Hayashi, M. Rupp and C. Arnold, *Nanomater. (Basel, Switzerland)*, 2023, **13**, 2210.

266 Z.-Y. Mao, Y.-P. Sun and K. Scott, *J. Electroanal. Chem.*, 2016, **766**, 107–119.

267 M. Hahn, D. Rosenbach, A. Krimalowski, T. Nazarenus, R. Moos, M. Thelakkat and M. A. Danzer, *Electrochim. Acta*, 2020, **344**, 136060.

268 A. J. Pearse, E. Gillette, S. B. Lee and G. W. Rubloff, *Phys. Chem. Chem. Phys.*, 2016, **18**, 19093–19102.

269 O. J. Borkiewicz, K. W. Chapman and P. J. Chupas, *Phys. Chem. Chem. Phys.*, 2013, **15**, 8466.

270 B. Chen, H. Huang, Y. Wang, Z. Shen, L. Li, Y. Wang, X. Wang, X. Li and Y. Wang, *ChemElectroChem*, 2022, **9**, e202101277.

271 J. Tan, X. Li, Q. Li, Z. Wang, H. Guo, G. Yan, J. Wang and G. Li, *Ionics (Kiel).*, 2022, **28**, 3233–3241.

272 K. Nie, X. Wang, J. Qiu, Y. Wang, Q. Yang, J. Xu, X. Yu, H. Li, X. Huang and L. Chen, *ACS Energy Lett.*, 2020, **5**, 826–832.

273 W. Zhang, S. Gui, W. Li, S. Tu, G. Li, Y. Zhang, Y. Sun, J. Xie, H. Zhou and H. Yang, *ACS Appl. Mater. Interfaces*, 2022, **14**, 51954–51964.

274 C. Huang, A. Kim, D. J. Chung, E. Park, N. P. Young, K. Jurkschat, H. Kim and P. S. Grant, *ACS Appl. Mater. Interfaces*, 2018, **10**, 15624–15633.

275 X. H. Liu and J. Y. Huang, *Energy Environ. Sci.*, 2011, **4**, 3844–3860.

276 T. Zhang, J. Gao, H. P. Zhang, L. C. Yang, Y. P. Wu and H. Q. Wu, *Electrochem. commun.*, 2007, **9**, 886–890.

277 P. Li, H. Kim, S.-T. Myung and Y.-K. Sun, *Energy Storage Mater.*, 2021, **35**, 550–576.

278 K. Feng, M. Li, W. Liu, A. G. Kashkooli, X. Xiao, M. Cai and Z. Chen, *Small*, 2018, **14**, 1702737.

279 F. Shi, Z. Song, P. N. Ross, G. A. Somorjai, R. O. Ritchie and K. Komvopoulos, *Nat. Commun.*, 2016, **7**, 11886.

280 E. Moyassari, T. Roth, S. Kücher, C.-C. Chang, S.-C. Hou, F. B. Spingler and A. Jossen, *J. Electrochem. Soc.*, 2022, **169**, 10504.

281 S.-B. Son, L. Cao, T. Yoon, A. Cresce, S. E. Hafner, J. Liu, M. Groner, K. Xu and C. Ban, *Adv. Sci.*, 2019, **6**, 1801007.

282 J. R. Szczech and S. Jin, *Energy Environ. Sci.*, 2011, **4**, 56–72.

283 M. Li, X. Hou, Y. Sha, J. Wang, S. Hu, X. Liu and Z. Shao, *J. Power Sources*, 2014, **248**, 721–728.

284 L. Chen, X. Xie, B. Wang, K. Wang and J. Xie, *Mater. Sci. Eng. B*, 2006, **131**, 186–190.

285 T. Yim, S. J. Choi, Y. N. Jo, T.-H. Kim, K. J. Kim, G. Jeong and Y.-J. Kim, *Electrochim. Acta*, 2014, **136**, 112–120.

286 H. Jo, J. Kim, D.-T. Nguyen, K. K. Kang, D.-M. Jeon, A.-R. Yang and S.-W. Song, *J. Phys. Chem. C*, 2016, **120**, 22466–22475.

287 H. Kang, H. Kim, C. Yeom and M. J. Park, *ACS Appl. Energy Mater.*, 2022, **5**, 4673–4683.

288 L. Hu, W. Xia, R. Tang, R. Hu, L. Ouyang, T. Sun and H. Wang, *Front. Chem.*, 2020, **8**, 529142.

289 X. Li, G. Zhang, L. Zhang, M. Zhong and X. Yuan, *Int. J. Electrochem. Sci.*, 2015, **10**, 2802–2811.

290 J. Kim, J. Choi, K. Park, S. Kim, K. W. Nam, K. Char and J. W. Choi, *Adv. Energy Mater.*, 2022, **12**, 2103718.

291 N. S. Hochgatterer, M. R. Schweiger, S. Koller, P. R. Raimann, T. Wöhrle, C. Wurm and M. Winter, *Electrochem. Solid-State Lett.*, 2008, **11**, A76.

292 S. He, S. Huang, S. Wang, I. Mizota, X. Liu and X. Hou, *Energy & Fuels*, 2021, **35**, 944–964.

293 J. Chen, X. Fan, Q. Li, H. Yang, M. R. Khoshi, Y. Xu, S. Hwang, L. Chen, X. Ji, C. Yang, H. He, C. Wang, E. Garfunkel, D. Su, O. Borodin and C. Wang, *Nat. Energy*, 2020, **5**, 386–397.

294 S.-H. Ng, J. Wang, D. Wexler, K. Konstantinov, Z.-P. Guo and H.-K. Liu, *Angew. Chemie Int. Ed.*, 2006, **45**, 6896–6899.

295 L. Liu, P. Guan and C. Liu, *J. Electrochem. Soc.*, 2017, **164**, A3163.

296 N. Kana, S. Olivier-Archambaud, T. Devic and B. Lestriez, *Electrochem. commun.*, 2023, **151**, 107495.

297 S. Lawes, Q. Sun, A. Lushington, B. Xiao, Y. Liu and X. Sun, *Nano Energy*, 2017, **36**, 313–321.

298 M. Zheng, C. Wang, Y. Xu, K. Li and D. Liu, *Electrochim. Acta*, 2019, **305**, 555–562.

299 C. G. Kolb, M. Lehmann, D. Kulmer and M. F. Zaeh, *Heliyon*, 2022, **8**, e11988.

300 L. Liu, M. A. Gonzalez-Olivares, H. Bai, H. Yi and S. Song, *Chem. Phys.*,

2019, **525**, 110405.

301 C. Huang, A. Kim, D. J. Chung, E. Park, N. P. Young, K. Jurkschat, H. Kim and P. S. Grant, *ACS Appl. Mater. Interfaces*, 2018, **10**, 15624–15633.

302 K. A. Hays, R. E. Ruther, A. J. Kukay, P. Cao, T. Saito, D. L. Wood and J. Li, *J. Power Sources*, 2018, **384**, 136–144.

303 X. Zhao, S. Niketic, C.-H. Yim, J. Zhou, J. Wang and Y. Abu-Lebdeh, *ACS Omega*, 2018, **3**, 11684–11690.

304 A. Pénicaud and C. Drummond, *Acc. Chem. Res.*, 2013, **46**, 129–137.

305 L. Vaisman, H. D. Wagner and G. Marom, *Adv. Colloid Interface Sci.*, 2006, **128**–**130**, 37–46.

306 Y. Ha, C. Stetson, S. P. Harvey, G. Teeter, B. J. Tremolet de Villers, C.-S. Jiang, M. Schnabel, P. Stradins, A. Burrell and S.-D. Han, *ACS Appl. Mater. Interfaces*, 2020, **12**, 49563–49573.

307 S. J. An, J. Li, C. Daniel, D. Mohanty, S. Nagpure and D. L. Wood, *Carbon N. Y.*, 2016, **105**, 52–76.

308 K. W. Schroder, H. Celio, L. J. Webb and K. J. Stevenson, *J. Phys. Chem. C*, 2012, **116**, 19737–19747.

309 J. Asenbauer, T. Eisenmann, M. Kuenzel, A. Kazzazi, Z. Chen and D. Bresser, *Sustain. Energy Fuels*, 2020, **4**, 5387–5416.